

STAR
mc

QUARTERLY PROGRESS REPORT

No. 82

JULY 15, 1966

GPO PRICE	\$	_____
CFSTI PRICE(S)	\$	_____
Hard copy (HC)	\$	7.00
Microfiche (MF)		1

ff 653 July 65

MASSACHUSETTS INSTITUTE OF TECHNOLOGY
RESEARCH LABORATORY OF ELECTRONICS
CAMBRIDGE, MASSACHUSETTS

FACILITY FORM 602	N66-37215	(THRU)
	312	1
	CR-78264	23
	(PAGES)	(CODE)
	(NASA CR OR TMX OR AD NUMBER)	(CATEGORY)

The Research Laboratory of Electronics is an interdepartmental laboratory in which faculty members and graduate students from numerous academic departments conduct research.

The research reported in this document was made possible by support extended the Massachusetts Institute of Technology, Research Laboratory of Electronics, by the following agencies.

Joint Services Electronics Programs (U.S. Army, U.S. Navy, and U.S. Air Force)

Contract DA 36-039-AMC-03200(E)

U.S. Air Force—Electronic Systems Division

Contract AF 19(628)-2487

U.S. Air Force—Research and Technology Division

Contract AF 33(615)-3885

Contract AF 33(615)-3489

U.S. Navy—Office of Naval Research

Contract Nonr-1841-(42)

/ National Aeronautics and Space Administration

Grant NsG-496

Grant NsG-22-009-(163)

Grant NGR-22-009-091

Grant NsG-334

Grant NsG-419

Contract NSR-22-009-120

National Institutes of Health

Grant 2 PO1 MH-04737-06

Grant 5 RO1 NB-04985-03

National Science Foundation

Grant GK-835

Grant GK-57

Grant GK-614

U.S. Atomic Energy Commission

Contract AT (30-1)-3581

Contract AT (30-1)-3285

Contract AT (30-1)-1842

The Teagle Foundation, Inc. Grant

Support of projects is acknowledged in footnotes to the appropriate sections.

Reproduction in whole or in part is permitted for any purpose of the United States Government.

MASSACHUSETTS INSTITUTE OF TECHNOLOGY
RESEARCH LABORATORY OF ELECTRONICS

QUARTERLY PROGRESS REPORT No. 82

July 15, 1966

Submitted by: H. J. Zimmermann
G. G. Harvey

TABLE OF CONTENTS

Personnel	viii
Publications and Reports	xvi
Introduction	

GENERAL PHYSICS

I.	Molecular Beams	1
	Neutrality of the Neutron	1
II.	Molecular Collisions	7
III.	Microwave Spectroscopy	9
	Work Completed	9
	Ultrasonic Attenuation and Size Effect in Gallium	9
	Use of EMR to Study Magnetic Field Homogeneity and Cavity Configurations for Large Aqueous Samples	10
	Bolometric Detection of Coherent Phonons in Quartz	10
	Apparatus for Measuring Phonon Dispersion in Single Crystal-line Material	11
	Superconducting Bolometers: Detection of Ambient Acoustic Noise	11
	Bolometric Detection of Coherent 9-GHz Longitudinal Phonons in X-Cut Quartz	12
	Erratum: Minimum Detectable Power in Superconducting Bolometers	16
IV.	Radio Astronomy	17
	Absolute Flux Measurements of Cassiopeia A and Taurus A at 3.64 and 1.94 cm	17
	Radio Detection of Interstellar O ¹⁸ H ¹	31
	K-band Measurements	33
	Atmospheric Absorption at 72 Gc/sec	33
	Observations of Microwave Emission from Atmospheric Oxygen	36
V.	Solid State Microwave Electronics	43
VI.	Optical and Infrared Spectroscopy	45
	Work Completed	45
	Infrared Reflectivity and Optical Constants of Tektites	45
	Low-Frequency Vibrations in Ammonium-Chloride and Ammonium-Bromide Crystals	48

CONTENTS

VII.	Noise in Electron Devices	55
	Quantum Noise in the Laser Oscillator with Finite Material Bandwidth	55
VIII.	Physical Electronics and Surface Physics	65
	Surface Physics	65
	Single Phonon Accomodation Coefficients	65
	Surface Properties of Thermionic Electrodes	71
	Thermionic Characteristics of Single-Crystal Tungsten Filament Exposed to Oxygen	71
	Contact Potential Measurements of the Work Function of Tantalum as a Function of Cesium Coverage	77
	Free-Molecule Flow Fields	83
	Investigation of Free-Molecule Flow Fields	83
IX.	Physical Acoustics	87
	Acoustic Wave Amplification	87
	Erratum: Lateral Acoustic Instability	90
X.	Electrodynamics of Moving Media	91
	Status of Research	91
	Amplification at Subcritical Drift Velocities	91

PLASMA DYNAMICS

XI.	Plasma Physics	93
	Electromechanical Device to Feed Experimental Data Automatically into a Time-shared Computer System - I.	93
	Diffusion Waves in Hollow-Cathode Arc	97
	Spatially Resolved Measurements of Emission Line Profiles	99
	Microwave Scattering from an Electron-Beam Produced Plasma	109
	Bubble Windows for Far Infrared Radiation	114
XII.	Gaseous Electronics	123
	Low-Frequency Oscillations in a Electron-Cyclotron Resonance Discharge	123

CONTENTS

XIII.	Plasmas and Controlled Nuclear Fusion	127
	Active Plasma Systems	127
	System C: Ion-Cyclotron Wave Generation	127
	Beam-Plasma Discharge: System D	131
	Electron Density Measurements for Beam-Plasma Systems with a 4-mm Interferometer	138
	Spectrographic Measurement of Electron Temperature in the Beam-Plasma Discharge	144
	Computer Simulation of the Beam-Plasma Discharge	146
	Theory of Plasma Excitation by a Line-Charge Source	152
	Cross-Field Beam-Plasma Interactions	154
	Dynamics of the Plasma Boundary	157
	Applied Plasma Physics Related to Controlled Nuclear Fusion	163
	Generation of a Quiescent Arc Plasma	163
	Universal Instability in a Collision-Dominated Plasma	169
XIV.	Energy Conversion Research	173
	Power Systems with Liquid-Metal Generators	173
	Magnetohydrodynamic Power Generation for Nuclear- Powered Sea-Going Vessels	173
	Interaction of a Single Sphere or Cylinder with Traveling Magnetic Field	177
	Alkali-Metal Magnetohydrodynamic Generators	183
	Status of Research: Alkali-Metal Vapor Magnetohydrodynamic Generators	183
	Hall Instabilities and Their Effect on Magnetohydrodynamic Generators	184
	Stability Criterion for Magnetoacoustic Waves	184
XV.	Spontaneous Radiofrequency Emission from Hot-Electron Plasmas	187
	Observation of Enhanced Cyclotron Radiation from an Electron-Cyclotron Resonance Discharge	187
XVI.	Interaction of Laser Radiation with Plasmas and Nonadiabatic Motion of Particles in Magnetic Fields	193
	Laser Radiation Thomson-Scattered by an Electron Beam	193
	Nonadiabatic Trapping Experiment	193

CONTENTS

q

COMMUNICATION SCIENCES AND ENGINEERING

XVII.	Statistical Communication Theory	207
	Work Completed	207
	Statistics of Switching-Time Jitter for a Tunnel Diode Threshold-Crossing Detector	207
	State-Variable Approach to Continuous Estimation	207
	Direct-Current Converter Using Two-State Modulation	207
	Digital Simulation of an FM Band-Dividing Demodulator	208
	Effects of Directional Radiation from Violins upon Their Recorded Sound	208
	A Transistorized Filter for the Reduction of Pulse-type Noise	208
	Subjective Studies of Speech Quantization	208
	Design and Construction of a Tape Delay System	208
XVIII.	Processing and Transmission of Information	209
	Block-Coding Bound for Communication on an Incoherent White Gaussian Noise Channel	209
XIX.	Linguistics	215
	A Characterization of Essentially Context-Sensitive Languages	215
XX.	Cognitive Information Processing	221
	Cognitive Processes	221
	An Illusion That Dissociates Motion, Object, and Meaning	221
	Picture Processing	223
	Optimum Binary Code	223
	Error in Fixed-Length Nonredundant Codes	225
	Effect of BSC on PCM Picture Quality	228
	Pattern-Recognition Studies	237
	Computer Simulation of Biological Pattern Generation: A Preliminary Report	237

CONTENTS

XXI.	Communications Biophysics	
	Work Completed	
	High Speed Electromechanical Shutter for Visual Neurophysiology	
	Computer Simulation of Sequence of Activation in Fibrillating Heart	
	Control of a Servo Respirator Using Muscle Potentials	249
	Cochlear Potentials in Guinea Pigs with Surgically Produced Endolymphatic Hydrops	249
	Temperature- and Humidity-Regulating Apparatus for a Microscope-Stage Incubator	249
	A High Speed Analog-Digital Converter Input and Comparator Circuit Design	249
	Psychoacoustics	250
	General Remarks	250
	Analysis of Phase-Detector Model of Binaural Unmasking	251
	Subjective Octaves	251
	Just-Noticeable Differences in Frequency Ratio	252
	CBL 16-B: An Instrument for Multisubject Two-Alternative Forced-Choice Experiments	252
	Psychlops: A System for Using the PDP-4 Computer for On-Line Adaptive Psychophysical Experiments	252
	General-Purpose Computer Facility	254
	Tissue Dynamics of Brain Tissue <u>in vitro</u>	258
	Time Pattern of Complex Basilar-Membrane Vibrations and Its Relation to Pitch Phenomena	263
	Statistical Theory of Fields	267
XXII.	Neurophysiology	275
	Summary of Research Progress: Theory of the Reticular Formation	275
	Realizability of a Neural Network Capable of All Possible Modes of Oscillation	280
XXIII.	Cardiovascular Systems	287
	Status of Research	287
XXIV.	Computation Research	293
	A Computer Indexing Program	293
	Example of Symbolic Manipulation of Polynomials in MAD	294
	Author Index	297

PERSONNEL

Administration

Prof. H. J. Zimmermann, Director
Prof. G. G. Harvey, Associate Director
Mr. R. A. Sayers, Assistant Director

Advisory Committee

Dean G. S. Brown
Prof. W. W. Buechner
Prof. W. B. Davenport, Jr.
Prof. P. Elias
Prof. G. G. Harvey
Prof. A. G. Hill
Prof. I. W. Sizer
Dean J. B. Wiesner
Prof. H. J. Zimmermann
(Chairman)

Research Committee

Dean S. C. Brown
Prof. L. J. Chu
Prof. M. Halle
Prof. G. G. Harvey
Prof. W. A. Rosenblith
Mr. R. A. Sayers
Prof. W. M. Siebert
Prof. L. D. Smullin
Prof. M. W. P. Strandberg
Prof. P. D. Wall
Prof. J. R. Zacharias
Prof. H. J. Zimmermann
(Chairman)

Professors

Allis, W. P.
Barrett, A. H.
Bitter, F.
Brown, S. C.
Burke, B. F.
Chomsky, N. A.
Chu, L. J. (Absent)
Eden, M.
Edgerton, H. E.
Elias, P.
Gyftopoulos, E. P.
Halle, M.

Harvey, G. G.
Haus, H. A.
Hill, A. G.
Huffman, D. A.
Jakobson, R.
Kerrebrock, J. L.
King, J. G.
Kurylowicz, J. (Visiting)
Lee, Y. W.
Mason, S. J.
Minsky, M. L.
Rose, D. J.
Rosenblith, W. A.

Shannon, C. E.
Shapiro, A. H.
Siebert, W. M.
Smullin, L. D. (Absent)
Stevens, K. N.
Strandberg, M. W. P.
Wall, P. D.
Warren, B. E.
Waugh, J. S.
Wozencraft, J. M. (Absent)
Zacharias, J. R.
Zimmermann, H. J.

Associate Professors

Bekefi, G.
Bers, A.
Bose, A. G.
Brown, G. A.
Dennis, J. B.
Fodor, J. A.
Gallager, R. G.
Garland, C. W.

Geselowitz, D. B. (Visiting)
Hoffman, M. A.
Ingard, K. U.
Jackson, W. D. (Absent)
Jacobs, I. M.
Katz, J. J.
Klima, E. S.
Kuhl, R. L.

Loewenthal, M.
Matthews, G. H.
McCune, J. E.
Oates, G. C.
Peake, W. T.
Pomorska, Krystyna
Rafuse, R. P.
Schreiber, W. (Absent)

PERSONNEL

Associate Professors (continued)

Searle, C. L.
Taillet, J. (Visiting)

Taylor, E. F. (Visiting)
Teager, H. M.

Van Trees, H. L.
Watkins, C.

Assistant Professors

Anderson, J. (1)
Bernard, G. D. (1)
Billman, K. W.
Black, W. L. (1)
Blum, M.
Bowers, K. W.
Brown, J. E.
Bruce, J. D.
Carabateas, E. N. (Absent)
Cheng, H.
Dean, L. W., III
Dupree, T. H.
Fiocco, G.
Getty, W. D.
Goutmann, M. M. (1)

Gray, P. R. (1)
Heiser, W. H.
Hennie, F. C., III
Hoversten, E. V. (1)
Huang, T. S.
Ingraham, J. C.
Kahn, R. E. (1)
Katona, P. G. (1)
Kennedy, R. S.
Kinsey, J. L.
Kiparsky, R. P. V.
Klatt, D. H. (1)
Lee, H. B.
Lenoir, W. B. (1)

Lidsky, L. M.
Oppenheim, A. V. (1)
Perry, C. H.
Pierson, E. S.
Siambis, J. G. (1)
Staelin, D. H. (1)
Stickney, R. E.
Stockham, T. G., Jr.
Suzuki, R. (Visiting)
Tretiak, O. J.
Troxel, D. E.
Weiss, R.
Weiss, T. F.
Yip, S.
Zare, R. N.

Lecturers

Cohen, D. (Visiting)
Cooper, R. S.

Ferretti, E. F.
Graham, J. W.

Instructors

Bauer, R. F.
Burns, S. K.
Crystal, T. H.
Henke, W. L.
Kuroda, S-Y.

Nelsen, D. E.
Perker, R. R.
Prabhu, V. K.
Sachs, M. B.

Schafer, R. W.
Schindall, J. E.
Schneider, H. M.
Snyder, D. L.
Spann, R. N.

Research Associates

Barnett, G. O.
Bromberger, S.
Durlach, N. I.
Garrett, M. F.
Grams, G. W.

Hall, R. D.
Herzberger, H. G.
Kolers, P. A.
Kornacker, K.
Lee, F. F.
Lettvin, J. Y.

Newmark, R. A.
Papert, S. A.
Sears, R. E. J.
Smith, T. G., Jr.
Zisk, S. H.

Guests

Beddoes, M. P.
Bullowa, Margaret
Chang, Teresa

Fraser, J. B.
Kessler, A. R.
Nevo, E.

Peterson, P. L.
Sezaki, N.
Walker, D. E.

(1) Engineering Postdoctoral Fellow

PERSONNEL

Visiting Scientists

Moreno-Diaz, R.
Nomoto, M. (5)

Research Affiliates

Barlow, J. S.
Brodey, W. M.
Brown, R. M.

Crist, A. H.
Cunningham, J. E.
Fohl, T.

Howland, B.
Langbein, D.
McLardy, T.

Postdoctoral Fellows

Charney, Elinor K. (3)
Hartman, H. (1)
Lampis, G. (2)

Natapoff, A. (1)
Pickard, Barbara C. G. (1)
Pickard, W. F. (1)
Schwartz, A. (1)

Slawson, A. W. (3)
Songster, G. F. (1)
Taub, A. (1)

R. L. E. Research Staff

Andrews, J. M.
Barrett, J. W.
Benhaim, N.
Burgess, R. G.
Chung, S-H
Crowther, Patricia P.
Cunningham, A. W. B.
Currano, J. J.
Davis, Heather
Edwards, D. J.
Fischler, H.
Fontaine, C. L.
Fratar, Gail M.
Harwitt, Joan
Ingersoll, J. G.

Ingham, K. R.
Jensen, E. R.
Johnston, W. D., Jr.
Kiang, N. Y. S.
Kierstead, J. D.
Levy, Rachel J.
Mattison, E. M.
McCarthy, J. J.
McCulloch, W. S.
McLoud, Veronica E.
Menyuk, Paula
Mulligan, W. J.
Nacamuli, R. M.
Novenski, A. F.

O'Brien, F. J.
Pennell, Martha M.
Perkell, J. S.
Pitts, W. H.
Portinari, J. C.
River, Eleanor C.
Rojas Carona, R.R.
Rosebury, F.
Ryan, L. W. (Absent)
Shaw, M. L.
Tse, F. Y-F
Vidale, Eda Berger
Viertel, J. J.
Wawzonek, J. J.
Wickelgren, G. L.

Research Assistants

Austin, M. E. (4)
Bartsch, R. R.
Bhushan, A. K.
Brown, T. S.
Catto, P. J.
Chan, S. W-C
Chandra, A. N.
Chapin, P. G.
Chase, D.
Ching, H.
Citron, A.

Colombant, D. G.
Cornew, R. W.
Dean, Janet P.
DeRijk, R. P. G.
DeWolf, J. B.
Evers, W. H., Jr.
Ezekiel, S.
Fisher, C. H.
Flynn, R. W.
Fisher, C. H.

Frediani, J. K.
Gabrielian, A.
Gadzuk, J. W.
Good, W. E., Jr.
Graham, D. N.
Gustafson, K. T.
Ham, D. O.
Hebel, W. T., Jr.
Herba, F.
Hill, R. A.
Hougen, M. L.

(1) National Institutes of Health Fellow
(2) Senior Fellow
(3) R. L. E. Fellow

(4) Lincoln Laboratory Staff Associate
(5) International Postdoctoral
National Institutes of Health Fellow

PERSONNEL

Research Assistants (continued)

Huang, T.	McNary, C. A.	Snyder, D. D.
Khanna, M.	Mendelsohn, R. L.	Speck, C. E.
Kirk, R.	Milne, D. C.	Spiridon, A.
Kitrosser, D. F.	Moir, R. W.	Steinbrecher, D. H.
Klouman, P. H. B.	Moldon, J. C.	Stone, E. T.
Koons, H. C.	Moran, J. M.	Taylor, M. G.
Kusse, B. R.	Moses, J.	Thome, R. J.
Lavoie, G. A.	Naqvi, M.	Tomlinson, R. S.
Levy, E. K.	Oates, D. E.	Wagner, C. E.
Lieberman, M. A.	Offenberger, A. A.	Wallace, R. N.
Liu, J-H	Papadopoulos, G. D.	Weinberg, S.
Logan, R. M.	Peterson, D. D.	Williams, J. A.
Lou, D. Y-S	Poussart, D. J. M.	Woo, J. C.
Mangano, J. A.	Pruslin, D. H.	Yamamoto, S.
Makhoul, J. J.	Qualls, C. B.	Young, R. A.
Maul, M. K.	Ribbeck, C. S.	Zeiders, G. W., Jr.
	Rogers, A. E. E.	

Graduate Assistants

Andrews, M. L.	Kronquist, R. L.	Reifenstein, E. C. , III
Cohen, A. J.	Kukulich, S. G.	Reznek, S. R.
Ewing, H.	Langdon, R. M., Jr.	Rogoff, G. L.
Fertel, Jeanne H.	Llewellyn-Jones, D. T.	Silk, J. K.
Free, J. U., Jr.	Macon, J. L.	Smith, T. B.
Garosi, G. A.	Manheimer, W. M.	Wilheit, T. T., Jr.
Geis, M. L.	McClintock, J. E.	Wright, B. L.
Golub, R.	Muehlner, D. J.	Young, E. F.
Guttreich, G. L.	Pleasance, L. D.	Yung, B. N.

Teaching Assistants

Anderson, G. B.	Fehrs, D. L.	Metz, P. J.
Bice, P. K.	Freeman, J. A.	Moxon, E. C.
Blessner, B.	Glaser, J.	Ng, L. C.
Brown, T. R.	Greenwood, R. E.	Peters, P. S., Jr.
Bruce, R. D.	Guttman, D. S.	Plummer, W. W.
Colburn, H. S.	Harris, R. V., III	Portner, E. M., Jr.
Crane, D. E.	Helman, H. L.	Poulo, L. R.
Dum, C. T.	Hull, A.	Samis, M. A.
Edwards, R. K.	Kosowski, J. F.	Schaefer, D. W.
Eisenberg, M.	Lazarus, M. B.	Seitz, C. L.
Evans, J. E.	Levin, M. I.	Singer, J. J.

Graduate Students

Allen, R. J. (1)	Bedell, G. D., IV (4)	Bruek, S. R. J. (3)
Anderson, J. A. (2)	Bever, T. G. (5)	Bucher, E. A. (3)
Arnstein, D. S.	Bigham, T. D., Jr. (6)	Cain, C. A.
Baggeroer, A. B. (3)	Blum, G. D. (3)	Caldwell, D. (3)
Barnwell, T. P., III (3)	Braida, L. D. (3)	Callen, J. D. (7)
	Browne, E. W. (4)	

(1) RCA Fellow

(2) National Institutes of Health Fellow

(3) National Science Foundation Fellow

(4) National Defense Education Act Fellow

(5) Harvard Fellow

(6) Bell Telephone Laboratories Fellow

(7) Atomic Energy Commission Fellow

PERSONNEL

Graduate Students (continued)

Carter, R. J. (1)	Kayne, R. S. (10)	Rolland, A. E.
Chapin, P. G. (13)	Kimball, J. P. (1)	Ross, A. H. M. (4)
Clark, N. A. (4)	Krakauer, L. J. (4)	Ross, J. A. (4)
Clarke, J. F. (2)	Leonardi-Cattolica, A. M. (17)	Ross, J. R. (1)
Collins, L. D. (4)	Lopez, O. (14)	Saleh, Adel A. M. (32)
Cruise, T. J. (4)	Lubin, M. D.	Schulz, H. M., III (4)
Davis, A. M. (6)	Mark, R. G.	Shoap, S. C. (14)
Davis, J. A. (4)	Max, J.	Shupe, D. S. (4)
Decher, R. (7)	Mazza, C. (30)	Simpson, J. I. (4)
Doane, J. L. (8)	McDowell, G. O. (4)	Smith, M. G.
Dougherty, R. C. (1)	Mendell, L. M. (1)	Snow, M. S. (4)
Emonds, J. E. (1)	Merrill, E. G. (19)	Spielman, C. A. (10)
Falconer, D. D. (9)	Mildonian, A. A., Jr. (6)	Stafford, J. C. (6)
Feldman, D. A.	Mozzi, R. L. (18)	Stanley, R. J. (4)
Fetz, E. E. (4)	Mueller, P. E. (20)	Stephenson, R. S.
Fidelholtz, J. L. (10)	Murakami, M. (21)	Strong, R. M. (8)
Flannery, D. L. (4)	Myers, Amy E. (10)	Swain, D. W. (25)
Fukumoto, A. (11)	Naro, A. J. (10)	Tate, R. H. (6)
Gaut, N. E. (7)	Nelson, G. P. (3)	Thomae, I. H. (4)
George, E. V. (12)	Newell, J. E. (6)	Thomas, R. H. (7)
Goldberg, A. J. (14)	Nolan, J. J., Jr.	Thornburg, C. O., Jr.
Goldfield, R. (10)	Odette, G. (2)	Toop, R. W.
Greenspan, R. L.	Owolo, D. (16)	Tremain, R. E., Jr. (14)
Gruber, J. S. (10)	Parrish, J. H. (4)	Tsien, R. W.
Guinan, J. J., Jr. (4)	Perlmutter, D. M. (10)	von Bismarck, G.
Guldi, R. L. (14)	Perozek, D. M. (14)	Vugrinec, Z. (27)
Haccoun, D.	Peterson, R.	Walker, J. L.
Harris, J. W. (3)	Pilc, R. (6)	Wang, C. H. (28)
Hartline, D. K. (3)	Pinkston, J. T., III (4)	Weinstein, C. J. (14)
Hartmann, P. H. (15)	Pittenger, L. C. (2)	Westerfeld, E. C.
Heggstad, H. M.	Rabiner, L. R. (4)	Wickelgren, Barbara G. (4)
Heller, J. A. (16)	Rack, H. J.	Wiederhold, M. L. (3)
Hofmann, T. R. (1)	Ramshaw, J. D. (4)	Wilson, T. L. (4)
Houtsma, A. J. M.	Raymond, S. A.	Wolaver, D. H. (4)
Hsiao, H. S.	Reeves, J. P. (1)	Wolf, J. J.
Hudis, M. (2)	Reilly, R. D. (4)	Woo, Nancy H. (1)
Huntington, T. A.	Richters, J. S. (4)	Wright, D. A. (29)
Jackendoff, R. S. (10)	Riehl, J. W. (23)	Wright, W. A.
Jameson, P. W.	Rizk, H. M. (24)	wu, W.
Katyl, R. H. (4)	Roberson, J. E. (6)	Ysek, R. (6)

- (1) National Institutes of Health Trainee
- (2) Atomic Energy Commission Fellow
- (3) National Institutes of Health Fellow
- (4) National Science Foundation Fellow
- (5) Sperry-Rand Fellow
- (6) Bell Telephone Laboratories Fellow
- (7) NASA Fellow
- (8) Hertz Foundation Fellow
- (9) Hughes Aircraft Fellow
- (10) National Defense Education Act
- (11) Kennicott Copper Corporation Fellow
- (12) RCA Fellow
- (13) Danforth Fellow
- (14) National Science Foundation Trainee
- (15) Grass Fund Fellow
- (16) Xerox Fellow

- (17) Whitney Predoctoral Fellow
- (18) Raytheon Fellow
- (19) Public Health Service Trainee
- (20) American Can Company Fellow
- (21) Hyogo Prefecture-Japan Scholarship
- (22) National Research Council Fellow
- (23) Proctor and Gamble Fellow
- (24) International A. E. C. Fellow
- (25) NASA Trainee
- (26) Fulbright Fellow
- (27) United Nations Fellow
- (28) Woodrow Wilson Fellow
- (29) Royal Canadian Air Force
- (30) Science Teaching Center Grant
- (31) National Science Foundation Co-op Fellow
- (32) U. A. R. Scholarship

PERSONNEL

Undergraduates (Thesis or Special Problems)

Babitch, D.
Byrd, G. C., III
 Chase, D. L.
 Costa, R. A.
 Davidow, J. E.
 Eckstein, P. F.
 Eggers, T. W.
 Galiger, P. E.
 Goodman, J. M.
 Greenberg, S.
 Hayashi, S. J.
 Hiatt, J. B.

Hildebrand, S. J.
 Jones, R. L.
 Juvkam-Wold, H. C.
 King, A. P.
 Leary, A. R.
 Lipsey, S. D.
 Mallary, M. L.
 Mannos, J. L.
 Masters, J. M.
 Memishian, J., Jr.
 Morgan, H. D.

Patterson, J.
 Plice, W. A.
 Pursell, R. A.
 Rhyne, T. L.
 Solin, J. R.
 Steele, J. M.
 Strand, T. F.
 Warshaw, A. S.
 Weidner, M. Y.
 Williams, F. K.
 Wolfe, P. D.
 Zimmerman, R. R.

Student Employees

Ackerman, W. B.
 Ashton, B. H.
 DeAngelis, D. L.
 Diener, Merle S.
 Famiglietti, Rita A.
 Funderburg, J. C.
 Hung, H. L.
 Johnson, L. G.
 Lackner, J. R.
 Law, Sara

Lesser, E.
 Li, E.
 Marandino, G. F.
Michel, A.
 Mitchell, M. M.
 Naqvi, A. A.
 O'Lague, P. H.
 Partridge, L. D.
 Perkins, D. N., Jr.
 Postol, T. A.

Ray, J. N.
 Reintjes, J. F.
 Rosen, M. A.
 Sahagen, Judith A.
 Solarz, R. W.
 Spalding, J. W.
 Stamm, P. L.
 Sturges, R. H., Jr.
 Toong, H-M.
 Zucker, R. S.

R. L. E. Administrative Staff

Duffy, D. F.
 Hewitt, J. H.
 Keyes, R. V., Jr.

Sayers, R. A.
 Smith, P. L.
 Thomas, Helen L.

Administrative Assistant

Bella, C. J.

Office Clerks

Barron, Gladys G.
 Billings, W. J.
 Chase, Arbella P.
 Dilworth, Doris L.
 Engler, R. R.

Fishman, Bette
 Greene, Yvonne E.
 Gregor, C. A.
 Ippolito, Dorothy A.

Peck, J. S.
 Ruggere, P. A.
 Scalleri, Mary B.
 Stagliola, Eleanor E.
 Toebes, Rita K.

Typists

Foley, Ruth E.
 Murphy, Mary R.

Myers, Alberta L.

Smith, Mary L.
 Young, Nancy E.

PERSONNEL

Technical Typists

Capron, Evelyn L.
Jones, Elizabeth
Mullin, Priscilla A.

Secretaries

Bedrosian, Isabel
Blum, Elaine
Bullard, **Ann B.**
Carbone, Angelina
Chorba, Linda D.
Cohen, Phyllis J.
Conwicke, Vera
Cummings, Jane F.
DiPietro, Toni R.
Geller, Elaine J.
Hamilton, Martha C.

Holden, Meredith
Hurvitz, Rose S.
Imperato, Eleanor M.
Ingersoll, Nancy L. B.
Johnson, Barbara A.
Kaloyanides, Venetia
Kirk, Marshall
Lipchinsky, Cheryl A.
Loeb, Charlotte G.
Lynch, Kathy Ann
McCarthy, Barbara L.
McEntee, Doris C.

Murray, Maureen P.
O'Neil, Patricia A.
Owens, Mary E.
Parrella, Cynthia A.
Pierce, Marilyn A.
Reid, Gloria C.
Ricker, Barbara J.
Russell, Susan P.
Smith, Clare, F.
Van Wezel, Ruth
Wanner, Patricia A.

Engineering Assistants

Berg, A. E.
Crist, F. X.

McKenzie, J. A.

Papa, D. C.
Thompson, J. B.

Technical Assistants

Byers, F. H.
Grande, Esther D.
Iverson, Alice I.
Major, Diane

Newman, Charlotte M.
Rabin, Sylvia G.
Rosenthal, Kathryn F.

Salacinski, Barbara A.
Shipley, Jenot W.
Swenson, Judith E.
Yaffee, M. A.

Technicians

Andrews, G. T.
Aucella, Alice G.
Babcock, E. R.
Barrows, F. W.
Butler, R. E., Jr.
Connolly, J. T.
DiPietro, P. J.
Fitzgerald, E. W., Jr.

Gage, R. B., Jr.
Gay, H. D.
Hill, R. F.
Iovine, M. A.
Kaufman, D. E.
Kelly, M. A.
Lewis, R. R.
McLean, J. J.

Neal, R. W.
North, D. K.
Schwabe, W. J.
Sears, A. R.
Sholder, J. A.
Sprague, L. E.
Stevens, J. A.
Tortolano, A. J.

Technicians' Shop

Lorden, G. J., Foreman

Fownes, Marilyn R.

Laboratory Assistants

Barrows, Helene G.
Beaton, Catherine M.

Cardia, P. F.
MacDonald, K. B.

Miller, S. A.
Wood, H.

PERSONNEL

Drafting Room

Navedonsky, C. P., Foreman
Donahue, J. B.

Hillier, **Anna** M.

Porter, Jean M.
Rollins, I. E.

Photographic Shop

Aradi, M. G.
Cook, J. F.
Karas, P.

Machine Shop

Keefe, J. B. Foreman
Aalrud, R. W.
Bletzer, P. W.
Brennan, J.
Bunick, F. J.
Cabral, M., Jr.

Carter, C. E.
Harvey, A. O.
Liljeholm, F. H.
Muse, W. J.
O'Connell, J. G., Jr.

Reiman, W.
Ridge, P. A.
Ryan, J. F.
Sanroma, J. B.
Shmid, E.
Wentworth, W. G., Jr.

Tube Laboratory

Rosebury, F.

Griffin, J. L.
Leach, G. H., Jr.
MacDonald, A. A.

Glass Shop

DiGiacomo, R. M.
Doucette, W. F.

Stock Clerks

Doherty, R. H.

Legier, D. O.
Haggerty, R. H.

Sharib, G.

Utility and Maintenance

Doiron, E. J., Foreman
Audette, A. G.

Lucas, W. G.
McDermott, J. F.
Riley, J. F.

Sincuk, J., Jr.
Thibodeau, D. S.

PUBLICATIONS AND REPORTS

MEETING PAPERS PRESENTED

Mental Health Training Seminar, Brain Research Institute, University of California, Los Angeles, California

January 12-13, 1966

J. S. Barlow, Some Electrophysiological and Behavioral Correlates of Perception (invited)

Biological Systems Analysis Seminar, California Institute of Technology, Pasadena, California

January 17, 1966

J. S. Barlow, Electrophysiological and Behavioral Aspects of Perception of Visual Stimuli in Man (invited)

Lecture, Barrow Neurological Institute, Phoenix, Arizona

February 21, 1966

J. S. Barlow, Electrophysiological and Behavioral Correlates of Perception (invited)

Second Conference on Information and Control Processes in Living Systems (sponsored by the New York Academy of Sciences), Civic Palisades, California

February 27-March 2, 1966

R. Alter, Special Aspects of Prosthetic Devices (invited)

Journées Informatique, Toulouse, France

March 7-10, 1966

M. Eden, Medical Diagnosis as a Problem in Pattern Recognition (invited)

Brain Research Institute Seminar, University of California Medical Center, Los Angeles, California

March 8, 1966

J. S. Barlow, The Vestibular System in Relation to Animal Navigation (invited)

Physics Colloquium, New York University, New York

March 14, 1966

J. G. King, Atomic Beams below the Lambda Point (invited)

Lecture, Los Angeles Society of Neurology and Psychiatry, Los Angeles, California

March 16, 1966

J. S. Barlow, Studies of Neurological Diseases with the Aid of Computer Techniques (invited)

IEEE International Convention, New York

March 21-25, 1966

H. A. Haus, Model for Force Density in Moving Magnetized Material

D. E. Nelsen, Statistics of Switching-Time Jitter for a Tunnel Diode Threshold-Crossing Detector

P. Penfield, Jr., Thermodynamics and Force of Electromagnetic Origin

MEETING PAPERS PRESENTED (continued)

Conference on Symbolic and Algebraic Manipulations, Washington, D. C.

March 27-29, 1966

J. Moses, Solution of Systems of Polynomial Equations by Elimination

Department of Zoology Seminar, University of Iowa, Iowa City, Iowa

April 5, 1966

J. S. Barlow, The Neurophysiological Basis of Animal Navigation (invited)

Department of Neurology and Medical Statistics Seminar, Mayo Clinic, Rochester, Minnesota

April 6, 1966

J. S. Barlow, The Comparative Geography of Multiple Sclerosis, Rheumatic Fever, and Rheumatoid Arthritis (invited)

International Quantum Electronics Conference, Phoenix, Arizona

April 12-15, 1966

C. Freed and H. A. Haus, Photoelectron Statistics Produced by a Laser Operating below and above the Threshold of Oscillation

Department of Pathobiology Seminar, School of Hygiene and Public Health, The Johns Hopkins University, Baltimore, Maryland

April 13, 1966

J. S. Barlow, Animal Navigation and Inertial Navigation (invited)

Federation Proceedings of Experimental Biology, Atlantic City, New Jersey

April 13, 1966

A. W. B. Cunningham and P. H. O'Lague, Microelectrode Studies of **14-day** Chick Embryo Telencephalon in vitro

Special Lecture Series in Physiology, The Johns Hopkins University School of Medicine, Baltimore, Maryland

April 13, 1966

J. S. Barlow, The Electroencephalogram as a Communications Signal in the Study of Brain Mechanisms (invited)

Eastern Psychological Association Thirty-seventh Annual Meeting, New York City

April 14-16, 1966

R. D. Hall and R. G. Mark, Auditory Evoked Potentials in the Rat During Conditioning

P. A. Kolers, Reading Linguistically Mixed Materials

International Symposium on Generalized Networks, Polytechnic Institute of Brooklyn, New York

April 14-16, 1966

P. Penfield, Jr., Thermodynamics of Frequency Conversion

V. Prabhu, Invariants of Multifrequency Noisy Networks

MEETING PAPERS PRESENTED (continued)

Council for Exceptional Children, Annual International Convention, Toronto, Canada
April 17-24, 1966

Paula Menyuk, Generative Grammar and Studying the Language of the Exceptional Child

Annual Spring Meeting of the International Scientific Radio Union, Commission 5,
Washington, D. C.

April 18-20, 1966

R. J. Allen and A. H. Barrett, Variations in the Centimeter Radio Emission **from**
3C273

Forty-seventh Annual Meeting, American Geophysical Union, Washington, D. C.

April 19-22, 1966

G. Grams and G. Fiocco, Studies of Stratospheric Aerosols and Correlations with
Ozone

Sherwood Theoretical Meeting, San Diego, California

April 21-22, 1966

A. Bers and F. C. Hoh, Mechanism of Energy Transfer from Resonant Particles
to Magnetic Field Perturbations

T. H. Dupree, Particle-Wave Interaction in Turbulent Plasma

Wistar Institute Conference on Neo-Darwinian Evolution, Philadelphia, Pennsylvania

April 25, 1966

M. Eden, Inadequacies of Neo-Darwinian Evolution as a Scientific Theory (invited)

American Physical Society Meeting, Washington, D. C.

April 25-28, 1966

K. W. Billman, C. G. Chull, and F. A. Wedgwood, Neutrality of the Atom

W. D. Johnston, Jr. and J. G. King, Velocity Distributions of Helium Beams
from Liquid Helium II

S. G. Kukolich, and J. G. King, Ammonia Hyperfine Structure

C. O. Thornburg, Jr. and J. G. King, Search for an Electric Dipole Moment in
the Cesium Atom

Laboratorio Gas Ionizzati Seminars, Frascati, Italy

April 27, 1966

S. C. Brown, Far Infrared Plasma Diagnostics (invited)

Use of Computers **for** Bibliographic Search (invited)

A. E. C. Conference, University of Miami, Coral Gables, Florida

May 2-5, 1966

J. C. Ingraham, Anomalous Plasma Loss Processes

Bionics Symposium, Dayton, Ohio

May 2-5, 1966

J. Y. Lettvin and R. C. Gesteland, A Code in the Nose

MEETING PAPERS PRESENTED (continued)

NASA Electronics Research Center Seminar, Cambridge, Massachusetts

May 4, 1966

C. H. Perry, Applications of Interferometric Spectroscopy in the Infrared
(invited)

Sperry-Rand Research Center Colloquium, Sudbury, Massachusetts

May 9, 1966

U. Ingard, Acoustic Wave Generation and Amplification in a Plasma (invited)

National Telemetering Conference, Boston, Massachusetts

May 10-12, 1966

T. S. Huang and O. J. Tretiak, An Efficient Facsimile Transmission System

JOURNAL PAPERS ACCEPTED FOR PUBLICATION

(Reprints, if available, may be obtained from the Document Room,
26-327, Research Laboratory of Electronics, Massachusetts Institute of Technology, Cambridge, Massachusetts 02139.)

- J. S. Barlow, Correlation Analysis of EEG-Tremor Relationships in Man (EEG Clin. Neurophysiol. Supplement)
- J. S. Barlow, A Simple Time-Division Multiflexing System for Low-Frequency Bioelectric Signals (IEEE Trans. (BME))
- T. Brown and D. J. Rose, Plasma Diagnostics Using Lasers: Relations between Scattered Spectrum and Electron Velocity Distribution (J. Appl. Phys.)
- A. W. B. Cunningham, P. O'Lague, R. Rojas-Corona, and J. A. Freeman, Micro-electrode Studies of Spontaneous Potentials from Chick Embryo Telencephalon & vitro (Experientia)
- E. T. Gerry and D. J. Rose, Plasma Diagnostics by Thomson Scattering of a Laser Beam (J. Appl. Phys.)
- E. T. Gerry and D. J. Rose, Combined Anode-Cathode Feed of a Hollow-Cathode Arc (J. Appl. Phys.)
- P. A. Kolers and M. T. Katzman, Naming Sequentially Presented Letters and Words (Language and Speech)
- W. Lea, The 'Spectrum' of Weak Generative Power of Grammars (MT)
- J. H. Loehlin, P. G. Mennitt, and J. S. Waugh, Proton Resonance Study of Molecular Motion and Phase Behavior of Solid H_2S and H_2Se (J. Chem. Phys.)
- J. Moses, Solution of Systems of Polynomial Equations by Elimination (Commun. Assoc. Computing Machinery)
- J. D. Macomber and J. S. Waugh, Theory of the Nuclear Resonance Spectrum of a Polar Liquid in an Alternating Electric Field (J. Chem. Phys.)

JOURNAL PAPERS ACCEPTED FOR PUBLICATION (continued)

- L. R. Rabiner, C. L. Lawrence, and N. I. Durlach, Further Results on Binaural Unmasking and the EC Model (J. Acoust. Soc. Am.)
- K. N. Stevens, A. S. House and A. P. Paul, Acoustic Description of Syllabic Nuclei: An Interpretation in Terms of a Dynamic Model of Articulation (J. Acoust. Soc. Am.)

LETTERS TO THE EDITOR ACCEPTED FOR PUBLICATION

- A. H. Barrett and A. E. E. Rogers, Observations of Circularly Polarized OH Emission and Narrow Spectral Features (Nature)
- J. M. Deutch and J. S. Waugh, Erratum: **On** the Detectability of the Quadratic NMR Electric-Field Effect in Liquids [J. Chem. Phys. **43**, 2568 (1965)] (J. Chem. Phys.)
- J. H. Fertel, C. H. Perry, A. Sabatini, L. Sacconi and V. Schettino, Correction to "Long-Wave Infrared Spectra of Alkali Salts to Platinum Halide Complexes" by J. H. Fertel and C. H. Perry [J. Phys. Chem. Solids **26**, 1773 (1965)] (J. Phys. Chem. Solids)
- H. A. Haus, Higher Order Trapped Light Beam Solutions (Appl. Phys. Letters)
- U. Ingard and W. M. Manheimer, Energy Density in a Plasma Oscillation (Phys. Fluids)
- J. J. Katz, Mr. Pfeifer on Questions of Reference (Foundations of Language)
- H. B. Lee, An Alternate Derivation of the Fujisawa Condition (IEEE Trans. (CT))
- V. Prabhu, Noise Performance of Abrupt-Junction Varactor Frequency Multipliers (Proc. IEEE)

TECHNICAL REPORTS PUBLISHED

(These and previously published technical reports, if available, may be obtained from the Document Room, **26-327**, Research Laboratory of Electronics, Massachusetts Institute of Technology, Cambridge, Massachusetts **02139**.)

- 443** John S. MacDonald, Experimental Studies of Handwriting Signals
- 444** Robert Bruce Parente, Functional Analysis of Systems Characterized by Nonlinear Differential Equations
- 448** Paul M. Ebert, Error Bounds for Parallel Communication Channels
- 450** C. W. Niessen, An Experimental Facility for Sequential Decoding
- 451** Peter R. Gray, Statistical Analysis of Electrophysiological Data from Auditory Nerve Fibers in Cat
- 452** Bernard Gold, Word-Recognition Computer Program

SPECIAL PUBLICATIONS

- J. C. Ingraham, Electron-Atom Collision Cross-Section Measurements in the After-glow of a Pulsed Cesium Plasma (Proc. Seventh International Conference on Phenomena in Ionized Gases, edited by B. Perović and D. Tošić, Institute of Nuclear Sciences, Beograd, July 1966)
- J. C. Ingraham, Anomalous Plasma Loss Processes (Proc. A.E.C. Conference, University of Miami, Coral Gables, Florida, May 2-5, 1966)
- E. S. Klima, Negation in English, a chapter in Readings in the Philosophy of Language, edited by J. J. Katz and J. A. Fodor (Prentice-Hall, Inc., Englewood Cliffs, New Jersey)
- P. A. Kolers, Recall of Bilingually Presented Words (Abstract, Proc. Ninth Congress of the Inter-American Society of Psychology, Miami Beach, Florida, Dec. 17-22, 1964, p. 393)
- D. E. Nelsen, Statistics of Switching-Time Jitter for a Tunnel Diode Threshold-Crossing Detector (1966 IEEE International Convention Record)
- P. Penfield, Jr., Thermodynamics and Force of Electromagnetic Origin (1966 IEEE International Convention Record)

INTRODUCTION

This report, the eighty-second in a series of quarterly progress reports issued by the Research Laboratory of Electronics, contains a review of the research activities of the Laboratory for the three-month period ending May 31, 1966. Since this is a report on work in progress, some of the results may not be final.

GENERAL PHYSICS

I. MOLECULAR BEAMS*

Academic and Research Staff

Prof. J. R. Zacharias
Prof. K. W. Billman

Prof. J. G. King
Prof. C. L. Searle
Prof. E. F. Taylor

F. J. O'Brien
M. A. Yaffee

Graduate Students

J. F. Brenner
R. Golub

G. L. Guttrich
W. D. Johnston, Jr.
S. G. Kukolich

C. O. Thornburg, Jr.
L. H. Veneklasen

A. NEUTRALITY OF THE NEUTRON

An experiment has been undertaken to examine more closely the limit that may be placed on a possible charge possessed by the free neutron. The implications associated with such a charge are numerous. A neutron charge of approximately 2×10^{-18} electron charge (e) would explain the expanding universe on the basis of electrostatic repulsion.¹ A neutron charge of approximately 2.5×10^{-19} e would explain the magnetic fields of the earth and sun.² Finally, the independence of three conservation laws — Conservation of Baryons, Conservation of Leptons, and Conservation of Charge — is linked to the strict neutrality of the neutron and the equality of the magnitude of the electron and proton charges.

The experimental technique employed here was to subject a beam of neutrons to a strong, uniform, transverse electric field, E. If the neutrons are assumed to possess a charge q, this would result in an angular deflection of the beam

$$\theta = \frac{Eq}{m} \frac{L}{v^2} \quad (1)$$

for small θ . Here, m is the neutron mass, L is the length of the deflection region, and v is the longitudinal beam velocity. Reversing the sense of E would give rise to a deflection $-\theta$; that is, upon field reversal an angular change of $\Delta\theta = 2\theta$ would be expected. Thus the charge measurement reduces to the detection of small angular beam deflections.

Figure I-1 illustrates schematically the technique that was used. A beam of heavy-water-moderated neutrons from the M. I. T. reactor, operating between power levels of 2 to 5 Mwatts during the experiment, impinge on a perfect Si crystal with a flux of approximately 10^9 neutrons/second. This monochromating crystal Bragg reflects the desired neutrons of wavelength $\lambda = 2.40 \text{ \AA}$ with a scattering angle of 45° onto the second analyzer Si crystal. When the analyzer crystal is correctly adjusted, the neutrons are

*This work was supported by the Joint Services Electronics Programs (U. S. Army, U. S. Navy, and U. S. Air Force) under Contract DA 36-039-AMC-03200(E).

(I. MOLECULAR BEAMS)

reflected into the conventional BF_3 detector and counting system. It should be noted that another, "contamination" wavelength of $\lambda/3 = 0.8 \text{ \AA}$ is also reflected. Its effect was

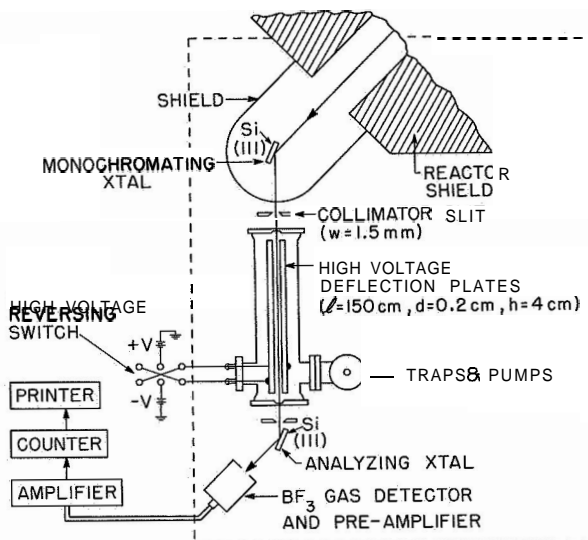


Fig. I-1. Schematic diagram of the neutron-neutrality experiment.

carefully measured and accounted for, and thus will not be mentioned in the sequel. Two boron-enriched slits limit the beam width so as to avoid reflection of the neutrons from the high-voltage electrodes. The absence of such reflections was carefully determined. The counting rate is an extremely sensitive function of the angle of incidence of the beam onto the analyzer. By providing a unique mounting for this crystal, and by carefully maintaining the apparatus in a constant temperature environment, sufficient stability was obtained to use the change in counting rate to detect a beam deflection when the transverse electric field was applied. The field was provided by the parallel-plate electrode structure shown in Fig. I-1. The construction and support were consistent with providing negligible gradients to the beam and to maintaining constant field magnitude when the electric field was reversed by means of the reversing switch. The entire electrode assembly was contained in a vacuum system, the neutron beam entering and leaving through thin aluminum windows.

Under the assumption that the neutrons did possess a charge of, say, $+10^{-17} e$, the angular deflection of the beam for this geometry would amount to ± 2 msec of arc when an electric field of ± 200 volts/cm was provided. Hence, as the electric field was automatically reversed at 5-min intervals, the angle of incidence of the beam onto the analyzer crystal would vary by this amount around some zero-field value, θ_0 .

Figure 1-2 shows a typical "rocking curve" of this double crystal arrangement; that is, the effect of varying the angle of incidence of the neutron beam onto the analyzer

crystal. This curve was actually obtained with the high-voltage electrode system in position, but with $E = 0$, and by rotation of the analyzer. From the slope of the curve

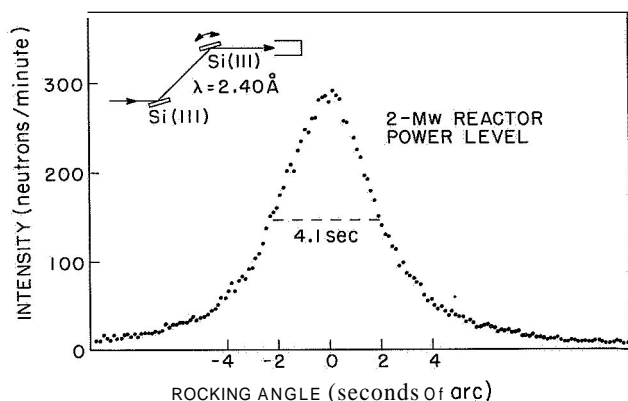


Fig. 1-2. Typical rocking curve of the double-crystal spectrometer.

in the region of θ_0 , the sensitivity of the experimental arrangement can be assessed. For low power level operation of the reactor, this was typically 75 n/min-sec of arc, and for high power level it was 200 n/min-sec of arc. The theoretical limit to the half-width of the rocking curve can be shown from diffraction theory to be

$$ti = \frac{Mb\lambda^2}{n \sin 2\theta} \quad (2)$$

where M is the atomic density of the crystal, b is the crystal structure factor, λ is the neutron wavelength, and θ is the Bragg angle. For the arrangement used here a theoretical θ of 3.2 sec is predicted, whereas an excellent value of 4.1 sec was attained.

A verification of the equivalence of using this rocking curve for the basis of the sensitivity to beam deflection was made. The beam was actually deflected by positioning an aluminum prism in the beam in the region between the two crystals. If the prism angle is a , the corresponding angular deviation of the beam can be shown to be

$$\beta = 2(1-n) \tan a = 2 \frac{Mb\lambda^2}{2n} \tan a, \quad (3)$$

where n is the index of refraction, M the atomic density, and b the absolute scattering amplitude of aluminum. It should be noted that such a deflection is fully equivalent to a neutron charge deflection in its wavelength dependence, as can be seen from Eq. 1 when the de Broglie relation $v = \frac{h}{m\lambda}$ is used to eliminate the velocity. Figure 1-3 shows the agreement obtained between the change in angular deflection of the beam as the aluminum prism was rotated 180°, as predicted by Eq. 3, and that computed from the measured change in neutron count rate and the corresponding angular change ascertained from the rocking curve.

The experimental results are exhibited in Fig. 1-4. The ordinate axis is the angular deflection, $\Delta\theta$, to the field when on to the field turned off; that is, it is one half of the angular deflection change under reversal of the sense of the electric field. The error brackets are found to agree extremely well with those to be expected on the basis of \sqrt{n} . For obvious reasons, much more data were accumulated at the highest value of the

(I. MOLECULAR BEAMS)

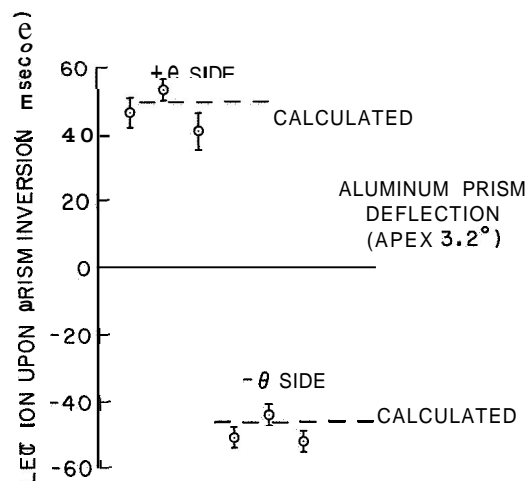


Fig. 1-3. Experimental verification of apparatus sensitivity as determined from the rocking curve.

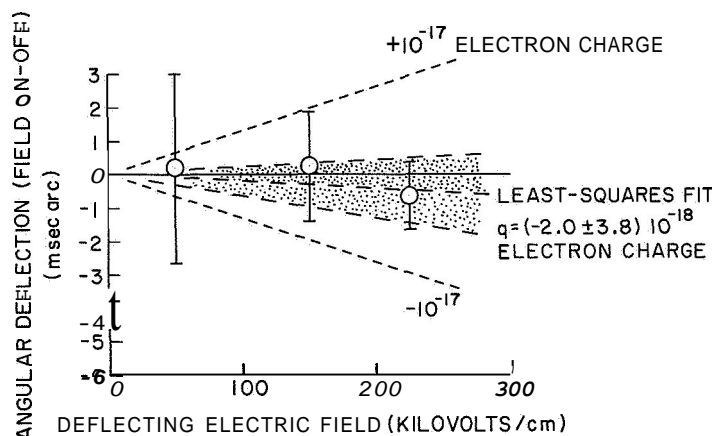


Fig. 1-4. Experimental results.

electric field which could be attained. The dotted lines indicate what angular deflection would have been measured if the neutron charge were as large as $\pm 10^{-17}$ e. A least-squares fit gives $(-2.0 \pm 3.8) 10^{-18}$ e; that is, if the neutron does possess a charge, we have shown that, with a 68 per cent confidence level, it must lie somewhere within the dotted band illustrated in Fig. 1-4.

K. W. Billman, C. G. Skull, F. A. Wedgwood.

[Professor C. G. Skull and Dr. F. A. Wedgwood are at The Center for Materials Science and Engineering. This work was supported in part by the National Science Foundation,

References

1. R. A. Lyttleton and H. Bondi, Proc. Roy. Soc. (London) A252, 313 (1959).
2. A. Piccard and E. Kessler, Arch. Sci. Phys. et Nat. (Geneva) 7, 340 (1925).
3. G. Feinberg and M. Goldhaber, Proc. Natl. Acad. Sci. U.S. 45, 1301 (1959).

II. MOLECULAR COLLISIONS*

Academic and Research Staff

Prof. J. L. Kinsey

Graduate Students

R. P. English
C. H. Fisher

M. H. Klumpp
J. R. Lawter

RESEARCH OBJECTIVES

Our interest is in molecular collisions at thermal energies. These phenomena are studied mainly through crossed molecular beam scattering experiments. Two kinds of collision processes are of interest to this group: (i) collisions which can lead to chemical reactions; (ii) elastic and inelastic nonreactive collisions.

In the chemical studies our aim is to determine some of the finer details of reactive collisions, such as the anisotropy of product velocities and the distribution of available amounts of energy, momentum, and angular momentum among the various accessible modes. The nonreactive studies are mainly concentrated on processes that have some relevance to chemical processes or energy transfer processes.

This work is supported by National Science Foundation Grant GP-5099, which is not administered by the Research Laboratory of Electronics.

J. L. Kinsey

* This work is supported in part by the Joint Services Electronics Programs (U. S. Army, U. S. Navy, and U. S. Air Force) under Contract DA 36-039-AMC-03200(E).

III. MICROWAVE SPECTROSCOPY*

Academic and Research Staff

Prof. M. W. P. Strandberg
Prof. R. L. Kyhl

Dr. J. M. Andrews

J. G. Ingersoll
J. D. Kierstead

Graduate Students

V. Castellani
J. U. Free, Jr.
A. Fukumoto

R. M. Langdon, Jr.
M. K. Maul

T. E. McEnally
S. R. Reznick
B. N. Yung

Undergraduate Students

S. Greenberg
D. D. Milligan

D. W. Vahey
F. Williams

A. WORK COMPLETED

1. ULTRASONIC ATTENUATION AND SIZE EFFECT IN GALLIUM

This work has been completed by Akira Fukumoto and submitted as a thesis to the Department of Physics, M. I. T. , June 1966, in partial fulfillment of the requirements for the degree of Doctor of Philosophy. A summary of the thesis research follows.

Two different techniques were used to study the Fermi surface of Gallium by geometric resonance, ultrasonic attenuation (UA) and Gantmakher resonance (GR).

The theory of UA in metals is reviewed and a general expression for the attenuation coefficient is obtained. The surface impedance of a semi-infinite metal is calculated and the result is used to obtain the surface impedance of a finite plate. These results are used to discuss the various observable factors of the experiments.

The UA experiment was performed at a frequency of 900 Mc, and geometric resonances were observed at the magnetic field below 1 kgauss. A method to fabricate a well-oriented crystal, ~0.2 mm thick for use in GR experiment was developed. Gantmakher resonances of various line shapes were observed at the magnetic field below 500 gauss.

The experimental results of UA and GR were very similar, and showed very good agreement with the Fermi surface calculated by the augmented plane-wave (APW) model. APW bands 7 and 8 were verified in three orthogonal planes with an accuracy of less than 30 per cent. APW band 4 was verified in two orthogonal planes, and the deviation was less than 25 per cent. The existence of APW band 5 is strongly indicated by the experiment and part of this band agreed with the data with less than 15 per cent accuracy.

The line shape of GR signals is discussed. Kaner's theory is extended and a

* This work was supported by the Joint Services Electronics Programs (U. S. Army, U. S. Navy, and U. S. Air Force) under Contract DA 36-039-AMC-03200(E).

(111. MICROWAVE SPECTROSCOPY)

discussion and calculation of the effect of interference of the electric fields arising from the two opposing surfaces of a thin sample, as is the case in the usual experimental arrangement, is given. The interference effect of the electric fields arising from the two surfaces was studied by comparing the line shapes of the samples with and without shielding on one side of the sample. The dependence of the line shape on the radio frequency and the polarization of the high-frequency field were studied, and a method was developed to obtain the correct value of the wave vector corresponding to the extremal orbits of the electrons.

Temperature dependence of the attenuation coefficient of the UA experiment is discussed briefly.

M. W. P. Strandberg

2. USE OF EMR TO STUDY MAGNETIC FIELD HOMOGENEITY AND CAVITY CONFIGURATIONS FOR LARGE AQUEOUS SAMPLES

This work has been completed by David D. Milligan and submitted as a thesis to the Department of Physics, M. I. T. , June 1966, in partial fulfillment of the requirements for the degree of Bachelor of Science. A summary of the thesis research follows.

The sensitivity of a helical resonator for use as a microwave cavity in an EMR spectrometer was investigated. By using experimental techniques and a theoretical analysis, the sensitivity of this type of helical resonator in studying aqueous samples was found to be inherently three orders of magnitude below the sensitivity obtained by using a standard cylindrical cavity with an unloaded Q of 25,000.

A simple and accurate technique for measuring static magnetic field homogeneity with the use of an EMR spectrometer is discussed and the use of "Rose Shims" to reduce inhomogeneity was studied. The magnetic field used in this laboratory is found to have an inhomogeneity of 0.15 gauss per centimeter near the geometric center of the pole pieces.

M. W. P. Strandberg

3. BOLOMETRIC DETECTION OF COHERENT PHONONS IN QUARTZ

This work has been completed by David W. Vahey and submitted as a thesis to the Department of Physics, M. I. T. , June 1966, in partial fulfillment of the requirements for the degree of Bachelor of Science. A summary of the thesis research follows.

Echoes of coherent phonons propagating through x-cut quartz were detected with a tin superconducting bolometer. The experiments were performed at liquid-helium temperatures with the use of a re-entrant microwave cavity capable of generating phonons near 9 Gc.

Experimental results on bolometer responsivity are described and tentatively found to agree fairly well with the theory for bias currents up to 40 ma.

(111. MICROWAVE SPECTROSCOPY)

In other work, the decay constant for coherent 9-Gc phonon energy in the quartz-bolometer system has been measured bolometrically to be $(0.13 \pm 0.035) \text{ cm}^{-1}$. This value is almost a factor of two less than that obtained under similar conditions with a microwave-reflection technique, and is believed to demonstrate the phase-sensitive properties of that method of measurement.

Finally, the basis for experiments on phonon transmission across a quartz-indium interface is described in an appendix, and the results of a preliminary investigations are presented.

M. W. P. Strandberg

4. APPARATUS FOR MEASURING PHONON DISPERSION IN SINGLE CRYSTALLINE MATERIAL

This work has been completed by William B. Robbins and submitted as a thesis to the department of Physics, M. I. T. , January 1966, in partial fulfillment of the requirements for the degree of Bachelor of Science. A summary of the thesis research follows.

Circuitry meeting the requirements for detection of phonon dispersion was developed in order to match a low impedance (2-ohm) superconducting bolometer to a higher impedance (500-ohm) low-noise amplifier. The circuit operates at cryogenic temperatures, has a 10-90% rise time of 80 msec, produces less than 5% overshoot, and droops less than 20% for pulses of 10 psec duration. Theoretical calculations predict a droop $\sim 18\%$ and a rise time of ~ 100 nsec. The total circuit loss is less than 1.6 db. No heat-pulse dispersion measurements were made, because of lack of time.

M. W. P. Strandberg

B. SUPERCONDUCTING BOLOMETERS: DETECTION OF AMBIENT ACOUSTIC NOISE

We have observed the low-frequency (20 cps-20 kc) noise spectrum of a superconducting tin bolometer, and find that it has the following characteristics.

1. The noise spectral density varies as $(\text{frequency})^{-n}$, where n is 2 or slightly greater.
2. The magnitude of the noise spectral density depends upon whether or not the bolometer is immersed in the liquid-helium bath.
3. The magnitude of the noise spectral density depends upon the phase of the liquid-helium bath, that is, whether it is Helium I or II.

A plot of the noise spectral density is given in Fig. 111-1.

The characteristic frequency of the noise is so low (approaching zero frequency), and so much lower in magnitude in nonbubbling Helium II than in bubbling Helium I, that we are forced to conclude that the electrical output noise arises from the detection, by the bolometer, of the acoustic noise in bubbling liquid helium. The residual noise that is present when the bolometer is not physically immersed in liquid Helium II, may arise

(111. MICROWAVE SPECTROSCOPY)

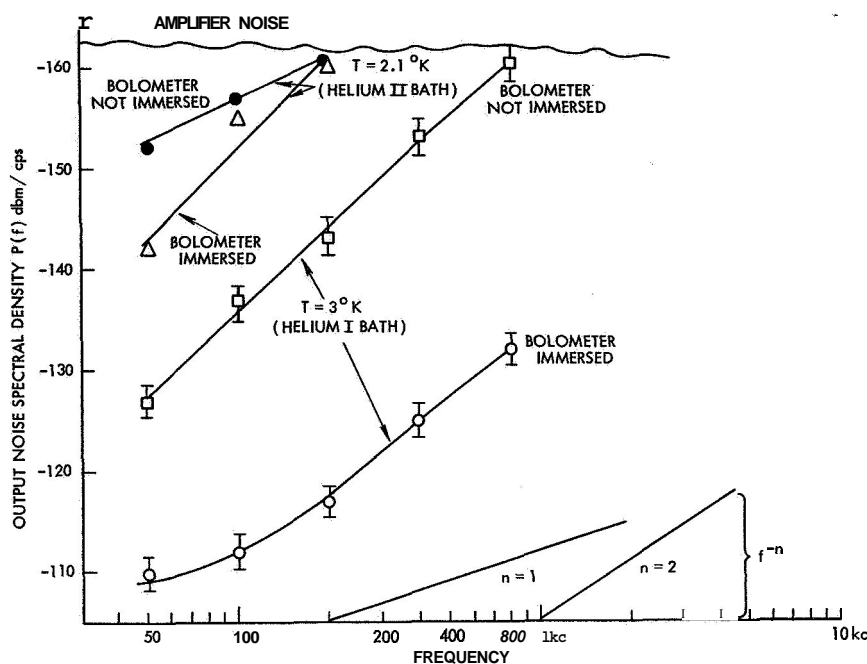


Fig. 111-1. Spectral noise density in a superconducting tin bolometer.

from critical-point fluctuation in the bolometer superconducting normal phase transition. At the critical point this fluctuation spectrum would also have a characteristic frequency that approaches zero. This critical-point fluctuation noise should be independent of whether or not the bolometer is in physical contact with the liquid Helium bath; it is more probable that the residual noise is simply laboratory ambient acoustic noise detected by the bolometer.

The increase in the magnitude of the noise with immersion of the bolometer in the liquid-helium bath would seem to eliminate the transit of quantized flux vertices¹ as a source of this noise.

M. W. P. Strandberg, J. D. Kierstead

References

1. D. J. van Ooijen and G. J. van Gorp, Phys. Letters **17**, 230 (15 July 1966).

C. BOLOMETRIC DETECTION OF COHERENT 9-GHz LONGITUDINAL PHONONS IN x-CUT QUARTZ

A superconducting bolometer¹ has been utilized for the detection of coherent 9.0-GHz longitudinal phonons in an x-cut quartz rod. A bolometer is an energy-sensing device,

(III. MICROWAVE SPECTROSCOPY)

and the complications associated with the phase-averaging process within the re-entrant cavity of a conventional microwave ultrasonic receiver, often giving rise to ragged, nonexponential echo-decay envelopes,²⁻⁶ and are thereby circumvented. It has been pointed out,⁶ furthermore, that even when nearly exponential decay envelopes are observed in conventional microwave ultrasonic experiments, the apparent loss of ultrasonic energy associated with the geometric effect of nonparallelism of the sample end faces combined with crystalline axis misalignment may greatly exceed the actual intrinsic loss caused by crystalline imperfections.

In studies of the temperature dependence of phonon-phonon scattering, an exponential decay envelope is not needed. The height of an echo that has made many passes through the sample is measured relative to its value at **4.2°K**, where the phonon-phonon scattering is negligible in comparison with the temperature-independent residual attenuation. Thus, although phonon-phonon scattering at microwave frequencies has been investigated in considerable detail in a wide variety of materials and at frequencies as high as 70 GHz in quartz,¹ the absolute value of the residual attenuation at temperatures below **4.2. °K** has remained a moot issue, because of the evolution of an unknown phase distribution of the microwave field over the receiving surface of the sample in multiple-reflection experiments.

For our experiment a quartz rod was selected that was known to have a rather high residual attenuation below **4.2 °K**. Thus the attenuation was sufficiently high to greatly diminish the usual "beating" effects often observed in microwave ultrasonic attenuation experiments,²⁻⁶ and a very nearly exponential decay of the pulse-echo envelope was observed with the microwave receiver, by utilizing a calibration pulse for pulse-height comparison measurements. As shown in Fig. 111-1, microwave ultrasonic generation and reception is performed in the same X-band re-entrant cavity at one end of the quartz rod. The measurements of pulse-echo power, detected in the microwave cavity, are shown by the upper line in Fig. III-3. Clearly, beating effects are not very evident in these measurements. The quartz rod utilized in this experiment was 19 mm long, and therefore the ultrasonic attenuation coefficient derived from these microwave measurements at 9.0 GHz was 1 db/cm.

At the other end of the quartz rod shown in Fig. 111-2, a tin film, approximately 0.1 μ thick, was deposited. The experiments were carried out at the superconducting transition temperature of the tin (**3.7°K**) so that the ultrasonic pulses could also be detected bolometrically. These measurements are shown by the lower line in Fig. III-3. The ultrasonic attenuation coefficient derived from the bolometric measurements at 9.0 GHz was **0.6 db/cm**.

Comparison of the data taken from the **two** types of attenuation measurements, as shown in Fig. 111-3, indicates that the microwave re-entrant cavity technique introduces an additional factor of **0.4 db/cm** in the apparent attenuation measurement. This

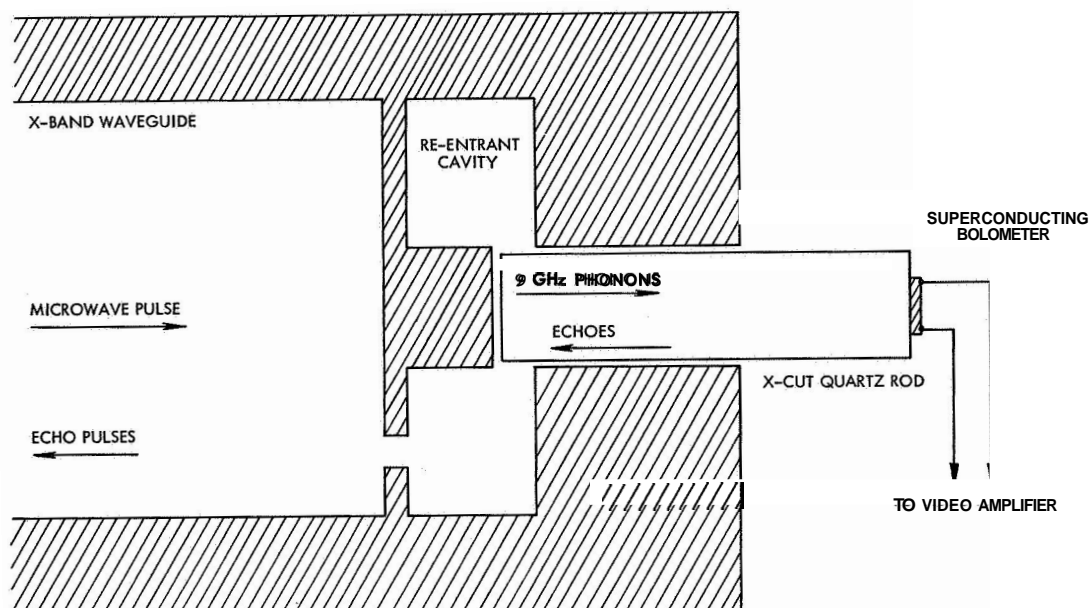


Fig. III-2. Generation and detection of microwave phonons at **9.0 GHz**. Microwave ultrasonic pulses propagating in the x-cut quartz rod are detected by the conventional, re-entrant cavity method at the left end, and by a superconducting bolometer at the right end.

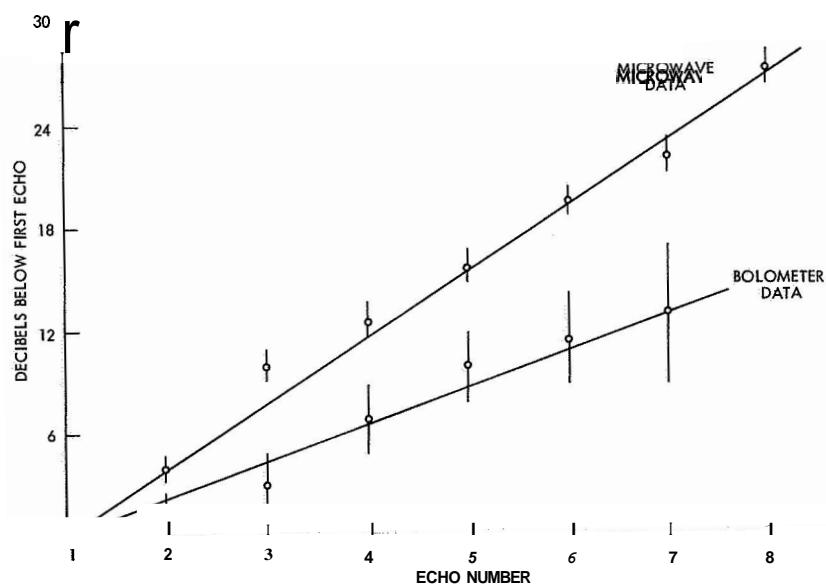


Fig. III-3. Measurements of the ultrasonic attenuation of longitudinal **9.0-GHz** phonons in an x-cut quartz rod, 19 mm long. The upper line represents measurements of microwave pulses received by the re-entrant cavity. The lower line represents measurements of the same pulses received by a superconducting bolometer at the opposite end of the quartz rod. The higher attenuation observed in the re-entrant cavity is attributed to unknown phase averaging of the microwave field over the end face of the quartz rod.

(III. MICROWAVE SPECTROSCOPY)

discrepancy is ostensibly related to the averaging of the **unknown** phase distribution of the microwave field over the receiving surface of the x-cut quartz sample.

The use of a metallic film for the detection of ultrasonic energy raises the disquieting question of how much of the energy is absorbed by the film in the detection process. At low temperatures the conduction electrons contribute heavily to the ultrasonic attenuation process in metals whenever their mean-free path becomes comparable to the ultrasonic wave length. In our bolometric film the electronic mean-free path is limited by boundary scattering to approximately one-third of the ultrasonic wavelength. The theory of the electronic contribution to the ultrasonic attenuation in metals derived by Pippard⁸ yields an absorption of approximately 0.03 db per echo in the superconducting film. This small value is consistent with the fact that we could see no change in the microwave attenuation as the tin film was driven from the superconducting to the normal state by means of an external magnetic field.

The highest frequency at which Pippard's theory has been verified is 0.9 GHz.⁹ It is therefore desirable to have an additional experimental check at 9 GHz. This has been carried out by evaporating a relatively thick (1 μ) indium film on another quartz rod in place of the bolometer and performing microwave attenuation measurements in this rod with the apparatus shown in Fig. 111-2.

The ultrasonic impedance of the longitudinal mode in indium is very nearly equal to

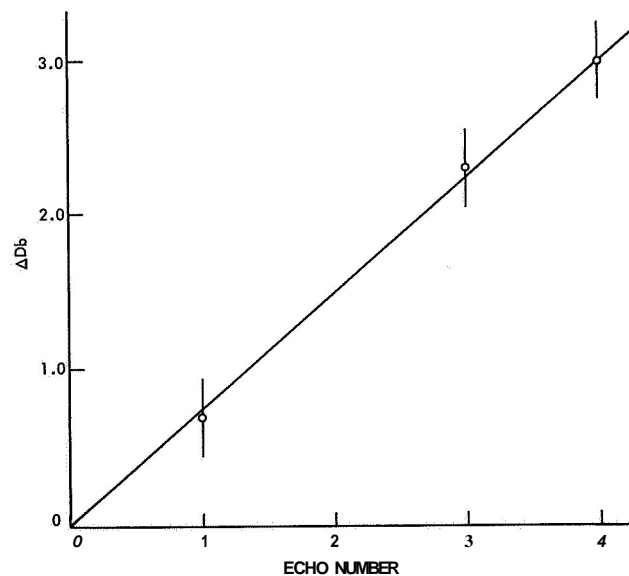


Fig. III-4. Electronic contribution to ultrasonic attenuation at 9.0 GHz in an indium film, approximately 1 μ thick. The difference in pulse-echo height, as the film is driven from the superconducting to the normal state, is represented by **A**.

that in x-cut quartz. It is therefore reasonable to assume that virtually all of the ultrasonic energy incident upon the quartz-metal interface is transmitted into the film. This contention is supported by the comparison of our experimental results with theory. The indium film was driven from the superconducting to the normal state by the application of an external magnetic field, and the relative changes in the heights of three echoes were measured. These data are shown in Fig. 11-4. An absorption of 0.07 db per echo is consistent with Pippard's theory if the effective number of free electrons per atom is taken as two. This is the same value as that required in a comparison of the Pippard theory with ultrasonic attenuation measurements in indium at 0.165 and 0.91 GHz.⁹

The ultrasonic attenuation measurement in the thick film supports our previous estimate of the relatively small absorption coefficient of our bolometric detector. Furthermore, these detectors can be made considerably thinner than 0.1 μ . It therefore appears that the superconducting bolometer may be useful as a phase-insensitive detector that can be utilized for absolute ultrasonic attenuation measurements at microwave frequencies where unknown phase averaging of the microwave field complicates the interpretation of data obtained by conventional re-entrant cavity reception.

The author would like to acknowledge the assistance of David W. Vahey who performed some of the experiments.

J. M. Andrews, Jr.

References

1. J. M. Andrews, Jr., and M. W. P. Strandberg, Proc. IEEE 54, 523-528 (1966).
2. R. Nava, R. Azrt, I. Ciccarello, and K. Dransfeld, Phys. Rev. 134, A581-589 (1964).
3. I. S. Ciccarello and K. Dransfeld, Phys. Rev. 134, A1517-1520 (1964).
4. E. Gates, Appl. Phys. Letters?, 187-189 (1965).
5. E. G. Spencer, P. V. Lenzo, and K. Nassau, Appl. Phys. Letters 7, 67 (1965).
6. E. Gates, Proc. IEEE 52, 1129-1137 (1964).
7. J. B. Thaxter and P. E. Tannenwald, Proc. IEEE Trans. on Sonics and Ultrasonics (to be published).
8. A. B. Pippard, Repts. Progr. Phys. 23, 176 (1960).
9. J. M. Andrews, Jr., Ph. D. Thesis, Massachusetts Institute of Technology, Cambridge, Mass., February 1964 (unpublished).

D. ERRATUM: MINIMUM DETECTABLE POWER IN SUPERCONDUCTING BOLOMETERS

In Quarterly Progress Report No. 81, page 1, the last line should be changed to read: "the rms equivalent input noise power arising from the three processes is given by".

J. M. Andrews, Jr.

IV. RADIO ASTRONOMY*

Academic and Research Staff

Prof. A. H. Barrett
Prof. B. F. Burke
Prof. M. Loewenthal

Prof. L. B. Lenoir
Prof. D. H. Staelin

Dr. S. H. Zisk
Patricia P. Crowther
E. R. Jensen

Graduate Students

R. J. Allen
N. E. Gaut
J. M. Moran, Jr.

G. D. Papadopoulos
E. C. Reifenstein III

A. E. E. Rogers
K. D. Thompson
T. L. Wilson

A. ABSOLUTE FLUX MEASUREMENTS OF CASSIOPEIA A AND TAURUS A AT 3.64 AND 1.94 CM

1. Introduction

During December 1965 and January 1966, a series of observations of the two strong radio sources Cassiopeia A and Taurus A was conducted at the Haystack Research Facility of Lincoln Laboratory, M.I.T. The antenna, a cornucopia horn reflector of approximately 6 m^2 aperture, has been measured extensively on a ground reflection antenna pattern range. Drift-scan observations were made at transit for both sources at two frequencies, 8.25 GHz and 15.50 GHz. The radiometers were examined for nonlinearity, and the gas-tube noise calibration sources were referred to standard terminations at liquid-nitrogen temperature. Data were collected on punched paper tape, and drift scans were individually processed on a digital computer. After baseline subtraction and scaling, each scan was approximated by a one-dimensional Gaussian curve through an iteration procedure, with the use of a set of equations developed from the minimum least-squares error criterion. The data were corrected for atmospheric attenuation, waveguide losses, integration time constant, source size, and, in the case of Taurus A, polarization, then converted to absolute flux by using the measured efficiency of the antenna.

Although mention of this work has been made in a previous progress report,¹ the present report constitutes a full description of the measurement techniques and the method of data reduction.

*This work was supported principally by the National Aeronautics and Space Administration (Grant NsG-419 and Contract NSR-22-009-120); and in part by Lincoln Laboratory Purchase Order No. 748.

(IV. RADIO ASTRONOMY)

2. System Parameters

a. Aperture Efficiency of the Horn Antenna

Measurements of the gain of the cornucopia antenna from 2.7 to 16.0 GHz were performed by A. Sotiropoulos. The substitution method was used on a simulated free-space range. The data have been analyzed by A. Sotiropoulos and J. Ruze, of Lincoln Laboratory, and their results have been published in a technical report.¹ The conclusions pertinent to the present observations are presented in Table IV-1, where η = aperture efficiency, defined as the ratio of the effective area to the actual area of the aperture A_g . The quantity $p = 2k/\eta A_g$ is the number that converts antenna temperature from an unpolarized point source to flux in units of $10^{-26} \text{ Wm}^{-2} \text{ Hz}^{-1}$ according to $S_v = p T_A$. Because of uncertainties in the measurement of η , the quantity p has an rms error of 4 per cent at both frequencies.

Table IV-1. Results.

Frequency (GHz)	η	p
8.25	$0.719 \pm .028$	633 ± 25
15.50	$0.578 \pm .023$	787 ± 31

b. Rotary Joint and Waveguide Losses

The cornucopia antenna is mounted in such a way as to allow rotation about its longitudinal axis. Figure IV-1 shows the arrangement. The rotational axis is aligned East-West, so that the antenna beam is movable in elevation along the meridian plane. The radiometric instrument box is shown attached to the antenna. The antenna is connected to the radiometer through a rotary joint, a 6-inch piece of flexible waveguide, and a 6-inch piece of solid waveguide. Figure IV-2 shows the arrangement.

The calibrations of the radiometer were referred to the indicated flange (Fig. IV-2). To account for the loss plus VSWR combination of the rotary joint and connecting waveguide, the following measurements were taken at both frequencies: The antenna was replaced with a gas-tube noise source and connected to the rotary joint through a precision attenuator. The radiometer was left attached to the connecting waveguide. The precision attenuator was then varied and the temperatures measured by the radiometer were recorded at T_a . The second step was to remove

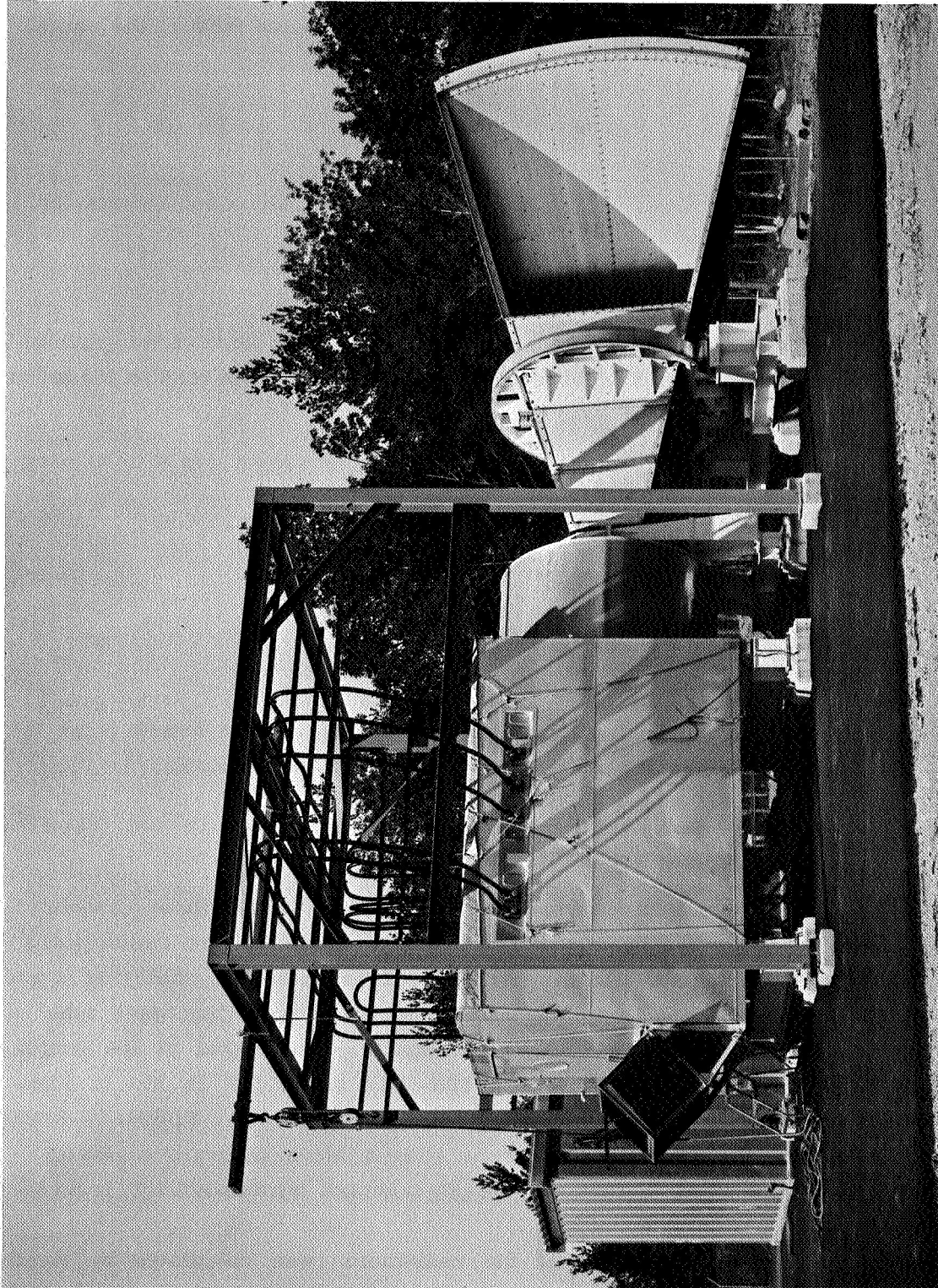


Fig. IV-1. Cornucopia horn-reflector antenna. The radiometers are housed in the boxlike room on the left, which is approximately 8 ft high.

(IV. RADIO ASTRONOMY)

the rotary joint and waveguide, and connect the precision attenuator directly to the calibration flange of the radiometer. The attenuator was then varied through the same

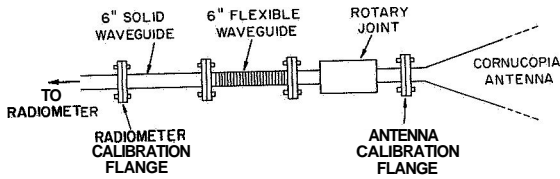


Fig. IV-2. Sketch of the plumbing between the antenna and radiometer.

values as before, and the radiometer output recorded as T_o . The slope of the graph of T_o vs T_a then yields the quantity and the correction factor desired. The results are given in Table IV-2.

Table IV-2. Results.

Frequency (GHz)	a
8.25	1.049 ± 0.005
15.50	1.062 ± 0.007

The uncertainty in a arises from the slight changes as the rotary joint is rotated. The error quoted is the maximum deviation that was found.

c. Radiometer System

The radiometric system was designed by S. Weinreb, and built at Lincoln Laboratory. A description has been given elsewhere.³ Briefly, the radiometers at both frequencies are simple Dicke-switched t. r. f. receivers, employing a cascade of wideband tunnel-diode amplifiers followed by a travelling-wave tube amplifier. The amplifiers have 1000-MHz bandwidth. The signal at the output of the final RF amplifier is split into two 500-MHz bands (as an aid in identifying interference) and delivered to the square-law detectors. Figure IV-3 shows the control panel for one of the radiometers with a block diagram of the RF components. After square-law detection, the signals are synchronously demodulated and applied to linear integrators.

The equivalent noise temperature of the radiometer was calculated by measuring the over-all sensitivity as a function of integration time, with the radiometer balanced on a room-temperature load. The relevant equation is

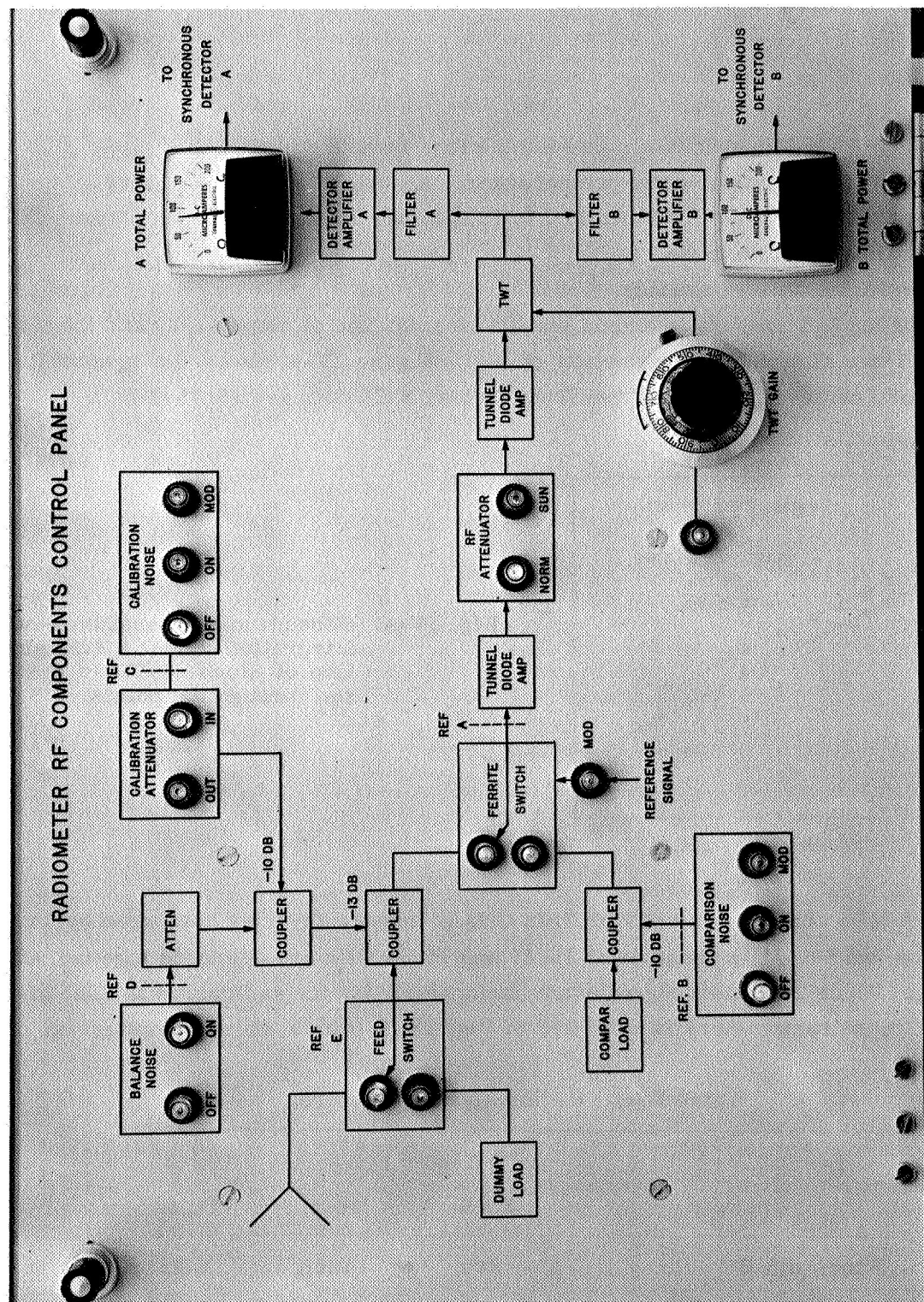


Fig. IV-3 Control panel for the radiometer, showing a block diagram of the RF components.

(IV. RADIO ASTRONOMY)

$$(\Delta T)_{\text{rms}} = \frac{2(T_R + T_a)}{\sqrt{B\tau}},$$

where

$(\Delta T)_{\text{rms}}$ = Root-Mean-Square noise fluctuation, measured in °K

T_R = equivalent receiver noise temperature, °K

T_a = temperature of the load attached to radiometer input, °K

B = system bandwidth in Hz

τ = integration time in seconds.

A plot of $\log (\Delta T)_{\text{rms}}$ vs τ should yield a straight line of slope $-1/2$, and the intercept at $\tau = 1$ sec allows a determination of T_R . Figure IV-4 shows the graphs for a 500-MHz band centered at each of two frequencies, 8.25 GHz and 15.75 GHz.

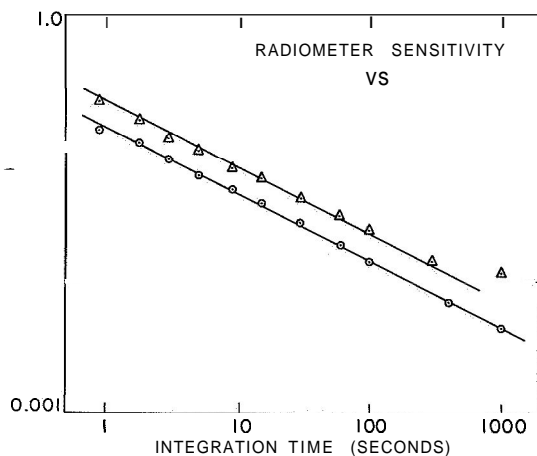


Fig. IV-4. Dependence of sensitivity on integration time. A straight line of slope $-1/2$ has been run through the points.

The 500-MHz channel centered at 7.75 GHz is usually severely hampered by interference; the two 500-MHz channels at 15.25 and 15.75 GHz are averaged together after processing. Table IV-3 lists the relevant parameters for the radiometers. The great stability of these radiometers is exhibited in Fig. IV-5, which shows a histogram of

Table IV-3. Radiometer parameters.

Quantity	Center Frequency (GHz)		Units
	8.25	15.50	
Bandwidth B	500	1000	MHz
Noise Temperature T_R	1300	2150	°K
Sensitivity for $\tau = 1$ sec	0.10	0.16	°K

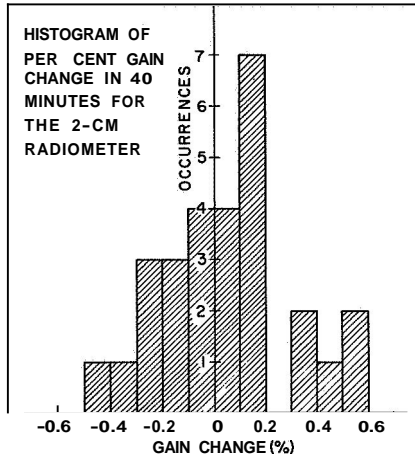


Fig. IV-5. Histogram of the per cent gain change in a 40-minute time interval for the 2-cm radiometer.

the radiometer, departures from linearity with such a relatively small input signal should be negligible, and the measurements bear this out. Let us assume that a reasonable representation of the relationship between the synchronous detector

gain change of the 15.50-GHz system over a 40-minute time interval.

The over-all linearity of the system was investigated in the following manner: A gas-discharge noise source was connected to the radiometer through a precision variable attenuator, and the synchronous detector output voltage recorded at various settings of this attenuator. Signals from zero to approximately 30°K were used, since this figure is approximately the size of the calibration signal in the radiometer. Because of the high noise temperature of the synchronous detector output voltage V_o and the input signal T_i in $^\circ\text{K}$, after subtracting the baseline, is

$$T_i = aV_o = bV_o^2. \quad (1)$$

We desire to evaluate the correction factor to be applied to the data under the assumption that the detector output voltage V_o and the input signal T_i are linearly related by

$$T_{iL} = cV_o. \quad (2)$$

The effects of nonlinearity are represented by the b coefficient in Eq. 1.

The coefficient c of Eq. 2 is chosen

so that both equations yield the calibration signal, T_{CAL} , when the detector output voltage is V_c . Figure IV-6 clarifies the procedure. Equating Eqs. 1 and 2 with $V_o = V_c$ gives

$$a = c - bV_c.$$

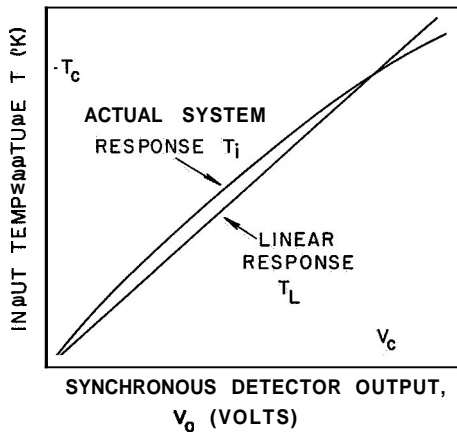


Fig. IV-6. Sketch of a possible departure from linearity in the radiometric system.

(IV. RADIO ASTRONOMY)

When this is used in Eq. 1 it gives

$$T_i = \left[1 - \frac{b}{c} (V_c - V_o) \right] T_{iL} \equiv \beta T_{iL}.$$

For the observations reported here, $V_c = 8.5$ volts, $V_o = 0.2$ volt (typical). Values of a , b , c , and β , determined from measurements, are given in Table IV-4. As expected, the correction for nonlinearity β is less than 1 per cent and was neglected in the subsequent analysis.

Frequency	a	b	c	β
GHz	°K/volt	°K/(volt) ²	°K/volt	
8.25	3.37	2.46×10^{-3}	3.39	0.994
15.5	3.04	3.36×10^{-4}	3.04	0.999

The temperature of the calibration noise tube in each radiometer was referred to the difference between a room-temperature load and a termination at the temperature of liquid nitrogen.* The accuracy of the measurement hinges on the uncertainty of the value of the temperature at the input flange of the cold load. After correction for VSWR, this amounts to 0.5°K at 8.25 GHz, and less than 1°K at 15.50 GHz. Since the hot-cold load temperature difference $\approx 215^\circ\text{K}$, this error is less than 0.5 per cent at both frequencies. A measurement of the calibration noise temperature consisted of allowing the gas tube to warm up for 10 seconds, and then averaging the output for precisely 2 minutes. This procedure was necessary, since the noise temperature of the tube was found to decrease slightly with time in a very reproducible fashion, an effect which has been noticed previously in gas discharges. Table IV-5 shows the results of measurements separated by a 3-month time interval.

Table IV-5. Results of measurements.

Date	Frequency (GHz)			
	7.75	8.25	15.25	15.75
October 7, 1965	29.37°K	28.87°K	25.74°K	26.08°K
Jan. 18, 1966	29.14°K	28.72°K	25.68°K	25.85°K

It is notable that the calibration signals on January 18, 1966, differed in all cases

by less than 1 per cent from the values on October 7, 1965. With these values of calibration temperatures taken, the 15.5-GHz radiometer was used to measure the temperature of a termination immersed in a slush mixture of melting ice, and the results compared with temperatures on a mercury thermometer. Including the mismatch at the load, the radiometric temperature was $20.96 \pm 0.05^\circ\text{C}$ (rms error), whereas the mercury thermometer read 21.0°C . The agreement substantiates the "less than 1%" error estimate of the calibration-noise temperature.

3. Observations

An attempt to begin measurements was thwarted, in 1964, by a bewildering lack of reproducibility in the data. The trouble was traced to a faulty antenna elevation indicator. The solution consisted in first fastening a scribed reference block on the stationary part of the antenna mount, close to the large support ring, (see Fig. IV-1). Next, a reference marker was attached to the movable support ring at the nominal elevation of transit for each radio source, thereby making a "setting circle." Because of the large diameter of the ring, 1/32 inch on the reference marker is equivalent to 2.20 minutes of arc. The reproducibility of aligning a given reference mark with the scribed block is estimated to be better than 20 seconds of arc — quite adequate for the job.

An observation consists of the following sequence of events: The horn antenna is elevated to the desired setting on the reference marker. The paper tape punch is started, and begins recording the output of the linear integrators every 10 seconds. Approximately 20 minutes before the source is due to transit, the calibration noise tube is turned on for 2 minutes. The source then drifts through the antenna beam, and 20 minutes later the noise tube is turned on again. Figure IV-7 shows the analog record of a typical observation.

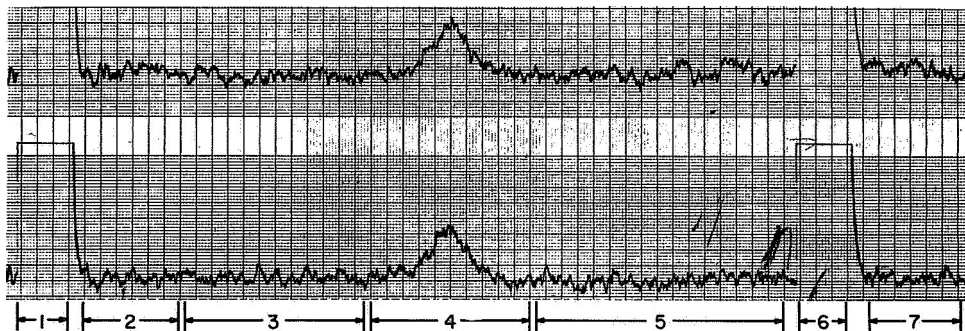


Fig. IV-7. Drift scan of Taurus A at 2 cm with the cornucopia horn antenna on January 16, 1966. The recording time constant is 10 seconds, and the time lapse from region 1 to region 6 is approximately 40 minutes.

(IV. RADIO ASTRONOMY)

The calibration is off-scale on the analog records, but is recorded correctly on the paper tape punch. The signal shown is approximately 0.4°K , and the recorder RC time constant is 10 seconds. Transit drift scans were taken of each source at each frequency at various elevation offsets as measured on the reference marker.

4. Data Reduction

A computer program was written to process the data automatically. The computer first reads the tape, recording and numbering the incoming data points sequentially, and produces a plot of signal versus point number on the high-speed printer. The observer then examines the analog record {see Fig. IV-7) to decide which parts of the observation

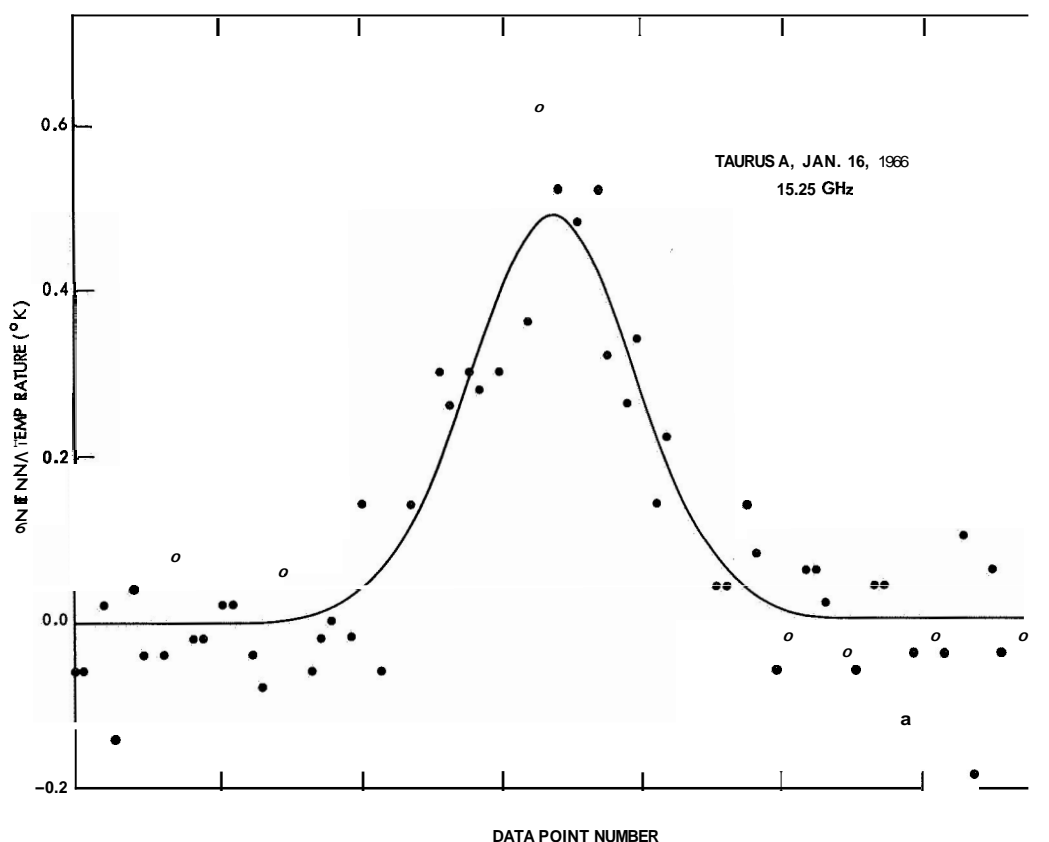


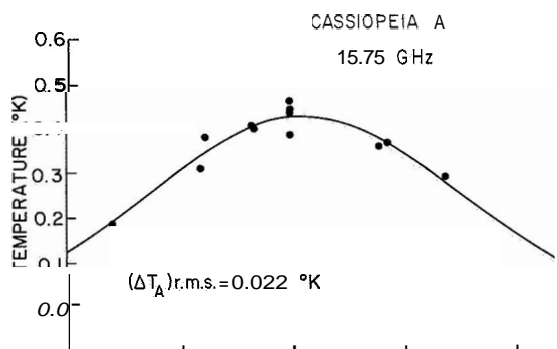
Fig. IV-8. Region 4 from Fig. IV-7, showing the data points and the Gaussian curve fitted through them by the computer program.

are to be considered as calibration, baseline, and transit data. Upon correlating the analog record with the printer plot, the observer then informs the computer of the point number for the beginning and end of each type of data. Figure IV-7 is marked off in the relevant ranges as follows:

(IV. RADIO ASTRONOMY)

1. First calibration signal.
2. Baseline for first calibration signal.
3. Baseline for observation before transit.
4. Transit of radio source.
5. Baseline for observation after transit.
6. Second calibration signal.
7. Baseline for second calibration signal.

The program then averages the signals for the first calibration and subtracts the average signal on the first calibration baseline. The same operation is done on the second calibration. Using the value of this calibration in degrees Kelvin, the computer proceeds to correct the data between the calibrations for any linear gain changes (a procedure later found to be unnecessary) and scales the numbers to temperature. Then, the two blocks of data labelled "baseline" before and after transit are fitted by least squares to a straight line and this baseline subtracted from the transit data. The uncorrected transit observation is then fitted by a least-squares iteration procedure to a Gaussian curve, and the results are printed out. Figure 8 shows the curve calculated from the corrected data of Fig. IV-7.



Each run is corrected individually for atmospheric attenuation. Ground-level relative humidity is monitored at the radio telescope site and the total atmospheric attenuation is determined from theoretical expressions. Typical zenith attenuations, during wintertime conditions, amounted to 1.8 per cent at 8.25 GHz and 2.5 per cent at 15.5 GHz.

The peak temperatures for all runs at all different elevation offsets are then fitted to another Gaussian by the same program to yield finally the peak temperature for the source. Figure IV-9 shows the data and the computed curve for one of the sources.

5. Results

The results of all of these measurements are best presented in tabular form.

Table IV-6. Results of measurements for Cass A.

Cassiopeia A	Frequency (GHz)			
Quantity	8.25	15.25	15.75	Comments
Aa (arc minutes)	45.9	30.0	30.0	Right Ascension response width
$\Delta\delta$ (arc minutes)	59.4	28.2	35.3	Declination response width
Peak temperature ($^{\circ}\text{K}$)	0.925	0.479	0.425	Parallactic angle of feed = 90°
(ΔT) rms	0.004	0.025	0.022	
Rotary joint loss	1.049	1.062	1.062	Correction factors See Note
10-sec linear integrator	1.000	1.000	1.000	
Source size	1.002	1.008	1.008	
Total correction factor	1.051	1.070	1.070	
Corrected temperature	0.972	0.512	0.455	Degrees Kelvin
Flux Sv	616	399	362	Units $10^{-26} \text{ Wm}^{-2} \text{ Hz}^{-1}$
Total rms error (%)	4.5	6.5	6.5	See Table IV-8
Epoch	1965.9	1966.0	1966.0	

Note: The source size correction used for Cassiopeia A is the mean of the correction factors for a disc 4:0 diameter and for a thin ring 4:0 diameter. The beamwidths used in this calculation were the response widths in Right Ascension and Declination listed in Tables IV-6 and IV-7.

Table IV-7. Results of measurements for Tau A.

Taurus A	Frequency (GHz)			
Quantity	8.25	15.25	15.75	Comments
Aa (arc minutes)	47.1	31.3	31.1	Right Ascension response width
Ab (arc minutes)	58.0	34.0	35.8	Declination response width
Peak temperature ($^{\circ}\text{K}$)	0.822	0.548	0.507	Parallactic angle of feed = 90°
(ΔT) rms	0.005	0.029	0.022	
Rotary joint loss	1.049	1.062	1.062	
10-sec linear integrator	1.000	1.000	1.000	
Source size	1.0047	1.0120	1.0120	4:2 X 2:9 Gaussian
Polarization	1.033	1.033	1.033	See Note
Total correction factor	1.0887	1.110	1.110	
Corrected temperature	0.895	0.608	0.563	
Flux Sv	567	474	448	
Total rms error (%)	4.5	6.5	6.5	See Table IV-8
Epoch	1966.0	1966.0	1966.0	

Note: The polarization averaged over the source Taurus A at 8.25 GHz has been measured with the Haystack antenna to be 8.0% at parallactic angle 147° . The recent data of Boland et al.⁵ at 2.07 cm indicate that the same correction factor may be applied to the present data at 15.5 GHz.

(IV. RADIO ASTRONOMY)

Table IV-6 shows the results for Cassiopeia A, and Table IV-7 the results for Taurus A. The rms errors involved in the final result are listed in Table IV-8 in percentages.

Table IV-8. RMS errors.

Description of Source of Error	Frequency (GHz)	
	8.25	15.50
Measurement of peak temperature	0.7%	5.0%
Rotary joint losses (rotation)	0.5	0.7
Source model	0.2	0.3
Antenna efficiency	4.0	4.0
Calibration noise	0.5	0.7
Total rms error	4.5%	6.5%

The data obtained have been plotted on a graph containing all absolute flux measurements that are now available. The results for Cassiopeia A were corrected to **1964.0**, under the assumption of a secular decrease of 1.1 per cent per year in the flux, and the data are shown in Fig. IV-10. Similar results are shown in Fig. IV-11 for Taurus.

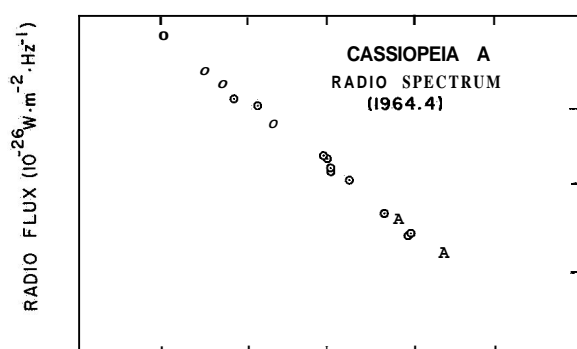


Fig. IV-10.

Radio spectrum of Cassiopeia A. Open circles denote other published values of greater than 10 per cent precision. The present measurements are indicated by open triangles.

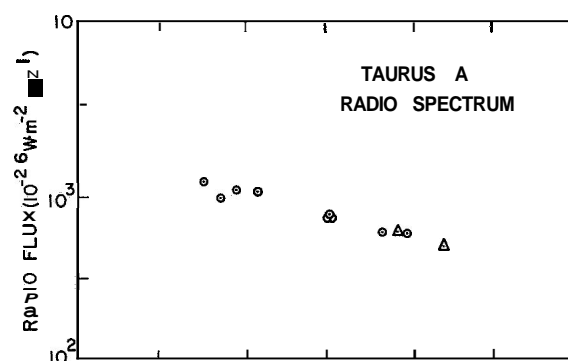


Fig. IV-11.

Radio spectrum of Taurus A. Data selected as in Fig. IV-10.

It is clear that the change in spectral index above 7 GHz for Cassiopeia A, as reported by Baars and his co-workers,⁶ has not been found. The radio spectrum is well

(IV. RADIO ASTRONOMY)

approximated by a law of the form $X = k\nu^{-a}$ (where ν = frequency, and k is some constant) for a constant value of $a = 0.75 \pm .05$ over the entire range of data shown.

The data for Taurus also suggest a constant spectral index, a . The lower frequency value of 0.25 is in reasonable accord with the present results, although the data as a whole exhibit greater scatter from a smooth curve than for Cassiopeia.

The research described in this report has been made possible through the kind cooperation of the staff of the Haystack Research Facility, Lincoln Laboratory, M. I. T. We wish to acknowledge especially the assistance of John A. Ball, who made some of the 15.5-GHz observations and offered many helpful criticisms. Also, the data-reduction problem was greatly facilitated by the CDC 3200 computer, made available by J. Morriello, and by a paper-tape reading program provided by Patricia P. Crowther for the Univac 490 computer.

R. J. Allen, A. H. Barrett

References

1. R. J. Allen and A. H. Barrett, Quarterly Progress Report No. 81, Research Laboratory of Electronics, M. I. T., April 15, 1966, p. 13.
2. A. Sotiropoulos and J. Ruze, "Haystack Calibration Antenna," Technical Report No. 367, Lincoln Laboratory, M. I. T., Lexington, Mass., December 15, 1964.
3. H. G. Weiss, "The Haystack Experimental Facility," Technical Report No. 365, Lincoln Laboratory, M. I. T., Lexington, Mass., September 15, 1964.
4. These terminations are a manufactured item, consisting of a well-matched load in a Styrofoam potentiometer. They have greatly facilitated the frequent calibrations of the radiometers.
5. J. W. Boland, J. P. Hollinger, C. H. Mayer, and T. P. McCullough, *Astrophys. J.* **144**, 437 (1966).
6. J. W. M. Baars, P. G. Mezger, and H. Wendker, *Astrophys. J.* **142**, 122 (1965).

B. RADIO DETECTION OF INTERSTELLAR $O^{18}H^1$

Previous radio observations of interstellar OH have been due to the most abundant isotopic species $O^{16}H^1$. These observations have allowed the computation¹ of the detection possibilities and accurate line frequencies of the isotopic species $O^{18}H^1$. In particular, the $F = 2-2$, $^2\pi_{3/2}$, $J = 3/2$, A-doublet transition was calculated to occur at 1630.3 ± 0.2 Mc/sec. We have observed this line in the absorption spectrum of the galactic center (Sagittarius A) using the 140-ft radio telescope of the National Radio Astronomy Observatory. The observations were made during April 30-May 4, 1966, and consisted in a total of 18 hours of integration. The observations reveal absorptions of approximately 0.4°K and 0.1°K at radial velocities of +40 km/sec and -135 km/sec, respectively, if the rest frequency is taken to be 1639.460 Mc/sec. The velocities of

(IV. RADIO ASTRONOMY)

absorption are in excellent agreement² with those of $O^{16}H^1$, and the rest frequency agrees very well with the predicted value. The results of the observations are shown in Fig. VI-12. A spectral width of 2.0 Mc/sec was the maximum that could be examined within our assigned time on the antenna. This also precluded making observations of the line expected at 1637.3 ± 0.2 Mc/sec which might be as much as a factor of two less intense and, therefore, require four times as much observing time for the same

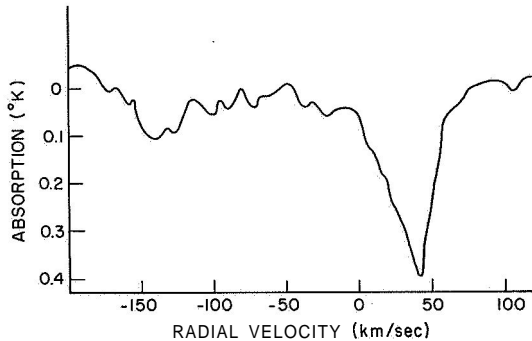


Fig. IV-12. $O^{18}H^1$ absorption profile in the direction of the galactic center (Sagittarius A).

$\Delta\nu$ (resolution), 50 kHz
 $\tau = 18$ hr
Theoretical rms, $0.03^\circ K$
Rest frequency, 1639.460 MHz.

signal-to-noise ratio.

The theoretical rms noise for 18 hours of integration is $0.03^\circ K$, and it is apparent that this value is almost realized. Severe problems arise in spectral-line radiometers when very long integration times are involved. A dual-switching technique to eliminate instrumental effects was used. First, a load-switching technique was used on each hour of observation and the correlator computed the difference in autocorrelation functions looking at the antenna and then at the load. Then for each hour observation the local oscillator was shifted to displace any signal from Sagittarius A by 250 kc/sec, from the previous position in a three-position cycle. The data were then averaged by shifting the spectra appropriately so that the signals line up in frequency. The data were also averaged by using shifts opposite to those required to line up the signal data. The difference of the two averages was then taken and compensation made for the smeared signal data in the reference spectrum. This last technique eliminated any instrumental spectra from the correlator which amounted to several degrees. The instrumental effect in the correlator was due to the fact that errors in the sampler were not entirely random and independent of the load-switching cycle. This combination of load and frequency switching may always be desirable, however, for long integration times, even with improved samples performance.

It is difficult to estimate the O^{18}/O^{16} isotopic abundance ratio from the results of the observations because of some uncertainty in the interpretation of the $O^{16}H^1$ absorption. Robinson and co-workers³ give an $O^{16}H^1$ optical depth of 0.9 for the ± 40 km/sec absorption feature in Sagittarius A, and similar arguments can be used to infer an

(IV. RADIO ASTRONOMY)

optical depth of 0.35 for the -135 km/sec feature if the more recent observations of Bolton and co-workers² are used. Our observations can be interpreted in terms of $O^{18}H^1$ optical depths of 2×10^{-3} and 5×10^{-4} for the +40 km/sec and -135 km/sec features, respectively. If we make the plausible assumption that the $O^{18}H^1$ and $O^{16}H^1$ dipole matrix elements are the same, and the more uncertain assumption that the $O^{18}H^1$ and $O^{16}H^1$ optical depths are in the direct ratio of the O^{18}/O^{16} abundances, then we derive O^{18}/O^{16} isotopic abundance ratios of 1/450 and 1/700 for the two absorption features. These are in good agreement with the terrestrial abundance ratio of 1/490. Departures of the interstellar ratios from the terrestrial value could easily be explained by the uncertainty in the observed data, interpretation of the $O^{16}H^1$ observations or different excitation and/or formation mechanisms for the two isotopic species of OH. To the best of our knowledge, the observations yield the first measure of any isotopic abundance ratios for the interstellar medium.

We wish to acknowledge the cooperation of personnel of the National Radio Astronomy Observatory and the use of the 140-ft radio telescope for our observations.

A. H. Barrett, A. E. E. Rogers

References

1. A. H. Barrett and A. E. E. Rogers, Nature **204**, 62 (1964).
2. J. G. Bolton, F. F. Gardner, R. X. McGee, and B. J. Robinson, Nature **204**, 30 (1964).
3. B. J. Robinson, F. F. Gardner, K. J. van Damme, and J. G. Bolton, Nature **202**, 989 (1964).

C. K-BAND MEASUREMENTS

Measurements of Venus, Jupiter, the Sun, Moon, Taurus A, and 3C273 were made during the period from January to March, 1966, at wavelengths of 1.18, 1.28, 1.35, 1.43, and 1.58 cm. The five-channel Dicke radiometer and 28-ft antenna were essentially those described in a previous report.¹ The major additions to the system were IF gain modulators to permit separate balancing of each channel, and a new antenna feed to permit operation at lower frequencies.

The preliminary results indicate that the average spectra of Venus and Jupiter exhibited no resonant features at the 1.35-cm wavelength water-vapor resonance.

D. H. Staelin, N. E. Gaut, R. W. Neal,
G. D. Papadopoulos, E. C. Reifstein

References

1. D. H. Staelin and A. H. Barrett, Quarterly Progress Report No. 78, Research Laboratory of Electronics, M. I. T., July 15, 1965, p. 21.

D. ATMOSPHERIC ABSORPTION AT 72 Gc/sec

An experiment to measure the atmospheric opacity at 72 Gc/sec was performed to investigate absorption on the wings of the millimeter resonance lines of molecular oxygen. Solar-extinction measurements were made with the 4-mm radiometric system on the roof of Building 26 at M. I. T., in Cambridge. Radiosonde measurements of the temperature, pressure, and water-vapor density profiles were obtained from the Aerospace Instrumentation Laboratory at the Air Force Cambridge Research Laboratories for the days of the observations.

On a clear day, the total atmospheric opacity, τ , at 72 Gc/sec will be the sum of the opacities arising from molecular oxygen absorption and water-vapor absorption.

$$\tau = \tau_{\text{O}_2} + \tau_{\text{H}_2\text{O}} \quad (1)$$

Generally, $\tau_{\text{H}_2\text{O}}$ is of the order of 1/3-1/2 of τ_{O_2} at this frequency for typical winter atmospheres. For each of the days of observation, theoretical values of the opacity, based on the radiosonde data, were computed for comparison with the measured opacities. The opacity resulting from water-vapor absorption was computed by using the absorption coefficient of Barrett and Chung¹ as modified by Staelin.² Two separate oxygen opacities were computed for each observing day. In one, the resonance line shape of Van Vleck and Weisskopf,³

(IV. RADIO ASTRONOMY)

$$F_{VV-W}(\nu, \nu_0, \Delta\nu) = \frac{\nu}{\pi\nu_0} \left[\frac{\Delta\nu}{(\nu-\nu_0)^2 + \Delta\nu^2} + \frac{\Delta\nu}{(\nu+\nu_0)^2 + \Delta\nu^2} \right], \quad (2)$$

was used for each of the millimeter resonance lines of oxygen; in the other, the line shape of Zhevakin and Naumov,⁴

$$F_{Z-N}(\nu, \nu_0, \Delta\nu) = \frac{4\nu\nu_0}{\pi} \frac{\Delta\nu}{(\nu^2 - \nu_0^2)^2 + 4\nu^2\Delta\nu^2}, \quad (3)$$

was used. The expression for the linewidth parameter, $\Delta\nu$, appearing in both the line-shape expressions was taken as that of Meeks and Lilley.⁵

Table IV-9 shows the measurements compared with each of the theoretical computations.

Table IV-9. Atmospheric opacities.

	$\tau_{W-W} = \tau_{O_2_{VV-W}} + \tau_{H_2O}$ $\tau_{Z-N} = \tau_{O_2_{Z-N}} + \tau_{H_2O}$		
	τ measured (db)	τ_{VV-W} (db)	τ_{Z-N} (db)
18 March 1966	1.71 ± 0.15	2.09	1.83
21 March 1966	1.29 ± 0.21	1.94	1.66
29 March 1966	1.37 ± 0.17	1.67	1.35
4 April 1966	1.65 ± 0.23	1.84	1.59
15 April 1966	1.62 ± 0.19	1.94	1.68

The measurements appear to be in fairly good agreement with the computations based on the Zhevakin-Naumov line shape. It is possible, however, to explain the measured results within the context of the Van Vleck-Weisskopf line shape if the linewidth parameter, $\Delta\nu$, is taken as 0.85 of the value used in the computations. At the pressures of interest this is not an unreasonable value for $\Delta\nu$.

Atmospheric opacity measurements both above and below the 60 Gc/sec complex of oxygen lines are suggested to resolve this conflict. The line-shape difference is an asymmetric one, with the VV-W line shape giving more absorption above the resonance and less below it than the Z-N line shape; whereas a smaller $\Delta\nu$ gives less absorption both above and below the resonance.

Also, recent laboratory measurements of the millimeter and submillimeter

(IV. RADIO ASTRONOMY)

water-vapor lines should be incorporated *into* a more accurate expression for absorption at frequencies near **72 Gc/sec.**

P. R. Schwartz, W. B. Lenoir

References

1. **A. H. Barrett and V. K. Chung**, J. Geophys. Res. **67**, 4259-4266 (1962).
2. **D. H. Staelin**, Sc.D. Thesis, Department of Electrical Engineering, M.I.T. February **1965**.
3. **J. H. Van Vleck and V. F. Weisskopf**, Rev. Mod. Phys. **17**, 227-236 (1945).
4. **S. A. Zhevakin and A. P. Naumov**, Radio tekhnika i Elektronika **9** (8), 1327 (1964).
5. **M. L. Meeks and A. E. Lilley**, J. Geophys. Res. **68**, 1683-1695 (1963).

(IV. RADIO ASTRONOMY)

E. OBSERVATIONS OF MICROWAVE EMISSION FROM ATMOSPHERIC OXYGEN

The data taken during the balloon flights in July, 1965, have been reduced.' The results of the ascent portion of Flight 154-P are shown in Fig. IV-13. The solid lines are theoretical computations based on the Van Vleck-Weisskopf pressure-broadened

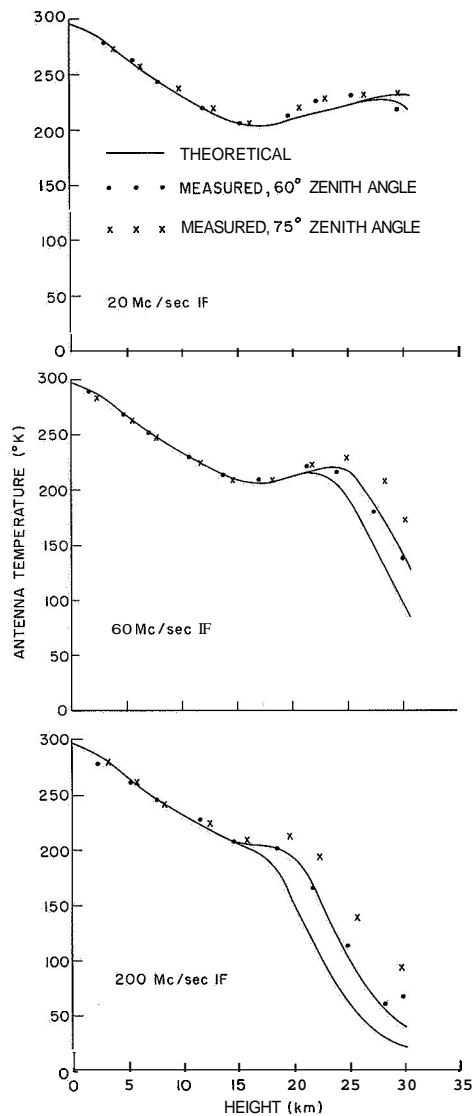


Fig. IV-13. Results of ascent part of Flight 154-P.

resonance line shape. The true atmospheric temperature profile (as measured on ascent) was used in the theoretical computations.

The data of Fig. IV-13 are generally consistent with those taken during previous balloon flights.² The theoretical antenna temperatures agree with the measured values for low heights, at which both are equal to the atmospheric temperature because the optical

(IV. RADIO ASTRONOMY)

depth is large for all channels. The antenna temperatures of the 200-Mc/sec channels are the first to depart from the atmospheric temperature at -18-20 km; the antenna temperatures of the 60-Mc/sec and 20-Mc/sec channels do likewise at 22-24 km and 28-30 km, respectively.

Differences between the measured and theoretical values are evident. On the 200-Mc/sec and 60-Mc/sec channels the measured antenna temperatures are higher than predicted above the height at which departure from the atmospheric temperature occurs;

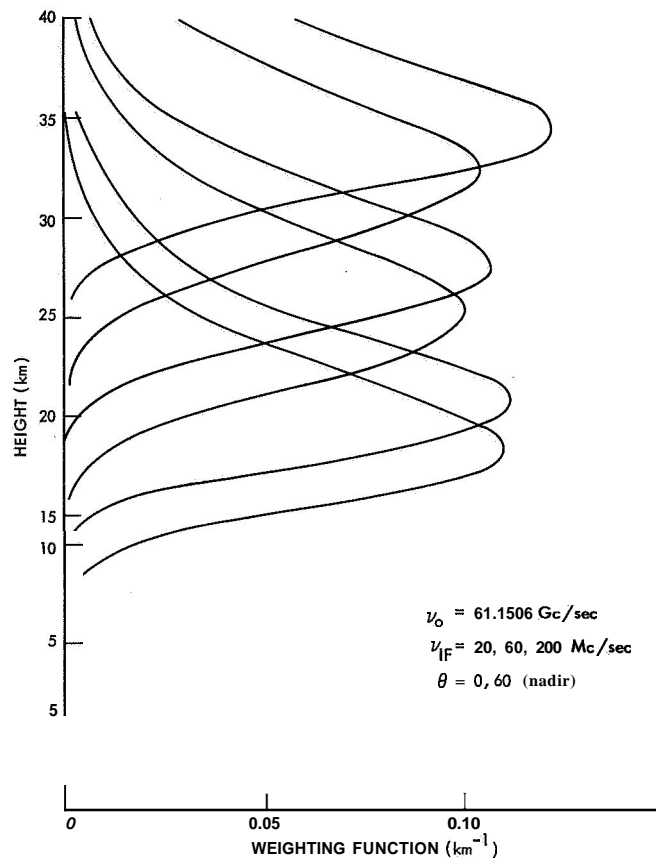


Fig. IV-14. Temperature weighting functions for Flights 152-P and 153-P.

Table IV-10. Summary of Winter balloon flight experiments.

Flight	Date	Duration	Float Altitude	Comments
198-LP	27 Jan.	8 hr	38 km	Successful
199-LP	2 Feb.	1 1/2 hr	none	Beacon Failure
200-LP	3 Feb.	8 hr	39 km	Successful

(IV. RADIO ASTRONOMY)

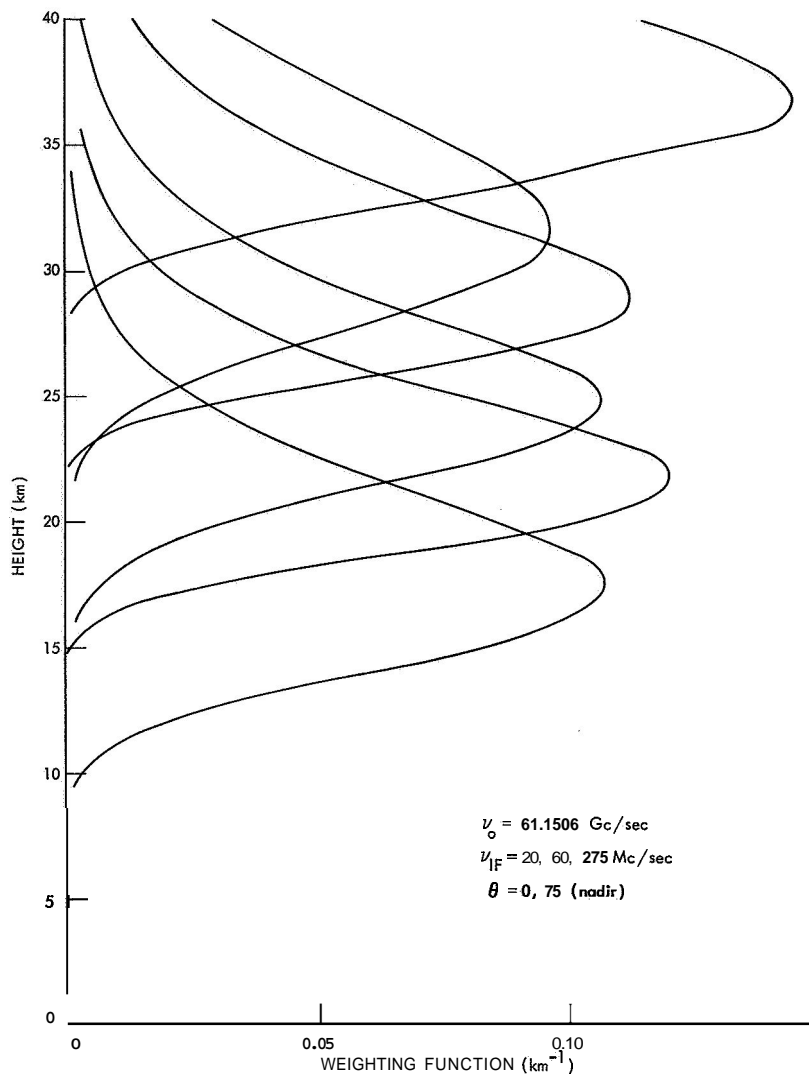


Fig. IV-15. Weighting functions for Flights 198-LP, 199-LP, and 200-LP.

whereas the 20-Mc/sec channels behave approximately as predicted by theory. These results would appear to indicate a higher absorption than predicted at $\pm 200 \text{ Mc/sec}$ and $\pm 60 \text{ Mc/sec}$ from the resonance frequency, and an absorption equal to the predicted value at $\pm 20 \text{ Mc/sec}$ from the resonance.

The discrepancy may lie in the theoretical assumption that the absorption coefficient resulting from many overlapping resonance lines is the sum of the individual absorption coefficients. There has been some evidence that this is not the case in the wings of overlapping lines, but that the true absorption coefficient is larger than the sum of the individual ones.

Analysis of the data from Flight 154-P continues; in particular, an inversion

Table IV-11. Summary of Flights 198-LP, 199-LP, and 200-LP.

$\nu_o = 61.1506 \text{ Gc/sec}$ (local-oscillator frequency)

$\Delta T_{\text{rms}} \sim 1\text{-}2^\circ \text{K}$

ν_{if} = center frequency of IF passband

BW_{if} = bandwidth of IF passband

h_o = height of weighting-function maximum

Δh = width of weighting function

T_B = brightness temperature predicted from model atmosphere

θ = angle of antenna direction (from nadir)

θ (deg)	ν_{if} (Mc/sec)	BW_{if} (Mc/sec)	h_o (km)	Δh (km)	T_B ($^\circ \text{K}$)
75	20	10	37	7	258
0	20	10	32	10	246
75	60	10	29	8	244
0	60	10	25	9	230
75	275	24	22	7	222
0	275	24	17.5	8	218

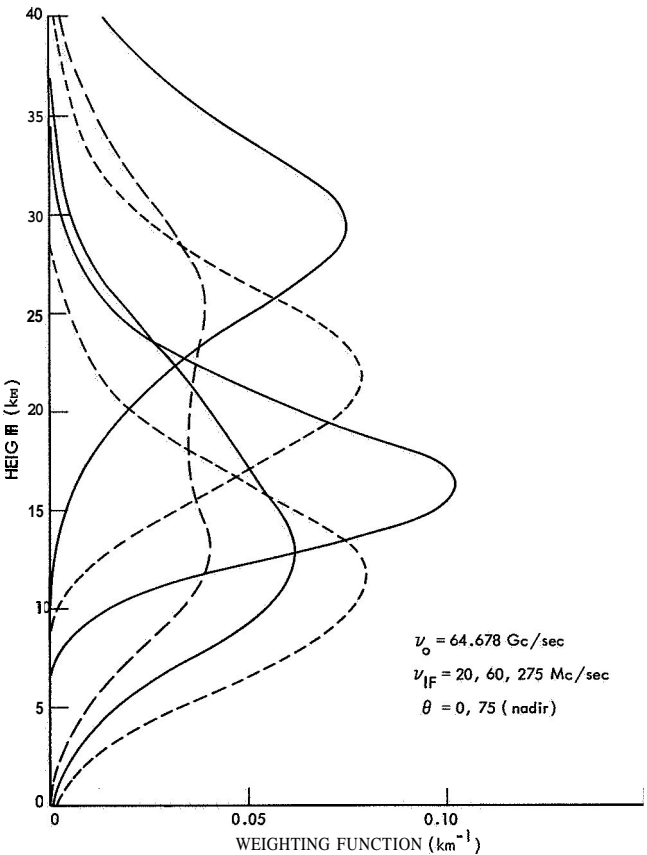


Fig. IV-16.
Predicted weighting functions for
flights in Summer, 1966.

(IV. RADIO ASTRONOMY)

method yielding the absorption coefficient at various heights for each of the channels is being developed. This information will make interpretation in terms of correct line shapes much easier.

The results of Flights 152-P and 153-P are being analyzed with emphasis on inverting the microwave antenna temperature measurements to obtain the atmospheric temperature profile in the 16-38 km height range. The temperature weighting functions for these flights are shown in Fig. IV-14.

Another series of balloon flights was undertaken in January-February, 1966, from Phoenix, Arizona. The purpose of these flights was similar to that for Flights 152-P and 153-P, namely to make microwave measurements that could be interpreted to yield the atmospheric temperature profile for a given height range. The flight characteristics and comments are summarized in Table IV-10. The weighting functions for these flights are shown in Fig. IV-15. The radiometer was modified slightly to give a better spread of weighting functions and to probe as deeply as possible for frequencies centered on the 9+ resonance line. The radiometer parameters and the height levels sounded by these experiments are summarized in Table IV-11. Analysis of these data is under way.

Table IV-12. Summary of flights in Summer, 1966.

$$\nu_o = 64.678 \text{ Gc/sec}$$

$$\Delta T_{\text{ems}} \quad 1-2^\circ\text{K}$$

θ (deg)	ν_{if} (Mc/sec)	BW _{if} (Mc/sec)	h_o (km)	Ah (km)	T_B (°K)
75	20	10	29	12	231
75	60	10	22	12	218
75	275	24	16	9	214
0	20	10	14-25	23	225
0	60	10	13	15	224
0	275	24	12	11	227

Future flights are planned for the summer of 1966. Major changes in the radiometer are being made; the local-oscillator frequency is being changed to 64.678 Gc/sec, the 21+ resonance which is much weaker than the 9t resonance, and the three IF will be operated simultaneously rather than singly. The new frequency will permit weighting functions that penetrate the tropopause to give inversion methods a real test.

The predicted weighting functions for these flights are shown in Fig. IV-16. The radiometer parameters and the height levels sounded by these experiments are summarized in Table IV-12.

W. B. Lenoir

References

1. W. B. Lenoir, Quarterly Progress Report No. 79, Research Laboratory of Electronics, M.I.T., October 15, 1965, pp. 17-19.
2. A. H. Barrett, J. W. Kuiper, and W. B. Lenoir (submitted to J. Geophys. Res.).

V. SOLID-STATE MICROWAVE ELECTRONICS*

Academic and Research Staff

Prof. R. P. Rafuse

Graduate Students

D. H. Steinbrecker
K. D. Thompson

A. Vander Vorst
Z. Vugrinec

RESEARCH OBJECTIVES

This group, formerly a part of the Radio Astronomy Group, has decided that its aims are wider than those of the Radio Astronomy Group. As a consequence of this decision, a new group has been formed. The general areas of interest are in the generation and amplification of microwave power by solid-state mechanisms with an emphasis on millimeter wavelengths.

Recent developments include a VHF mixer with 130-db dynamic range (5-db noise figure, 100-kc IF bandwidth, and 40-db down third-order intermodulation limit) a 3-GHz, single-sideband mixer with 2-db over-all system noise figure (achieved by careful control of the image impedance in a very good mixer, and a 0.5-db noise figure IF), and a new and very powerful technique for high-efficiency, high-order harmonic multiplication.

Present plans include development of X-band and 4-mm mixers using Schottky-barrier diodes (in order to achieve noise figures of 5 db and lower), continuing investigations of varactor multipliers of high order, high power and high efficiency, with an eventual goal of a 100-watt, cw, solid-state transmitter at 2.5 GHz with an over-all DC-to-RF conversion frequency of better than 50 per cent.

Work also continues on the characterization of millimeter-wave varactors and on synthesis problems associated with low-noise parametric amplifiers at millimeter wavelengths.

R. P. Rafuse

*

This work is supported by the National Aeronautics and Space Administration (Grant NsG-22-009-163).

PRECEDING PAGE BLANK NOT FILMED.

VI. OPTICAL AND INFRARED SPECTROSCOPY*

Academic and Research Staff

Prof. C. H. Perry

Graduate Students

Jeanne H. Fertel
D. J. Muehlner

J. F. Parrish
E. F. Young

Undergraduate Students

T. F. McNelly
J. F. Reintjes, Jr.
J. D. Wrigley, Jr.

A. WORK COMPLETED

The theses with titles and authors listed below were submitted to the Department of Physics, M. I. T. , May 1966, in partial fulfillment of the requirements for the degree of Bachelor of Science.

T. F. McNelly, "Reflectivity and Raman Studies of KTaO_3 and $(\text{K}, \text{Na})\text{TaO}_3$."

J. F. Reintjes, Jr., "Temperature Dependence of the Reflectivity and Raman Spectra in Ammonium Chloride and Ammonium Bromide."

C. H. Perry

B. INFRARED REFLECTIVITY AND OPTICAL CONSTANTS OF TEKTITES

The room-temperature reflectance of three Tektites having carrying compositions has been studied from $2.5\text{-}500\ \mu$ ($4000\text{-}20\ \text{cm}^{-1}$), with the use of a variety of instruments.^{1,2}

The optical constants were obtained from a Kramers-Kronig analysis of the reflectivity data.³ A classical dispersion formula was used to fit the measured reflectivity curve,⁴ and approximate values for the frequencies (ω), oscillator strengths (s^2), and damping constants (γ) were obtained for the two strongest vibrations. The results are the following

$$\omega_1 = 457 \pm 1\ \text{cm}^{-1}$$

$$\omega_2 = 1060 \pm 5\ \text{cm}^{-1}$$

$$s_1^2 = 1.85 \pm .01 \times 10^5\ (\text{cm}^{-1})^2$$

$$s_2^2 = 5.63 \pm .01 \times 10^5\ (\text{cm}^{-1})^2$$

$$\gamma_1 = 55 \pm 5\ \text{cm}^{-1}$$

$$\gamma_2 = 80 \pm 5\ \text{cm}^{-1}$$

The Tektites that were investigated had been completely analyzed for the major constituent~which are listed in Table VI-1. The reflectivity curves for a Moldavite (T5309)

* This work was supported by the Joint Services Electronics Programs (U. S. Army, U. S. Navy, and U. S. Air Force) under Contract DA 36-039-AMC-03200(E).

PRECEDING PAGE BLANK NOT FILMED.

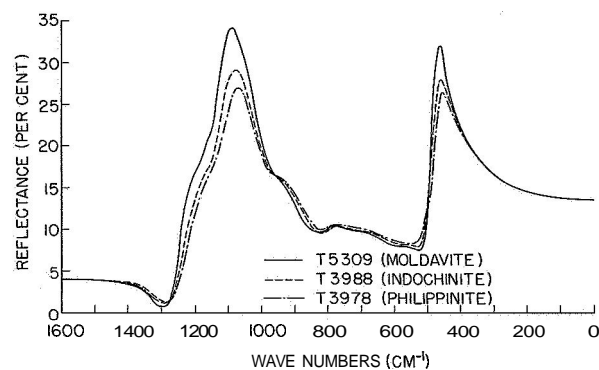


Fig. VI-1. Reflectivity curves for three Tektite samples.

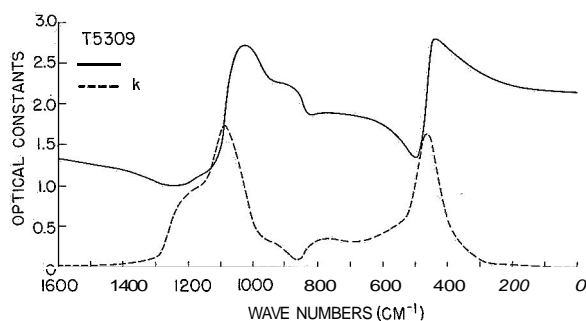


Fig. VI-2. Optical constants of Tektites (Moldavite T5309).

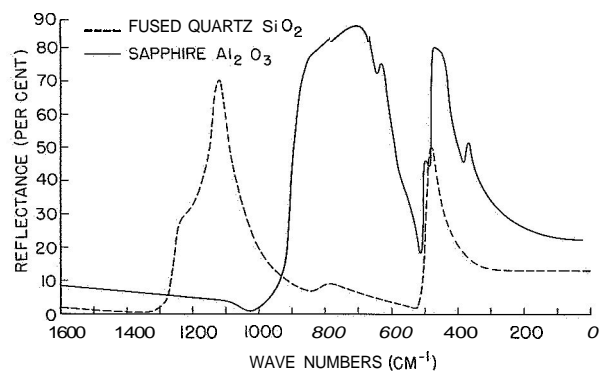


Fig. VI-3. Reflectivity curves for fused quartz (SiO_2) and Sapphire (Al_2O_3).

(VI. OPTICAL AND INFRARED SPECTROSCOPY)

Table VI-1. Major constituents of the Tektites investigated.

	Moldavite T5309	Indochinite T3988	Philippinite T3987
SiO ₂	79.6	73.3	70.1
Al ₂ O ₃	10.7	12.4	14.7
CaO	2.8	2.0	3.3
K ₂ O	3.5	2.5	2.6
FeO	1.5	4.2	4.2
MgO	1.9	2.3	2.4

an Indochinite (T5309) and a Philippinite (T3978) are shown in Fig. VI-1. The Moldavite had the largest percentage of SiO₂, and this appears to be the major contribution to the reflectivity curve, although all three samples show essentially similar features.

The optical constants n and k for the moldavite sample only are shown in Fig. VI-2, as the values are essentially the same for all three materials. The reflectivity curve (Fig. VI-1) shows slight shoulders in the region of 1200 cm^{-1} , 925 cm^{-1} , 750 cm^{-1} , and 400 cm^{-1} , as well as the major peaks in the reflectivity at $\sim 1080\text{ cm}^{-1}$ and 460 cm^{-1} .

Figure VI-3 shows the reflectivity curves for fused quartz and sapphire. The Tektite reflectivity measurements are similar in most respects to a composite curve of these materials when the relative compositions of the two major constituents are taken into account by weighting their individual dielectric dispersion curves. A thin slice, approximately $50\text{ }\mu$ thick, of the T5309 sample was used for transmission measurements and the curve is shown in Fig. VI-4. Owing to the large absorption coefficient, no measurable transmission could be obtained in the region of the lattice bands, but two broad bands were observed at 1600 cm^{-1} and 1850 cm^{-1} and a shoulder at 1950 cm^{-1} .

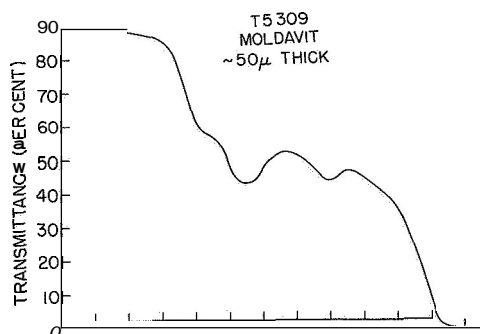


Fig. VI-4. Transmittance of $50\text{-}\mu$ thick slice of the Moldavite sample (T5309).

(VI. OPTICAL AND INFRARED SPECTROSCOPY)

The interpretation of these bands is not understood, as they could be due to second-order effects or absorption caused by the minor constituents in the materials. It is possible that studies of thin slices of the other two materials could help in the identification of these bands, but no measurable shift in the band centers or sharpening of the bands was observed on cooling the sample to liquid-nitrogen temperature.

Although the results of these studies do not specifically lead to the mode of origin for Tektites, the reflectivity curves are consistent with the major constituents and do show a measurable difference in intensity, which depends on the geographic location. The curves may be of significant importance in the identification of the major constituents of the lunar surface, for example, when studied by infrared techniques.

We would like to thank Professor W. H. Pinson, Jr., Department of Geology and Geophysics, M. I. T., for the samples.

C. H. Perry, J. D. Wrigley, Jr.

[The work of J. D. Wrigley, Jr. was supported in part by the Air Force Cambridge Research Laboratories under Contract AF19(628)-395.]

References

1. C. H. Perry, "Techniques of Far Infrared Study," Quarterly Progress Report No. 70, Research Laboratory of Electronics, M. I. T., July 15, 1963, p. 19.
2. C. H. Perry, Japan. J. Appl. Phys., Suppl. I, p. 564, 1965.
3. C. H. Perry, B. N. Khanna, and G. Rupprecht, Phys. Rev. **135**, A408 (1964).
4. W. G. Spitzer and D. A. Kleinman, Phys. Rev. **121**, 1324 (1961).
5. C. C. Schnetler and W. H. Pinson, Jr., Geochim. Cosmochim. Acta **28**, 793 (1964).

C. LOW-FREQUENCY VIBRATIONS IN AMMONIUM-CHLORIDE AND AMMONIUM-BROMIDE CRYSTALS

1. Introduction

Ammonium chloride has a well-known order-disorder transition¹ at **242.8°K**, and the Cs Cl structure both above and below the transition, with the ammonium ion in the center of a cube of eight chloride ions.² The deuterated compound ND₄Cl has the same structure, with a similar transition at 249.5 °K.

Ammonium bromide has an order-disorder transition¹ at 235°K, which is accompanied by a structure change from cubic to tetragonal, with two molecules per unit cell, and has a further transition back to body-centered cubic at **78°K**. This structure is an ordered one similar to the low-temperature phase of ammonium chloride. A thermal hysteresis of approximately 30° in specific-heat measurements has been observed in the lower transition temperature by Professor C. C. Stevenson, Department of

Physical Chemistry, M. I. T.

Hettich³ found that ammonium chloride becomes piezoelectric below the transition, and Kamiyoshi⁴ observed discontinuities in the static dielectric constants of both ammonium chloride and ammonium bromide. Menzies and Mills,⁵ in 1935, reported the appearance of a low-frequency line in the Raman spectrum of the chloride below the transition, and Krishnan⁶ has reported several low-frequency Raman lines in the bromide below its transition at 235°K. The far infrared reflection spectrum of NH_4Cl at room temperature was measured by Hojendahl,⁷ in 1938, and the reflection spectrum of NH_4Br was reported by Rubens and Wartenburg,⁸ in 1914.

Since all previous investigations had been performed more than thirty years ago, we decided to repeat both the infrared and Raman studies with the considerably improved instrumentation now available. The measurements were extended over a wider temperature range, more careful studies were made in the region of the transitions, and the results of both investigations were correlated and interpreted in terms of the low-frequency lattice vibrations.

2. Experimental Results

The reflectivity curves of NH_4Cl at room temperature and liquid-nitrogen temperature are shown in Fig. VI-5 and the reflectivity curves of NH_4Br at room temperature, dry-ice temperature and liquid-nitrogen temperature are shown in Fig. VI-6.

The reststrahlen frequency of NH_4Cl occurs at 193 cm^{-1} at room temperature and shifts to 210 cm^{-1} at liquid-nitrogen temperature. There is a sideband on the high-frequency side of the reflection peak which moves to higher frequencies as the temperature is lowered.

The reststrahlen frequency of NH_4Br occurs at 162 cm^{-1} at room temperature, 172 cm^{-1} at CO_2 temperature, and 175 cm^{-1} at liquid-nitrogen temperature.

The real and imaginary parts of the dielectric constant were obtained with a Kramers-Kronig analysis, and values of ϵ_0 , E_∞ , ω_t and ω_l are shown in Table VI-2.

The Lyddane-Sachs-Teller relation $\left(\frac{\omega_l^2}{\omega_t^2} = \frac{\epsilon_0}{\epsilon_\infty}\right)$ was satisfied by the frequency of NH_4Br at room temperature and of NH_4Cl at room temperature and liquid-nitrogen temperature.

The effective charges of the ions in the lattice were calculated, and the results are shown in Table VI-3.

The Raman spectra of NH_4Cl , ND_4Cl and NH_4Br are shown in Fig. VI-7.

A low-frequency line appears in the NH_4Cl spectra when the sample is cooled below 241°K. A similar line appears in the ND_4Cl spectra when the sample is cooled below 249.5°K. The shift in frequency of the line from the light to the heavy compound is

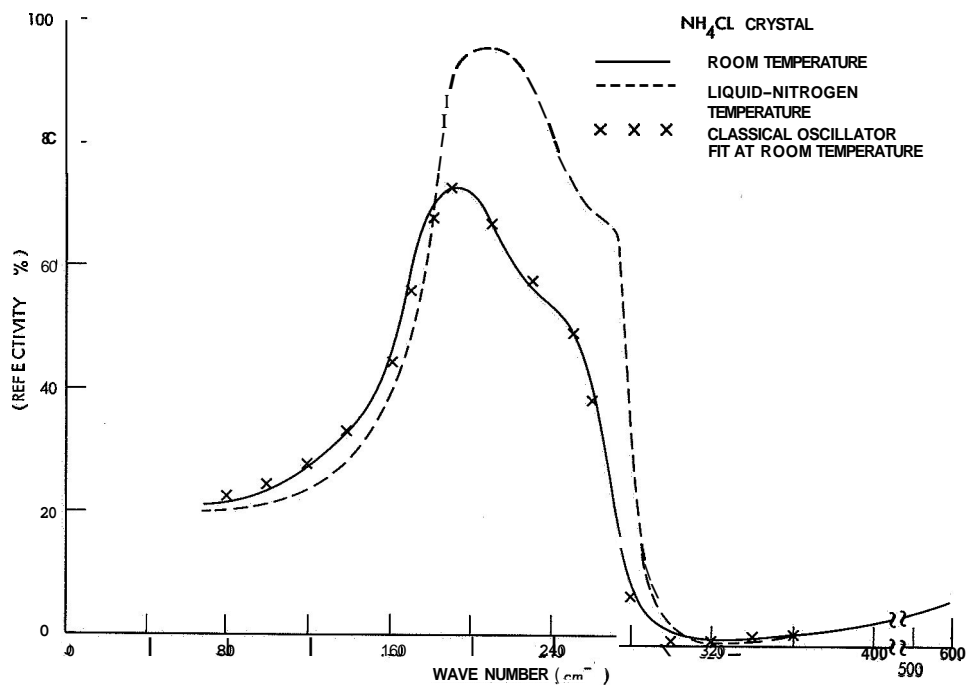


Fig. VI-5. Reflectivity curves of NH₄Cl at room temperature and liquid-nitrogen temperature.

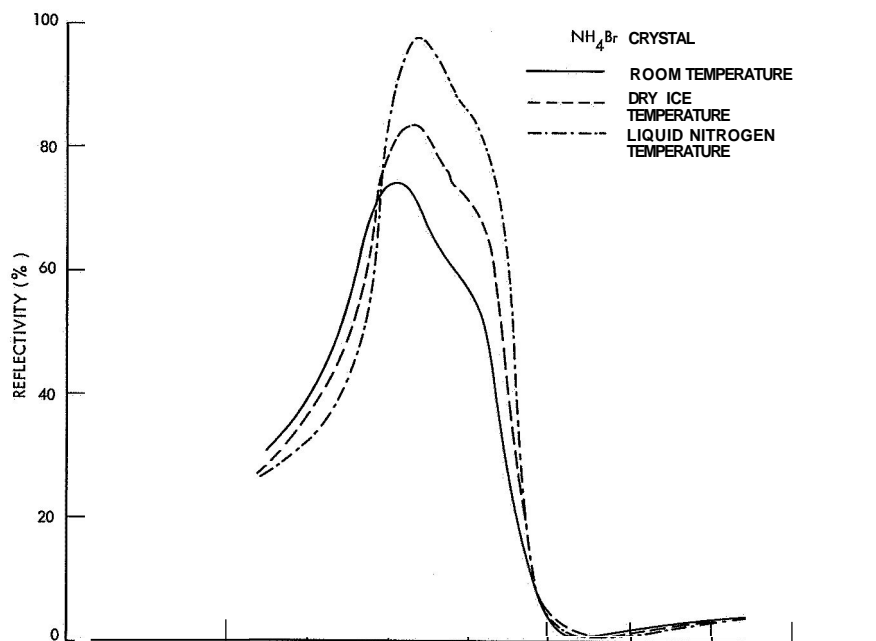


Fig. VI-6. Reflectivity curves of NH₄Br at room temperature, dry-ice temperature, and liquid-nitrogen temperature.

Table VI-2. Dielectric constants and vibrational frequencies of NH_4Cl and NH_4Br .

	ϵ_0	ϵ_∞	ω_t	ω_l	$\left(\frac{\epsilon_0}{\epsilon_\infty}\right)\omega_t$ (calc.)
NH_4Cl Room Temperature	7.25	2.94	175.0 cm^{-1}	272.8 cm^{-1}	275.0 cm^{-1}
NH_4Cl Nitrogen Temperature	6.70	2.94	188.0 cm^{-1}	281.5 cm^{-1}	284.0 cm^{-1}
NH_4Br Room Temperature	7.10	3.19	146.8 cm^{-1}	224.3 cm^{-1}	219.0 cm^{-1}
NH_4Br CO_2 Temperature	7.10	3.19	154.0 cm^{-1}	226.8 cm^{-1}	
NH_4Br Nitrogen Temperature	7.10	3.19	159.0 cm^{-1}	229.0 cm^{-1}	

Table VI-3. Effective charges for NH_4Cl and NH_4Br in cubic phase.

	O_{eff}
NH_4Cl Room Temperature	0.820
NH_4Cl Nitrogen Temperature	0.815
NH_4Br Room Temperature	0.753

Note: These values of O_{eff} are of the same magnitude as those obtained for the alkali halides.

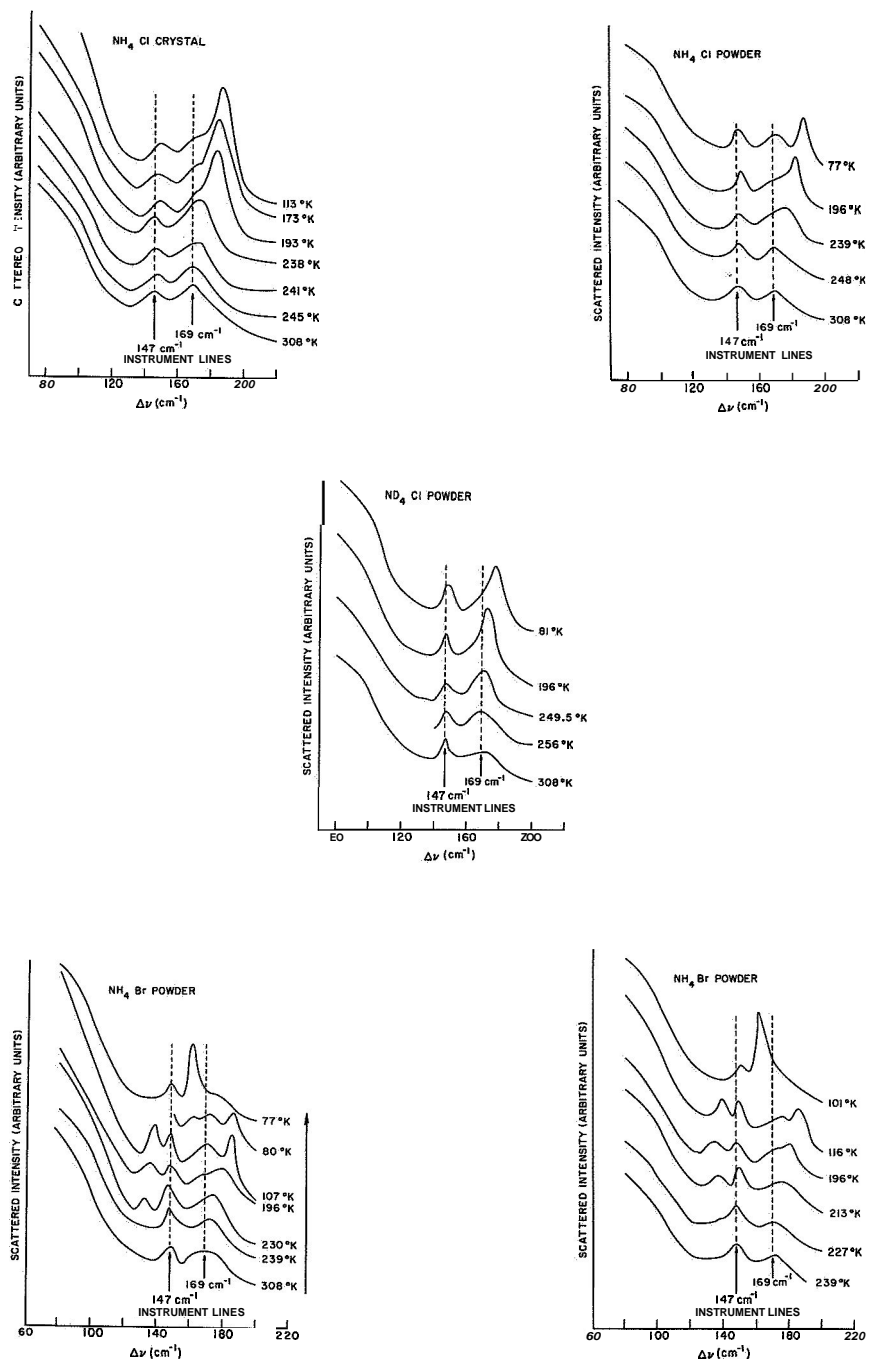


Fig. VI-7. Raman spectra of NH₄Cl, ND₄Cl, and NH₄Br.

(VI. OPTICAL AND INFRARED SPECTROSCOPY)

accounted for by the increase in mass of the ammonium ion.

The spectra of NH_4Br have two low-frequency lines for temperatures below 230°K , and one low-frequency line at 77°K . A 30° hysteresis was observed in the temperature of the lower transition, with the single line remaining until the temperature was raised to 116°K , in agreement with the specific-heat data of Professor Stevenson.

Table VI-4. Raman and infrared frequencies of NH_4Cl and NH_4Br .

	RT		-196"		77°	
	IR	R	IR	R	IR	R
NH_4Cl	175	—		184	188	188
NH_4Br	146.8	—	154	134,180	159	162

The Raman and infrared frequencies are compared in Table VI-4. The good agreement between the transverse optical frequencies and the Raman frequencies at 77°K indicates that the Raman lines are due to lattice vibrations. The presence of these lines in the Raman spectrum indicates a deviation from ideal cubic symmetry in the low-temperature ordered phase.

The presence of two lines in the Raman spectrum at 196°K agrees with measurements of a tetragonal structure at this temperature. The appearance of only one line in the reflection curve may be due to the insensitivity of this method of measurement.

The investigation of the temperature dependence of the eigen vibrations by infrared transmission measurements of thin films of these materials is now in progress.

We would like to thank Professor C. W. Garland, Department of Chemistry, M. I. T., (and Materials Center for Science and Engineering) for supplying most of the crystals used in this work, and Mr. Joseph Lastovka for supplying a large NH_4Cl crystal used for the reflectivity measurements.

J. F. Reintjes, Jr., C. H. Perry

References

1. E. L. Wigner and D. F. Hornig, J. Chem. Phys. 18, 296 (1950).
2. A. Smits and C. MacGillivray, Z. Physik. Chem. (Frankfurt) A166, 97 (1933).
3. A. Hettick and A. Schleede, Z. Physik 50, 249 (1928).
4. K. Kamiyoshi, Sci. Res. Inst., Tohoku U. A8, 252 (1956).
5. A. C. Menzies and H. R. Mills, Proc. Roy. Soc. (London) 148A, 407 (1935).
6. R. S. Krishnan, Proc. Indian Acad. Sci. A27, 321 (1948).
7. K. Hojendahl, Kgl. Danske Videnskab. Selskab, Mat.-Fys. Medd. 16, 2 (1938).
8. H. Rubens and H. V. Wartenburg, Sitzber. preuss. Akad. Wiss. 169 (1914).

VII. NOISE IN ELECTRON DEVICES*

Academic and Research Staff

Prof. H. A. Haus
Prof. P. Penfield, Jr.

Graduate Students

J. L. Doane
R. L. Guldi

H. J. Pauwels
V. K. Prabhu

A. QUANTUM NOISE IN THE LASER OSCILLATOR WITH FINITE MATERIAL BANDWIDTH

1. Introduction

Haus¹ has obtained results for the phase and amplitude fluctuations of the laser oscillator above threshold by means of a classical model in which the semiclassical Van der Pol equation contains noise sources that correctly represent the properties of the field below threshold. We have shown in a previous report² that this model is "equivalent" to the quantum analysis (apart from small "saturation" and "quantum" corrections), provided the bandwidth of the material is much wider than the cold-cavity bandwidth. In this report we describe an equivalent classical model for a laser in which the material bandwidth is arbitrary. "Sufficiently" below threshold it correctly predicts the moments of the normally ordered products of the creation and annihilation operators of the field. "Sufficiently" above threshold it predicts the field moments with an accuracy that is very good but not good enough to distinguish between normally and unnormally ordered products. The proof of the equivalence of this model is published elsewhere.³

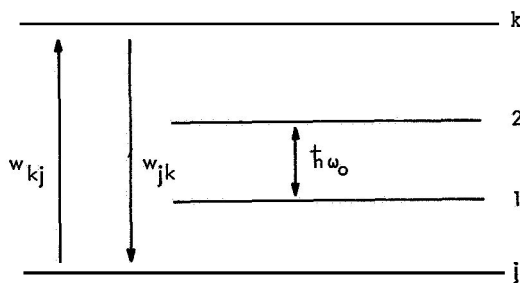


Fig. VII-1. Level pair (1,2) of the many-level system; transition probabilities w between two arbitrary levels.

2. Laser Model

The laser oscillates in one mode with resonance angular frequency ω_0 . The material system consists of a large number of many-level systems. In each of these there is one level pair with resonance angular frequency ω_0 (Fig. VII-1). This level pair is dipole coupled the field mode. The modulus κ of the coupling constant is assumed to be independent of

* This work was supported by the Joint Services Electronics Programs (U. S. Army, U. S. Navy, and U. S. Air Force) under Contract DA 36-039-AMC-03200(E).

(VII. NOISE IN ELECTRON DEVICES)

position. The upper and lower levels of such a level pair will be denoted by subscripts 2 and 1, respectively. The field mode is also coupled to a loss system that represents radiation into the space outside; the material system is also coupled to a material reservoir that introduces pumping, nonradiative decay (or radiative decay into black-body modes) and randomization into the material system.

The notations used in this report includes the following: the decay constant of the field as caused by the loss system is denoted μ and the cold-cavity bandwidth is then 2μ ; the amplification constant of the field as caused by the unsaturated material (if the material bandwidth were infinitely wide) is denoted by y ; the hot-cavity bandwidth is defined $\omega_h = 2(y-\mu)$; the material bandwidth is denoted 2Γ ; we shall also introduce the decay constant Γ_p of the inversion.

3. Loaded LC Circuit Driven by Noise

An LC circuit loaded by a conductance G and driven by a noise-source current i_n (Fig. VII-2) is described by the equations

$$-L \frac{dI}{dt} = V; \quad C \frac{dV}{dt} + GV - I = i_n. \quad (1)$$

If we set $\omega_o = (LC)^{-1/2}$; $V = (\hbar\omega_o/2C)^{1/2} i(a-a^\dagger)$ and $I = (\hbar\omega_o/2L)^{1/2} (a+a^\dagger)$, so that the energy $\frac{1}{2} (LI^2 + CV^2)$ in the LC circuit equals $\hbar\omega_o a^\dagger a$, then Eqs. 1 can be transformed to

$$\begin{aligned} \frac{da}{dt} &= -i\omega_o a - (G/2C)(a-a^\dagger) - i(2\hbar\omega_o C)^{-1/2} i_n \\ \frac{da^\dagger}{dt} &= i\omega_o a^\dagger - (G/2C)(a^\dagger - a) + i(2\hbar\omega_o C)^{-1/2} i_n \end{aligned} \quad (2)$$

We introduce new slowly time-variant variables by setting $i_n = i_n^+(t) \exp(i\omega_o t) + i_n^-(t) \exp(-i\omega_o t)$; $a = a(t) \exp(-i\omega_o t)$; $a^\dagger = a^\dagger(t) \exp(i\omega_o t)$. We assume that the LC circuit has a high Q and that $i_n^+(t)$ and $i_n^-(t)$ contain only slow time variations with respect to $\exp(\pm i\omega_o t)$. We can then neglect the double-frequency drives in Eqs. 2 and obtain

$$\frac{da(t)}{dt} + ga(t) = x^-(t); \quad \frac{da^\dagger(t)}{dt} + ga^\dagger(t) = x^+(t), \quad (3)$$

where

$$g = (G/2C); \quad x^\pm(t) = \pm i(2\hbar\omega_o C)^{-1/2} i_n^\pm(t). \quad (4)$$

The plus and minus signs in Eq. 4 correspond to each other. Eventually we shall use time-domain and frequency-domain notation. Spectra and correlation functions are related by

$$\begin{aligned}
\langle u(t+\tau) v(t) \rangle &= \int_{-\infty}^{+\infty} \langle u(\omega) v(-\omega) \rangle e^{i\omega\tau} \frac{d\omega}{2\pi} \\
\langle u(\omega) v(-\omega) \rangle &= \int_{-\infty}^{+\infty} \langle u(t+\tau) v(t) \rangle e^{-i\omega\tau} d\tau.
\end{aligned}
\tag{5}$$

If spectra are said to be "frequency independent," this means that they are frequency-independent over a range around $\omega = 0$ which is very large compared with the various

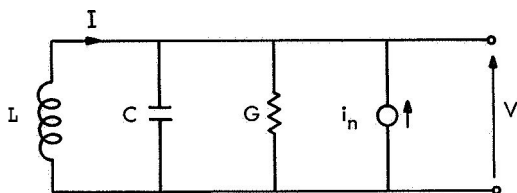


Fig. VII-2. Noisy loaded LC circuit.

relaxation constants, but very small compared with ω_0 . We shall denote such spectra by $\langle uv \rangle$. The conversion from frequency domain to time domain is described by

$$u(t) \rightarrow u(\omega); \quad \frac{du(t)}{dt} \rightarrow i\omega u(\omega). \tag{6}$$

4. Steady State below Threshold

The equivalent classical model is obtained by assuming that the (normalized) conductance g consists of a loss conductance and a frequency-dependent gain conductance. With each of these are associated independent Gaussian noise sources with zero mean. In the frequency-domain we have

$$\begin{aligned}
g(\omega) &= \mu - \frac{\Gamma}{i\omega + \Gamma} \gamma \\
x_L^-(\omega) &= x_L^-(\omega) + \frac{\Gamma}{i\omega + \Gamma} x_m^-(\omega); \quad \text{and complex conjugate,}
\end{aligned}
\tag{7}$$

where 2μ is the cold-cavity bandwidth, 2Γ is the material bandwidth, and γ is the amplification constant of the field (at zero frequency or infinite material bandwidth) caused by the inverted material. Operation below threshold requires $\mu > \gamma$. The spectra of the noise sources x_L^\pm and x_m^\pm are frequency-independent and are given by

$$\begin{aligned}
\langle x_L^+ x_L^- \rangle &= \langle x_L^- x_L^+ \rangle = 2\mu\beta_L; & \langle x_m^+ x_m^- \rangle &= \langle x_m^- x_m^+ \rangle = 2\gamma(1+\beta_m) \\
\langle x_L^+ x_L^+ \rangle &= \langle x_L^- x_L^- \rangle = 0; & \langle x_m^+ x_m^+ \rangle &= \langle x_m^- x_m^- \rangle = 0.
\end{aligned}
\tag{8}$$

(VII. NOISE IN ELECTRON DEVICES)

If T_L is the temperature of the loss system and P_2^0 and P_1^0 are the populations of the upper and lower level as established by the material reservoir alone, then

$$\beta_L = [\exp(\hbar\omega_0/kT_L) - 1]^{-1}; \quad \beta_m = P_1^0 / (P_2^0 - P_1^0). \quad (9)$$

Note that the spectrum of the noise source associated with the frequency-dependent gain conductance is also frequency dependent:

$$\left\langle \frac{\Gamma}{i\omega + \Gamma} x_m^+(\omega) \frac{\Gamma}{-i\omega + \Gamma} x_m^-(\omega) \right\rangle = \frac{\Gamma^2}{\omega^2 + \Gamma^2} 2\gamma(1 + \beta_m). \quad (10)$$

Equations 3 can be written in the time-domain

$$\frac{d^2 a(t)}{dt^2} + (\Gamma + \mu) \frac{da(t)}{dt} + \Gamma(\mu - \gamma) a(t) = \left(\frac{d}{dt} + \Gamma \right) x_L^-(t) + \Gamma x_m^-(t); \quad \text{and conjugate} \quad (11)$$

It is straightforward to obtain the spectrum $\langle a^+(\omega) a(-\omega) \rangle$ from Eq. 11.

$$\begin{aligned} \langle a^+(\omega) a(-\omega) \rangle &= (A + B\omega^2) / D(\omega), \\ A &= \Gamma^2 [2\mu\beta_L + 2\gamma(1 + \beta_m)]; \quad B = 2\mu\beta_L; \\ D(\omega) &= [\Gamma(\mu - \gamma) - \omega^2]^2 + (\Gamma + \mu)^2 \omega^2. \end{aligned} \quad (12)$$

By means of Eq. 5, we can obtain the correlation function $\langle a^+(t+\tau) a(t) \rangle$. Higher order moments are obtained from the fact that $a^{\dagger}(t)$ and $a(t')$ are Gaussian. A discussion of Eq. 12 has been given elsewhere.³

5. Steady-State above Threshold

The equivalent classical model is obtained by setting

$$g(\omega) = \mu - \frac{\Gamma}{i\omega + \Gamma} (\kappa^2 / \Gamma) P(\omega); \quad x^-(\omega) = x_L^-(\omega) + \frac{\Gamma}{i\omega + \Gamma} x_m^-(\omega), \quad (13)$$

where x_L^{\pm} and x_m^{\pm} are independent Gaussian noise sources with zero mean, the frequency-independent spectra of which are given by

$$\begin{aligned} \langle x_L^+ x_L^- \rangle &= 2\mu \left(\frac{1}{2} + \beta_L \right); \quad \langle x_m^+ x_m^- \rangle = 2\mu \left(\frac{1}{2} + \beta_m^s \right); \\ \beta_L &= [\exp(\hbar\omega_0/kT_L) - 1]^{-1}; \quad \beta_m^s = P_1^s / (P_2^s - P_1^s), \end{aligned} \quad (14)$$

where T_L is the temperature of the loss system, and P_2^s and P_1^s are the steady-state populations of upper and lower levels, respectively, as established by the field and the

(VII. NOISE IN ELECTRON DEVICES)

material reservoir. Equations 3 can now be written in the time domain as

$$\frac{d^2 a(t)}{dt^2} + (\Gamma + \mu) \frac{da(t)}{dt} + \Gamma [\mu - (\kappa^2/\Gamma) P(t)] a(t) = \left(\frac{d}{dt} + \Gamma \right) x_L^-(t) + \Gamma x_m^-(t); \quad \text{and} \\ \text{complex conjugate.} \quad (15)$$

The net population difference $P(t) = P_2(t) - P_1(t)$ is determined by a set of coupled rate equations that express conservation of populations and photon number, that is,

$$\frac{dP_k(t)}{dt} + (\delta_{2k} - \delta_{1k}) \left[\frac{da^\dagger a(t)}{dt} + 2\mu a^\dagger a(t) \right] + \Gamma_k P_k(t) - \sum_j w_{kj} P_j(t) \\ = X_k(t) (\delta_{2k} - \delta_{1k}) (a^\dagger x_L^- + x_L^+ a), \quad (16)$$

where w_{kj} is the transition probability from level j into level k ($w_{kk} = 0$), and $\Gamma_k = \sum_j w_{jk}$ is the total transition probability out of level k . The variables on the right-hand side of Eq. 16 are Gaussian shot-noise sources with zero mean, associated with population transfer induced by the material reservoir, and with photon transfer between the field mode and the loss system. The second-order moments of these noise sources will be described below.

If one sets all noise sources equal to zero, one obtains the semiclassical steady-state solution (subscript s) with

$$\mu = (\kappa^2/\Gamma) P_s; \quad a_s = R_s e^{-i\theta_s}; \quad a_s^\dagger = R_s e^{i\theta_s}; \\ (\delta_{2k} - \delta_{1k}) (2\mu R_s^2) + \Gamma_k P_k^s - \sum_j w_{kj} P_j^s = 0. \quad (17)$$

Equations 15 and 16 are solved by setting

$$a(t) = [R_s + r(t)] e^{-i\theta(t)}; \quad a^\dagger(t) = [R_s + r(t)] e^{i\theta(t)} \\ P_k(t) = P_k^s + p_k(t), \quad (18)$$

and linearizing in r , p_k , and $d\theta/dt$. We approximate da/dt and d^2a/dt^2 by

$$\frac{da}{dt} = \left[-iR_s \frac{d\theta}{dt} + \frac{dr}{dt} \right] e^{-i\theta}; \quad \text{and complex conjugate} \\ \frac{d^2a}{dt^2} = \left[-iR_s \frac{d^2\theta}{dt^2} + \frac{d^2r}{dt^2} \right] e^{-i\theta}, \quad \text{and complex conjugate} \quad (19)$$

(VII. NOISE IN ELECTRON DEVICES)

and obtain

$$R_s \left[\frac{d^2 \theta}{dt^2} + (\Gamma + \mu) \frac{d\theta}{dt} \right] = \left(\frac{d}{dt} + \Gamma \right) C_L + \Gamma C_m \quad (20a)$$

$$\frac{d^2 (2R_s r)}{dt^2} + (\Gamma + \mu) \frac{d(2R_s r)}{dt} - 2\kappa^2 R_s^2 p(t) = \left(\frac{d}{dt} + \Gamma \right) (2R_s S_L) + \Gamma (2R_s S_m) \quad (20b)$$

$$\begin{aligned} \frac{dp_k}{dt} + (\delta_{2k} - \delta_{1k}) \left[\frac{d}{dt} (2R_s r) + 2\mu (2R_s r) \right] + \Gamma_k p_k - \sum_j w_{kj} p_j \\ = X_k + (\delta_{2k} - \delta_{1k}) (2R_s S_L), \end{aligned} \quad (20c)$$

where

$$\begin{aligned} C_L &= \frac{1}{2i} \left[x_L^+ e^{-i\theta} - x_L^- e^{i\theta} \right]; \quad C_m = \frac{1}{2i} \left[x_m^+ e^{-i\theta} - x_m^- e^{i\theta} \right] \\ S_L &= \frac{1}{2} \left[x_L^+ e^{-i\theta} + x_L^- e^{i\theta} \right]; \quad S_m = \frac{1}{2} \left[x_m^+ e^{-i\theta} + x_m^- e^{i\theta} \right]. \end{aligned} \quad (21)$$

In order to evaluate the moments of the S and C noise sources, one treats θ as being independent of x_L^\pm and x_m^\pm . One obtains

$$\langle C_L C_L \rangle = \langle S_L S_L \rangle = \mu \left(\frac{1}{2} + \beta_L \right); \quad \langle C_m C_m \rangle = \langle S_m S_m \rangle = \mu \left(\frac{1}{2} + \beta_m^s \right) \quad (22a)$$

$$\langle X_k X_k \rangle = \Gamma_k P_k^s t \sum_j w_{kj} P_j^s = (1/2) \text{ (atomic rate in t out)} \quad (22b)$$

$$\langle X_k X_j \rangle = - \left(w_{kj} P_j^s t w_{jk} P_k^s \right) = -(1/2) \text{ (atomic transfer rate)} \quad (22c)$$

$$\langle X_k S_m \rangle = (\mu R_s / \Gamma) \left[\frac{1}{2} \Gamma_k (\delta_{2k} + \delta_{1k}) - \frac{1}{2} (w_{k2} + w_{k1}) \right]. \quad (22d)$$

The noise sources C_L and C_m are independent of the noise sources S_L , S_m , and X_k . The noise source S_L is also independent of X_k . The moments of the noise sources X_k , $2R_s S_L$, and $2R_s S_m$ describe, respectively, shot noise associated with population transfer induced by the material reservoir, photon transfer between the field mode and the loss reservoir (Fig. VII-3), and photon emission and absorption by the material system. The cross moment of the noise sources X_k and $2R_s S_m$ is hard to interpret; it is proportional to $(2\mu R_s^2 / \Gamma)$, that is, to the number of photons emitted by the material in the mean time $(\Gamma)^{-1}$; this number is a measure of the expectation value of the off-diagonal $(1, 2)$ -elements of the material density matrix in the steady state. The

noise sources of Eq. 20a have been said to be independent of the noise sources of Eqs. 20b and 20c. In the quantum analysis the expectation value of the anticommutator of the corresponding operator noise sources is indeed zero, but the expectation value of the commutator is not zero; for example,

$$\begin{aligned}\langle [X_k, C_m] \rangle &= \frac{\mu R_s}{i\Gamma} [(\delta_{2k} - \delta_{1k}) \Gamma_k + (w_{k1} - w_{k2})] \\ \langle [S_m + S_L, C_m + C_L] \rangle &= \frac{2\mu R_s^2}{\Gamma} (2\mu R_s^2 / \Gamma P_s).\end{aligned}\quad (23)$$

These commutators are neglected in our equivalent analysis, which is the cause of its lack of "quantum accuracy," that is, our analysis is not accurate enough to distinguish between the various orderings of the creation and annihilation operators of the field mode in the field moments. In particular, it does not allow us to calculate the field commutator or yield the difference between the second-order Glauber function and the correlation function of the photon number operator.

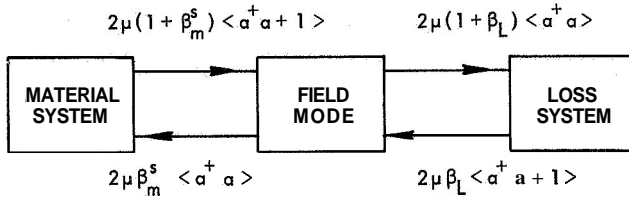


Fig. VII-3.

Transfer rates of photons between the field mode and the loss system and emission and absorption rates of photons in the material system.

Equation 20a can be solved immediately for phase fluctuations. We neglect $d^2\theta/dt^2$ and dC_L/dt and take into account the fact that the noise sources are Gaussian. Then we obtain

$$\langle \exp[i\theta(t+\tau) - i\theta(t)] \rangle = \exp\left(-\frac{1}{2} \omega_{ph} |\tau|\right) \quad (24a)$$

$$\omega_{ph} = \left(\frac{2\Gamma\mu}{\Gamma+\mu}\right)^2 \frac{\hbar\omega_o}{2P_{tr.}} (1 + \beta_L + \beta_m^s), \quad (24b)$$

where $P_{tr} = 2\mu\hbar\omega_o R_s^2$ is the average power in the laser beam. For $\Gamma \gg \mu$, this result reduces to the result derived in a previous report.²

The solution of the coupled equations (20b and 20c) for the moments of $2R_s r(t)$ is straightforward but can become very involved for an arbitrary material system. We give here only the solution for the case in which the material system consists of N strictly two-level systems. We introduce the following notation:

(VII. NOISE IN ELECTRON DEVICES)

$$\Gamma_p = w_{21} + w_{12}; \quad P_o = N(w_{21} - w_{12})/\Gamma_p; \quad \gamma = (\kappa^2/\Gamma)P_o. \quad (25a)$$

From the semiclassical equations (Eqs. 17), it follows that Γ_p is the decay constant of the inversion, P_o is the inversion as established by the material reservoir alone, γ is the amplification of the field (at zero frequency) as caused by this inversion, and the field amplitude is given by

$$4\mu R_s^2 = \Gamma_p(P_o - P_s); \quad \mu = (\kappa^2/\Gamma)P_s. \quad (25b)$$

We also introduce

$$e = (\gamma - \mu)/\mu = aR_s^2; \quad a = 4\kappa^2(\Gamma\Gamma_p)^{-1}; \quad \omega_h = 2(\gamma - \mu)$$

$$\epsilon = \Gamma/(\Gamma + \mu + \Gamma e) \leq 1; \quad \delta = \Gamma_p/2\Gamma \leq 1. \quad (25c)$$

In previous reports² ω_h has been called the "hot-cavity bandwidth" (the bandwidth of the intensity fluctuations if the material has infinite bandwidth); e is the ratio of the hot-to-cold cavity bandwidth and is directly proportional to power output and normally very small close to threshold; e^{-1} has been called the "enhancement factor"; a is the nonlinear constant of the material; E and δ are two new parameters; δ is smaller or equal to one because $\Gamma = \frac{1}{2}\Gamma_p + \Gamma_{ph}$.³ From the equivalent model (Eqs. 20-22), we obtain

$$\langle r(\omega) r(-\omega) \rangle = \frac{A + B\omega^2 + C\omega^4}{D(\omega)} \quad (26a)$$

$$A = \mu\epsilon^2 \left[\left(\frac{1}{2} + \beta_L \right) (1+e)^2 + \left(\frac{1}{2} + \beta_m^s \right) (1+e) - \frac{1}{2} \frac{P_o}{N} (1+2\delta) e \right] \quad (26b)$$

$$B\omega^2 = \mu\epsilon^2 \left[\left(\frac{1}{2} + \beta_L \right) (1+4\delta^2 - 4e\delta) + \left(\frac{1}{2} + \beta_m^s \right) \right] \left(\omega^2/\Gamma_p^2 \right) \quad (26c)$$

$$C\omega^4 = \mu\epsilon^2 \left(\frac{1}{2} + \beta_L \right) \left(\omega^4/\Gamma_p^4 \right) 4\delta^2 \quad (26d)$$

$$D(\omega) = \left[\epsilon\omega_h - \left(\omega^2/\Gamma_p \right) (1 - \epsilon e + 2\epsilon\delta) \right]^2 + \omega^2 \left[1 - (\omega/\Gamma_p)^2 2\epsilon\delta \right]^2 \quad (26e)$$

$$D(\omega) = (\epsilon\omega_h)^2 + \omega^2 [1 - 2(\epsilon\omega_h/\Gamma_p)(1 - \epsilon e + 2\epsilon\delta)]$$

$$+ \omega^2 (\omega/\Gamma_p)^2 [(1 - \epsilon e)^2 + 4\epsilon^2 \delta(\delta - e)] + \omega^2 (\omega/\Gamma_p)^4 4\epsilon^2 \delta^2. \quad (26f)$$

By means of Eqs. 5 we can calculate $\langle r(t+\tau) r(t) \rangle$. From Eqs. 18 and 24 and the fact that θ is independent of r , we can then derive moments of $a^{\dagger}(t)$ and $a(t)$.

The spectrum of Eq. 26 is of third order in ω^2 . It is hard to discuss it in general without plugging in specific numbers for various lasers. We can, however, clarify some aspects of these results through the following remarks.

(i) Neglecting the shot-noise sources that drive the rate equations (16) results in setting $e = 0$ in Eqs. 26b, 26c, and 26d. Since on the one hand the region close to threshold is the most important one for intensity fluctuations (verify that for $\omega = 0$), and on the other hand e is much smaller than 1 in that region, we conclude that these noise sources are not very important and that the important noise sources are those that drive Eq. 15 and that are described in Eqs. 13 and 14.

(ii) Neglecting d^2a/dt^2 and dx_L/dt in Eq. 15 results in setting $\delta = 0$ in Eqs. 26. A careful investigation of Eqs. 26 shows that such an approximation is justified if δ and $\epsilon\delta$ are much smaller than one (say, one order of magnitude smaller than one). Equations 15 and 16 can then be transformed to "modified" rate equations. These have been discussed elsewhere.³ The spectrum of r becomes then of second order in ω^2 . It can have a resonance peak for ω somewhere between $\epsilon\omega_h$ and Γ_p . If one also sets $E = (1+e)^{-1}$, the modified rate equations reduce to the rate equations discussed by McCumber⁴; the conditions $\delta \ll 1$, $E = (1+e)^{-1}$ are fulfilled if the material bandwidth 2Γ is much larger than the cold-cavity bandwidth 2μ and the decay constant Γ_p of the inversion.

(iii) If $\Gamma_p \gg \epsilon\omega_h$, then one may approximate Eq. 26a by

$$\langle r(\omega) r(-\omega) \rangle = \frac{A}{\omega^2 + (\epsilon\omega_h)^2}. \quad (27)$$

Although one may lose an experimental verifiable resonance peak for $\omega \neq 0$ in this approximation, this resonance peak will be much smaller than the spectrum near $\omega = 0$. The result (27) was derived previously for $E = 1$.^{1,2} We thus see that the bandwidth of the intensity fluctuations is narrowed by the factor $E = [1 + (\mu/\Gamma) + e]^{-1}$, that is, mainly by the effect of a finite material bandwidth (e is present in this reduction factor E because in this analysis we did not approximate the full nonlinear term $(1 + \alpha R_s^2)^{-1}$ by $1 - \alpha R_s^2$, as one does in the Van der Pol equation).

H. J. Pauwels

References

1. H. A. Haus, "Analysis of Noise in Optical Maser Oscillator," Quarterly Progress Report No. 72, Research Laboratory of Electronics, M. I. T., January 15, 1964, pp. 53-56.

(VII. NOISE IN ELECTRON DEVICES)

2. **H. J. Pauwels**, "Quantum Analysis of Noise in the Laser Oscillator," Quarterly Progress Report No. 79, Research Laboratory of Electronics, M. I. T., October 15, 1965, pp. 58-64.
3. **H. J. Pauwels**, "Noise Sources Describing Quantum Effects in the Laser Oscillator" (to appear as Technical Report 453, Research Laboratory of Electronics, M. I. T.).
4. **D. E. McCumber**, "Intensity Fluctuations in the Output of cw Laser Oscillators, I," Phys. Rev. 141, 306-322 (1966).

VIII. PHYSICAL ELECTRONICS AND SURFACE PHYSICS

A. Surface Physics*

Academic and Research Staff

Prof. R. E. Stickney
Dr. M. L. Shaw

Graduate Students

J. W. Gadzuk
R. M. Logan
D. S. Shupe

1. SINGLE PHONON ACCOMMODATION COEFFICIENTS

Introduction

It is our present purpose to report some recent improvements in quantum-mechanical accommodation theory.⁻⁵ This study will be reported in detail later.

The essence of the existing theories may be described as follows. An inert gas atom such as helium, described by an initial wave function $\phi'(\mathbf{r})$, undergoes a collision with a bound surface atom of a lattice described by an assumed harmonic oscillator wave function $\psi_n(\mathbf{u})$. A single quantum of energy is transferred in the process. The final state of the atom is taken to be $\phi(\mathbf{r})$, and that of the metal atom $\psi_{n\pm 1}(\mathbf{u})$. The matrix element for the process is given by

$$B_{n,n-1} = \iint d^3r d^3u \phi^*(\bar{\mathbf{r}}) \psi_n^*(\bar{\mathbf{u}}) \left[V_a(\bar{\mathbf{r}}-\bar{\mathbf{u}}) - V_a(\bar{\mathbf{r}}) \right] \psi_{n-1}(\bar{\mathbf{u}}) \phi'(\mathbf{r}), \quad (1)$$

with

$$V(\bar{\mathbf{r}}-\bar{\mathbf{u}}) = V(\bar{\mathbf{r}}) - \bar{\mathbf{u}} \cdot \nabla V(\bar{\mathbf{r}}) + \frac{1}{2} \bar{u}_i \bar{u}_j \cdot \nabla^2 V(\bar{\mathbf{r}}) - \dots \quad (2)$$

The accommodation coefficient is given by an expression of the form

$$a_o = \gamma |B_{n,n-1}|^2 \quad (3)$$

where γ contains statistical factors, density of states, constants, and so forth. The point is that a , the AC, is proportional to the square of the matrix element. These results are not necessarily in agreement with experimentally determined AC.

*

This work was supported by the Joint Services Electronics Programs (U. S. Army, U. S. Navy, and U. S. Air Force) under Contract DA 36-039-AMC-03200(E).

(VIII. PHYSICAL ELECTRONICS AND SURFACE PHYSICS)

Theory

There should be a great similarity between the lattice theories of neutron scattering, Mössbauer effect, and inert-gas scattering. In **all** cases the lattice is perturbed by some external probe — the neutron, recoiling nucleus **or** incident gas atom — and the number of phonons is the lattice displacement field changes by some small number, usually zero **or** one. Guided by the existing neutron⁶ and Mössbauer effect⁷ theories, we proceed in an extremely cavalier fashion.

The lattice is normal-mode analyzed and second-quantized in the manner of Pines.⁸ The lattice state is described in the occupation number representation in which the state vectors are eigenfunctions of the phonon number operator. With the use of Boson creation and annihilation operators, the necessary mathematical aspects of the Bosen field may be summarized:

$$H_L |n\rangle = \sum_{q,j} \hbar\omega_{q,j} (a_{q,j}^\dagger a_{q,j} + \frac{1}{2}) |n\rangle = \sum_{q,j} \hbar\omega_{q,j} (n_{q,j} + \frac{1}{2}) |n\rangle \quad \begin{matrix} \text{(Eigenfunction)} \\ \text{Equation} \end{matrix} \quad (4a)$$

$$[a_{q,j}^\dagger, a_{q',j'}] = \delta_{q,q'} \delta_{j,j'} \quad \text{(Commutation)} \quad (4b)$$

$$[a_{q,j}^\dagger, a_{q',j'}^\dagger] = [a_{q,j}, a_{q',j'}] = 0 \quad \begin{matrix} \text{(Orthonormality)} \\ \end{matrix} \quad (4c)$$

$$\langle n_q + 1 | a_q^\dagger | n_q \rangle = \sqrt{n_q + 1}$$

$$\langle n_q - 1 | a_q | n_q \rangle = \sqrt{n_q}$$

$$\langle m | n \rangle = \delta_{m,n}$$

$$n_{q,j} = \left[e^{\hbar\omega_{q,j}/kT} - 1 \right]^{-1} \quad \begin{matrix} \text{(Thermal)} \\ \text{(Equilibrium)} \end{matrix} \quad (4d)$$

It is assumed that the displacement of surface atoms is adequately described in terms of bulk-mode displacements. The surface atom undergoing collision is assumed to be at the origin of the coordinate system. Thus the usual expression for the atom displacement is

$$\bar{u}_l = \sum_{q,j} \left(\frac{\hbar}{2MN\omega_{q,j}} \right)^{1/2} (\hat{e}_{q,j} a_{q,j} + \hat{e}_{-q,j}^\dagger a_{q,j}^\dagger). \quad (5)$$

By following the lines of Lipkin,⁹ it can be shown that for small displacements, the

interaction of Eq. 2 can be expressed as

$$V_a(\vec{r}-\vec{u}) - V_a(\vec{r}) \simeq e^{-\vec{a} \cdot \vec{u}} \frac{1}{|a|} \nabla V_a(\vec{r}), \quad (6)$$

where a is a parameter controlling the range of interaction. This result, which will be more rigorously derived in a forthcoming paper, is independent of the functional form of the interaction.

By having the displacement-field operator in an exponential, we have recourse to some field theoretic results derived by Glauber.¹⁰ His result states that the operator deriving from $e^{-\vec{a} \cdot \vec{u}}$, which induces an n phonon transition is given by

$$\left\langle e^{-\vec{a} \cdot \vec{u}} \right\rangle_T^{(n)} = \frac{(-\vec{a} \cdot \vec{u})^n}{n!} e^{\frac{1}{2} \langle (\vec{a} \cdot \vec{u})^2 \rangle_T}, \quad (7)$$

where the expectation value of the square of the $\vec{a} \cdot \vec{u}$ operator is taken with respect to the thermally excited equilibrium state given by Eq. 4d. In single phonon transitions, this operator takes into consideration such single-phonon processes in the interaction expansion of Eq. 2 as occur from operators of the form $a_{q'}^\dagger a_{q'} a_{q'}^\dagger$, in which a virtual phonon in the q'^{th} mode is emitted and reabsorbed before the real phonon in the q^{th} mode is emitted. Processes of this sort give rise to the Debye-Waller factor in neutron and Mössbauer theory, and **also** give rise to a pseudo Debye-Waller factor in the atom-scattering phenomena.

Combining Eqs. 1, 4, 6, and 7 allows the new single-phonon matrix element to be written

$$B'_{n,n-1} = \frac{a}{|a|} \cdot \langle n|u|n-1 \rangle e^{\frac{1}{2} \langle (\vec{a} \cdot \vec{u})^2 \rangle_T} \int d^3 r \phi^*(\vec{r}) \nabla V_a(\vec{r}) \phi(\vec{r}). \quad (8)$$

Since

$$\frac{a}{|a|} \cdot \langle n|u|n-1 \rangle = \left(\frac{\hbar n}{2MN\omega} \right)^{1/2}$$

by virtue of Eqs. 4 and 5, it is equivalent to the harmonic oscillator matrix element of Eq. 1. Furthermore, since the atomic matrix element in Eq. 8 is also equivalent to that in Eq. 1, the new matrix element becomes

$$B'_{n,m} = e^{\frac{1}{2} \langle (\vec{a} \cdot \vec{u})^2 \rangle_T} B_{n,m}$$

and consequently

(VIII. PHYSICAL ELECTRONICS AND SURFACE PHYSICS)

$$\alpha_n = e^{\left\langle (\bar{a} \cdot \bar{u})^2 \right\rangle_T} \alpha_0. \quad (9)$$

Thus the new AC is simply the existing single-phonon AC multiplied by the pseudo Debye-Waller factor. It is a standard matter to evaluate the thermal mean-square displacement term in the exponent.⁸ It can readily be shown that

$$\left\langle (\bar{a} \cdot \bar{u})^2 \right\rangle_T = \frac{\hbar^2 a^2}{mk\theta_D} \left[\frac{1}{4} + \left(\frac{T}{\theta_D} \right)^2 \int_0^{\theta_D/T} \frac{x dx}{e^x - 1} \right] \quad (10)$$

with $x = \hbar\omega/kT$. Equation 10 is exactly evaluated in low- and high-temperature limits as

$$\lim_{T \rightarrow 0} \left\langle (\bar{a} \cdot \bar{u})^2 \right\rangle_T = \frac{\hbar^2 a^2}{mk\theta_D} \left[\frac{1}{4} + \frac{\pi^2}{6} \left(\frac{T}{\theta_D} \right)^2 \right]$$

and

$$\lim_{T \rightarrow \infty} \left\langle (\bar{a} \cdot \bar{u})^2 \right\rangle_T = \frac{\hbar^2 a^2}{mk\theta_D} \left(\frac{T}{\theta_D} \right). \quad (11)$$

Results

Theoretical AC may be obtained by using Eq. 10 or 11 in Eq. 9 if values for α_0 are known. Gilbey⁴ gives numerical values of α_0 vs temperature for helium. In most

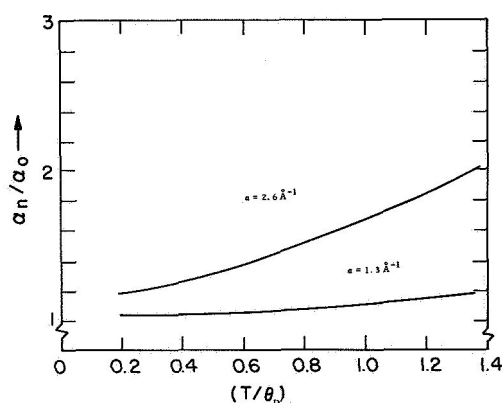


Fig. VIII-1.

Pseudo Debye-Waller correction factor for existing single quantum-accommodation-coefficient theories.

theories, a Morse or exponential repulsive potential describes the interaction. The value of the parameter z in Eq. 6 is closely related to the range parameter in the Morse potential. Since the repulsive portion of the Morse potential varies as $e^{-2a_1 r}$, we take $a_1 \leq a \leq 2a_1$. For the Ne-W system, $a_1 = 1.3 \text{ \AA}^{-1}$. We take $\theta_D = 300^\circ\text{K}$ for W.

(VIII. PHYSICAL ELECTRONICS AND SURFACE PHYSICS)

With these numbers, the quantity α_n/α_o vs temperature is drawn in Fig. VIII-1, with a treated parametrically for the temperature range less than the Debye temperature, the region in which the simple quantum-mechanical model is valid. It is seen that a non-trivial correction to the original AC results. In Fig. VIII-2 three AC are drawn: the

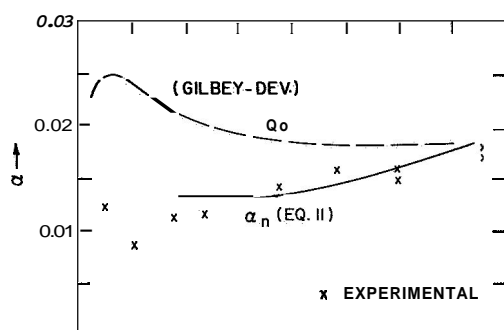


Fig. VIII-2.

Experimental and old and new theoretical accommodation coefficients as a function of temperature for He-W.

uncorrected α_o , the new theoretical α_n given by Eqs. 9 and 11, and experimentally determined AC.¹¹ All a have been adjusted so as to coincide at $T = 300^\circ\text{K}$. This amounts to multiplying α_o or α_n by a constant that shifts the axis but not the shape of the curve. Clearly, the new AC appears to be in better agreement with experiment than the previous quantum-mechanical expressions. Both the new expression and the data approach a high-temperature limit from below the limit, whereas the old theory approaches the same limit from above. It seems quite reasonable to say that if single-phonon AC are meaningful, then the existing theories should be modified by a pseudo Debye-Waller factor in order that there may be some quantitative agreement.

A more detailed treatment of this theory, together with an adequate discussion of the meaning and significance of these results, is forthcoming.

J. W. Gadzuk

References

1. J. M. Jackson, Proc. Camb. Phil. Soc. 28, 136 (1932).
2. A. F. Devonshire, Proc. Roy. Soc. (London) A158, 269 (1937).
3. J. E. Lennard-Jones and C. Strachen, Proc. Roy. Soc. (London) A150, 442 (1935).
4. D. M. Gilbey, J. Phys. Chem. Solids 23, 1453 (1962).
5. R. T. Allen and P. Feuer, J. Chem. Phys. 40, 2810 (1964).
6. L. S. Kothari and K. S. Sinwi, Solid State Phys. 8, 109 (1954).
7. H. Frauenfelder, The Mossbauer Effect (W. D. Benjamin, Inc., New York, 1963).
8. D. Pines, Elementary Excitations in Solids (W. D. Benjamin, Inc., New York, 1964), Chap. 2.

(VIII. PHYSICAL ELECTRONICS AND SURFACE PHYSICS)

9. H. J. Lipkin, Ann. Phys. (N.Y.) 2, 332 (1960).
10. R. J. Glauber, Phys. Rev. 84, 395 (1951); 98, 1692 (1955).
11. L. B. Thomas, "Determination of the Thermal Accommodation Coefficient and Research on the Conduction of Heat by Eilute Gases from Solid Surfaces and Its Uses as an indicator of Surface Condition," Final Report of work done under U. S. Army Contracts DA-23-072-ORD--388 and DA-23-072-ORD-990 at the University of Missouri, 1958.

VIII. PHYSICAL ELECTRONICS AND SURFACE PHYSICS

B. Surface Properties of Thermionic Electrodes^{*}

Academic and Research Staff

Prof. R. E. Stickney
J. G. Bergman

Graduate Students

W. Engelmaier
D. L. Fehrs

1. THERMIONIC CHARACTERISTICS OF A SINGLE-CRYSTAL TUNGSTEN FILAMENT EXPOSED TO OXYGEN

Introduction

More than forty years ago, Langmuir and Kingdon¹ observed that the thermionic emission from a cesiated tungsten filament could be increased markedly by adsorbing O_2 upon the filament. Although this problem has received very little attention in subsequent years, it is now being reconsidered because of its possible importance to thermionic energy conversion.² In the past five years the number of investigations of the effects of electronegative gases (such as O_2 and F_2) on the thermionic properties of cesiated refractory metals has increased.³

The present experiment is designed to investigate the effect of O_2 on the thermionic emission from a single-crystal tungsten filament. Our specific objective is to determine the dependence of the work functions of different crystallographic directions on O_2 pressure and filament temperature.

Descriptions of the experimental apparatus and the preliminary data have been reported in Quarterly Progress Report No. 79, pages 156-166. Hence, we shall concentrate here in the results that were obtained after improving the method of introducing O_2 into the vacuum system. The diffusion-type leak used previously has been replaced by a motor-driven Granville-Phillips valve connected to a one-liter flask of research grade O_2 .

Experimental Results

The results shown in Fig. VIII-3 were obtained by increasing the O_2 pressures in small steps while holding the filament at various temperatures. The effective work function, ϕ_E , is computed from the following form of the Richardson equation,

^{*}This work was supported by the National Aeronautics and Space Administration (Grant NGR-22-009-091).

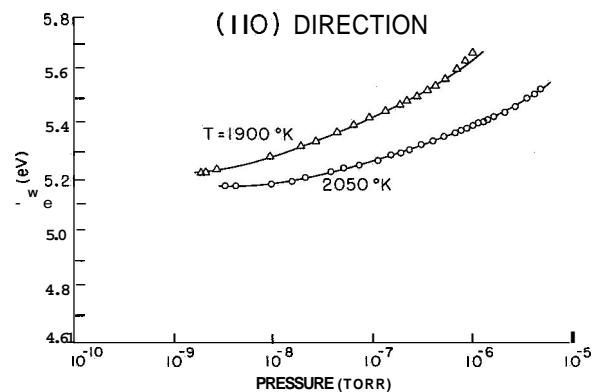
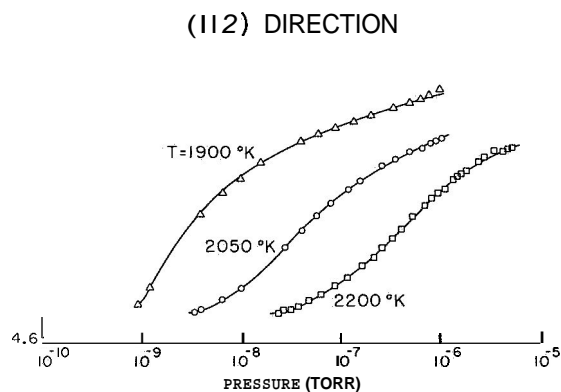
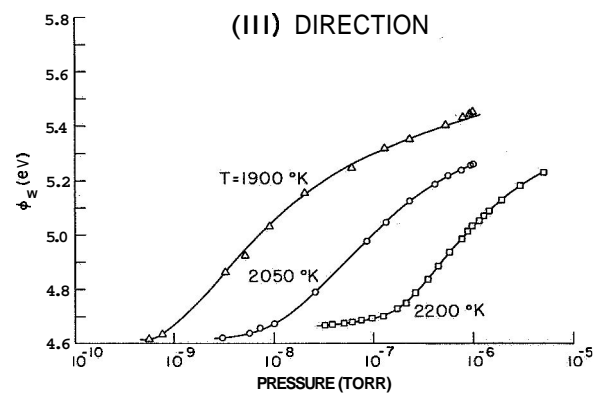
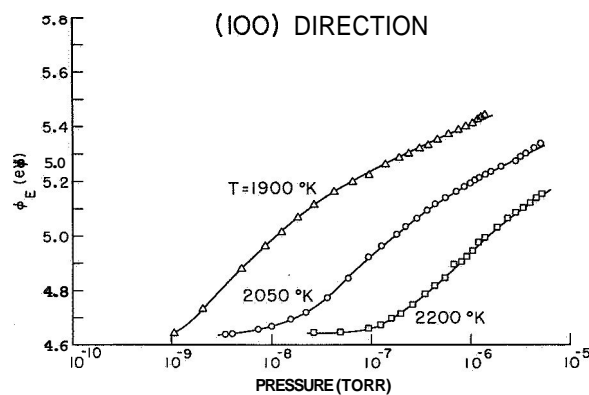


Fig. VIII-3. Effective workfunctions of the (100), (111), (112), and (110) crystallographic directions as a function of O_2 pressure and filament temperature.

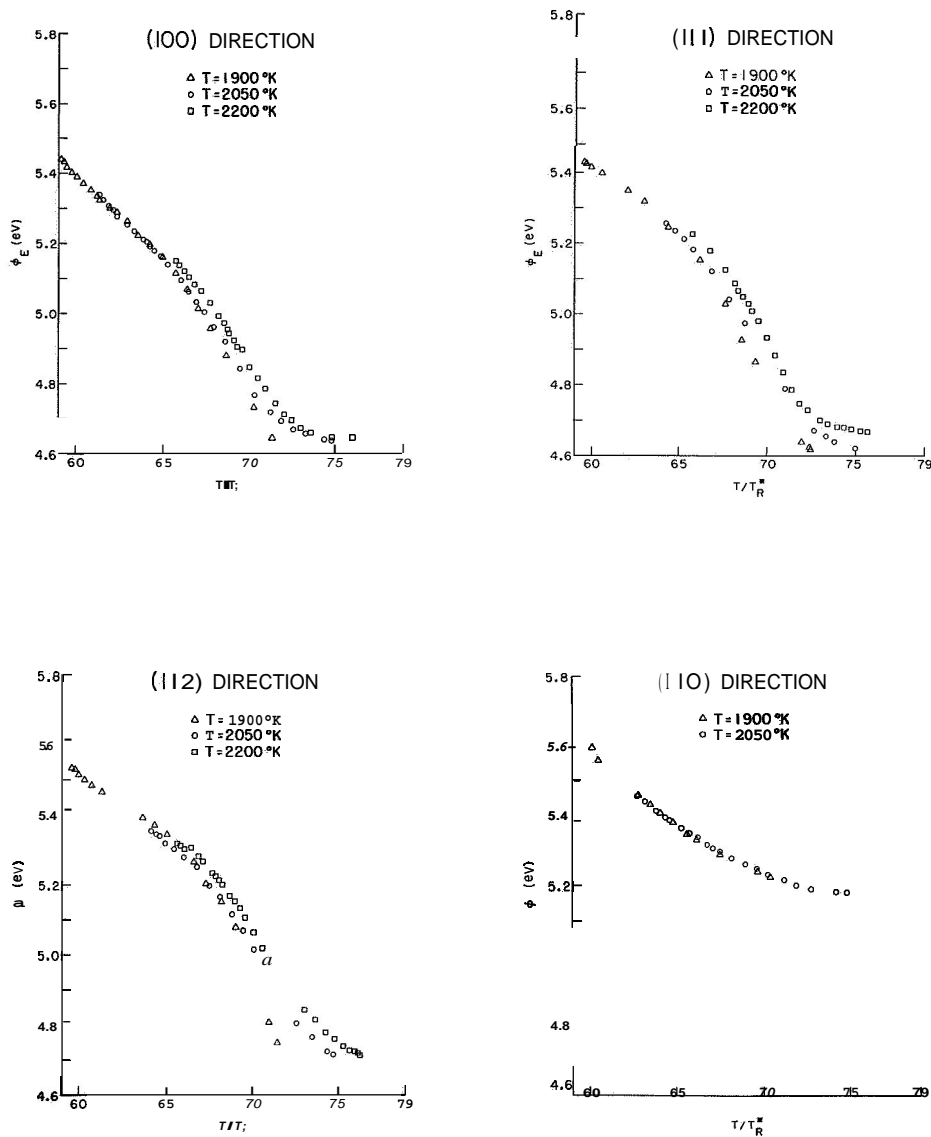


Fig. VIII-4. Effective function of the (100), (111), (112), and (110) crystallographic directions as a function of T/T_R^* .

(VIII. PHYSICAL ELECTRONICS AND SURFACE PHYSICS)

$$I = 120 ST^2 \exp\left(-\frac{\phi_E}{kT}\right), \quad (1)$$

where I is the measured collector current, S is the filament area subtended by the anode slit, k is Boltzmann's constant, and T is the filament temperature. We have not extrapolated the measurements of I to zero-field conditions because this correction has only a small effect on ϕ_E (~ 0.05 eV) for the anode voltage of 500 volts employed here.

The pressures reported in Fig. VIII-3 were measured with a General Electric ionization gauge (Model 22GT102). The thoria-coated iridium filament in the gauge was used to reduce the errors associated with interactions occurring at a hot filament. Since the sensitivity of ionization gauges is not well known for oxygen, we have chosen to express the pressure in terms of the equivalent nitrogen pressure. (The true O_2 pressure may differ from the equivalent N_2 pressure by as much as 25 per cent.)

The residual gas pressure increases with increasing filament temperature. This fact is illustrated in Fig. VIII-3; the minimum pressure shown for each filament temperature represents the pressure of the residual gases when the O_2 valve is closed. Hence the pressure readings are the sum of the O_2 pressure and the pressure of the unknown residual gases. Although this introduces an uncertainty in the low-pressure data, this effect becomes negligible at higher pressures.

Notice that the low-pressure limiting values of ϕ_E shown in Fig. VIII-3 are not the same for all filament temperatures. This result is to be expected if ϕ_E depends on temperature, if S is not measured accurately, or if the pre-exponential factor appearing in the Richardson equation is not 120 as assumed.

Since the O_2 coverage, θ , has not been measured in this experiment, we are unable to construct plots of ϕ_E versus θ . As an alternative, it is of interest to determine whether the parameter that is useful for correlating thermionic data for alkali metals⁴ will also be successful for oxygen. The parameter is T/T_R , where T is the substrate (i.e., filament) temperature and T_R is the saturation temperature corresponding to the particular operating pressure of the gaseous adsorbate. The effective saturation temperatures, T_R^* , employed in Fig. VIII-4 are computed from the following empirical expression which accurately describes data reported by Honig and Hook⁵ for the vapor pressure of oxygen:

$$\log_{10} p = 9.25 - \frac{486.45}{T_R^*}. \quad (2)$$

Since the reciprocal of T/T_R^* may be considered as a measure of the coverage, it follows that ϕ_E should approach the clean-surface value as T/T_R^* increases.

The correlation shown in Fig. VIII-4 is surprisingly good. The scatter appearing at high values of T/T_R^* may be caused by the factors discussed previously in connection with the data of Fig. VIII-3. The comparison of the different crystallographic directions

shown in Fig. VIII-3 is based on curves drawn through the data points of Fig. VIII-4.

Discussion of Results

The effect of O_2 on the thermionic emission from W was first studied by Kingdon, in 1924.⁶ A similar investigation was performed in greater detail by Johnson and Vick, in 1937.⁷ Polycrystalline tungsten filaments were employed in both experiments, and the O_2 pressure was not accurately measured.

Using the contact-potential method, Langmuir and Kingdon⁸ measured work-function changes for O_2 on W which were much smaller than those computed from the thermionic data of Kingdon.⁹ Reimann⁹ repeated the contact-potential measurements and obtained

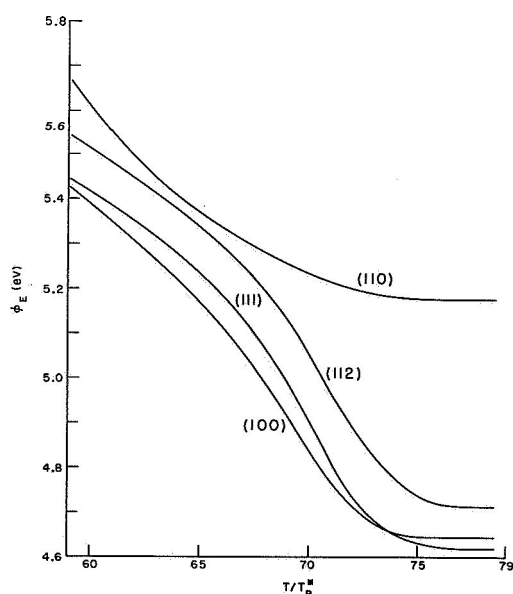


Fig. VIII-5.

Comparison of the average experimental results for O_2 on W; ϕ_E vs T/T_R^* for the (100), (111), (112), and (110) crystallographic directions.

Quantitative agreement is not expected, because of the significant differences in the experimental techniques. Mueller,¹³ Gomer and Hulm,¹⁴ and George and Stier¹⁵ have also used the field-emission microscope to study O_2 on W.

As seen in Fig. VIII-5, the maximum work-function change determined from the present data is -0.83 eV. This value is less than that measured in contact-potential studies because the filament temperature is sufficiently high to reduce the O_2 coverage below the maximum possible value. As inferred in the selection of T/T_R^* as the

a maximum contact-potential change of 1.7 eV for O_2 on W at room temperature. This value is in good agreement with that computed from Kingdon's data, and it has been verified in subsequent investigations both with the field-emission microscope and the contact-potential method.¹⁰ A detailed study of the change in contact potential with increasing O_2 coverage on polycrystalline W has been performed by Bosworth and Rideal.¹¹

Since the results of the present study are, to the best of our knowledge, the first thermionic measurements of the effect of O_2 on the work function of a single-crystal substrate, we have no standard comparison. Becker and Brandes¹² have, however, used the field-emission microscope to investigate the effect of O_2 on various crystallographic planes of W. The general characteristics of our results agree qualitatively with those of Becker and Brandes.

(VIII. PHYSICAL ELECTRONICS AND SURFACE PHYSICS)

correlation parameter, the coverage increases with increasing pressure and decreasing filament temperature. It is expected that, for the range of pressures and temperatures used here, the surface coverage does not exceed one monolayer of atomic oxygen.^{12, 16}

Although the structure of O₂ on W is not completely understood, there is evidence that absorption and surface rearrangement is greatest on crystallographic planes having an open-lattice structure.¹⁷ This provides a possible explanation for the fact that the work function of the (110) direction is not affected by O₂ as markedly as the other crystallographic directions (Fig. VIII-5). (We prefer to use the term "crystallographic direction" instead of "crystallographic plane" because the exact surface structure of the tungsten filament is not known.)

W. Engelmaier, R. E. Stickney

References

1. I. Langmuir and K. H. Kingdon, *Phys. Rev.* **23**, 112 (1923).
2. J. M. Houston and H. F. Webster, in *Advances in Electronics and Electron Physics*, Vol. 16, L. Marton (ed.) (Academic Press, New York, 1962), p. 167.
3. For example, see R. L. Aamodt, L. J. Brown, and B. D. Nichols, *J. Appl. Phys.* **33**, 2080 (1962); L. S. Swanson, R. W. Strayer, and F. M. Charbonnier, Report on Twenty-fourth Annual Conference on Physical Electronics, p. 120, 1964, C. H. Skeen, *J. Appl. Phys.* **36**, 84 (1965); also see the Reports on the 1964 and 1965 Thermionic Conversion Specialist Conferences.
4. N. S. Rasor and C. Warner, *J. Appl. Phys.* **35**, 2589 (1964); For a thermionic treatment, see E. N. Carabateas, *J. Appl. Phys.* **33**, 2698 (1962).
5. R. E. Honig and H. O. Hook, *R. C. A. Review* **21**, 360 (1960).
6. K. H. Kingdon, *Phys. Rev.* **24**, 510 (1924).
7. M. C. Johnson and F. A. Vick, *Proc. Roy. Soc. (London)* **A151**, 308 (1935).
8. I. Langmuir and K. H. Kingdon, *Phys. Rev.* **34**, 129 (1929).
9. A. L. Reimann, *Phil. Mag.* **20**, 594 (1935).
10. The results of these investigations have been summarized by R. V. Culver and F. C. Tompkins, *Advances in Catalysis* **11**, 67 (1959) (Academic Press, New York).
11. R. C. L. Bosworth and E. K. Rideal, *Physica* **4**, 925 (1937); also see R.C.L. Bosworth, *Proc. Roy. Soc. (New South Wales)* **79**, 190 (1946).
12. J. A. Becker and R. G. Brandes, *J. Chem. Phys.* **23**, 1323 (1955).
13. E. W. Mueller, *Ergeb. exakt. Naturw.* **29**, 290 (1953).
14. R. Gomer and J. K. Hulm, *J. Chem. Phys.* **27**, 1363 (1957).
15. T. H. George and P. M. Stier, *J. Chem. Phys.* **37**, 1935 (1962).
16. J. A. Becker, E. J. Becker, and R. G. Brandes, *J. Appl. Phys.* **32**, 411 (1961).
17. J. A. Becker, *Advances in Catalysis* **7**, 135 (1955); R. Gomer, *Advances in Catalysis* **7**, 93 (1955); N. J. Taylor, *Surface Science* **2**, 544 (1964); J. Anderson and W. E. Danforth, *J. Franklin Inst.* **279**, 160 (1965).

(VIII. PHYSICAL ELECTRONICS AND SURFACE PHYSICS)

2. CONTACT POTENTIAL MEASUREMENTS OF THE WORK FUNCTION OF TANTALUM AS A FUNCTION OF CESIUM COVERAGE

Introduction

The primary objective of this report is to describe an experimental apparatus designed to determine the dependence of the work function of a well-defined metallic substrate on alkali-metal coverage. As an illustration of the experimental technique to be used, preliminary results obtained for cesium upon a polycrystalline tantalum substrate are presented. In subsequent studies a single-crystal substrate will be employed to satisfy the condition of a reasonably well-defined, uniform surface.

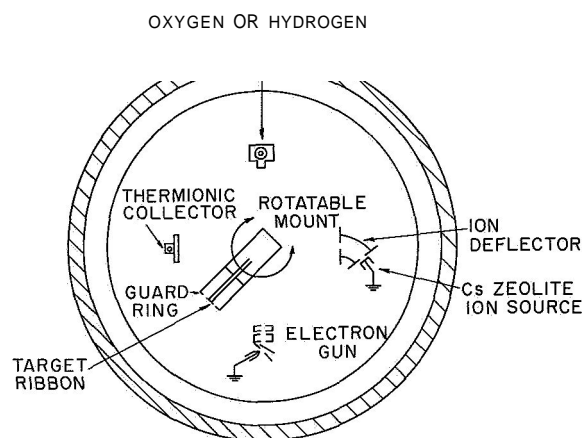


Fig. VIII-6. Schematic diagram of the apparatus.

Apparatus

As a prerequisite for any precise **surface** adsorption study, it is imperative that the surface of interest be kept free of contamination from background gases. Here, this condition is met by mounting the apparatus, shown schematically in Fig. VIII-6, within a Varian ultrahigh vacuum system. The stainless-steel chamber, with a working space of 45×90 cm, is evacuated by a 500 l/s ion pump. For additional pumping in the ultra-high vacuum region, titanium is sublimated upon liquid-nitrogen cold panel. Since this system can achieve pressures in the low 10^{-10} Torr range ($\sim 3 \times 10^{-10}$ Torr **for** these runs), it is possible to maintain contamination-free surface conditions for times much longer than those required for an experimental **run**.

The apparatus has been designed to furnish information in the most meaningful way to enable us to carry out our primary objective. The specimen to be studied is a tantalum ribbon, $0.0025 \times 0.127 \times 2.54$ cm, mounted on a rotatable shaft, (The preliminary runs utilized a polycrystalline specimen; in subsequent **runs** a (110) monocrystal will be studied.) Cleaning of the surface is achieved by direct resistive heating to -2500°K .

Alkali-metal deposition upon the target is obtained by using a zeolite ion source containing the desired alkali.' Since the target temperature is maintained at 300°K during a run, this method allows us to attain and maintain alkali-metal coverages without flooding the entire system with alkali vapor. Also, by monitoring the collected ion current, the number of alkali-metal ions deposited can be directly and accurately known. The source is a thin layer of alkali-metal zeolite fused to a platinum ribbon $0.005 \times 0.635 \times 5.1$ cm. **This** ribbon, heated by direct resistive heating,

(VIII. PHYSICAL ELECTRONICS AND SURFACE PHYSICS)

is run at 800-900°C to obtain sufficient ion emission (10^{-7} - 10^{-6} amps/cm² for the preliminary Cs runs). The emitted ions are accelerated through a 0.635×2.54 cm slit, electrostatically deflected in a 60° analyzer, and beamed on the target through another 0.635×2.54 cm slit. The electrostatic analyzer decreases the possibility of neutral contamination from the source. For the preliminary runs, the maximum potential applied between the target and the source is 8 volts.

Changes of substrate work function because of alkali-metal adsorption are measured by the contact-potential method.³ For this measurement, the target is positioned before a simple electron gun of the Farnsworth style.⁴ This gun has a polycrystalline tantalum filament mounted off-center to prevent photoelectric effects and direct contamination. Since the method requires constant emitter conditions, the filament is continually run at ~2100°K, and its center is grounded.

Used alone, the contact-potential method tells nothing about absolute work functions. If, however, the bare-surface work function is known subsequent contact-potential measurements can be converted to absolute values. In this apparatus, the thermionic work function of the clean target is measured by positioning the target at the thermionic measurement station. This station consists of a collector, subtending a center portion of the tantalum ribbon, bounded by two guard rings. The geometry of this station is planar.

As shown in Fig. VIII-6, the target may also be positioned before an oxygen/hydrogen molecular beam. Diffusion leaks are used to supply the oxygen or hydrogen required to form the beam. Such a beam serves a double purpose. First, oxygen is useful in the cleaning of the surface.⁵ Second, the molecular beam allows us to study the effect of additive gases on the work function of alkali-metal covered surfaces. Such studies, though interesting in their own right, serve as important standards against which the uncontaminated data may be checked.

As well as controlled contamination runs, quantitative studies will be made with the use of a G. E. monopole partial pressure analyzer. These studies will quantitatively check adsorbate purity and unwanted background contamination. The device is available and can easily be attached to the system.

A liquid-nitrogen cold finger may be added for two auxiliary studies. Cooling the surface will allow studies at high overlayer coverages and provide a check on the possible dependence of work function upon temperature.

Experimental Method

Changes in the target work function are measured by the contact-potential method. The principles of this method are schematically shown in Fig. VIII-7. The potential energy diagram for an emitter with a constant work function, ϕ_E , and a collector with a clean function, ϕ_O , is shown in drawing A. In the case shown, a voltage, $V_O = \phi_E - \phi_O$,

(VIII. PHYSICAL ELECTRONICS AND SURFACE PHYSICS)

is applied to the collector. This voltage is the contact potential difference between the emitter and the clean collector. Drawing A corresponds to the break point in the solid curve $\ln I$ vs V ; for collector voltages greater than V_0 , the electrons are retarded and the Boltzmann portion of the curve is obtained. If the work function of the collector is

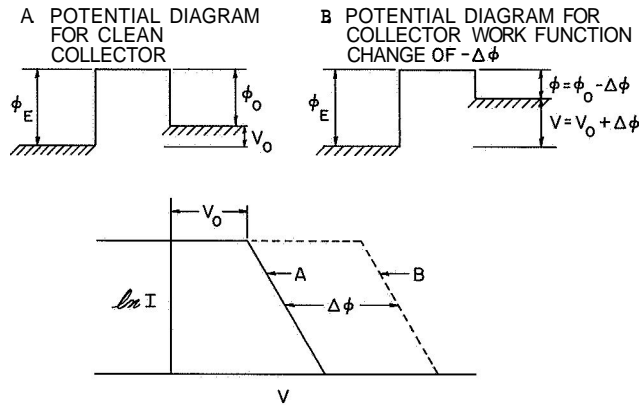


Fig. VIII-7. Illustrating the contact-potential method.

decreased, the situation is that shown in drawing B. Here again the voltage applied, $V = \phi_E - \phi_0 + A+$, is the contact potential. Thus, changing the work function of the collector (relative to the emitter) by $\Delta\phi$ changes the contact potential by $A+$. The net result is that the Boltzmann portion of the I - V plot is shifted, parallel to the clean plot, by an amount $\Delta\phi$. Thus, to measure changes in the collector work function, we need measure only the shift of the I - V plot relative to the clean plot.

The contact potential method has two primary advantages: it measures changes of work function directly; and since the collector is kept at $\sim 300^\circ\text{K}$, alkali-metal coverage

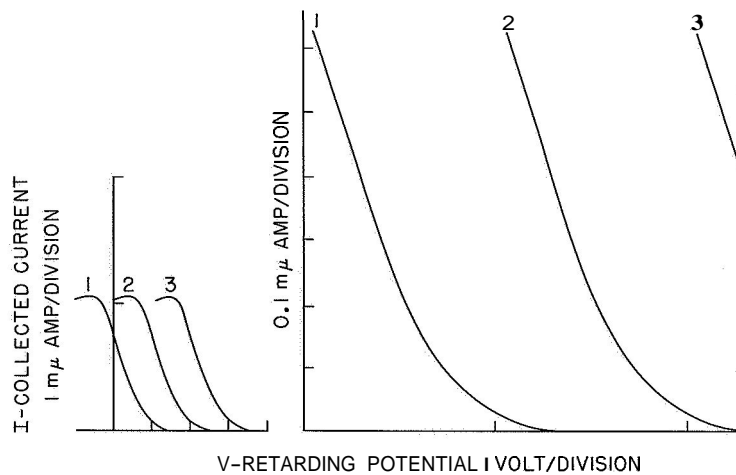


Fig. VIII-8. Typical retarding-potential plots.

(VIII. PHYSICAL ELECTRONICS AND SURFACE PHYSICS)

can be maintained without a high background pressure of alkali-metal vapor. The main disadvantage is that the method measures only changes and not absolute values; however, this is overcome by making an independent measurement of the thermionic work function of the surface. (The work function characterizing the emission of electrons at high temperatures will equal that characterizing the collection of electrons at room temperatures only if the properties of the surface are uniform and independent of temperature.)

The actual experimental method is best understood by referring to Fig. VIII-8. For each run, two retarding-potential plots are made. The small-scale plots, at the left in Fig. VIII-8, allow qualitative comparisons of different runs while the expanded-scale plots allow quantitative comparisons of the highly retarded portions of different runs. For instance, curve 1 represents a retarding-potential plot for a cleaned surface. Subsequent plots with adsorbed alkali-metal films (e.g., curves 2 and 3) are considered satisfactory for quantitative comparisons only if they are parallel to the clean curve (within ~ 0.03 eV) and show the same saturation current. In order for such standards to be valid, however, background contamination must be negligible.

The possibility of background contamination is checked in the following way. After each run with an adsorbed alkali-metal film, the surface is flashed and a retarding-potential plot is taken. To ensure reproducibility of the clean surface, this plot must always coincide with curve 1. An occasional contamination check is then made by allowing the clean surface to sit for a time (~ 20 minutes) longer than the maximum time for a run (~ 9 minutes). If, during this time, the surface contaminates enough to shift the curve by greater than ~ 0.02 eV, the previous runs are discarded.

Results for Cesium on Tantalum

The experimental results for cesium upon polycrystalline tantalum are shown in Fig. VIII-9 where work function change is plotted against the number of cesium ions applied. Three features of this plot are worth noting. First, at low coverage the work function decreases almost linearly with coverage. Second, the curve shows a maximum work function decrease (~ 2.47 eV at a coverage of 7×10^{13}). Third, though more high-coverage data are needed, the work-function change at high coverages appears to reach a limiting value (-2.21 eV).

To compare the data eventually with theoretical predictions, we must convert the number of cesium applied into a fractional coverage, θ . For convenience we have assumed one-monolayer coverage ($\theta = 1$) to be the point where the curve of Fig. VIII-9 becomes flat. Quantitatively, $\theta = 1$ is defined as the point where 15.5×10^{13} cesium particles have been applied to the surface. By this definition, the curve is linear up to approximately $\theta = 0.15$, and the minimum occurs at approximately $\theta = 0.5$. It is also interesting to note that if we divide the number of cesium in a monolayer (15.5×10^{13}) by the apparent target area exposed to the cesium beam (~ 0.322 cm²), the monolayer

(VIII. PHYSICAL ELECTRONICS AND SURFACE PHYSICS)

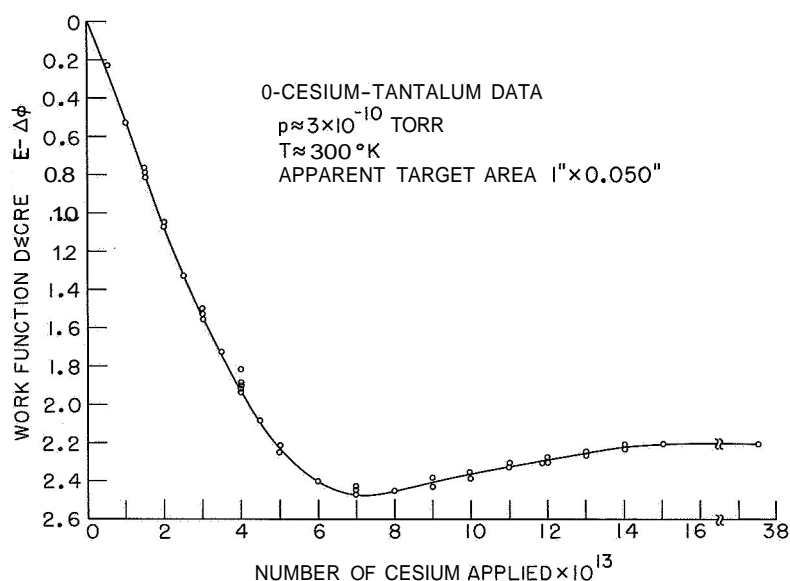


Fig. VIII-9. Experimental data for Cesium on Tantalum.

density of cesium is found to be $\sigma = 4.8 \times 10^{14}$ cesium/cm². This is the same value Taylor and Langmuir used for cesium upon a rough tungsten surface.⁶

Faulty design of the present thermionic measuring station made it difficult to obtain a reliable measurement of the work function of the bare tantalum surface. Despite this, a thermionic bare-surface work function of 4.15 ± 0.1 eV was estimated from the thermionic measurements. Based on this value, the minimum work function occurring near $\theta = 0.5$ is found to be 1.68 ± 0.1 eV, and the limiting value for full coverage is 1.94 ± 0.1 eV.

It must be recognized that these numbers are only approximations. For a patchy surface, a thermionic measurement will accentuate low work-function patches, while the contact-potential method attaches more relevance to an averaged work function.³ Using the thermionically measured work function for the 300°K surface is also dubious if the work function displays a strong dependence upon temperature.

Beyond these two points there is another serious point to be raised. If appreciable cesium atom desorption occurs at high coverages, serious doubt is cast upon our definitions of coverage. Since we have no way of measuring atomic desorption rates, two limiting cases have been calculated by using an expression derived by Rasor and Warner.⁷ If, as Rasor and Warner assume, the atomic heat of adsorption is constant at all coverages and has a value of ~ 1.6 eV for cesium upon tantalum, no appreciable desorption will occur until coverages near $\theta = 0.99$ are reached. If, on the other hand, the heat of adsorption at high coverage tends toward the value for vaporization of bulk cesium (~ 0.80 eV) serious desorption would begin at coverages of $\theta \approx 0.7$. The fact

(VIII. PHYSICAL ELECTRONICS AND SURFACE PHYSICS)

that the data give a reasonable value for monolayer density (σ) may indicate that the former case is the more likely.

Comparison with Existing Experimental Data

Houston⁸ has reported some emission data for cesium on polycrystalline tantalum. Since Houston did not measure coverage and it is difficult to compare thermionic data with contact potential data, only a qualitative comparison will be made. Most important, the data of Houston indicate the existence of a minimum work function and, for a bare work function of ~ 4.3 eV, the minimum value found is ~ 1.6 eV. Since our bare work function is ~ 4.15 eV, our minimum value of 1.68 eV is only in qualitative agreement with Houston's value.

D. L. Fehrs, R. E. Stickney

References

1. R. E. Weber and L. F. Cordes, Report on the Twenty-fifth Annual Conference on Physical Electronics, M. I. T., 1965, p. 378.
2. P. A. Anderson, Phys. Rev. **47**, 958 (1935).
3. W. B. Nottingham, Thermionic Emission, Technical Report: 321, Research Laboratory of Electronics, M. I. T., December 10, 1956, p. 110.
4. H. E. Farnsworth, Rev. Sci. Instr. **21**, 102 (1950).
5. J. A. Becker, E. J. Becker, and R. G. Brandes, J. Appl. Phys. **32**, 411 (1961).
6. J. B. Taylor and I. Langmuir, Phys. Rev. **44**, 433 (1933).
7. N. S. Rasor and C. Warner, III, J. Appl. Phys. **35**, 2589 (1964).
8. J. M. Houston and P. K. Dedrick, Report on the Thermionic Conversion Specialist Conference, Cleveland, Ohio, 1964, p. 77.

VIII. PHYSICAL ELECTRONICS AND SURFACE PHYSICS

C. Free-Molecule Flow Fields*

Academic and Research Staff

Prof. R. E. Stickney

Graduate Students

Y. S. Lou
S. Yamamoto

1. INVESTIGATION OF FREE-MOLECULE FLOW FIELDS

The general objective of this research project is to study the fluid dynamics of the transition regime existing between the free-molecule and continuum limits. Rather than using wind-tunnel techniques to study the transition flow around bodies, we have chosen to study the flow through orifices and tubes for the following reasons: (i) the orifice geometry is particularly well suited, since it minimizes the effect of unknown gas-surface interactions on the flow;¹ (ii) theoretical solutions are known, at least in principle, for the limiting cases of free-molecule and continuum flow through orifices and tubes;¹⁻³ (iii) the geometry of the apparatus permits us to measure the velocity distribution of the flow, thereby providing information that is more detailed than that generally available in wind tunnel tests; (iv) the cost and size of the apparatus are more reasonable; and (v) the experimental results will be relevant to engineering problems of molecular beam generation, exhaust of gases into space, and the flow of gases in vacuum systems.

We have recently completed an experimental investigation of the angular distribution of flow from orifices and tubes in the near-free molecule **regime**.⁴ Although these results provide useful information on the nature of the flow, measurements of the velocity distribution are now desirable because such data provide a complete description which could be used to check and to improve the existing theoretical treatments.

Although the velocity distributions of molecular beams have been studied by a number of investigators,⁵⁻¹² the results are incomplete because the experiments were limited to a small range of Knudsen numbers; the designs were such that measurements were restricted to one direction, that of the center line of the flow; and, in many cases, the experiments employed tubes or slits instead of sharp-edged orifices. (Since most theoretical treatments consider orifice flow,¹³⁻¹⁵ it is most important to obtain data for this type of aperture.) We believe that it is possible to circumvent all of these limitations by using the technique described below. Also, this technique enables us to

*This work was supported by the National Aeronautics and Space Administration (Grant NsG-496).

(VIII. PHYSICAL ELECTRONICS AND SURFACE PHYSICS)

make absolute measurements for cesium because all of the molecules striking the detector are ionized and recorded.

Since the basic features of the experimental apparatus have been described in previous progress reports, we shall concentrate here on the modifications that were required for measurements of the velocity distribution. The technique is similar to the time-of-flight method employed by Knauer¹¹ and Kofsky.¹² The molecular beam is interrupted periodically by a rotating disc driven by an electric motor, thereby creating pulses of molecules. The time, Δt , required for molecules in a given pulse to reach the detector is simply related to their speed, v , and the distance from the rotating disc to the detector, P ,

$$\Delta t = \frac{P}{v}.$$

Hence, the faster molecules will arrive at the detector before the slower ones. By displaying the detector signal on an oscilloscope, we obtain a waveform that may be related to the velocity distribution function. (A Moseley Waveform Translator (Type 101) may be used together with an X-Y recorder to obtain a permanent, enlarged record of the waveform.)

Some preliminary results are shown in Figs. VIII-10 and VIII-11. The solid curves represent the theoretical waveforms which would result if the flow were completely free molecular; the experimental data points are taken from waveform measurements. We would expect experiment to agree with theory when the Knudsen number (defined here as the ratio of the mean-free path, λ , to the orifice diameter, D) is sufficiently greater than unity. Hence, the agreement obtained for $\lambda/D = 10.2$ (Fig. VIII-10) is an indication that our apparatus is functioning properly.

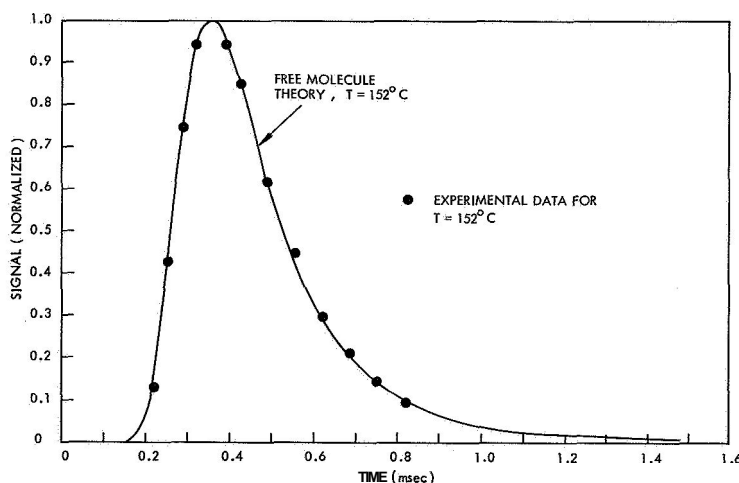


Fig. VIII-10. Experimental results for $T = 152^\circ\text{C}$.

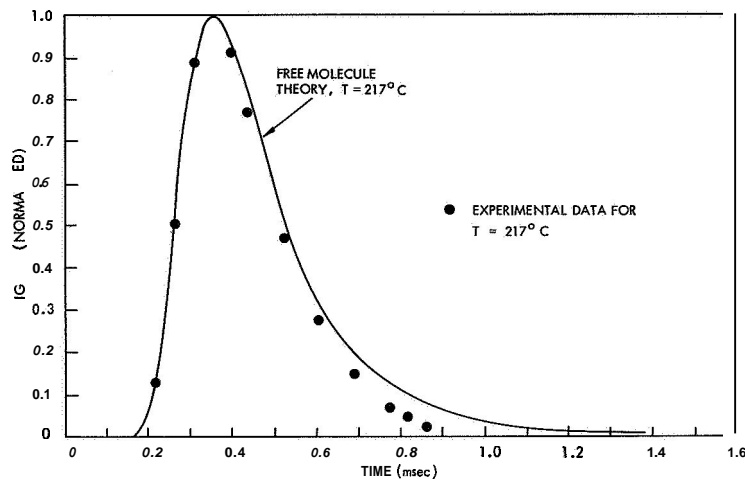


Fig. VIII-11. Experimental results for $T = 217^{\circ}\text{C}$.

According to the experimental⁶⁻¹¹ and theoretical results reported by others, the normalized velocity distribution for flow from an orifice should exhibit a deficiency of low-speed molecules when XD is of the order of unity. A deficiency of this nature is observed in Fig. VIII-11 for $XD = 0.85$. (As stated previously, the molecular speed is inversely proportional to time.)

At the present time we are obtaining data over a range of Knudsen numbers and for various angles from the flow center line. Tubes having different length-to-diameter ratios will be investigated after completing the orifice experiments.

R. E. Stickney, Y. S. Lou, S. Yamamoto

References

1. H. W. Liepmann, J. Fluid Mech. **10**, 65 (1961).
2. W. G. Pollard and R. D. Present, Phys. Rev. **73**, 762 (1948).
3. S. Dushman and J. M. Lafferty, Scientific Foundations of Vacuum Technique (John Wiley and Sons, Inc., New York, 1962).
4. See pages 19-21 of the Fifth Semiannual Progress Report, M. I. T. Center for Space Research, December 1965.
5. A review of the early measurements of velocity distribution is presented in E. H. Kennard, Kinetic Theory of Gases (McGraw-Hill Book Company, New York, 1938).
6. A. Ellett and V. W. Cohen, Phys. Rev. **52**, 509 (1937).
7. I. Estermann, O. C. Simpson, and O. Stern, Phys. Rev. **71**, 238 (1947).
8. A. Bennett, Phys. Rev. **95**, 608 (1954).
9. P. M. Marcus and J. H. McFee, in Recent Research in Molecular Beams, I. Estermann (ed.) [Academic Press, Inc., New York, 1959], p. 43.
10. J. E. Scott, H. S. Morton, J. A. Phipps, and J. F. Moonan, Proc. 4th International Symposium on Rarefied Gas Dynamics, 1964 (to be published).

(VIII. PHYSICAL ELECTRONICS AND SURFACE PHYSICS)

11. F. Knauer, *Z Physik* 126, 319 (1949).
12. I. L. Kofsky, S. M. Thesis, Physics Department., Syracuse University, 1948.
13. R. Narasimha, *J. Fluid Mech.* 10, 381 (1961).
14. D. R. Willis, *J. Fluid Mech.* 21, 21 (1965).
15. H. S. Morton, Project Squid Technical Report UVA-4-P-1, University of Virginia, 1948.

IX. PHYSICAL ACOUSTICS*

Academic and Research Staff

Prof. K. U. Ingard
Prof. L. W. Dean III
Dr. K. W. Gentle

Graduate Students

R. H. Katyl
J. L. Macon

W. M. Manheimer

J. A. Ross
H. M. Schulz III

A. ACOUSTIC WAVE AMPLIFICATION

Continued work on the problem of acoustic-wave amplification in a plasma² has led to the realization that the electron gas should be treated isothermally. The amplification mechanism, as described by Ingard,⁷ is a coherent heating of the neutral gas by the electrons, which are constrained to move in phase with the neutrals and ions.³ A calculation based on the fluid equations for the three-component system yields in the isothermal-electron limit the dispersion relation

$$k = (\omega/c)(1+i/\omega\tau)^{-1/2}, \quad (1)$$

where c is the adiabatic speed of sound for the neutral gas, and τ is an amplification time. This agrees with the initial result of Ingard,²

$$k = (\omega/c)(1-i/\omega\tau)^{1/2}, \quad (2)$$

in the limit $\omega\tau \gg 1$, but not for $\omega\tau \lesssim 1$. In fact, one finds that (2) is valid only when $\text{Re } k = \omega/c$, but since τ is such a large number ($10^{-2} \text{ sec} \lesssim \tau \lesssim 1 \text{ sec}$), an experimental distinction between (1) and (2) would be difficult to achieve.

Acoustic losses establish a threshold condition

$$\Gamma\tau < 1 \quad (3)$$

for the observation of an amplified wave. For propagation parallel to a cylindrical boundary of radius r , one finds

$$\Gamma = (2\omega/\rho r^2)^{1/2} t (\omega/c)^2 (7\eta/3\rho) \quad (4)$$

for a monatomic gas of viscosity η and density ρ . The dispersion relation actually observed under the expected quasi-adiabatic conditions, from an expansion of (1),

*This work was supported principally by the U. S. Navy (Office of Naval Research) under Contract Nonr-1841-(42); and in part by the Joint Services Electronics Programs (U. S. Army, U. S. Navy and U. S. Air Force) under Contract DA 36-039-AMC-03200(E).

(IX. PHYSICAL ACOUSTICS)

would be

$$k \approx (\omega/c) - i(1/2c\tau)(1-\Gamma\tau). \quad (5)$$

1. Lateral Acoustic Instability

Continuing work on the problem, described previously,^{4,5} of understanding why a constricted argon discharge kinks when the current is modulated at a lateral acoustic resonant frequency has led to a simple mechanism for explaining the effect. One may estimate the ionization rate, by intuition, as

$$R = \gamma N_e (\beta + N_e) N_n \exp(-aN_n/E),$$

where N_e and N_n are the densities of electrons and neutrals, E is the electric field, and a , β , and γ are positive constants. This model has the desired properties

1. $\partial R / \partial E > 0$
2. $\partial R / \partial N_n > 0$ for $aN_n/E < 1$
3. $\partial R / \partial N_n < 0$ for $aN_n/E > 1$.

If the modulation is sufficient to make both properties 2 and 3 realized during separate parts of the modulation cycle, the discharge will minimize E , thereby minimizing its power dissipation, by selecting the high-gas-density region when E is large and the low-gas-density region when E is small. Thus the path known to be favorable to the

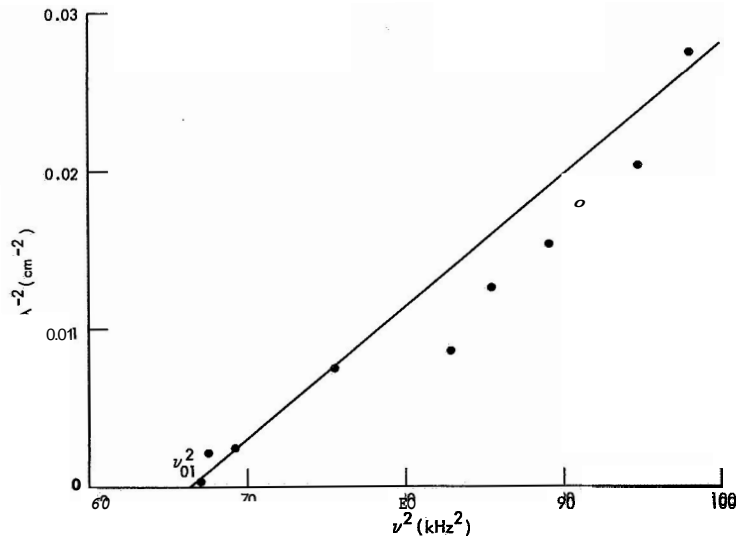


Fig. IX-1. Longitudinal structure in the mode $(nm) = (01)$, as evidenced by the lateral acoustic instability.

production of an acoustic wave is also preferred energetically in the presence of that wave. The path is stationary because the gas density and electric field at a given spatial location are periodic in time. The increase in path length serves to limit the degree of displacement.

The spatial regularity of the discharge path⁵ allows one to plot the wavelength λ against modulation frequency ν . This is done in Fig. IX-1 for the lowest mode ($n = 0$, $m = 1$), which displays through the linear relation between ν^2 and λ^{-2} the very definite excitation of a series of longitudinal modes based on the fundamental frequency ν_{01} . The line has slope c^{-2} , c being the speed of sound.

2. Acoustic Modulation of Microwave Transmission

Berlande, Goldan, and Goldstein⁶ have described an experiment in which the microwave transmission coefficient T of a decaying cryogenic helium plasma is demonstrably modulated by the sound produced by the decay of the electron temperature. An analysis now being conducted on this experiment seems to indicate that

(i) The electron temperature does not decay to the gas temperature (4.2°K), but to a temperature (-300°K) determined by the microwave signal used in making the measurement.

(ii) The initial electron density ($\sim 2 \times 10^{11} \text{ cm}^{-3}$) and temperature ($\sim 3 \times 10^4 \text{ }^\circ\text{K}$) are also unknown, so that quantitative agreement between theory and experiment can only be achieved by curve fitting.

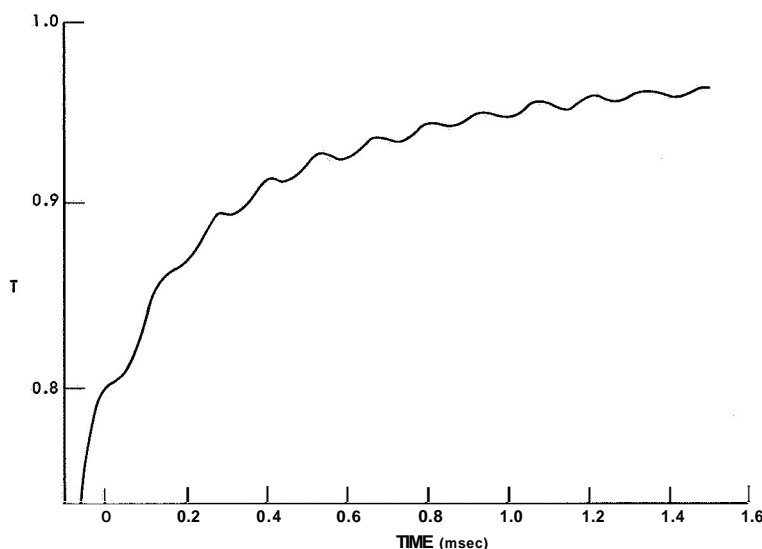


Fig. IX-2. Acoustic modulation of the microwave transmission coefficient of a decaying cryogenic plasma: theoretical plot for the parameters indicated in the text.

(IX. PHYSICAL ACOUSTICS)

(iii) The insensitivity of the acoustic amplitude to the size of the pulse generating the plasma may be due in part to an increase in gas temperature, which would defeat the purpose of raising the electron density and temperature by means of the larger pulse.

A theoretical curve with parameters as indicated in (i) and (ii) above, chosen so as to fit the experimental data, is shown in Fig. IX-2. The decay of the plasma is governed mainly by recombination rather than by diffusion. The transmission coefficient can be shown to be given approximately by

$$T = \exp\left(-\omega_p^2 \omega_c a / c \omega^2\right),$$

where a is the length of the plasma, c is the speed of light, and $\omega/2\pi$ is the microwave frequency. The plasma frequency ω_p and the collision frequency ω_c are modulated in phase with each other by the acoustic wave.

H. M. Schulz III

References

1. U. Ingard, Phys. Rev. **145**, **41** (1966).
2. H. M. Schulz III, Quarterly Progress Report No. **81**, Research Laboratory of Electronics, M. I. T., April **15**, **1966**, p. **43**.
3. U. Ingard and K. W. Gentle, Phys. Fluids **8**, **1396** (1965).
4. S. D. Strickler and A. B. Stewart, Phys. Rev. Letters **11**, **527** (1963).
5. H. M. Schulz III and K. W. Gentle, Quarterly Progress Report No. **81**, Research Laboratory of Electronics, M. I. T., April **15**, **1966**, p. **44**.
6. J. Berlande, P. D. Goldan, and L. Goldstein, Phys. Letters **5**, **51** (1964).

B. ERRATUM: LATERAL ACOUSTIC INSTABILITY

In Quarterly Progress Report No. **81**, p. **45**, Fig. VI-2, the photograph on the left-hand side marked "MODULATED" should read UNMODULATED.

H. M. Schulz III, K. W. Gentle

X. ELECTRODYNAMICS OF MOVING MEDIA*

Academic and Research Staff

Prof. H. A. Haus
Prof. P. Penfield, Jr.

A. STATUS OF RESEARCH

During the past quarter many of our previous results have been consolidated and refined, and will appear in a research monograph, to be published by The M. I. T. Press, Cambridge, Massachusetts (Special Technical Report Number 14 of the Research Laboratory of Electronics). The publication of this book terminates one phase of this study. Future work will be concerned with extensions to related areas, including but not limited to (i) force generation in novel media, (ii) general relativity, (iii) applications to specific experiments and devices, such as wave propagation in nonlinear media or the acoustic amplifier, and (iv) experimental tests of our theoretical results.

H. A. Haus, P. Penfield, Jr.

B. AMPLIFICATION AT SUBCRITICAL DRIFT VELOCITIES

[This report summarizes a paper to be presented at the Solid State Devices Research Conference, Chicago, Illinois, June 15-17, 1966.]

The helicon instability predicted by Baraff and Buchsbaum in layered semiconductor structures has been of considerable interest because the amplification occurs at "subcritical" drift velocities, i. e. , drift velocities less than the phase velocity of the wave. Sturrock's criterion developed for conservative (lossless) systems indicates that negative energy storage and hence amplification will exist if and only if the active system moves at a speed greater than the phase velocity of the wave under consideration. This criterion is violated in the Baraff-Buchsbaum case because the system is not conservative. We have investigated where and how the breakdown of the Sturrock criterion takes place in the hope that the findings will lead to realization of more practical devices in which amplification can be achieved at subcritical drift velocities.

It was found that in the Baraff-Buchsbaum case amplification occurs because of collisions at the interface between the drifting and stationary plasma. If the boundary conditions at the interface are made conservative by eliminating collisions and introducing surface currents, amplification at speeds less than the phase velocity does not occur. The role of collisions in converting dc energy to ac energy at the interface will be given a simple physical interpretation. Ways of realizing the same mechanisms in the bulk will also be discussed.

A. L. McWhorter, H. A. Haus

[Professor A. L. McWhorter is at Lincoln Laboratory, M. I. T.]

This work was supported by the Joint Services Electronics Programs (U. S. Army, U. S. Navy, and U. S. Air Force) under Contract DA 36-039-AMC-03200(E).

PLASMA DYNAMICS

PRECEDING PAGE BLANK NOT FILMED.

XI. PLASMA PHYSICS*

Academic and Research Staff

Prof. S. C. Brown
Prof. W. P. Allis

Prof. J. C. Ingraham
Dr. G. Lampis
J. J. McCarthy

E. M. Mattison
W. J. Mulligan

Graduate Students

M. L. Andrews
D. L. Flannery
E. V. George

P. W. Jameson
R. L. Kronquist
D. T. Llewellyn-Jones
G. L. Rogoff

J. K. Silk
D. W. Swain
F. Y-F. Tse

A. ELECTROMECHANICAL DEVICE TO FEED EXPERIMENTAL DATA AUTOMATICALLY INTO A TIME-SHARED COMPUTER SYSTEM - I.[†]

This report describes the purpose and principles of operation of the device that has been built. A succeeding report will describe in detail the construction of the device and its performance under actual operating conditions.

1. Introduction

An important area of application of the project MAC (Machine Aided Cognition - Multiple Access Computer) Compatible Time-Sharing System is in conjunction with external laboratory experiments, particularly those in the physical sciences. Here the experimenter, with a CTSS terminal next to his apparatus, can enjoy the luxury of an on-line computer for processing his experimental data as they are produced. In many cases the ability to feed the data into the computer automatically is highly desirable. This report describes a simple homemade device that can insert BCD (Binary Coded Decimal) data - in the present case generated in parallel form by a digital voltmeter (DVM) - into a Type 33KSR teletype terminal at rates up to the maximum of 10 characters per second allowed by the telephone lines, data sets, and so forth. Such a device could find application in many areas of physics, physical chemistry or engineering, where an experiment produces data at a rate no faster than, for example, one 6-digit number per second.

2. The Code

The signal sent to the computer by the teletype and data set consists of a series of square pulses at 110 cps, i. e. , a voltage alternating between two discrete levels, "mark" and "space. " When no signal is being sent, the data-set output remains at the

★

This work was supported by the United States Atomic Energy Commission (Contract AT(30-1)-1842).

[†]The work reported here was supported, through access to its computer facilities, by Project MAC, an M. I. T. research program sponsored by the Advanced Research Agency, Department of Defense, under Office of Naval Research Contract Nonr-4102(01).

PRECEDING PAGE BLANK NOT FILMED.

(XI. PLASMA PHYSICS)

When no signal is being sent, the data-set output remains at the "mark" voltage level.

One character in teletype code consists of 11 bits, each one of which is either a mark or a space of $1/110 \text{ sec} \approx 9 \text{ msec}$ duration. The first, or "start," bit of every character is a space. Eight information bits follow, then two "end" bits, which are always "marks." To avoid confusion, the 11 bits constituting the entire character will be referred to as C-bits, and the 8 information bits will be referred to as I-bits. Thus the first I-bit is the second C-bit, and so on.

In the teletype code used by Project MAC, every character has a "mark" for the eighth I-bit (ninth C-bit). Moreover, all numerals have the same configuration for I-bits 5-7, differing only in the first four I-bits. Since C-bit 1 is always a space, C-bits 9, 10, and 11 are always marks, and C-bits 6-8 are the same for all numerals, only C-bits 2-5 need be provided to specify a numeral, C-bits 1 and 6-11 remaining permanently set.

3. Teletype

Figure XI-1 is a simplified diagram of the hardware configuration. The teletype consists of three basic units: keyboard, printer, and data set.

When a key is depressed on the keyboard, a single-pole double-throw relay (hereafter called the "main relay") produces a series of contact closures that send to the printer a sequence of "mark" and "space" voltages in the appropriate character code

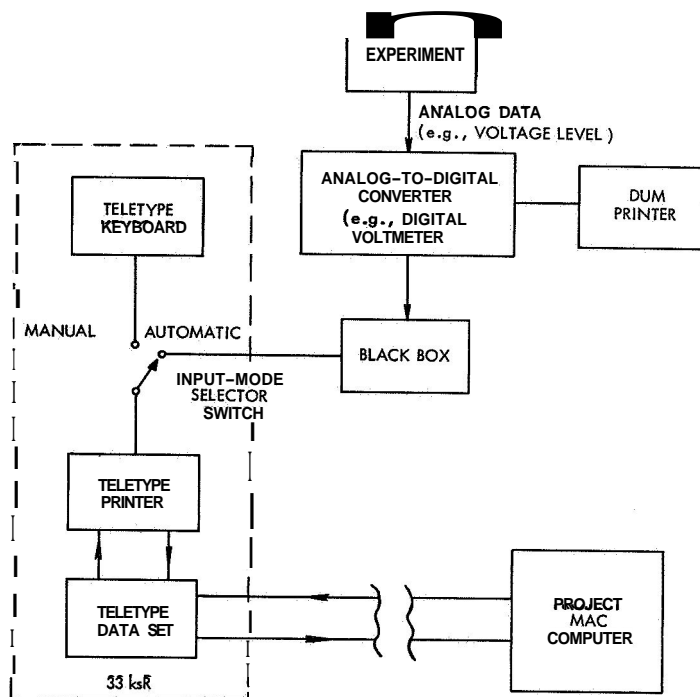


Fig. XI-1. Simplified schematic of experimental computer system.

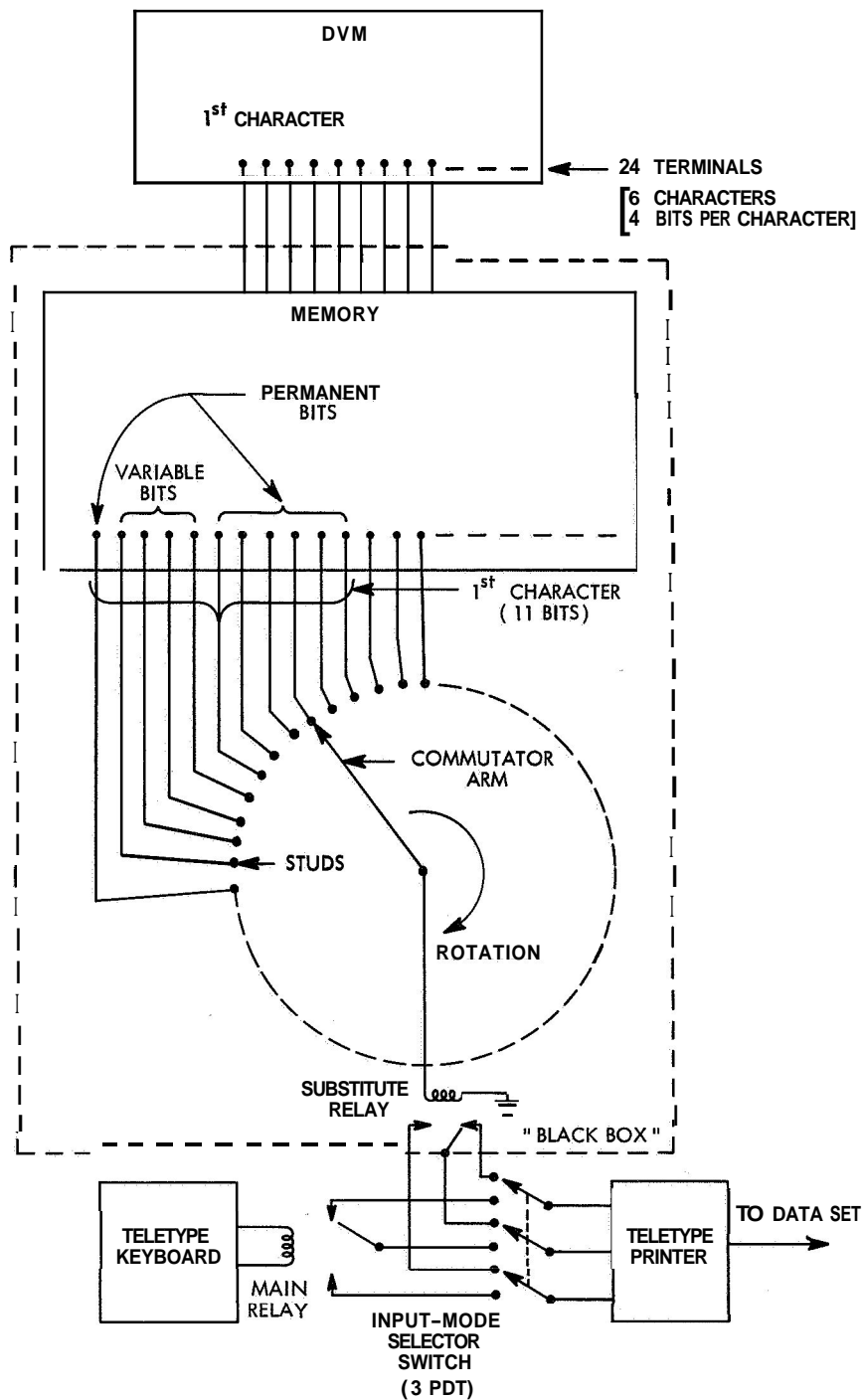


Fig. XI-2. Detail of the "Black Box."

(XI. PLASMA PHYSICS)

and at the proper rate. The data set then sends the character to the computer, while the printer types it on paper.

The data to be input to the computer is produced by the DVM in the form of a printed paper tape and BCD-coded voltages. Heretofore the data have been read from the tape and typed manually into the keyboard. At present, the equipment accepts the data in electrical form and feeds it directly to the printer and data set. The switch between the keyboard and printer replaces the main relay by a similar SPDT relay actuated by the black box, enabling the black box to act as an "automatic keyboard." Because the black box feeds the printer, a written record of the data is obtained at the same time as they are sent to the computer.

4. The Black Box

This device is essentially a serializer. The data bits, in the form of positive- or zero-voltage levels, are presented to it simultaneously. In the present application there are 4 bits per character: 1-2-4-8-BCD code. This string of 11 pulses, each of 9-msec duration, actuates the SPDT relay, which substitutes for the main relay and hence for the keyboard.

The parallel set of bits from the DVM is inserted, upon an appropriate command, into a memory, which is sampled sequentially by a commutator. The memory is necessary because the DVM presents the information for only a few milliseconds, whereas the time required to send the data through the teletype equals the number of characters $\times 0.1$ second per character. [Time per character = bits $\times 9$ msec/bit.]

Figure XI-2 shows how the information is removed serially from the memory and sent to the teletype. The memory consists of 24 SPDT latching (bistable) reed relays, whose arms are connected to the commutator studs. The memory relays place on the studs "marks" and "space" voltages, which are seen sequentially by the commutator and applied to the "substitute" relay. The last relay is also a latching reed relay; it holds each bit ("mark" or "space") until the following stud is sampled.

As mentioned before, C-bits 2-5 are the only ones that change during the transmission of numerical information. Thus C-bits 1 and 6-11 are "dummies" in the memory, permanently set at the appropriate voltages.

5. The Commutator

The commutator arm is driven by a 60-cpm synchronous electric motor to which it is connected by an electric clutch and brake. When the DVM presents the data it issues a "print" command pulse, primarily to actuate the DVM printer. The present device uses this pulse to: (a) connect the memory to the DVM; and (b) de-energize the brake and engage the clutch.

The commutator shaft has a cam which, upon completion of each revolution:

(a) disengages the clutch and energizes the brake; and (b) clears the memory. Thus the device as a whole has a duty cycle of just over one second (the time for revolution of the commutator shaft).

A more detailed description of the construction of this device, and a report on its performance under working conditions will appear subsequently.

D. T. Llewellyn-Jones, E. M. Mattison

B. DIFFUSION WAVES IN HOLLOW-CATHODE ARC

Attempts are being made to excite sinusoidal plasma density perturbations at the cathode of a hollow-cathode discharge. The resulting diffusion waves will be studied and should give data from which the effective diffusion coefficients, D_{\perp} and D_{\parallel} , of the highly ionized dense plasma may be determined.

The theory of diffusion waves was developed by Golubev¹ and successfully used by him to measure diffusion coefficients in a slightly ionized plasma in a magnetic field.² The results were in good agreement with classical neutral-dominated ambipolar diffusion theory. The present work is directed toward applying this diagnostic technique to a highly ionized (>30%), dense ($n > 10^{13} \text{ cm}^{-3}$) plasma, in which enhanced diffusion may occur. The plasma is assumed to be characterized by the two ambipolar coefficients, D_{\perp} and D_{\parallel} , and the diffusion equation is solved in cylindrical coordinates with the requirement of sinusoidal time dependence and complex exponential axial (x) dependence. The resulting separated-variables equation for the transverse coordinate function $R(\vec{r}_{\perp})$ is a Helmholtz equation. A discrete infinity of R solutions, or transverse modes, exists, each having a different z-dependence through the separation constant. For a cylinder, the R functions are the Bessel functions forced to zero at the plasma boundary and multiplied by an azimuthal function of the form $e^{im\phi}$. The unique solution (mode amplitudes) is fixed by superimposing modes to match the boundary conditions at the ends of the cylinder. Golubev had a plasma source at one end, and his tube was long enough to approximate a semi-infinite cylinder so that the boundary condition at the other end was essentially "no reflected waves." The dependence of each mode is

$$n_j(r, \phi, z, t) = A_j R_j(r, \phi) \operatorname{Re}\{e^{j\omega t - yz}\},$$

where $y_j \equiv \pm \left(\frac{D_{\perp} \beta_j^2 + i\omega}{D_{\parallel}} \right)^{1/2}$; A_j is mode amplitude; β_j is the separation constant determined for the mode. For example, β is $(2.4/R)$ for the first J_0 mode. The real part of y is the axial decay rate, and the imaginary part of y is the wave number for spatial oscillation in the axial direction. Since we do not expect growing diffusion solutions, the sign of the real part of y must always be chosen to give decay in the geometry that is being used.

(XI. PLASMA PHYSICS)

Since the decay rate increases with β_j , the mode with smallest β will dominate the solution for large z , regardless of the form of the excitation at $z = 0$. In the Golubev experiments this was true at points more than two diameters from the source. In the high-frequency limit, $\omega \gg D_{\perp} \beta_j^2$, we have

$$\gamma_j = \sqrt{\frac{\omega}{2D_{\parallel}}} (1 + i).$$

The decay rate and wave number are equal and do not depend on D_{\perp} or β_j , and thus are the same for all modes. This is the familiar result for one-dimensional diffusion waves, and quite naturally may also be viewed as the limit of small D_{\perp} , where axial motion predominates. For $\omega \ll D_{\perp} \beta_j^2$, we have

$$\gamma_j = \beta_j \sqrt{\frac{D_{\perp}}{D_{\parallel}}}.$$

The wave number is zero and pure decay results. The solution is essentially a slowly varying static diffusion solution. Under suitable conditions, the measurements of the decay lengths in the two limits can yield the values of D_{\perp} and D_{\parallel} . An important advantage of this method is that amplitude decay, rather than phase shift, is measured, since the latter is usually more difficult to measure accurately.

Since the cathode is believed to be a major source of plasma in the HCD, the device should be good for diffusion-wave studies, provided a suitable method can be found to modulate the plasma production rate at the cathode. This is being attempted at present.

Several problems inherent in the HCD device will complicate the diffusion wave theory needed to go with this experiment. The present geometry is a cylinder with L/D less than four; the length being limited by available magnetic field structure. The diameter could be decreased, but this would introduce other problems, such as pressure gradients caused by discharge pumping, and a column too thin for existing microwave diagnostics. Also, the plasma itself is a complicating factor. Since it is highly ionized, the diffusion coefficients depend on plasma density and therefore on position. Thermal gradients and diffusion are also present. There is a beam of streaming electrons from the cathode, although the bulk of electrons is contained in a Maxwellian distribution.

This work will continue with the goal of obtaining accurate measurement of effective diffusion coefficients in a highly ionized magnetically confined plasma in which enhanced or anomalous diffusion may exist.

D. L. Flannery

References

1. V. S. Golubev and V. A. Granovskii, Radio Engineering and Electronics (USSR) **7**, 624 (1962).
2. V. S. Golubev, Soviet Physics - JETP **16**, 1399 (June 1963).

C. SPATIALLY RESOLVED MEASUREMENTS OF EMISSION LINE PROFILES

1. Introduction

This report presents calculations of the performance of the optical system to be used in measurements of spectral-line profiles emitted by the hollow-cathode arc discharge. A Fabry-Perot etalon is to be used in the measurements. The computations presented here were performed to investigate the application of the optical system to spatially resolved measurements of line profiles.

An interferometer was chosen for this work because it provides high wavelength resolution, compact size, and relatively large aperture. The initial measurements will be performed with the use of a helium plasma, because of the large Doppler breadth of helium emission lines. Further experiments are planned with other gases to which small concentrations of helium have been added.

The optical system that will be used in the experiment consists of two lenses, the interferometer, and a pinhole. Light from the plasma is collected by the first lens, passes through the Fabry-Perot, and is focussed by the second lens on a pinhole. The light passing through the pinhole is detected by a photomultiplier.

This report presents a calculation of the fraction of light from a point source transmitted by the optical system as a function of the position of the source. The result of the computation is used to determine the performance of the optical system in spatially resolved measurements on nonuniform plasmas. For simplicity, the effects of the Fabry-Perot are assumed to be negligible and the calculations are made for a system of two lenses and a pinhole.

2. Computation of the Transmission Function

The computation presented here is that of the transmission function of the optical system shown in Fig. XI-3. The transmission function gives the fraction of the light

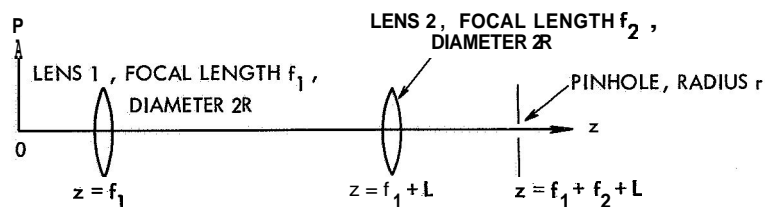


Fig. XI-3. Optical system.

intensity from an isotropically emitting point source which is transmitted by the optical system as a function of the position of the source. First, it is shown that rays passing through a small disk in the focal plane of Lens 1 are transmitted without loss. Then

(XI. PLASMA PHYSICS)

this information is used to derive an expression for the transmission function. Finally, an approximate expression for the transmission function is obtained which is valid for typical geometrical conditions.

a. Full-Transmission Disk

Rays passing through a small disk in the focal plane of Lens 1 are transmitted by the optical system without loss. To determine the size of this disk, consider a point source in the focal plane of Lens 1 at a distance ρ_0 from the axis. The rays from this source passing through Lens 1 form a parallel beam in the region between the two lenses. The rays are not parallel to the axis. Their slope can be determined immediately from the construction shown in Fig. XI-4. Ray 1, which is parallel to the axis before it reaches Lens 1, is refracted by that lens and passes through the focal point of the lens at $z = 2f_1$. Ray 2, which passes through the center of Lens 1 without deviation, is

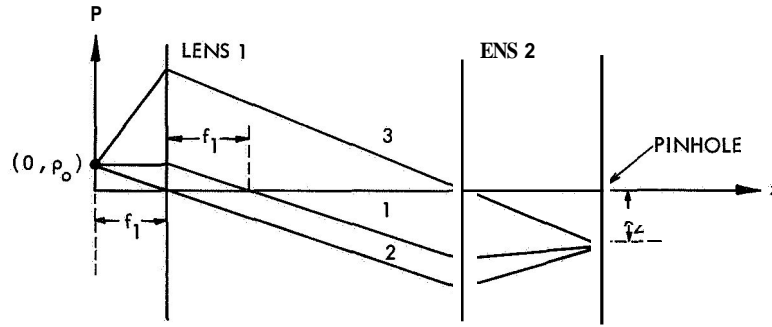


Fig. XI-4. Ray tracing for off-axis point in the focal plane of Lens 1.

parallel to Ray 1. Since these two rays are parallel, all other rays from the source at ρ_0 are parallel.

The light from the source at $(0, \rho_0)$ that reaches Lens 2 will be focussed at a point in the focal plane of the lens at $z = f_1 + f_2 + L$. The ρ coordinate of the focus can be found by considering Ray 3, which passes through the center of Lens 2 without deviation. It reaches the plane $z = f_1 + f_2 + L$ at $\rho = -\rho_2 = -\rho_0 f_2 / f_1$. Thus all the light from the source at $(0, \rho_0)$ is focussed at $(f_1 + f_2 + L, -\rho_2)$ and is transmitted if $(\rho_0 f_2 / f_1) < r$, that is,

$$\rho_0 < \frac{f_1}{f_2} r,$$

where r is the pinhole radius at $z = f_1 + f_2 + L$. No light goes through if $\rho_0 > (f_1 r / f_2)$.

Note that in this calculation it is assumed that all light from the source passing through Lens 1 also passes through Lens 2. This is not quite correct because the light

beam that reaches the plane of Lens 2 has a cross-section area equal to the area of the lens, but its center is displaced from the center of the lens. A simple calculation using the typical dimensions given in Sec. 2c shows that the loss at Lens 2 is as small as 5 per cent. It is reasonable to neglect this small loss at Lens 2.

b. General Expression for the Transmission Function

Rays passing through a disk of radius $\rho_0 = (f_1 r / f_2)$ are transmitted by the optical system without loss. Rays that do not pass through this disk are not transmitted. The fraction of the light from a point source emitting isotropically in all directions and located at an arbitrary position to the left of Lens 1 which is transmitted by the optical system is equal to the fraction of the light that apparently could have come from a source in the full-transmission disk. This fraction is given by $\Omega/4\pi$, where Ω is the solid angle containing all rays passing through the point source which also pass through both the full-transmission disk and Lens 1.

There is a different expression for the transmission function in each of the three regions shown in Fig. XI-5. The transmission function for a point source in region K (K=I, II, III) is given by

$$T = T_k = \frac{\Omega_k(\rho, z)}{4\pi},$$

where (ρ, z) is the location of the point source. For a point source in region I, all rays passing through the full-transmission disk also pass through Lens 1, so $\Omega_1(\rho, z)$ is the solid angle subtended by the full-transmission disk at (ρ, z) . For a point source in region II, all rays passing through Lens 1 also pass through the full-transmission disk, so $\Omega_2(\rho, z)$ is the solid angle subtended by Lens 1 at (ρ, z) . For a point source in region III, the rays that are transmitted are limited by both the full-transmission disk and by Lens 1, so $\Omega_3(\rho, z)$ is the solid angle defined in Fig. XI-5.

A good approximation for the solid angles Ω_1 and Ω_2 is easily computed by using

$$\Omega_k = 2\pi(1 - \cos \theta_k),$$

where θ_k is the interior half-angle of the cone of solid angle Ω_k :

$$\Omega_1(\rho, z) = 2\pi \left\{ 1 - \sqrt{\frac{\frac{1}{2} + \frac{1}{2} \frac{z^2 + \rho^2 - \rho_0^2}{[z^2 + (\rho - \rho_0)^2]^{1/2} [z^2 + (\rho + \rho_0)^2]^{1/2}}}{\frac{1}{2} + \frac{1}{2} \frac{(f_1 - z)^2 - (R - \rho)(R + \rho)}{[(f_1 - z)^2 + (R - \rho)^2]^{1/2} [(f_1 - z)^2 + (R + \rho)^2]^{1/2}}} \right\}$$

$$\Omega_2(\rho, z) = 2\pi \left\{ 1 - \sqrt{\frac{(f_1 - z)^2 - (R - \rho)(R + \rho)}{[(f_1 - z)^2 + (R - \rho)^2]^{1/2} [(f_1 - z)^2 + (R + \rho)^2]^{1/2}}} \right\}.$$

(XI. PLASMA PHYSICS)

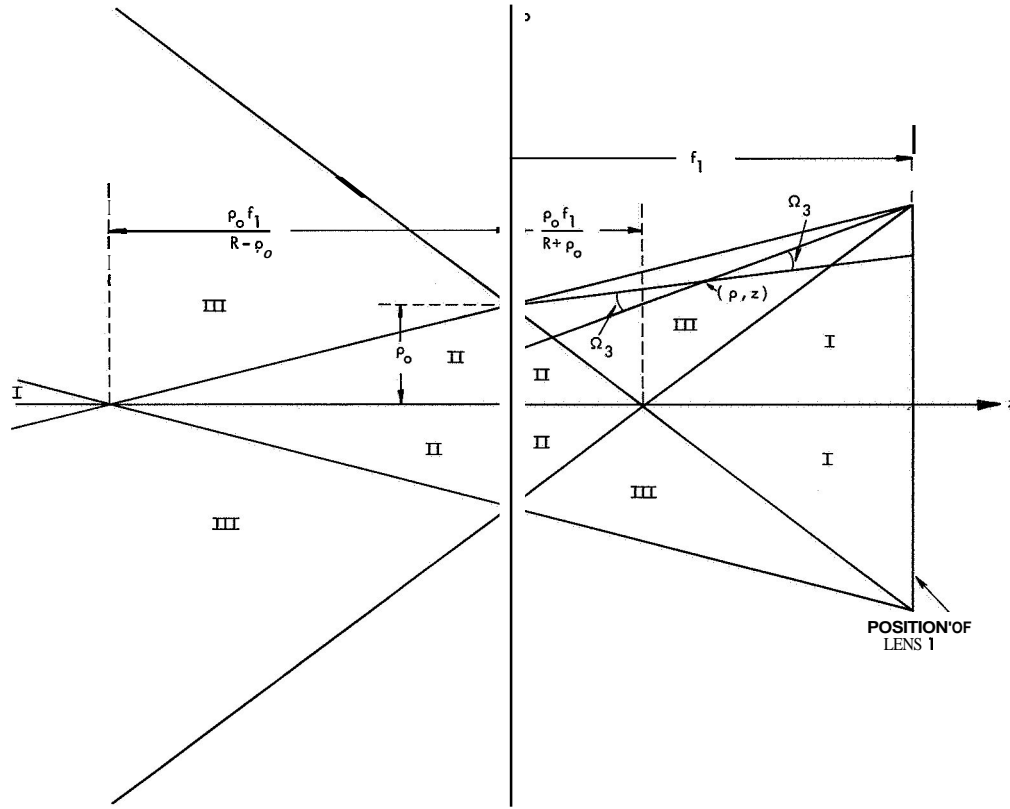


Fig. XI-5. Regions of applicability of three exact expressions for transmission function.

The expression for Ω_1 is a good approximation throughout region I, provided $R^2 \ll f_1^2$, and Ω_2 is a good approximation throughout region II, provided $\rho_o^2 \ll f_1^2$. This condition for Ω_2 is fulfilled, as long as the pinhole is small compared with the lenses.

The solid angle Ω_3 has a minimum value of zero at the outer edge of region III and a maximum value of

$$\Omega_3 = 2\pi \left\{ 1 - \sqrt{\frac{\frac{1}{2} + \frac{1}{2} \frac{f_1^2 \left(1 - \frac{rf_1}{Rf_2}\right)^2 - R^2}{f_1^2 \left(1 - \frac{rf_1}{Rf_2}\right)^2 + R^2}}{1}} \right\}$$

at the point on the z -axis which forms the common boundary of regions I, II, and III.

c. Approximate Expression for the Transmission Function

An approximation to the transmission function will now be obtained which is valid for typical geometrical conditions. The dimensions of the optical system to be used in the Fabry-Perot measurement of the profiles of lines emitted by the hollow-cathode arc discharge are $f_1 = 10$ cm, $f_2 = 20$ cm, $R = 2.5$ cm, $L = 50$ cm, $r = 1.225 \times 10^{-2}$ cm.

For these dimensions, Ω_1 and Ω_2 vary only slightly with p for fixed z . This can be seen by considering, for example a point (p, z) in region I. The solid angle Ω_1 is approximately the area of the full-transmission disk divided by the square of the distance from the point (p, z) to the disk, or

$$\Omega_1 \approx \frac{\pi \rho_o^2}{\rho^2 + z^2}.$$

For the dimensions given above $p < (1/4)z$ in region I and as p goes from zero to $(1/4)z$, Ω_1 changes by only 6 per cent. A similar calculation applies to Ω_2 . Such a small error is made in approximating $\Omega_k(p, z)$ ($k=1, 2$) by $\Omega_k(0, z)$ because the maximum variation in p is much less than the distance from (p, z) to the disk that defines Ω_k . Thus the first approximation that we make is that all points on any cross-section disk in regions I or II have the same transmission function, $T_k(0, z)$.

For the dimensions given above it is also a reasonable approximation to neglect the contribution of the light from region III. The volume of region III is only ≈ 0.3 per cent of the volume of region I, and the transmission function for points in region III is less than the transmission function for points in region I. If the radiation source were very inhomogeneous, it might not be valid to neglect radiation from region III. For example, if the emitted intensity changes by a factor of 100 over a distance comparable to a typical dimension, ρ_o , of region III, this approximation would be invalid.

In region I, $z \geq \rho_o f_1 / (R + \rho_o) \approx 4\rho_o$ for the dimensions given above, so that $z^2 \gg \rho_o^2$ and the expression for Ω_1 can be expanded, with terms of the order of $(\rho_o/z)^4$ and higher neglected. The resulting approximate expression for the transmission function is

$$T_1(p, z) \simeq T_1(0, z) = \frac{\Omega_1(0, z)}{4\pi} \simeq \frac{1}{4} \left(\frac{f_1}{f_2} \right)^2 \left(\frac{r}{z} \right)^2$$

Thus in region I the transmission function decreases as $1/z^2$.

In region II $z < \rho_o f_1 / (R + \rho_o) \approx 4\rho_o \approx 5 \times 10^{-2}$ cm, so that $z/f_1 \simeq 5 \times 10^{-3}$ cm $\ll 1$ cm, and also $(R^2/f_1^2) = 1/16 \ll 1$. The expression for Ω_2 can be expanded, with z/f_1 and $(R/f_1)^4$ and smaller terms relative to one neglected. The approximate expression for the transmission function that is obtained is

(XI. PLASMA PHYSICS)

$$T_2(\rho, z) \approx T_2(0, z) = \frac{\Omega_2(0, z)}{2\pi} \approx \frac{1}{4} \left(\frac{R}{f_1} \right)^2.$$

Thus in region II the transmission function is independent of z . Figure XI-6 shows the transmission function for $\rho = 0$ in regions I and II as a function of z for the chosen typical conditions.

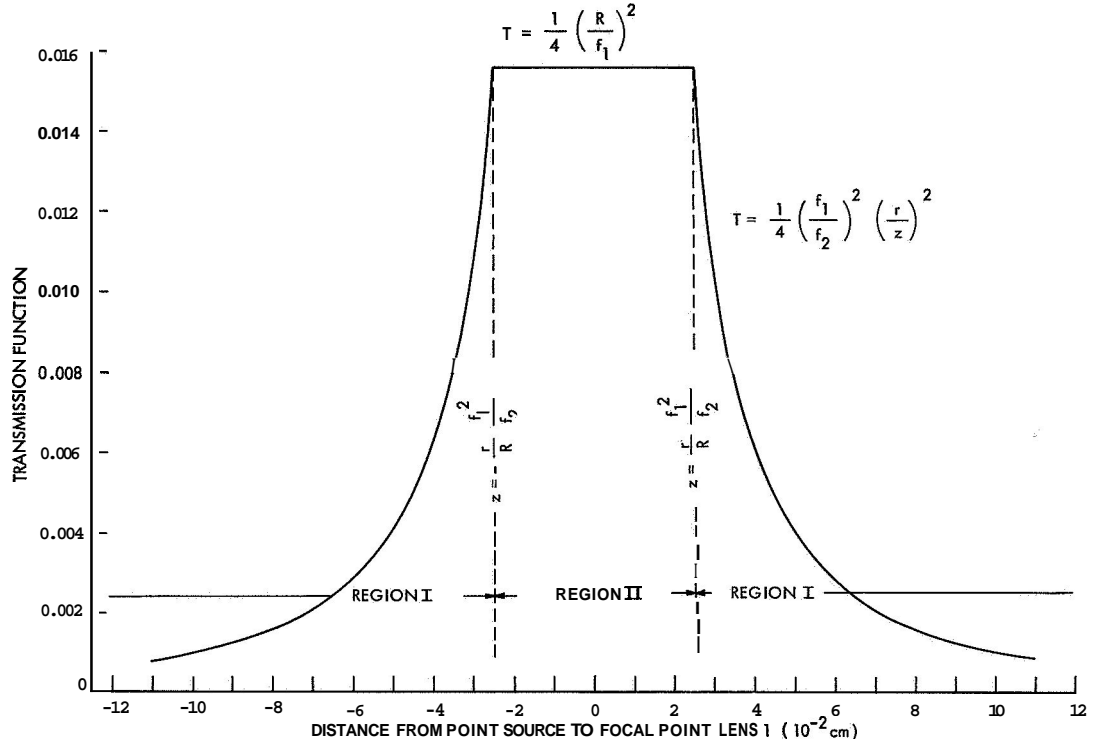


Fig. XI-6. Approximate transmission function vs distance of point source from focal point of Lens 1.

As a final approximation, ρ_0 is neglected in comparison with R in the expressions giving the boundary between regions I and II. In this approximation the volume from which the optical system accepts light is symmetric with respect to the plane $z=0$. The transmission function can be written

$$T(z) = T_1(z) = \frac{1}{4} \left(\frac{f_1}{f_2} \right)^2 \left(\frac{r}{z} \right)^2 \quad |z| \geq \frac{r}{R} \frac{f_1}{f_2}$$

$$T(z) = T_2(z) = \frac{1}{4} \left(\frac{R}{f_1} \right)^2 \quad |z| \leq \frac{r}{R} \frac{f_1}{f_2}$$

Note that the transmission function for a point in region I depends on the size of the pinhole, while the transmission function for a point in region II depends upon the size of the lenses. The transmission function for a point source anywhere in region II is the same as the transmission function for a point at the origin (that is, at the focal point of Lens 1). $T_2(z)$ is independent of the size of the pinhole because the cross-section area, at the plane of the pinhole, of a pencil of rays from a point source in region II is smaller than the pinhole. The size of region II is determined by the radius of the pinhole. Hence the total light intensity transmitted by the optics from region II in an extended source decreases with decreasing pinhole size, as is shown below.

$T_1(z)$ does not depend on the size of the lenses because the pinhole only transmits rays from a source in region I which pass through the full-transmission disk.

3. Application to Plasma Measurements

The approximate expression for the transmission function obtained above will be used here to determine the performance of the optical system of Fig. XI-3 in optical measurements on plasmas. The contributions of regions I and II of Fig. XI-5 to the intensity of light through the pinhole are computed for a uniform slab of plasma. For a cylindrical plasma in which the light flux from a unit volume varies parabolically with radius, it is shown that the Abel inversion can be used to determine the spatial distribution of light emission. For a cylindrical plasma in which the emitted intensity per unit volume is a general function, a numerical method must be used. To obtain the spatial distribution of a line profile, the power (light flux) emitted by a unit volume must be determined as a function of position at several wavelengths within the line breadth.

a. Uniform Plasma Slab

A computation of the contributions of regions I and II to the intensity of the light passing through the pinhole for a uniform slab of plasma will now be presented. The slab has thickness $2a$ and is centered at $z = 0$, that is, at the focal point of Lens 1. The power radiated by unit volume of the slab is taken to be unity. The power through the pinhole is given by

$$I = \int_V A(z) dx dy dz = \int_{-a}^{+a} A(z) T(z) dz,$$

where $A(z)$ is the area perpendicular to the z -axis of an elemental volume Adz , and V is the volume common to the plasma and the region from which light is accepted by the optical system. Using the approximations of Sec. 2c, the power of the light from region I transmitted by the pinhole is

(XI. PLASMA PHYSICS)

$$I_1 = 2 \int_{\frac{rf_1^2}{Rf_2}}^a T_1(z) A(z) dz = \frac{\pi}{2} \left(\frac{Rf_1}{f_2} \right)^2 \int_{\frac{rf_1^2}{Rf_2}}^a \frac{1}{z^2} \left(z - \frac{rf_1^2}{Rf_2} \right)^2 dz$$

$$\approx \frac{\pi}{2} \left(\frac{Rf_1}{f_2} \right)^2 a.$$

In evaluating the integral, terms of the order of $\frac{1}{a} \left(\frac{rf_1^2}{Rf_2} \right)^2$ have been neglected as compared with a , which is less than 1 per cent error for $a > 0.25$ cm. The power of the light from region II transmitted by the pinhole is $I_2 = T_2 V_2$, where V_2 is the volume of region II. Hence

$$I_2 = \frac{\pi}{6} \left(\frac{f_1}{f_2} \right)^2 \frac{r^3 R}{f_2}.$$

The ratio of the power from the small region II near the origin to the power from the rest of the plasma is

$$\frac{I_2}{I_1} = \frac{\pi}{3} \frac{f_1^2 r}{f_2 R A} \approx \frac{1}{E a}.$$

Thus $(I_2/I_1) < 3\%$ for $a > 0.25$ cm. Most of the light comes from the plasma in region I, despite the fact that the transmission coefficient is much smaller for a point in region I than for a point in region II. This is so because the volume of region I is much greater than that of region II. The ratio of the volumes $(V_1/V_2) > 103$ for $a > 0.25$ cm.

b. Cylindrical Plasma – Parabolic Distribution of Emission Intensity

A cylindrical plasma in which the power radiated per unit volume falls off parabolically with increasing distance from the axis will be considered here. The geometry is shown in Fig. XI-7. The axis of the plasma lies along the y-axis of the rectangular coordinate system. The plasma radius is b . The axis of the optical system is parallel to the z axis with the focal point of Lens 1 at $(x_s, 0, 0)$. Light is collected from the shaded region of the plasma. The power emitted by a unit volume of plasma is

$$\epsilon(r) = \left(1 - \frac{r^2}{b^2} \right),$$

where $r^2 = x^2 + z^2$.

If $\epsilon(r)$ does not drop off too rapidly with r , that is, for sufficiently large b , several simplifications can be made which permit the Abel integral inversion to be used. These approximations are valid to better than 1 per cent accuracy when $b > 0.25$ cm. For this condition, the contribution to the total intensity transmitted by the optical system from region II can be neglected for the typical dimensions used in Sec. 2c, even when the optical axis passes through the center of the plasma. Also, the emission per unit volume from all points on the disk shown in Fig. XI-7 can be taken to be $\epsilon(\bar{r})$, where $\bar{r} = \sqrt{z^2 + x_s^2}$. This means that the intensity emitted at any point on this disk is the same as the intensity emitted on the optical axis. Thus the power transmitted by the optical system is

$$I(x_s) = 2 \int_0^{z_m} E \left(\sqrt{z^2 + x_s^2} \right) A(z) T(z) dz = 2 \int_0^{z_m} \left(1 - \frac{z^2 + x_s^2}{b^2} \right) A(z) T(z) dz,$$

where $z_m = \sqrt{b^2 - x_s^2}$. This approximation for the upper limit of integration is the same as the standard approximation made when using the Abel inversion. It can be seen by referring to Fig. XI-7 that this assumption approximates the curved surface

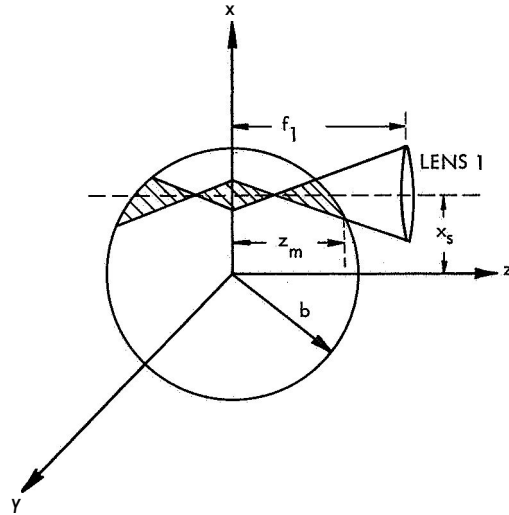


Fig. XI-7. Geometry for cylindrical plasma.

of the cylinder by a number of disk-shaped plane elements parallel to the x - y plane whose centers are at the intersection of the optical axis and the surface of the cylinder. This is a valid approximation because the cone of acceptance of the optical system is slender (the tangent of its interior half-angle is approximately $1/4$). Moreover, the region of the volume of acceptance which is influenced by the approximation is the region

(XI. PLASMA PHYSICS)

in which the emission intensity is small. Writing the lower limit of the integral as zero extends region I up to the x-y plane, an approximation that in part offsets neglecting light from region II.

The integral for $I(x_s)$ can be written in terms of r as

$$I(x_s) = \frac{\pi}{2} \left(\frac{Rr}{f_2} \right)^2 \int_{x_s}^b \frac{\epsilon(\bar{r}) \bar{r} d\bar{r}}{\sqrt{r^2 - x_s^2}}$$

by using the relation $\bar{r}^2 = z^2 + x_s^2$. The power radiated per unit volume $\epsilon(\bar{r})$ can be found by means of the Abel inversion. It is

$$\epsilon(r) = -\frac{2}{\pi^2} \left(\frac{f_2}{Rr} \right)^2 \int_r^b \frac{I'(x_s) dx_s}{\sqrt{x_s^2 - r^2}}.$$

The factor $\frac{2}{\pi^2} \left(\frac{f_2}{Rr} \right)^2$ displays the influence of the particular optical system considered in these calculations. In most experiments in which the Abel inversion is used to obtain the space distribution of light emission, the cross section of the acceptance volume of the optics is independent of z , and the factor $\frac{2}{\pi^2} \left(\frac{f_2}{Rr} \right)^2$ is simply $\frac{1}{\pi}$ times the reciprocal of the slit-area connected with the experiment.

c. Cylindrical Plasma - General Distribution of Emission Intensity

Here, the case of a cylindrically symmetric plasma in which the power radiated per unit volume is a general function of the radial coordinate is considered. The geometry is the same as that above and is shown in Fig. XI-7. For this case, the power transmitted by the optical system is

$$I(x_s) = \iiint_V dx dy dz \epsilon(r) T(z),$$

where V is the volume common to the acceptance region of the optical system and the plasma. This equation can be rewritten

$$I(x_s) = \left(\frac{R}{f_1} \right)^2 \int_0^{\rho_{o1} f_1 / R} h(z, x_s) dz - \left(\frac{f_1 r}{f_2} \right)^2 \int_{\rho_{o1} f_1 / R}^{z_m} h(z, x_s) \frac{dz}{z^2},$$

where

$$h(z, x_s) = \int_{x_s - \rho_0 + \frac{Rz}{f_1}}^{x_s + \rho_0 - \frac{Rz}{f_1}} dx \sqrt{\left(\rho_0 - \frac{Rz}{f_1}\right)^2 - (x - x_s)^2} \epsilon(r).$$

The first integral in the expression for $I(x_s)$ is the contribution from region II, and the second integral is the contribution from region I. The expression for $h(z, x_s)$ is derived under the assumption that the emission from the regions of the plasma near the surface may be calculated by approximating the plasma volume elements in this region by disk-shaped plane elements parallel to the x - y plane, as in the preceding section. Therefore, if the plasma is b , $z_m = \sqrt{b^2 - x_s^2}$.

In this case it is possible to determine $\epsilon(r)$ by assuming that it is given by a power series, $\epsilon(r) = \sum_{n=0}^N c_n (x^2 + z^2)^n$, and substituting this in the integrals above. This substitution yields a set of linear equations, of which the left-hand sides are the measured values of $I(x_s)$, and the right-hand sides are linear summations containing the coefficients c_n . These coefficients are determined by solving this set of equations with the aid of a computer.

These calculations will be applied to measurements that are to be made on a DC hollow-cathode arc.

J. D. Silk, J. C. Ingraham

D. MICROWAVE SCATTERING FROM AN ELECTRON-BEAM PRODUCED PLASMA

Observations have been made of the scattering of microwaves from electron density fluctuations in a plasma produced by an electron beam. The nature of the fluctuations is not yet clear, but the most likely possibility is that they are longitudinal plasma waves excited by the beam.

The theory of density fluctuations in plasmas and the scattering of electromagnetic radiation from these fluctuations has been analyzed by Fejer,¹ Ichimaru,² and Salpeter.³ The frequency of the scattered radiation is shifted from the incident frequency by $\pm f$, where f is the frequency of the density fluctuation responsible for the scattering. The amplitude of the scattered radiation is approximately proportional to the potential energy of the density fluctuation. Scattering of electromagnetic waves from plasmas provides a method for investigating the spectrum of density fluctuations, and scattering experiments have been carried out to investigate both thermal fluctuations⁴ and large-amplitude fluctuations associated with unstable plasma waves.⁵

In our experiment radiation at an X-band frequency was incident on the plasma from a waveguide, and a separate waveguide picked up the radiation that was scattered by the plasma. The scattered radiation was shifted in frequency from the incident radiation

(XI. PLASMA PHYSICS)

by the frequency of the density fluctuations which were observed independently by means of probes inserted into the plasma.

The experimental tube is illustrated in Fig. XI-8. The electron *gun*, located at one end of the tube, fires an electron beam into argon gas and ionized it. The axis of the

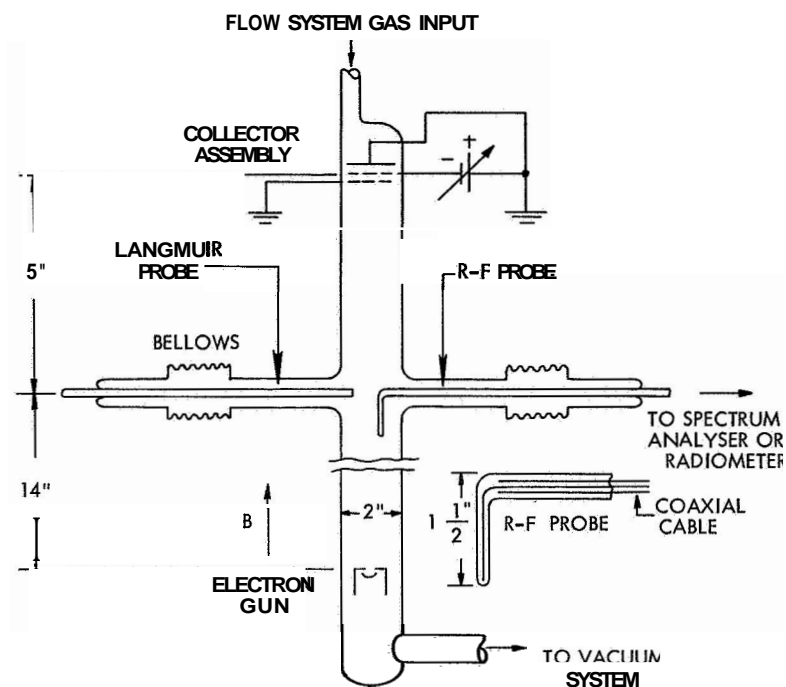


Fig. XI-8. Experimental tube.

tube is aligned along a uniform magnetic field, but the electron gun is shielded from the field, so that the beam electrons acquire transverse energy as they enter the magnetic field. There are two probes, a guard-ring Langmuir probe and an RF probe, which can be moved radially into the plasma by means of bellows. The RF probe is a coaxial cable enclosed completely in glass so that it draws no DC current from the plasma. At the far end of the tube is a collector assembly which consists of a flat circular plate with two grids in front of it. The grids could be biased to determine the axial velocity of the electron beam, but, ~~for~~ this experiment, the entire assembly was grounded as was the anode of the gun so that no axial electric field existed in the main section of the tube. Two pieces of X-band wave guide are mounted with their axes perpendicular to the axis of the tube as shown in Fig. XI-9. A block diagram of the experimental apparatus is shown in Fig. XI-10.

Both the RF probe and the Langmuir probe could be connected to a spectrum analyzer, and signals from each of them exhibited maxima at roughly the same

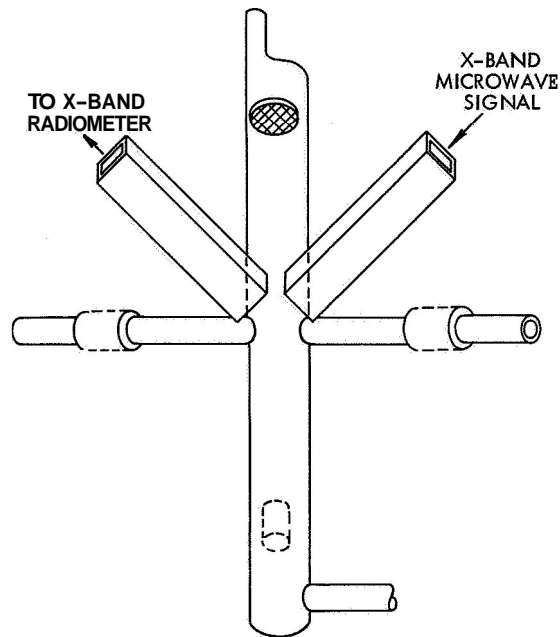


Fig. XI-9. Scattering geometry.

frequencies. A peak was observed whose frequency could be varied from approximately 200 Mc to 400 Mc by varying the gas pressure, magnetic field, and beam voltage and current. The frequency of the peak increased whenever the value of any of these parameters was increased, the others being held constant. The magnetic field was of the order of 250 Gauss, so the cyclotron frequency was approximately 700 Mc. Since the observed peak was well below this value, it could not be

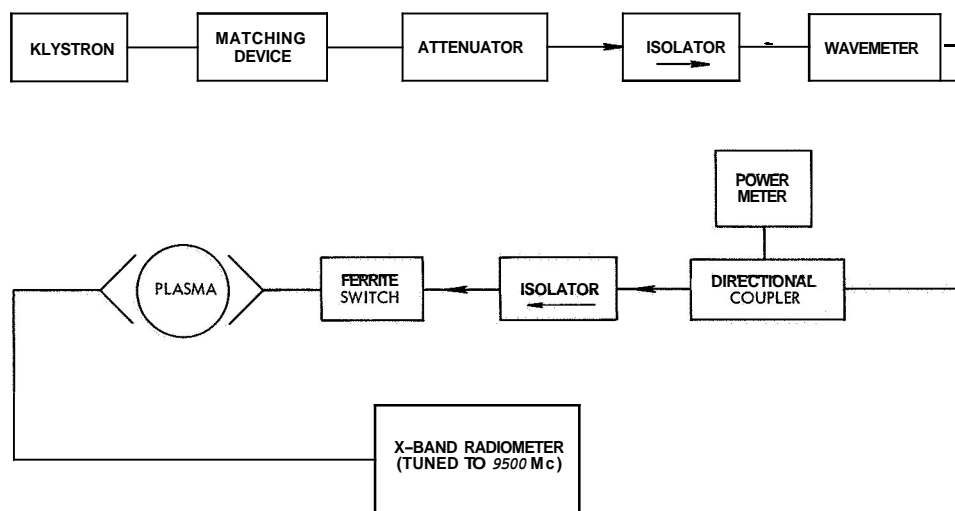


Fig. XI-10. Diagram of the experimental apparatus.

(XI. PLASMA PHYSICS)

interpreted as cyclotron radiation, nor could it be associated with the resonance at the upper hybrid frequency, $\omega = \sqrt{\omega_c^2 + \omega_p^2}$. The frequency values 200-400 Mc were reasonable values, however, for an assumed plasma frequency.

The radiometer detected microwave radiation at $f_o = 9500$ Mc coming from the plasma whenever all of the following conditions were satisfied.

1. Microwave radiation at frequency f_{inc} was incident on the plasma.
2. A disturbance at frequency f_{fluc} existed in the plasma, this signal being picked up by the RF probe and displayed on a spectrum analyzer.
3. The relation $f_o = f_{inc} \pm f_{fluc}$ was satisfied.

The frequency of the incident microwave radiation was varied, keeping the power constant, and the radiometer output was plotted against $\Delta f = f_o - f_{inc}$. The results from two separate data runs are shown in Fig. XI-11 by the dashed and solid lines. Also shown in Fig. XI-11 is the direct display on the spectrum analyzer of the fluctuation signal as seen by the RF probe.

The following comments should be made regarding Fig. XI-11.

1. The multiple peaks in the spectrum-analyzer display of the signal picked up by the RF probe were found to be instrumental. This fine structure resulted from standing waves in the coaxial cable connecting the RF probe to the spectrum analyzer. Considerable fine structure was also seen in the scattering data with somewhat different experimental parameters, and an effort will be made to determine whether this is also instrumental or if it can be related to standing waves in the plasma resulting from the finite geometry.
2. The base line for the scattering peaks falls well below zero. This is an instrumental effect caused by radiation at 9500 Mc in the wings of the incident klystron signal leaking through the ferrite switch and being detected by the radiometer. This effect was later corrected by placing a transmission cavity tuned to the incident frequency in the line between the klystron and the ferrite switch.
3. The scattering data indicated by the dashed line were taken approximately one hour after the data indicated by the solid line. The change in amplitude of the scattered signal may be associated with a drift in the experimental pressure or with a change in the emission from the electron gun.

It was observed that the noise signal from the plasma and the scattering effect disappeared suddenly when the gas pressure exceeded a critical value of $\approx 10^{-4}$ mm Hg.

Although no measurements of electron density and temperature were made for the plasma because of the poisoning of the cathode, the Langmuir probe was moved through the electron beam to determine its cross section when no gas was present. The beam current and voltage were also measured, and the electron density of the beam was calculated from the relation $i = N_b e v A$. This gave $N_b = 1.4 \times 10^8$ electrons/cm³. If the

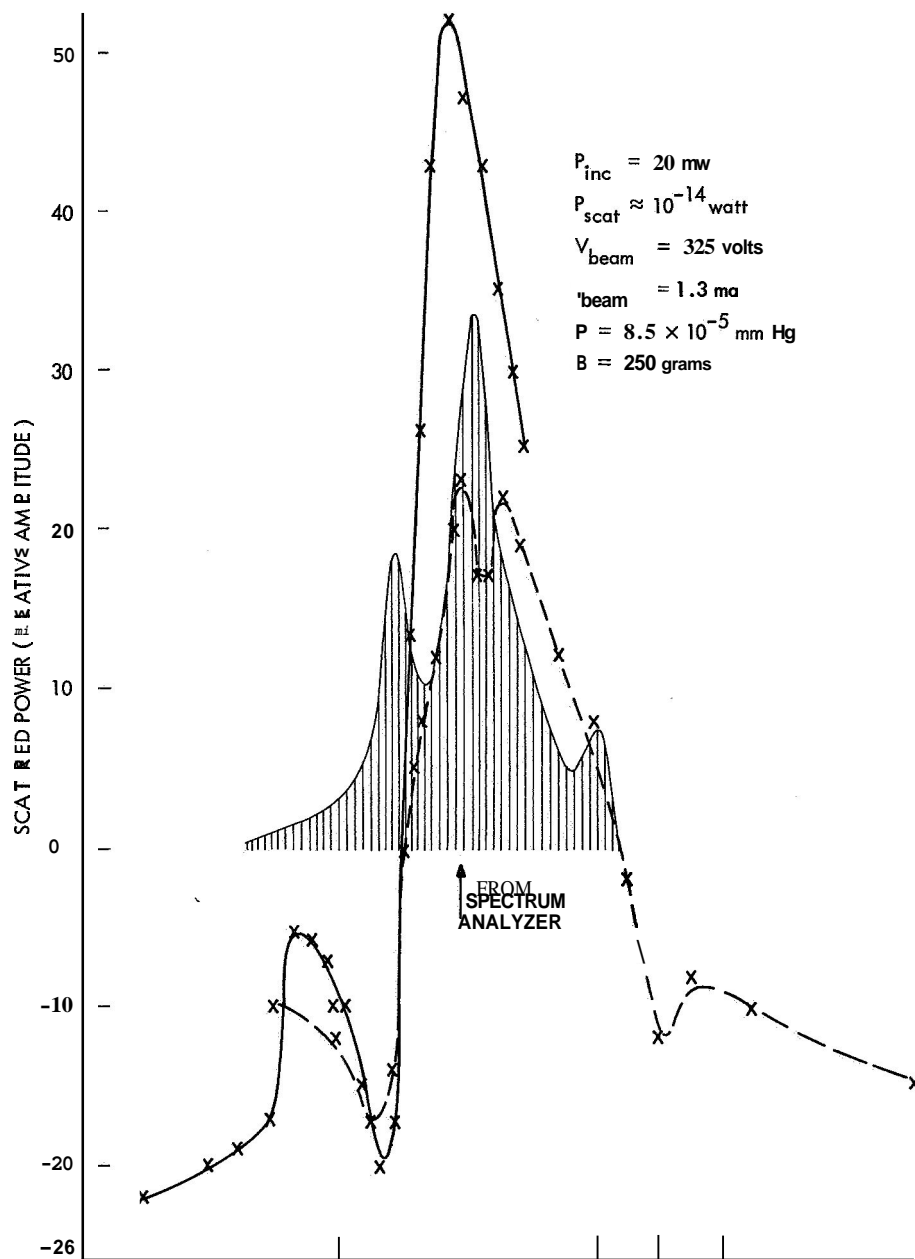


Fig. XI-11. Scattered microwave power and RF probe power vs frequency.

(XI. PLASMA PHYSICS)

total electron density (plasma plus beam) were $\approx 1.1 \times 10^9$ electrons/cm³ when argon gas at a pressure of 8.5×10^{-5} mm Hg was present, the plasma frequency would be 330 Mc/sec, equal to the frequency of the observed signal.

Since quantitative measurements were not made, comments regarding the nature of the disturbance in the plasma from which the scattering occurred can only be speculative. The observations above suggest, however, the possibility that the scattering was from electron density fluctuations associated with a longitudinal plasma wave, which was unstable because of a coupling with the electron beam, the instability becoming quenched when damping caused by electron neutral collisions became too high.

R. L. Kronquist

References

1. J. A. Fejer, Can. J. Phys. **38**, 1114-1133 (1960).
2. S. Ichimaru, Ann. Phys. (N.Y.) **20**, 78-118 (1962).
3. E. E. Salpeter, Phys. Rev. **120**, 1528-1535 (1960).
4. K. L. Bowles, Phys. Rev. Letters **1**, 454 (1958).
5. V. Arunasalam and S. C. Brown, Phys. Rev. **140**, A471 (1965).

E. BUBBLE WINDOWS FOR FAR INFRARED RADIATION

Plasma tubes used in far infrared experiments ($0.1 \text{ mm} < A < 1.0 \text{ mm}$) are usually equipped with crystal quartz windows, because of the high transmission of crystal quartz in this spectral region.¹ Since radiant energy is at a premium at far infrared wavelengths, this advantage of crystal quartz usually outweighs such a disadvantage as not being able to fuse the windows onto the plasma tube envelope. (They are usually mounted with rubber O-ring type assemblies.) Fused quartz does not have this disadvantage, but its transmission is significantly lower than that of crystal quartz.¹ Another consideration is important, however, in comparing these two materials. It has been shown by Filippov and Yaroslavskii² that the transmission of crystal quartz changes with temperature, whereas that of fused quartz does not. For example, at 150- μ wavelength, the transmission of a plate of crystal quartz, 2 mm thick, changes from ~ 75 to $\sim 71\%$ for a temperature change from 300°K to 350°K. This represents more than a 5% decrease in transmission. The transmission of an equally thick plate of fused quartz remains constant at $\sim 25\%$ for the same temperature change. The temperature dependence of crystal-quartz transmission may be a significant disadvantage in some experiments. For example, in an emission or propagation experiment in which the plasma heats the windows and the far infrared power level measured with the plasma on is compared with the level measured with the plasma off. Of course, changes in

window transmission become increasingly important, the more passes the radiation makes through the windows.

In experiments in which the temperature dependence of crystal-quartz transmission is important, fused-quartz windows should be used in spite of their lower transmission. To overcome the disadvantage of the lower transmission, the windows must be **as** thin as possible; however, relatively large windows are usually necessary, since energy considerations usually require far infrared beams of large area. Thus a large, thin window must form part of the wall of the evacuated plasma chamber. Such a window, if it is flat, would collapse under atmospheric pressure unless supported internally, possibly by a metallic grid of some kind. An alternative is a thin-walled quartz bubble blown inward (convex toward the low-pressure region), so that it is always under tension when subjected to the large pressure differential. If properly constructed, such a window can be self-supporting and extremely thin (a few thousandths of an inch thick), and may have far infrared transmission coefficients comparable to **or** larger than those of typical crystal-quartz windows. Such a bubble window is similar to those sometimes used on nuclear counters.

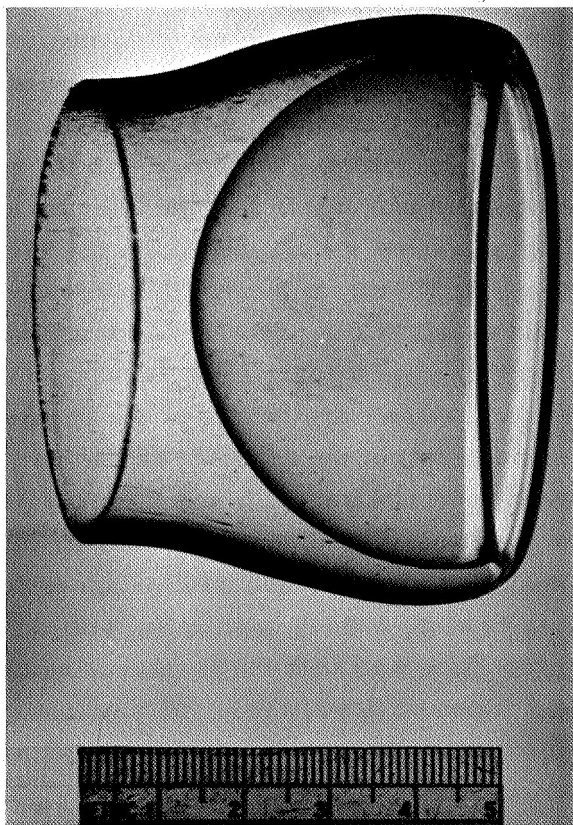


Fig. XI-12. Photograph of the bubble window.

(XI. PLASMA PHYSICS)

Figure XI-12 shows a bubble window that has been constructed.³ The diameter of the bubble opening is 5.8 cm. The bubble is approximately 0.0045 inch thick in the region that would be traversed by a 5-cm diameter beam (the beam size for which the bubble was constructed), varying from -0.00425 inch in a few regions near the center to -0.006 inch in some regions, particularly near its periphery. The ability of this window to withstand atmospheric pressure when evacuated has been tested and verified.

The imperfections visible in the photograph are, for the most part, on the quartz wall surrounding the bubble rather than on the bubble itself. On the bubble, however, there are "draw lines" characteristic of drawn quartz and some small but visible bubbles and inclusions. The image distortions produced by these imperfections should be of little consequence in most plasma emission or absorption experiments.

The far infrared transmission of this window has been measured from wave number ($\nu \equiv 1/\lambda$) $\nu \approx 3 \text{ cm}^{-1}$ ($\lambda \approx 3.33 \text{ mm}$) to $\nu \approx 55 \text{ cm}^{-1}$ ($\lambda \approx 182 \mu$) by using a far infrared Michelson interferometer.⁴ Some results of these measurements are shown in Fig. XI-13, in which the three curves correspond to three different positions of the window in the interferometer. The rapid fluctuations are due to such effects as instrumental noise and are unrelated to window properties. Each of the curves represents the ratio of two spectra, one obtained with the window in the optical path of the instrument (numerator), the other with the window removed (denominator). In all cases an aperture of 4-cm diameter was kept fixed, close to the window location, in order to define a beam and to eliminate any effects that the outer edges or walls of the window might have on the transmitted radiation. Curves a and b correspond to a window location between the beam splitter and detector of the interferometer (the window was ≈ 13 inches from the detector). Curve a corresponds to the beam 'coming out' through the window, (left to right in Fig. XI-12), and curve b corresponds to the beam 'going in' through the window (right to left in Fig. XI-12). As might be expected, there is no apparent difference between these two transmission curves. Curve c corresponds to a window position between the mercury arc source of the interferometer and the beam splitter with the beam 'coming out' of the window, as for curve a. In all cases the transmission varies between approximately 70% and 90%.

All three curves show the channel spectrum produced by interference of internally reflected radiation. The spacing of maxima and minima agree reasonably well with what would be expected for a quartz slab, 0.0045 inch thick, with a refractive index of 1.95. This refractive index agrees quite well with the measured value for fused quartz.⁵ It was found that for thicker windows (~ 0.010 inch) of similar over-all dimensions the channel spectrum tends to disappear, with the transmission remaining fairly flat at $\sim 80\%$. This value is approximately the same as the average value of the transmission curves (Fig. XI-13) of the thinner window; this suggests that transmission losses are due primarily to reflection rather than absorption.

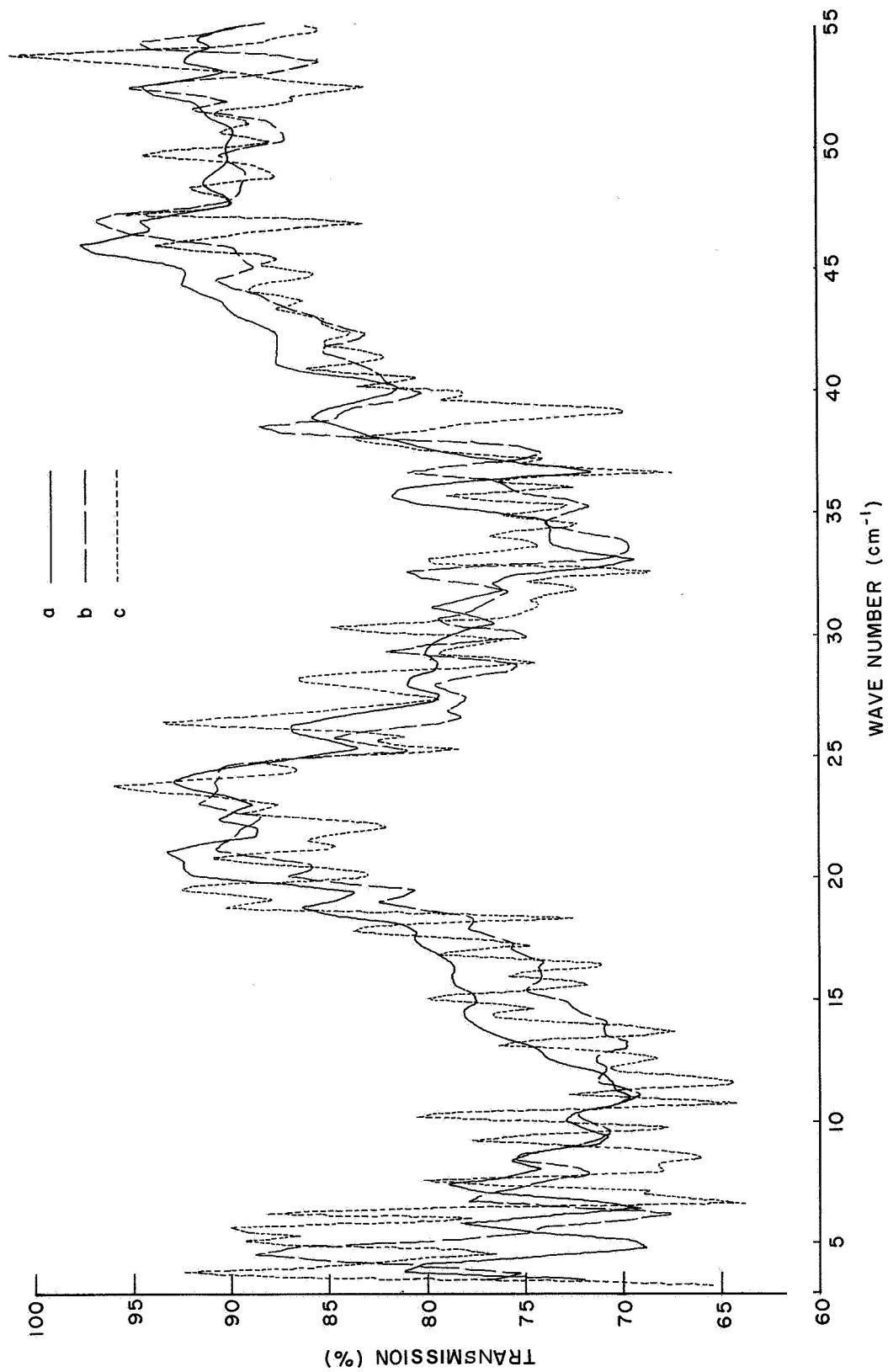


Fig. XI-13. Transmission spectra of the bubble window.

A window of this type might be expected to act as a negative meniscus lens, a diverging lens (thinner at the center than at the edges) with the centers of curvature of both surfaces located on the same side of the lens. Any beam divergence, or "lens effect," should appear as a decrease in transmission when the window is moved farther from the detector. Curve c shows the transmission of the window when it is located almost three times farther from the detector than for curves a and b. No lens effect is apparent in these measurements. A lens effect is not observed because the window, although it has significant curvature, is extremely thin and its thickness is reasonably uniform over the region traversed by the beam.

The effect of the window in phase-shift measurements (e. g. , window in one arm of the interferometer) has not been checked. Any such effect is of no consequence for the present intended application of the window, which involves only its power-transmission properties.

The effect of the window on an arbitrary ray is not very different from that of a flat slab of the same thickness, since the surface normal at the point of incidence on one surface is almost parallel to the normal at the point of emergence from the other surface. Consequently, the effect of the window is to shift the ray laterally because of its finite thickness, and to give the emerging ray only a slight angular displacement with respect to the incident ray. Clearly, both of these effects are small; however, since the angular displacement, unlike the lateral displacement, causes a point along the ray to deviate from its original position (i.e. , with no window present) increasingly as the

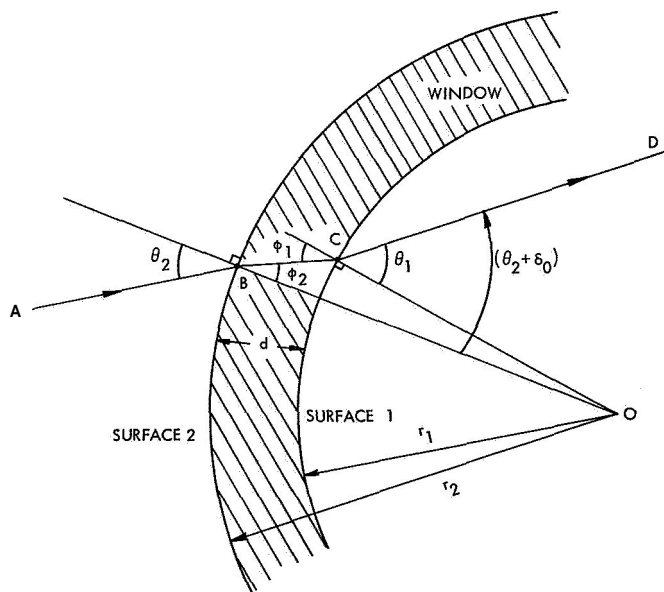


Fig. XI-14. Geometrical construction for calculating ray divergence.

distance from the window increases, an estimate of the magnitude of this effect would be valuable.

In Fig. XI-14 ABCD is an arbitrary ray, and the shaded region represents the window. Its thickness, d , is small compared with the radii of curvature (r_1, r_2 ; $r_1 < r_2$) of its surfaces, which are assumed to be spherical and concentric. θ_2 and θ_1 are the (external) angles of incidence and emergence, respectively; ϕ_2 and ϕ_1 are the (internal) angles of refraction and incidence at surfaces 2 and 1, respectively. It can be shown quite easily that the angle δ_o between the outgoing ray (CD) and the incident ray (AB) is given by

$$\delta_o \approx \frac{d}{r_1} (\tan \theta_2 - \tan \phi_1). \quad (1)$$

For a ray traveling in the reverse direction (DCBA) the angular deviation measured with respect to surface normal CO is

$$\delta_i \approx -\frac{d}{r_2} (\tan \theta_1 - \tan \phi_1). \quad (2)$$

Since in both cases $\theta_{1,2} > \phi_{1,2}$, δ_o is always positive, and δ_i is always negative, thereby indicating that for a ray incident on the outer surface (δ_o) the emerging ray deviates away from the direction of the surface normal, and for a ray incident on the inner surface (δ_i) the ray deviates toward the direction of the surface normal. The magnitudes of the angular deviation are approximately equal in both cases. This means, for example, that a bundle of rays initially parallel to the window axis would diverge if incident on the window from either side, as expected.⁶ From Eq. 1, we find that for a window refractive index of 1.95, $d = 0.005$ inch, $r_1 = 1$ inch, and $\theta_2 = 60^\circ$, we get $\delta_o \approx 6.2$ mrad; this implies that a parallel beam initially of 5-cm diameter will diverge to a diameter of only -6.24 cm at a distance of one meter beyond the window.

Reflection losses from the curved window become significant only near its periphery where the incoming light rays have large angles of incidence. Figure XI-15 shows the reflectance for a dielectric material with a refractive index of 1.95 as a function of angle of incidence. These reflectances were calculated by means of the Fresnel reflection formulas for an air-dielectric interface. ρ_\perp and ρ_\parallel are the reflectances for radiation polarized perpendicular to and parallel to the plane of incidence, respectively. $\bar{\rho}$ is their average value, which is characteristic of unpolarized light. $\bar{\rho}$ is also characteristic of a polarized beam that is uniform both in intensity and polarization over an annulus on the window given by a fixed value of θ . In this case, $\bar{\rho}$ represents the average reflectance of the annulus.

Figure XI-15 also gives the internal reflection loss at the second dielectric-air interface of θ is identified with the angle of refraction at that surface (i.e., the angle between

(XI. PLASMA PHYSICS)

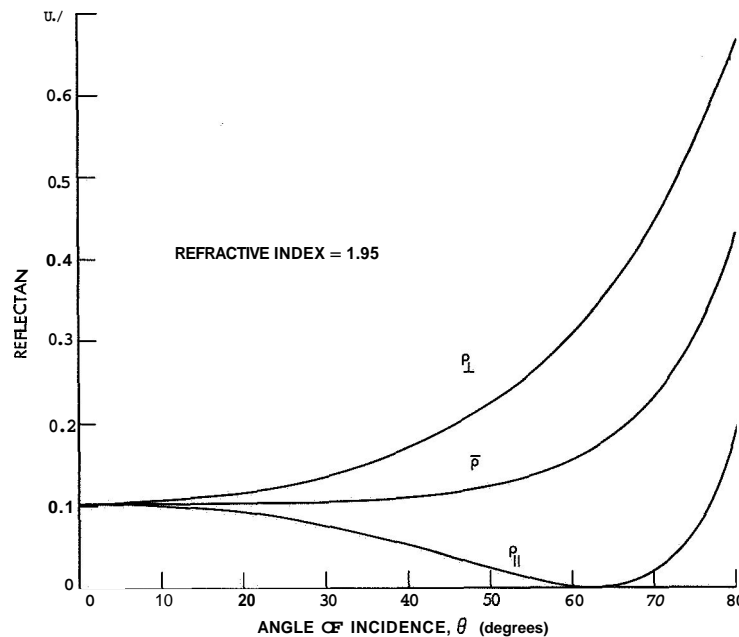


Fig. XI-15. Calculated reflectance of the fused-quartz surface.

the outgoing ray and surface normal). Because the window is very thin, this angle is approximately equal to the angle of incidence at the first boundary; this indicates that the percentage power loss by reflection is approximately the same at both boundaries.

The reflection loss remains fairly constant at small angles and does not become significant until $\theta > 60^\circ$ (at $\theta \approx 60^\circ$, $\bar{\rho} \approx 15\%$). For the window shown in Fig. XI-12 all rays in a 5 cm diameter beam of parallel light have angles of incidence $\theta \leq 60^\circ$. In connection with the reflection effects of the window it should be noted that the curvature of the window causes most of the reflected radiation to be directed out of the beam rather than back into the beam. This can be a definite advantage in some experimental situations.

The transmission measurements discussed in this report were made with the generous assistance of D. T. Llewellyn-Jones, both in the operation of his interferometer and in the processing of the data.

G. L. Rogoff

Footnotes and References

1. T. K. McCubbin, Jr., and W. M. Sinton, J. Opt. Soc. Am. **40**, 537 (1950).
2. O. K. Filippov and N. G. Yaroslavskii, Opt. Spectry. (USSR) **15**, 299 (1963).
3. This bubble window was constructed by G. B. Finkenbeiner of G. Finkenbeiner, Inc., 23 Alaska Avenue, Bedford, Massachusetts. The material used was "Vitreosil" (trade name) obtained from Thermal American Fused Quartz Co., Route 202 and Change Bridge Road, Montville, New Jersey.
4. D. T. Llewellyn-Jones, Quarterly Progress Report No. **74**, Research Laboratory of Electronics, M. I. T., July 15, 1964, pp. 81-89.

5. R. Geick, *Z. Physik*, 161, 116 (1961).
6. Although the sign of δ is different for the two directions of propagation of a given ray, the position of the surface normal to which δ is referred changes from, say, above the emergent ray for one direction of propagation to below the emergent ray for the other direction of propagation. Thus the emergent ray in both cases diverges from the window axis.

XII. GASEOUS ELECTRONICS*

Academic and Research Staff

Prof. S. C. Brown
Prof. W. P. Allis

Prof. J. C. Ingraham
J. J. McCarthy

W. J. Mulligan
A. E. Novenski

Graduate Students

A. J. Cohen
G. A. Garosi

J. E. McClintock
L. D. Pleasance

T. T. Wilheit, Jr.
B. L. Wright

A. LOW-FREQUENCY OSCILLATIONS IN AN ELECTRON-CYCLOTRON RESONANCE DISCHARGE

An experiment has been initiated to study the low-frequency plasma waves that are excited in a volume of plasma produced by microwave breakdown at the electron-cyclotron frequency. The experiment will be described and preliminary results quoted.

The plasma is contained in a cylindrical quartz tube of 1.3-cm inner diameter which is aligned parallel to a DC magnetic field. The tube is also inserted through the center of the broad face of a rectangular 1 X 2 in. brass waveguide so that the tube axis is at an angle of 5.7° relative to the waveguide axis. During the experiment the tube is filled with helium gas at pressures of 0.005-0.100 Torr and a microwave signal of approximately 1 watt power and 6000-Mc frequency is transmitted through the plasma. For values of the magnetic field sufficiently close to the electron-cyclotron resonance value a plasma is produced in the volume of gas within the waveguide. The resultant electron density is estimated to be between 10^{10} and 10^{11} cm⁻³, and the electron temperature to be between 1 and 10 eV.

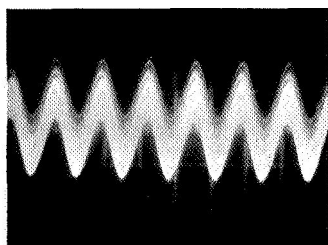
The magnetic field is varied manually across the range of values (AB-100 gauss) for which a plasma can be produced, and the amplitudes of the microwave power transmitted through and reflected from the plasma are monitored on an oscilloscope. For several smaller ranges of values of the magnetic field (AB-2 gauss) within the 100-gauss range of magnetic-field values, the microwave amplitudes are modulated at definite frequencies from 30 kc to 1000 kc, thereby indicating the presence of a low-frequency wave in the plasma. In some cases more than one modulation frequency is present at the same time. In between the magnetic field values at which the microwave signal is modulated at well-defined frequencies the modulation is still present but it is not possible to define a definite frequency (or frequencies) of oscillation. Figure XII-1 shows photographs of typical amplitude modulations of the transmitted microwave signal as displayed on the oscilloscope.

Figure XII-2 displays typical data taken for a fixed microwave power (1.22 watts)

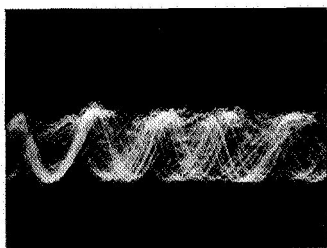
*This work was supported by the Joint Services Electronics Programs (U. S. Army, U. S. Navy, and U. S. Air Force) under Contract DA 36-039-AMC-03200(E).

(XII. GASEOUS ELECTRONICS)

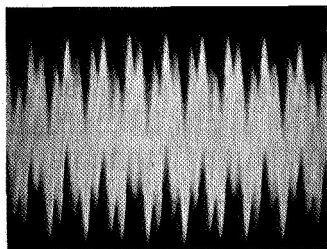
and frequency (6025 Mc). Electron-cyclotron resonance is indicated by a vertical line at the appropriate magnetic field and the ion-cyclotron frequency is plotted as a linearly increasing function of magnetic field.



(a)



(b)



(c)

Fig. XII-1.

(a) 715-kc oscillation for 6025-Mc excitation, $p = 0.05$ Torr, time-scale $2 \mu\text{sec/division}$.
(b) 100-kc signal for 6025-Mc excitation, $p = 0.015$ Torr, time-scale $5 \mu\text{sec/division}$.
(c) 100-kc and 675-kc signals for 6025-Mc excitation, time-scale $10 \mu\text{sec/division}$.

The oscillation frequencies occur below the ion-cyclotron frequency. At higher pressures only the higher frequency oscillations occur. The 667-kc and 500-kc frequencies recurred most often throughout the experiments.

Fluctuations in the light emitted from the plasma, as a function of position along the length of the plasma, were observed by using a photomultiplier and fiber optic light guide that made it possible to view the plasma light emitted through a longitudinal slit cut along the middle of the broad waveguide face. No variation of the light signal amplitude along the plasma length was observed which indicated the absence of standing waves parallel to the tube axis having wavelengths shorter than twice the tube length.

Further measurements of the relative phase of light emitted from two different points along the tube length or from two different points around the tube circumference are planned. Measurements of this kind are necessary before a meaningful analysis of the nature of these waves can be made. Furthermore, it must be determined whether the

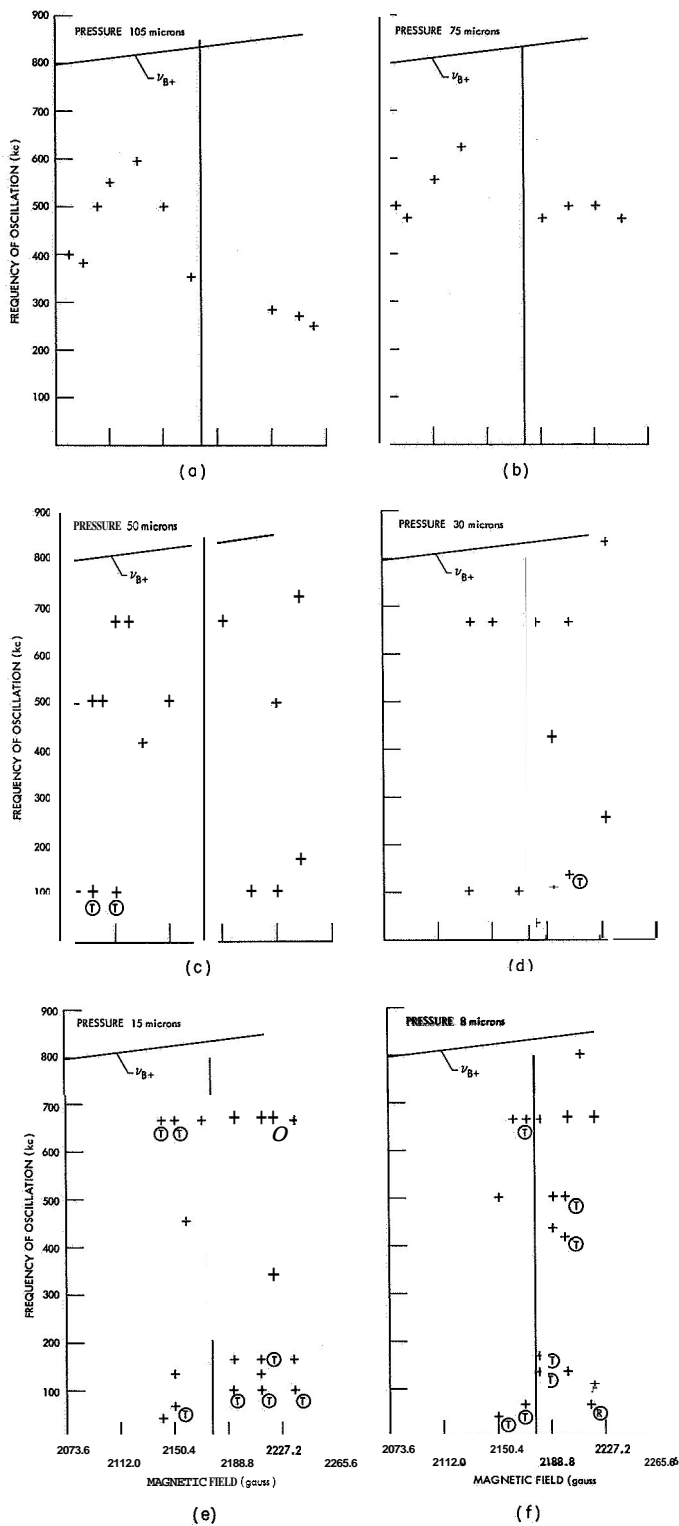


Fig. XII-2.

A display of typical data at six different helium pressures, klystron frequency 6025 Mc, and klystron power 1.22 watt. The graphs show the frequency of oscillation and the magnetic field at which it was observed. The magnetic field corresponding to electron-cyclotron resonance is indicated by a vertical line, and the frequency corresponding to ion-cyclotron frequency is labeled ν_{B+} . The symbols " \oplus " or " \otimes " adjacent to data points indicate that the frequency was observed only in the transmitted microwave signal or in the reflected microwave signal.

(XII. GASEOUS ELECTRONICS)

strong coupling of the microwave ionizing energy to the plasma alters the dispersion relation of these waves from what it would be in a similar plasma but with the microwave power absent.

We shall now calculate some typical frequencies for plasma waves that could propagate within the plasma column. If the electron temperature is $10^5 \text{ }^\circ\text{K}$, an ion-acoustic wave propagating parallel to the magnetic field with 60-cm wavelength (twice the plasma length) will have a 30-kc frequency corresponding roughly to the lowest observed frequencies. For this same plasma the low-frequency ion-cyclotron wave¹ propagating at an angle θ with respect to the magnetic field has a frequency equal to the ion-cyclotron frequency reduced by the factor $\cos \theta$, and is nearly independent of the wavelength (provided the wavelength is less than the circumference of the plasma tube under the present conditions). This wave would have frequencies within the range of the experimental data. Finally, the electrostatic drift wave,² driven by the electron density gradient perpendicular to the magnetic field, has a frequency given by

$$f = -\frac{1}{2\pi} \frac{kT_e}{eB} \left(\frac{1}{n_o} \frac{\partial n_o}{\partial r} \right) \frac{2\pi}{\lambda_{\perp}}.$$

If we take $T_e = 10^5 \text{ }^\circ\text{K}$, $\frac{1}{n_o} \frac{\partial n_o}{\partial r} = -\frac{2.4}{R}$, $\lambda = 2\pi R$, $B \approx 2000 \text{ gauss}$, and $R = 0.65 \times 10^{-2} \text{ meter}$, we obtain $f \approx 400 \text{ kc}$, which also falls within the limits of the observed frequencies.

J. C. Ingraham, A. E. Novenski

References

1. T. E. Stringer, "Plasma Physics," J. Nucl. Eng. Part C 5, 89 (1963).
2. F. F. Chen, Phys. Fluids 8, 912 (1965).

XIII. PLASMAS AND CONTROLLED NUCLEAR FUSION

A. Active Plasma Systems*

Academic and Research Staff

Prof. A. Bers
Prof. G. D. Bernard

Prof. W. D. Getty

Prof. J. G. Siambis
Prof. J. Taillet

Graduate Students

R. R. Bartsch
S. R. J. Brueck
J. A. Davis
F. N. Herba

B. R. Kusse
M. A. Lieberman
J. A. Mangano
R. R. Parker

D. M. Perozek
R. D. Reilly
H. M. Schneider
R. N. Wallace

1. SYSTEM C: ION-CYCLOTRON WAVE GENERATION

We have continued to study generation and propagation of waves in System C near the ion-cyclotron frequency. Since the last report, we have installed a coil in the center of

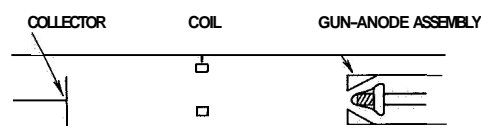


Fig. XIII-1. Illustrating coil position.

the system, midway between anode and collector (see Fig. XIII-1). The coil consists of 9 turns of No. 16 wire insulated by ceramic tubing and supported by stainless-steel wires arranged in such a way as to minimize electrostatic coupling. We are now investigating ion-cyclotron wave generation by the coil and comparing its efficiency of

wave generation with that by concentric electrodes.' In this report we discuss a theory of wave generation by the coil and compare it with preliminary experimental results.

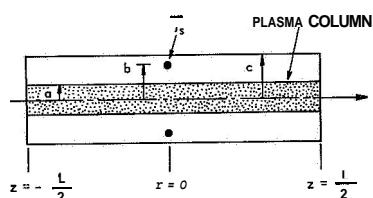


Fig. XIII-2. Illustrating the problem.

Theoretical Discussion

We consider a uniform column of plasma of length L and radius a , surrounded by a perfectly conducting cylinder of radius c , and driven by a circular current filament of radius b . (See Fig. XIII-2). We denote by z the distance from the coil, and assume perfect electric shorts at $z = \pm \frac{L}{2}$. We

assume that the dynamics of the plasma can be accounted for by a local dielectric tensor, $\overline{K}(\omega)$, of the form

*This work was supported by the National Science Foundation (Grants GK-57 and GK-614).

(XIII. PLASMAS AND CONTROLLED NUCLEAR FUSION)

$$\bar{K} = K_{\perp} \bar{\delta} \hat{t} K_x \hat{i}_z \times \bar{\delta} \hat{t} K_{\parallel} \hat{i}_z \hat{i}_z.$$

The scalars K_{\perp} , K_x , and K_{\parallel} have various forms that depend on the model assumed for the plasma. For example, if one assumes cold, collisionless plasma one has

$$\left. \begin{aligned} K_{\perp 0} &= \frac{\omega_{pi}^2}{\omega_{ci}^2 - \omega^2} + \frac{\omega_{pe}^2}{\omega_{ce}^2 - \omega^2} + 1 \\ K_{x0} &= j \frac{\omega \omega_{pi}^2 / \omega_{ci}}{\omega_{ci}^2 - \omega^2} + j \frac{\omega \omega_{pe}^2 / \omega_{ce}}{\omega_{ce}^2 - \omega^2} \\ K_{\parallel 0} &= -\frac{\omega_{pi}^2}{\omega^2} - \frac{\omega_{pe}^2}{\omega^2} + 1, \end{aligned} \right\} \quad (1)$$

while, for a plasma with ion-electron collisions one has

$$\bar{K}_{\eta} = \left(\bar{K}_0^{-1} + j\omega \epsilon_0 \eta \bar{\delta} \right)^{-1}, \quad (2)$$

where η is the resistivity (assumed to be a scalar). Ion-neutral collisions may be accounted for in a phenomenological way by replacing the ion mass in set (1) by $m_i(1 + u/j\omega)$, where u is the ion-neutral collision frequency for momentum transfer.

The problem is now simply formulated by Maxwell's equations

$$\nabla \times \bar{H} = j\omega \epsilon_0 \bar{K} \cdot \bar{E} + \bar{j}_s \quad (3)$$

$$\nabla \times \bar{E} = -j\omega \mu_0 \bar{H}, \quad (4)$$

where $\bar{j}_s = NI \delta(r-b) \delta(z) \hat{i}_{\theta}$ accounts for the current in the coil. The boundary condition is zero tangential electric field. The boundary conditions at $z = \pm \frac{L}{2}$ may be eliminated by replacing the geometry of Fig. XIII-2 with a cylinder of infinite extent driven by the current source

$$\bar{j}_s' = \sum_{n=-\infty}^{\infty} (-1)^n \bar{j}_s(z-nL).$$

If, then, Eq. 3 (with \bar{j}_s replaced by \bar{j}_s') and Eq. 4 are Fourier-analyzed in the z -direction, we obtain the following equation for the transverse component of the electric field, \bar{E}_T ,

$$\nabla_T \times \nabla_T \times \bar{\mathbf{E}}_T - \nabla_T \frac{1}{K_{\parallel}} \nabla_T \cdot \bar{\mathbf{K}}_T \cdot \bar{\mathbf{E}}_T - k_0^2 \bar{\mathbf{K}}_T \cdot \bar{\mathbf{E}}_T + \beta^2 \bar{\mathbf{E}}_T = -i_{\theta} j \omega \mu_0 N I \times \delta(r-b) \times \sum_{n=-\infty}^{\infty} (-1)^n e^{-jn\beta L}. \quad (5)$$

Here, ∇_T is the transverse part of ∇ , $\bar{\mathbf{K}}_T$ is the transverse part of $\bar{\mathbf{K}}$, and $k_0 = \omega/c$.

A formal solution to Eq. 5 may be obtained by expanding $\bar{\mathbf{E}}_T$ and the right-hand side of Eq. 5 in terms of the eigenvectors of the equation

$$\nabla_T \times \nabla_T \times \bar{\mathbf{e}} - \nabla_T \frac{1}{K_{\parallel}} \nabla_T \cdot \bar{\mathbf{K}}_T \cdot \bar{\mathbf{e}} - k_0^2 \bar{\mathbf{K}}_T \cdot \bar{\mathbf{e}} + k^2 \bar{\mathbf{e}} = 0. \quad (6)$$

To do this we need the eigenvectors of the adjoint equation

$$\nabla_T \times \nabla_T \times \bar{\mathbf{e}} - \bar{\mathbf{K}}_T^{\dagger} \cdot \nabla_T \frac{1}{K^*} \nabla_T \cdot \bar{\mathbf{e}} - k_0^2 \bar{\mathbf{K}}_T^{\dagger} \cdot \bar{\mathbf{e}} + k^2 \bar{\mathbf{e}} = 0, \quad (7)$$

where the symbol $(\)^{\dagger}$ denotes complex-conjugate transpose. The boundary conditions for Eq. 6 are tangential $\bar{\mathbf{e}}$ and $\nabla_T \cdot \bar{\mathbf{K}}_T \cdot \bar{\mathbf{e}}$ equal to zero on the boundary, while boundary conditions for Eq. 7 are tangential $\bar{\mathbf{e}}$ and $\nabla_T \cdot \bar{\mathbf{e}}$ equal to zero on the boundary. In terms of the assumed complete set $\bar{\mathbf{e}}_i$ of solutions to Eq. 6 and the set $\bar{\mathbf{e}}_j$ of solutions to Eq. 7, we may obtain a formal solution to Eq. 5 which, after performing the inverse Fourier transform in the z -direction, becomes

$$\bar{\mathbf{E}}_T = -j\omega\mu_0 N I \sum_i \frac{b \bar{\mathbf{e}}_i^* \cdot \hat{\mathbf{i}}_{\theta} |_{r=b} \bar{\mathbf{e}}_i}{\int_0^c r dr \bar{\mathbf{e}}_i^* \cdot \bar{\mathbf{e}}_i} \cdot \frac{1}{2k_i} \cdot \frac{\sin k_i \left(\frac{L}{2} - |z| \right)}{\cos \frac{k_i L}{2}}, \quad (8)$$

where the k_i are the eigenvalues of Eq. 6. The problem is then completely solved by obtaining the eigenvalues and eigenvectors of (6).

An assumption often made in treating problems of this sort² is that of zero electron mass, which, from the point of view of Eq. 6 removes the term $\nabla_T \frac{1}{K_{\parallel}} \nabla_T \cdot \bar{\mathbf{K}}_T \cdot \bar{\mathbf{e}}$. The resulting solution involves a discontinuity in $\bar{\mathbf{K}}_T \cdot \bar{\mathbf{e}}$, a feature that is inconsistent with the assumption that $\nabla_T \frac{1}{K_{\parallel}} \nabla_T \cdot \bar{\mathbf{K}}_T \cdot \bar{\mathbf{e}}$ is small in comparison with other terms. We are working on other approximate solutions to (6) which have more validity for the conditions of our experiment.

One feature of Eq. 8, which is apparent even without detailed knowledge of $\bar{\mathbf{e}}_i$ and $\bar{\mathbf{e}}_j$, is the possibility of a body resonance slightly below ω_{ci} , where $k_i L \sim \pi$. This suggests the possibility of efficient coupling of energy to the ions by exciting this resonance.

Experimental Results

The frequency dependence of $B_z = \frac{1}{j\omega} \nabla_T \times \bar{\mathbf{E}}_T$ near ω_{ci} has been measured by using

(XIII. PLASMAS AND CONTROLLED NUCLEAR FUSION)

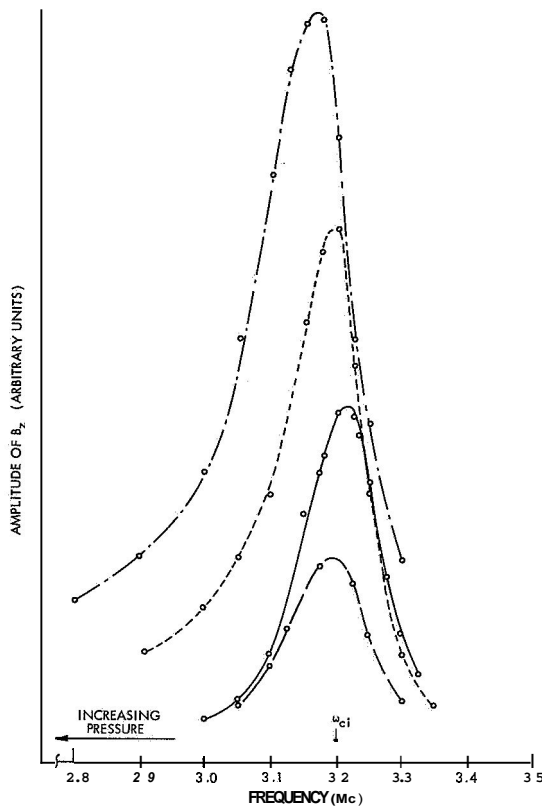


Fig. XIII-3.
Amplitude of B_z versus frequency for four pressures 100 psec after turn-off. The pressures are in the ratio 1:1.3:1.7:3.4.

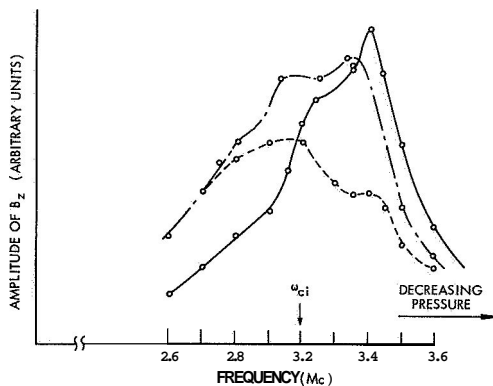


Fig. XIII-4. Amplitude of B_z versus frequency for three pressures at turnoff. The pressures are in the ratio 1:2:3.

a small pickup coil positioned approximately midway between the anode and the driving coil against the wall. Two sets of results are shown in Fig. XIII-3 and XIII-4. The curves of Fig. XIII-3 were obtained with a low-power beam (3 kV and 7 amps) 100 psec after turnoff, and appear to be associated with a resonance of the usual type. The curves of Fig. XIII-4 were obtained with a higher power beam and were taken immediately after turnoff. We believe that the resonance that develops below ω_{ci} for

(XIII. PLASMAS AND CONTROLLED NUCLEAR FUSION)

increasing pressure (and therefore density) may be associated with the body resonance discussed above.

R. R. Parker

References

1. R. R. Parker, Quarterly Progress Report No. 81, Research Laboratory of Electronics, M.I. T., April 15, 1966, pp. 72-75.
2. T. H. Stix, The Theory of Plasma Waves, (McGraw-Hill Book Company, New York, 1962).

2. BEAM-PLASMA DISCHARGE: SYSTEM D

Introduction

During the last quarter studies were made of the plasma density and electron temperature in System D. The results of different methods of density measurements agree reasonably well, although further refinements must be made. The direct measurements of density made thus far are by the methods of fundamental cavity-mode shift, higher order cavity-mode shift, 8-mm Fabry-Perot interferometry, and 4-mm interferometry. The density range covered by these four approaches is 10^9 - 10^{14} cm^{-3} . There are regions of overlap between methods so that a check for consistency is possible.

The density measurements require additional data concerning the density profile. These data are not yet available and consequently there is some spread in the results of the four methods. In the fundamental mode-shift measurement, uncertainty about the exact cavity mode that was used may account for differences between this and the other measurements.

The 4-mm interferometer is used to measure the density during the electron beam pulse (see Sec. XIII-A.3). Under the assumption that the plasma is 10 cm in diameter, a typical average density of 5×10^{12} cm^{-3} is found during the beam pulse. A sharp drop in density occurs in the first few milliseconds after beam turnoff, and the plasma enters a decay period in which the loss rate is determined by electron-neutral scattering. During the decay period the density is tracked by the 8-mm interferometer and the mode-shift technique. These methods, at present, agree within a factor of 5 but it is expected that further refinements will lead to better agreement. The density is typically 10^{11} cm^{-3} at 20 msec after beam turnoff for a hydrogen pressure in the range of 10^{-4} Torr. The plasma consists of a cold-electron component and approximately a 1% hot-electron component during this decay period.

Electron temperature measurements were made by spectrographic methods. The measurements are discussed in detail in Section XIII-A.4. The result of this measurement is that the electrons have an effective temperature of 4-5 electron volts. This is

(XIII. PLASMAS AND CONTROLLED NUCLEAR FUSION)

presumably indicative of the average energy of the cold electrons in the plasma. The measurement was made during the electron beam pulse. The hot-electron component has an average energy of the order of 10 keV, and is evidenced by the generation of x radiation, diamagnetism, and the long decay time of the plasma.

The cold-electron temperature in System C has been measured by the same spectrographic technique (see Sec. XIII-A. 4), and checked by Langmuir probe measurements. The results are in qualitative agreement, and temperatures of 5 to 10 eV are obtained. In both Systems C and D, we find consistency between the temperature, density, and diamagnetism. The diamagnetic signals are almost entirely caused by the hot-electron component.

Gas Injection System

The peak pressure during the gas pulse has been determined for the Asco-valve injection apparatus now in use. A steady gas feed was found to give the same plasma diamagnetism during the beam pulse when the pressure in the system was adjusted to $2-3 \times 10^{-5}$ mm Hg as measured by a Veeco gauge. The true hydrogen pressure is approximately seven times higher than the measured value.¹ The boundary between a weak discharge and an intense discharge as determined by the diamagnetism during the

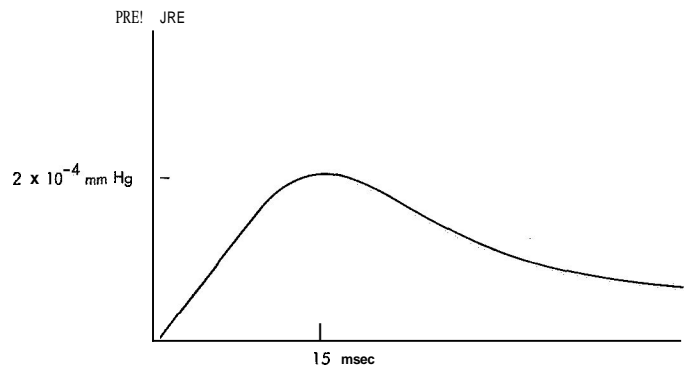


Fig. XIII-5. Asco valve pressure transient for adjustment that gives the longest plasma density decay.

beam pulse was found to be well defined when the steady-flow gas pressure was varied. Figure XIII-5 shows the pressure transient for the Asco-valve system.

Construction has been completed on the Marshall (shock-wave) valve² shown in Fig. XIII-6. Preliminary tests with a nude 6AH6 pressure transient sensor indicate that the Marshall valve is faster than the Asco valve. The pressure transient is shown in Fig. XIII-7. Additional speed will be obtained by removing the beam stop shown in Fig. XIII-8. An electric drive is now under construction.

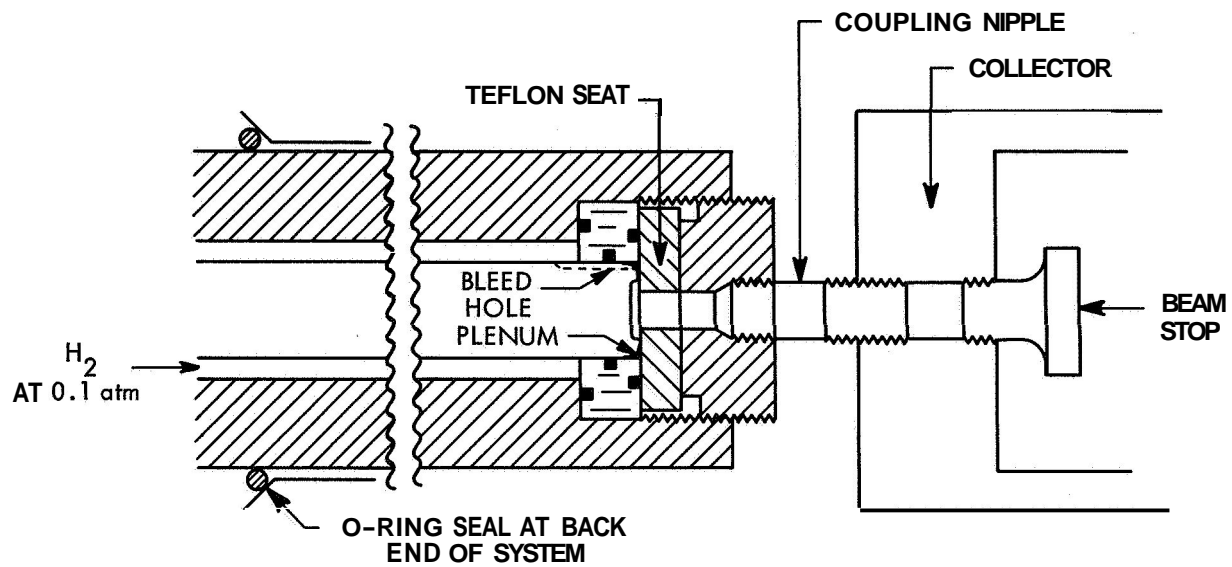


Fig. XIII-6. Marshall valve.

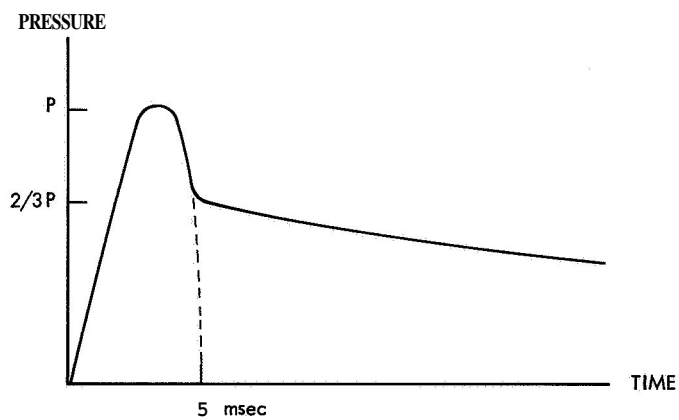


Fig. XIII-7. Marshall valve pressure transient.

Light and Plasma Diamagnetism Measurements

The light transient for a typical discharge is shown in Fig. XIII-8. The peak pressure of the gas pulse for the case shown is 15-50% above the minimum necessary for an intense discharge. The delay between the start of the gas injection and the firing of the electron beam was adjusted so that the beam fired just before the peak of the pressure pulse. The pressure transient is also shown in Fig. XIII-8. The final decay rate of the light signal is observed to be ~ 20 msec, which is the final decay rate observed for the electron density for the pressure transient shown. Since the light output is roughly proportional to the product of electron density and pressure, the light transient can be used to extrapolate the electron density' back to the end of the beam pulse. The resulting density is $\sim 10^{12} \text{ cm}^{-3}$, if the pressure is assumed to be constant.

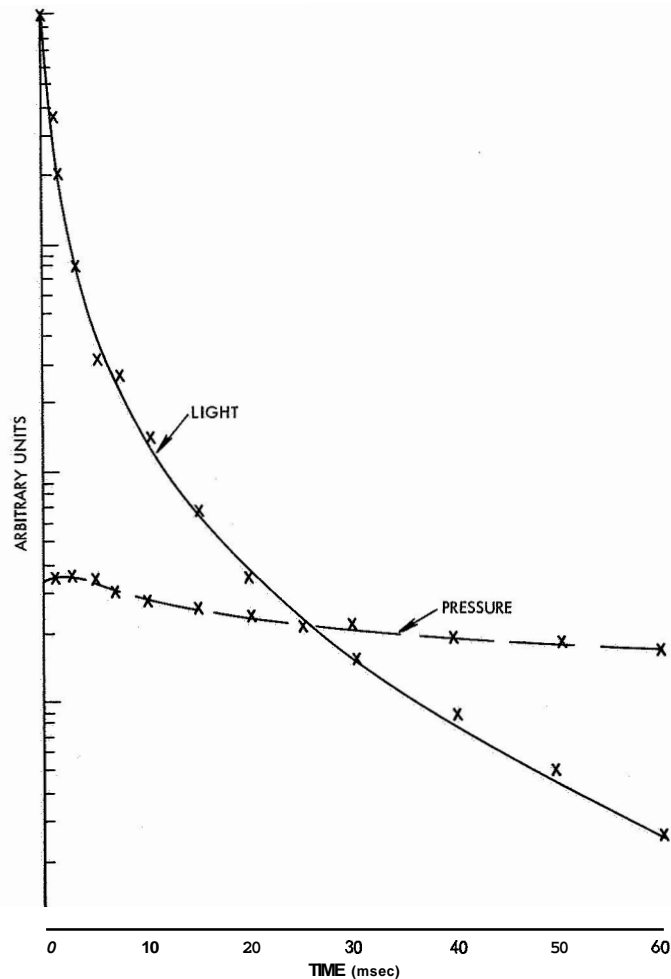


Fig. XIII-8. Light and pressure transient.

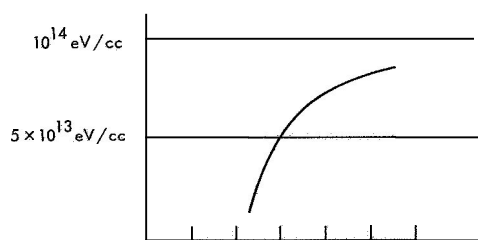


Fig. XIII-9. Perturbation of plasma diamagnetism by a Langmuir probe.

The initial decay time constant of the plasma diamagnetism due to the hot electrons is listed in Table XIII-1.

Table XIII-1, Initial diamagnetic decay time constant as a function of peak pressure.

Peak Pressure	$\tau_{k/e}$
3×10^{-4}	15.6 msec
6×10^{-4}	10.2
2×10^{-3}	4.7
9×10^{-3}	1.55

Langmuir probes used to measure the plasma profile were found to alter the discharge. The amplitude of the plasma diamagnetism as a function of the radial position of a tungsten ball of 0.040 inch diameter is shown in Fig. XIII-9.

Plasma Density Measurements

(i) 8-mm Interferometer Density Measurement

Plasma density measurements have been made up to approximately 10^{12} cm^{-3} with the Fabry-Perot interferometer arrangement shown in Fig. XIII-10. The shift of the

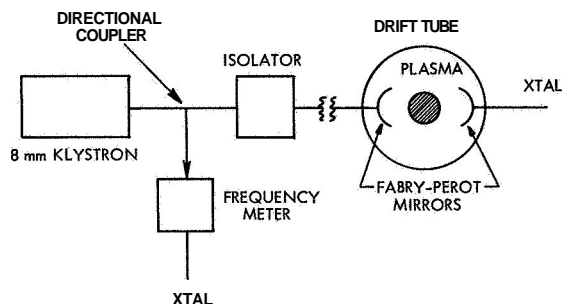


Fig. XIII-10. Fabry-Perot interferometer.

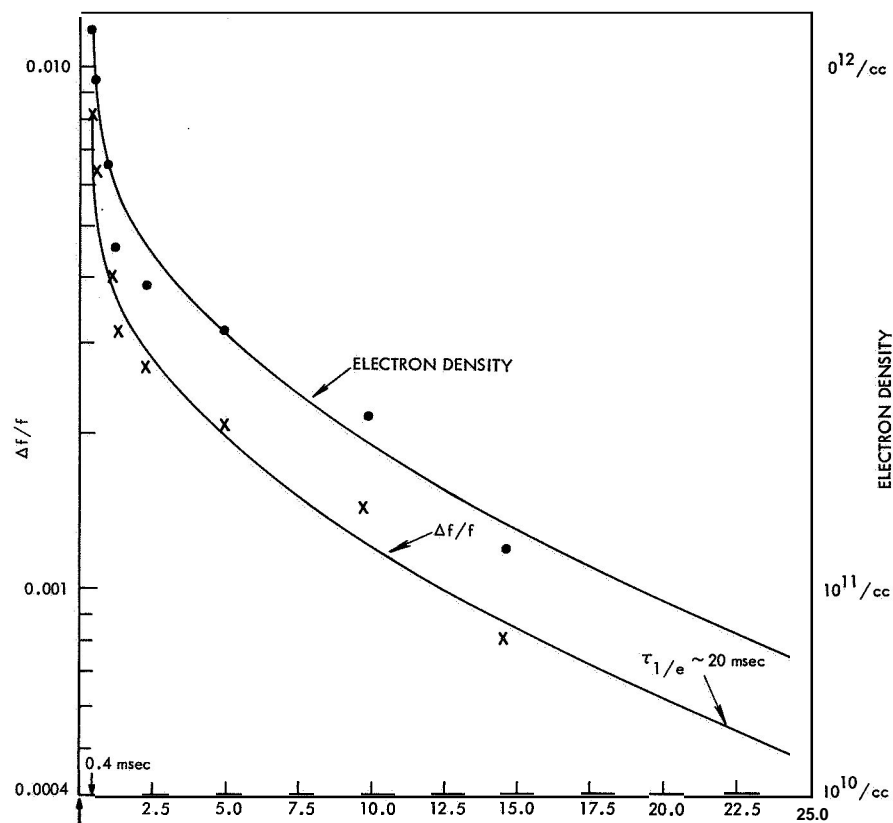


Fig. XIII-11. Fabry-Perot electron density measurement.

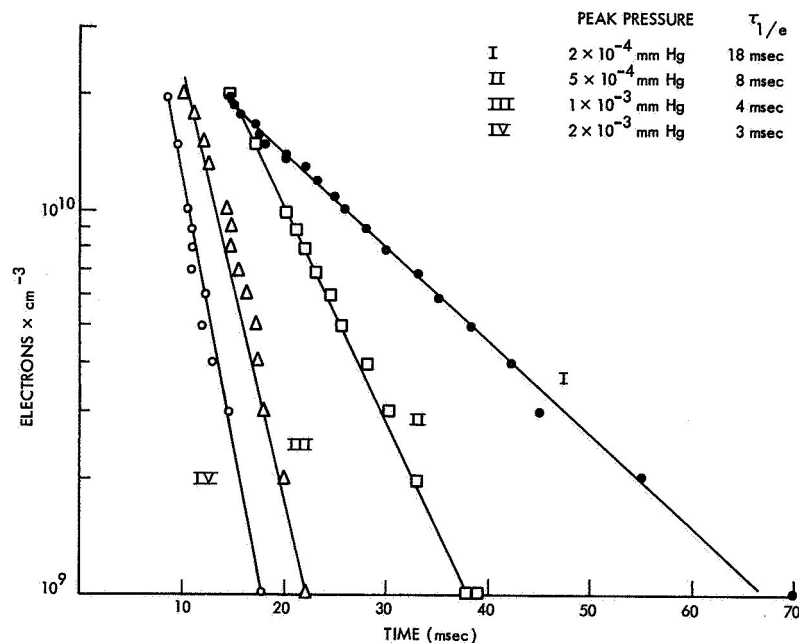


Fig. XIII-12. Density decay as a function of peak pressure.

(XIII. PLASMAS AND CONTROLLED NUCLEAR FUSION)

resonant frequency of the cavity formed by the spherical horns is related to the plasma density by

$$\frac{\Delta f}{f} = \frac{1}{4R} \frac{2 \int_0^{R_p} n_e(r) dr}{(2\pi f)^2} \frac{e^2}{m_e \epsilon_0},$$

where R is the drift-tube radius R_p is the plasma radius, f is the resonant frequency of the Fabry-Perot cavity (31.225 kMc), $n_e(r)$ is the electron density profile, e is the electronic charge, m_e is the electronic mass, the ϵ_0 is the dielectric constant of free space. $\Delta f/f$ is shown in Fig. XIII-11 for a discharge adjusted for long decay ($\tau_{1/e}$ - 20-30 msec). The plasma density shown in Fig. XIII-11 is found from the mode-shift information by assuming that the plasma density is given by

$$n_e(r) = \begin{cases} n_e(0) J_0\left(\frac{2.405 r}{R_p}\right) & 0 \leq r \leq R_p \\ 0 & R \geq r \geq R_p \end{cases}$$

$$R_p = \frac{1}{3} R.$$

(ii) UHF density measurement

UHF mode-shift density measurements have been made in which the cavity was excited with E probes in the end of the system. The density has been tracked back into the discharge to $2 \times 10^{10} \text{ cm}^{-3}$. The density decay as a function of pressure is determined from the pressure measurement discussed above, and is not the same as that assumed previously.³ The results of the measurement are shown in Fig. XIII-12, where the density decay is plotted for several pressures.

The authors wish to acknowledge the use of the facilities of the National Magnet Laboratory for this experiment.

R. R. Bartsch, W. D. Getty

References

1. T. J. Fessenden and M. A. Lieberman, private communication.
2. J. Marshall in Plasma Acceleration, edited by S. W. Kash (Stanford University Press, California, 1960), pp. 61-62.
3. R. R. Bartsch, Quarterly Progress Report No. 81, Research Laboratory of Electronics, M. I. T., April 15, 1966, p. 69.

(XIII. PLASMAS AND CONTROLLED NUCLEAR FUSION)

3. ELECTRON DENSITY MEASUREMENTS FOR BEAM PLASMA SYSTEMS WITH A 4-mm INTERFEROMETER

To obtain accurate electron density information with a minimum of discharge perturbation, a 4-mm microwave interferometer was used on Beam-Plasma Discharge Systems C and D. Such an interferometer measures the propagation constant of the plasma medium which may, under certain conditions, be simply related to the time-variant electron density.

The interferometer circuit (shown in Fig. XIII-13) consists of two microwave signal paths — a plasma path and a reference path. The sum and difference signals from the balanced mixer are each square-law-detected by crystals. The difference between the two detected signals is a measure of the amplitude and phase of the signal transmitted through the plasma. If the interferometer signal frequency is much higher than the plasma frequency, the plasma appears transparent, and there is essentially no amplitude change caused by attenuation in the plasma path. In the absence of a plasma the variable phase shifter in the reference path is adjusted to null the output signal. The output signal during the transient discharge is then proportional to the sine of the phase difference between the two paths and is therefore a measure of the phase constant of the plasma as a function of time.

Since the microwave horns and lenses focus the microwave radiation into a beam whose diameter is approximately 1/3 of the plasma diameter, the cylindrical plasma may be considered as a slab and the problem is reduced to one dimension. The phase constants of the vacuum and plasma are

$$\beta_v = \frac{2\pi}{\lambda} \quad (1)$$

$$\beta_p = \left[1 - \left(\frac{\omega_p}{\omega} \right)^2 \right]^{1/2} \quad \beta_v = \left[1 - \frac{n}{n_c} \right]^{1/2} \beta_v \quad (2)$$

when the microwave electric field is parallel to the static magnetic field, and collision frequency $\nu \ll \omega$. The critical density n_c is given by

$$n_c = m\epsilon_0 \omega^2 / e^2.$$

The phase shift that is due to the presence of the plasma is therefore

$$\Delta\phi = - \int [\beta_p - \beta_v] dx \quad (3)$$

or, in terms of Eqs. 1 and 2,

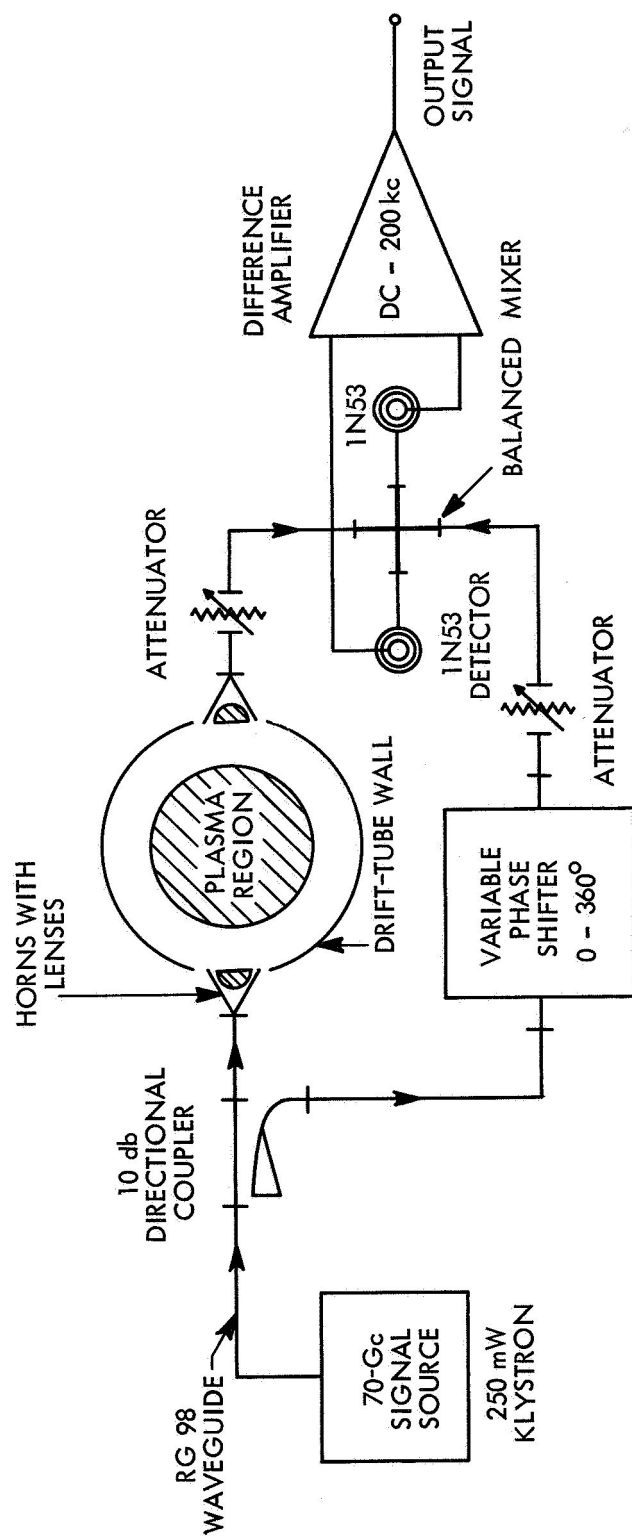


Fig. XIII-13. Four-millimeter interferometer system.

(XIII. PLASMAS AND CONTROLLED NUCLEAR FUSION)

$$\Delta\phi = \int \left\{ 1 - \left[1 - \frac{n(x)}{n_c} \right]^{1/2} \right\} \frac{2\pi}{\lambda} dx \quad (4)$$

which to first order in $n(x)/n_c$ is

$$A+ = \frac{\pi}{\lambda n_c} \int n(x) dx. \quad (5)$$

Hence, the relation between density and phase shift is

$$\int n(x) dx = \frac{\lambda n_c}{\pi} \Delta\phi = \frac{26.0 mc\omega A+}{e^2} \quad (6)$$

Since only the integral of the spatially varying electron density is given explicitly, independent knowledge of the density profile is required for quantitative measurements. A spatially averaged electron density may be obtained, however, by assuming a rectangular profile. For such a rectangular profile the integration of Eq. 6 is trivial, and gives

$$n_{av} = \frac{26.0 mc\omega \Delta\phi}{e^2 L} \quad \text{for } n \ll n_c. \quad (7)$$

In practical units, this equation can be written

$$n_{av} = \frac{2.6 \times 10^{13}}{L} \frac{\Delta\phi}{\pi} \text{ (cm}^{-3}\text{)},$$

where $A+$ is in radians, and L in centimeters. The parameter L is the effective width of the profile and is estimated experimentally by using a Langmuir probe.

Results

Density measurements were made on Beam-Plasma Discharge Systems C and D against system parameters such as axial magnetic field, beam voltage, and pressure. Representative results of these measurements are given in Figs. XIII-14 through XIII-17.

Figure XIII-14 shows the variation with electron beam voltage and axial magnetic field of the value of n_{av} during the beam pulse. It was observed that the integral of the density over the profile, Eq. 6, is nearly independent of the magnetic field; however, Langmuir probe data indicate that the effective width of the profile decreases with increasing field, giving rise to the spread in n_{av} between these curves.

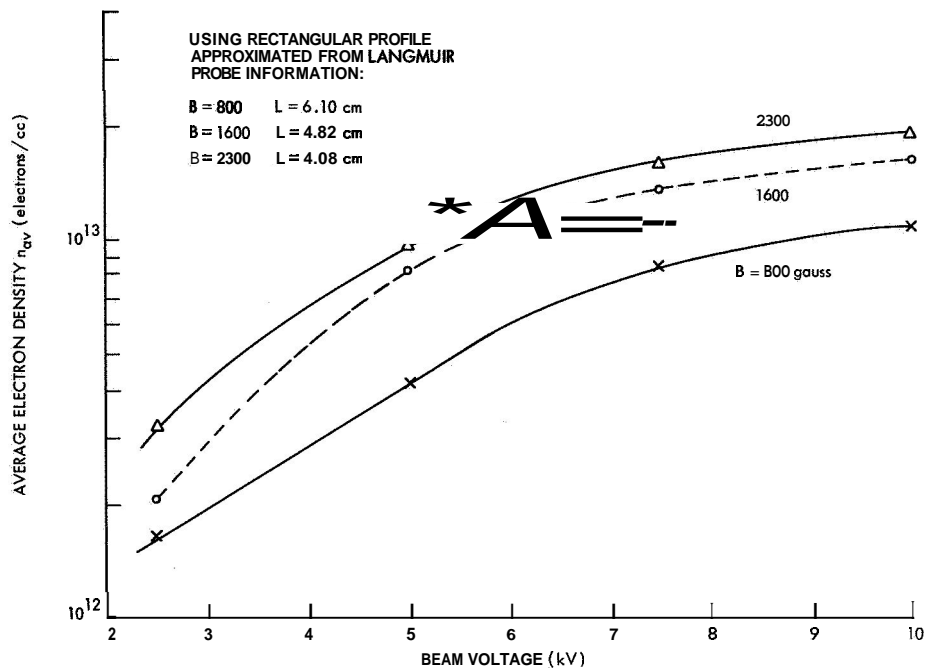


Fig. XIII-14. Average electron density in System C as a function of electron beam voltage for three values of midplane magnetic flux density. Hydrogen pressure for these curves was approximately 2×10^{-4} Torr.

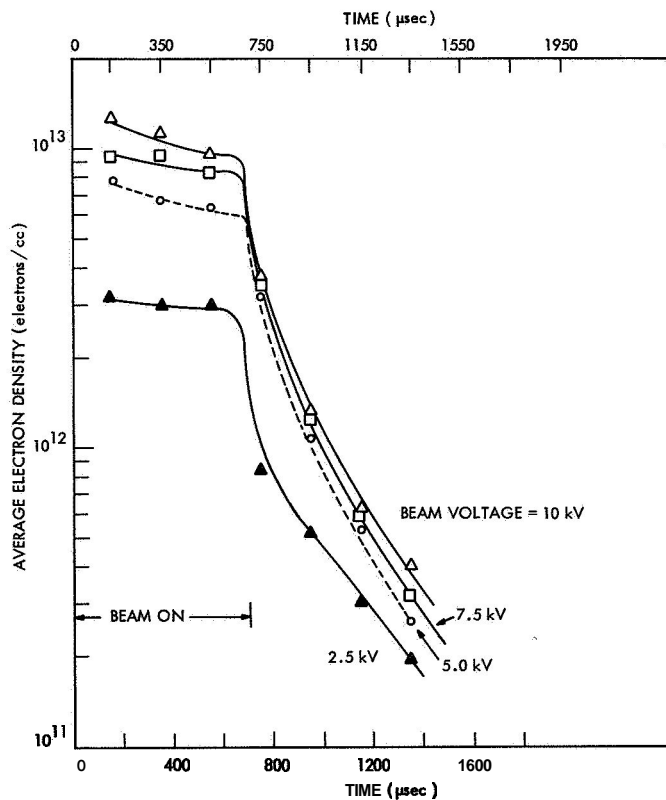


Fig. XIII-15. Density decay in System C for various electron-beam voltages. Hydrogen pressure, 2×10^{-4} Torr; midplane magnetic flux density, 2300 gauss; assumed plasma width, $L = 4.08$ cm.

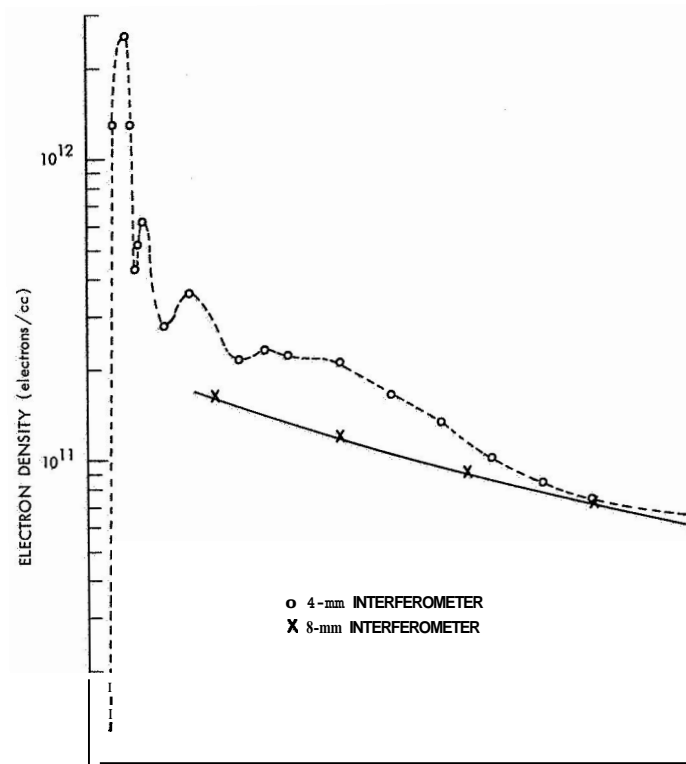


Fig. XIII-16. Density decay in System D. Assumed plasma width, $L = 10$ cm. 8-mm Fabry-Perot interferometer data from Section XIII-A. 2 are shown.

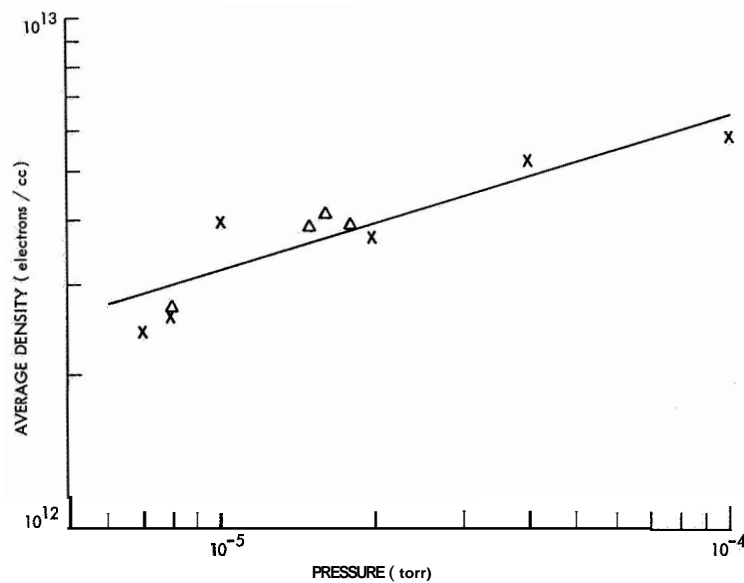


Fig. XIII-17. Variation of average density during beam pulse as a function of gas pressure for System D. Assumed plasma width, $L = 10$ cm.

(XIII. PLASMAS AND CONTROLLED NUCLEAR FUSION)

The density during the beam pulse is nearly constant at low operating pressures, but at higher pressures it may fluctuate considerably. The frequency of the fluctuations may be measured from the interferometer output signal and is of the order of 10-50 kc. The density decays smoothly in the afterglow period that begins at beam turn-off.

The density decay of the plasma was also measured. The sensitivity of the interferometer was sufficiently high to allow the density to be measured for 2 msec in the afterglow of System C and 20 msec in System D. Figures XIII-15 and XIII-16 show the density decay in Systems C and D, respectively. The observed decay rates for both Systems C and D are in agreement with their expected values. For System C, the plasma loss rate is determined by the rate of ion effusion out of the system. This rate is approximately $2\bar{v}_i/l$, where \bar{v}_i is the average ion velocity, and l is the length of the system. The plasma loss rate is determined by the ions in this case because no magnetic mirrors were used to reduce plasma end loss, and the plasma potential was therefore positive. The value of $2\bar{v}_i/l$ for room temperature ions is 250-300 psec; the curves in Fig. XIII-15 exhibit decay times of 350-400 psec. The plasma in System D contains a hot-electron component with an average energy of the order of 10 keV, and is confined by magnetic mirrors. The loss rate is determined by the rate of scattering of the hot electrons into the mirror loss cones. The decay curve of Fig. XIII-16 is typical for System D and indicates that the decay time is approximately 5 msec. This is in qualitative agreement with other measurements and with calculated values of decay time.³ The results of microwave measurements (see Sec. XIII-A. 2) with a Fabry-Perot interferometer at 8 mm are shown in Fig. XIII-16 for comparison with the 4-mm results. A plasma width of 10 cm was assumed for both cases.

The variation as a function of pressure of the average density during the beam pulse is shown in Fig. XIII-17 for System D. This graph shows the general tendency of the plasma density to increase with pressure. Relative values of pressure are used in Fig. XIII-17.

D. M. Perozek, W. D. Getty

References

1. M. A. Heald and C. B. Wharton, Plasma Diagnostics with Microwaves (John Wiley and Sons, Inc., New York, 1965), pp. 120-121.
2. T. J. Fessenden, Sc.D. Thesis, Department of Electrical Engineering, M. I. T., 1965, p. 96.
3. R. R. Bartsch, Quarterly Progress Report No. 81, Research Laboratory of Electronics, M.I. T., April 15, 1966.

4. SPECTROGRAPHIC MEASUREMENT OF ELECTRON TEMPERATURE IN THE BEAM-PLASMA DISCHARGE

The visible radiation emitted from a hydrogen plasma contains information about the average kinetic energy of the electrons. Emitted radiation is of two types; spectral lines (the Balmer series) and a continuum produced by recombination and Bremsstrahlung. The emitted intensities of line and continuum radiation are functions of temperature and, furthermore, the temperature dependences of the two are different. Griem¹ gives quantum-mechanical calculations that result in the temperature dependence of the ratio of the total line intensity and the total continuum intensity in a 100 Å band about the line. This result was used to find the electron temperatures of two plasmas from spectroscopic data. The two quantities whose ratio determines the temperature are shown in Fig. XIII-18.

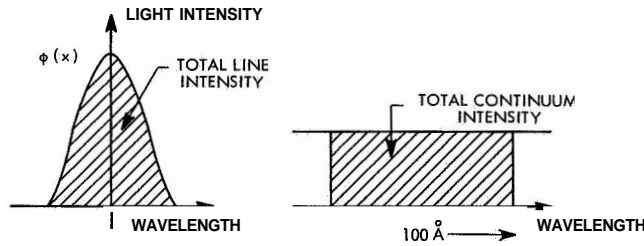


Fig. XIII-18. Areas of the line intensity and continuum intensity used for calculating the electron temperature.

The wavelength broadening of a Balmer line observed in the laboratory is due largely to distortions caused by the spectrometer. To obtain the true spectral line shape $\phi(x)$ from the measured spectrum, $f(x)$, the following integral equation must be solved:

$$f(x') = \int_{-\infty}^{\infty} a(x'-x) \phi(x) dx,$$

where $a(x)$ is an "apparatus function." The apparatus function is the apparent broadened spectral profile given to monochromatic light, whose true spectrum is a line of zero width, and it is measured experimentally for each entrance slit width to be used. The apparatus function was also calculated theoretically. In this work the integral equation was solved for $\phi(x)$ by use of Voigt functions, which are tabulated functions that can be fitted to experimental $a(x)$ and $f(x)$ and used to solve easily for $\phi(x)$. The details of the calculations are given elsewhere.²

For data taking, the entrance slit of the spectrometer is pointed at a window in the plasma, and a lens is used to collimate the light. A photomultiplier tube collects the

(XIII. PLASMAS AND CONTROLLED NUCLEAR FUSION)

light leaving the exit slit, and its anode current goes through an RC integrator to an oscilloscope. The tube response is in the form of bursts of electrons which can be seen individually if the light intensity falling on the tube is low. Each burst corresponds to an individual primary photoelectron. The integrating circuit counts the number of pulses occurring during the integration time, which is taken to be the beam pulse length.

Table XIII-2. System D.

	Peak pressure = 2×10^{-4} Torr		
Midplane Magnetic field (gauss)	550	1000	1200
Electron temperature (ev)	4.3	4.0	3.5
	Peak pressure = 10^{-5} Torr		
Electron temperature (ev)	-	4.0	-

Table XIII-3. System C.

	Peak pressure = 6×10^{-5} Torr		
Beam voltage (kv)	6.5	8	9
Beam current (amps)	15	22	30
Electron temperature (ev)	4	4	5

The measured spectrum $f(x)$ is the variation with wavelength of the output voltage of the integrating circuit as the spectrometer is scanned across the line. A 15-p entrance slit was used for line measurements and a 1000-p slit was used for the continuum, the wide slit being necessary because the intensity was weak. The integral equation was solved for $\phi(x)$ and the height of the continuum, with the use of experimental apparatus functions for 15- and 1000-p slits. The areas under the line and a 100 Å band of continuum were computed, and their ratio was used to find the electron temperature.

Data were taken on Beam-Plasma Discharge Systems C and D under various operating conditions. The results are shown in Tables XIII-2 and XIII-3.

R. D. Reilly, W. D. Getty

References

1. H. R. Griem, Plasma Spectroscopy (McGraw-Hill Publishing Company, New York, 1964).
2. R. D. Reilly, S.M. Thesis, Department of Electrical Engineering, M.I.T., June 1966.

(XIII. PLASMAS AND CONTROLLED NUCLEAR FUSION)

5. COMPUTER SIMULATION OF THE BEAM-PLASMA DISCHARGE

This quarter we continued¹ modelling the beam-plasma discharge by means of one-dimensional charge sheets. This time, however, we required the plasma to remain linear, and represented only the beam with sheets. The plasma is represented by its equivalent dielectric constant

$$\epsilon(\omega_1 k) = \left[1 - \frac{\omega_p^2}{\omega(\omega - i\nu)} \right]. \quad (1)$$

In the appendix it is shown that the response of the plasma to a sheet of charge q passing through it is

$$E(z, t) = -\frac{q}{\epsilon_0} \left(1 + \frac{\nu^2}{4\omega_0^2} \right)^{1/2} e^{-\frac{\nu}{2}[t-t_1(z)]} \cos \left\{ \omega_0[t-t_1(z)] - \tan^{-1} \frac{\nu}{2\omega_0} \right\} \times \mu_{-1}[t-t_1(z)], \quad (2)$$

where

$$\omega_0^2 = \omega_p^2 \left(1 - \nu^2 / 4\omega_p^2 \right), \quad (3)$$

and $t_1(z)$ is the time when the sheet passes the point z (if the velocity of the sheet does not reverse). This response is shown in Fig. XIII-19. Since the plasma is assumed to

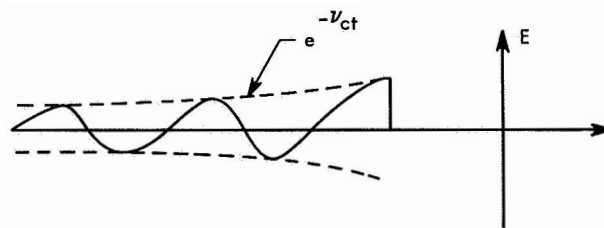


Fig. XIII-19. The electric field produced by a single sheet moving through the plasma. (Actual decay is exaggerated.)

be linear, we can superimpose the responses of the sheets to obtain the response for a continuously injected beam.

The sheets were injected into a previously empty plasma (free of sheets) with a velocity modulation of 2 percent and no density modulation. A Milne numerical integration routine was used to calculate the sheet trajectories. It is

$$x(t+\Delta t) = x(t) + x(t-2\Delta t) - x(t-3\Delta t) + \frac{(\Delta t)^2}{4} [5a(t) + 2a(t-\Delta t) - 5a(t-2\Delta t)] + \frac{17(\Delta t)^6}{240} \frac{d^6 x}{dt^6}.$$

(XIII. PLASMAS AND CONTROLLED NUCLEAR FUSION)

At all points spaced $\Delta x = v_o \Delta t$ apart (in these calculations $\Delta t = 0.2 \omega_p^{-1}$ the magnitude and phase of the electric field were derived. It is sufficient to specify the magnitude and phase of the electric field at each cell point, since the field attributable to each sheet varies sinusoidally in time, and when cosines add they produce another cosine. Interpolation of the field at a sheet located between two cell points was done by fitting a second-order polynomial to the values at three cell points bracketing the considered sheet. The Runge-Kutta integration method, which requires only present values of $\mathbf{x}(t)$, was used to start the Milne formula, which requires $\mathbf{x}(t)$ and its value at three previous time steps. The first four time steps were calculated by the Runge-Kutta method.

When sheet crossings occur, there is a discontinuity in the force, and the Milne integration formula, which is derived for a continuous force acting between t and $t + \Delta t$, would produce errors if no corrections were made. On crossing, the force attributable to one sheet, q^2/ϵ_o , is added to $a(t)$, $a(t-\Delta t)$, $a(t-2\Delta t)$ if the sheet crosses, and subtracted if it does not. This allows the acceleration to be a continuous function of time. This process is justified if it yields the correct acceleration, velocity, and position for times greater than the crossing time. For this to be true, $\mathbf{x}(t)$, $\mathbf{x}(t-\Delta t)$, $\mathbf{x}(t-2\Delta t)$, and $\mathbf{x}(t-3\Delta t)$ must also be modified. In Fig. XIII-20 we show how the corrections are made for the crossed sheet. The solid lines represent the old functions, which are correct for times less than the crossing time. The corrected functions, which are correct for times greater than the crossing time, are shown as dashed lines. We assume that the crossing sheet presents a constant force to the crossed sheet over time (Δt) . This is

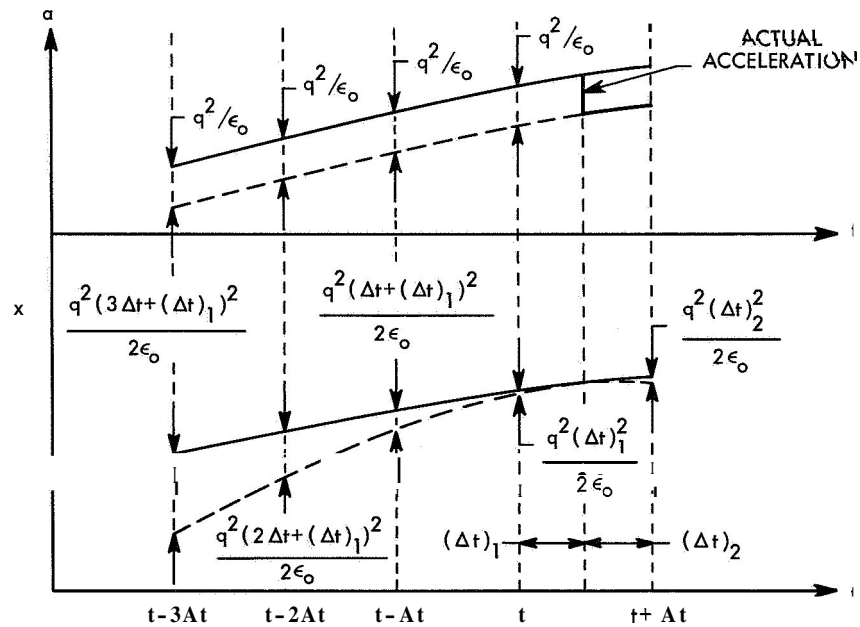


Fig. XIII-20. Corrections made to the acceleration and position to allow for crossings. (Corrections for the crossed sheet are shown.) $t + (\Delta t)_1$ is the time of crossing.

(XIII. PLASMAS AND CONTROLLED NUCLEAR FUSION)

a very good approximation if the sheets have nearly the same velocity. Note that if we reduce the acceleration for $t < t_c(At)_1$, we must increase the previous velocities for the sheet to have the same velocity at the crossing time. This is reflected in the reduced x 's for $t < t_c(At)$. The time of crossing is estimated by the formula

$$t + (\Delta t)_1 = t + \frac{x_{\text{crossed}}(t) - x_{\text{crossing}}(t)}{\frac{x_{\text{crossing}}(t+\Delta t) - x_{\text{crossing}}(t)}{\Delta t} - \frac{x_{\text{crossed}}(t+\Delta t) - x_{\text{crossed}}(t)}{\Delta t}} \quad (4)$$

where the $x(t+\Delta t)$ are calculated under the assumption of no crossing.

A "snapshot" of acceleration and beam sheet velocity is shown in Fig. XIII-21. In this case $t = 300.4 \omega_p^{-1}$, $\omega_{pb}^2 = \omega_{pp}^2/200$ and $v = 0.2 w_p$. This large value of v was required to keep the plasma linear ($\rho_{1p}/\rho_{0p} = v_{1p}/v_0 = 0.035$ at peak acceleration). From linear theory we would expect an exponential growth rate in space, under the

assumption of a steady state, of $\frac{\omega_{pb}}{v_0} \sqrt{\frac{\omega_p}{2v}}$, or, for our numbers, a doubling every wavelength. This is seen to be correct for small values of x . Both the acceleration and beam velocity develop a negative DC value in addition to the exponential growth.

The excited traveling wave has a phase velocity less than that of the beam. Initially, the sheets ride through the troughs and crests of this wave. The beam becomes trapped, however, when the beam velocity modulation builds up so that the minimum beam velocity approaches the wave phase velocity. A large charge bunch forms, although it has a considerable velocity spread. The electric field is maximumly decelerating at this point, thereby resulting in maximum energy transfer to the plasma.

The sheets near the velocity minimum form a "sub-bunch" that is rather tight in velocity, and produces sharp dips in the acceleration for distances considerably beyond the overtaking point. The sub-bunch eventually breaks up, but not until the sheet velocity is less than 20 per cent of the injected velocity.

Those sheets that are between the bunches find themselves in an accelerating field, and many seem to be accelerated into the bunch, and maintain the bunch and a wave component near the linear phase velocity for some distance past overtaking.

Eventually the bunches spread out. Unfortunately, the steady state cannot be assumed to exist for distances beyond $x = 280$, as determined by comparison with snapshots taken at previous times. The point of diminishing returns has been reached as far as computer time goes, since the time to reach the steady state is proportional to the drift times of the slowest electrons, which have become quite long.

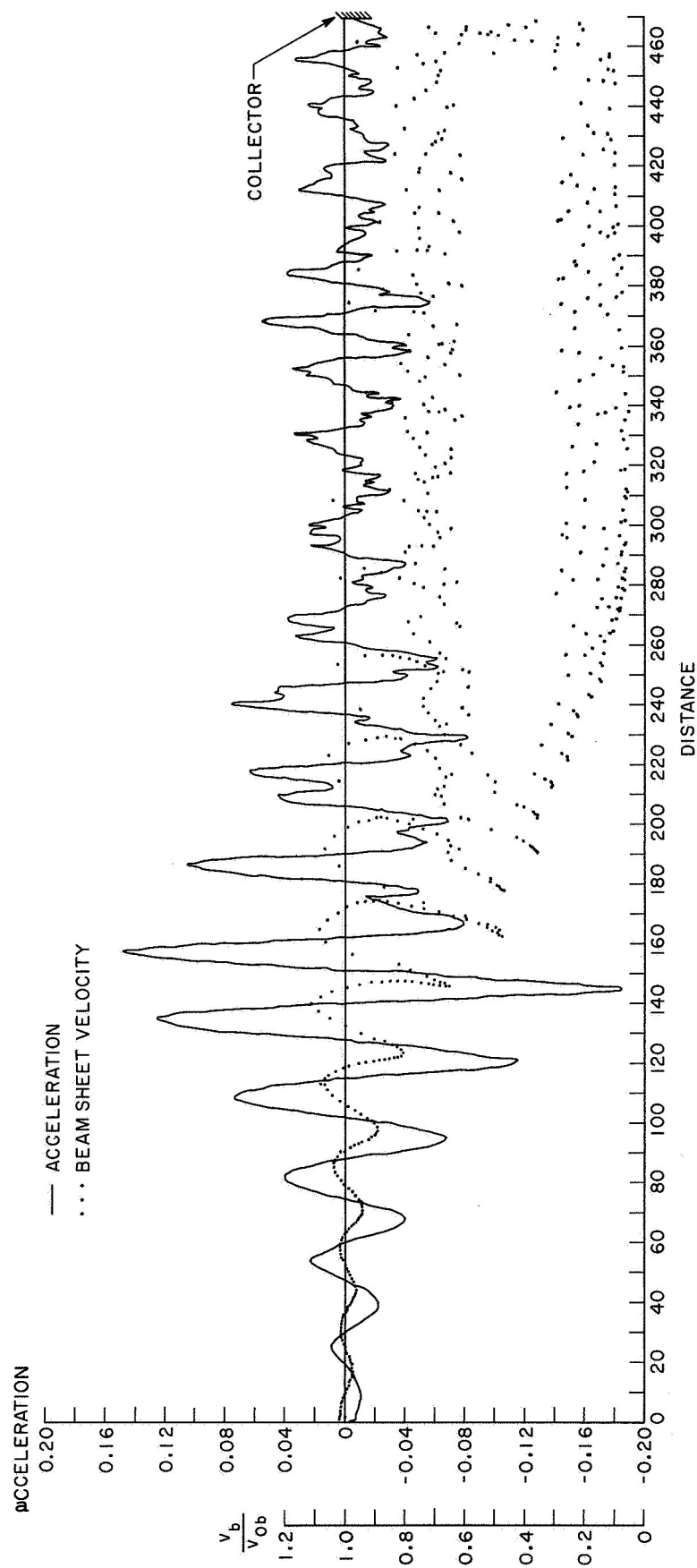


Fig. XIII-21. Acceleration and beam sheet velocity vs distance. Time = $300.4 \omega_p^{-1}$. Distances are normalized to $0.2 v_{ob}^{-1}$, accelerations to $0.2 v_{ob}$.

Appendix

Derivation of Response of Plasma to a Moving Charge Sheet (Eq. 2)

With the beam considered as free charge and the plasma charge included in the equivalent dielectric constant of Eq. 1, from Poisson's equations, we have

$$E(\omega, k) = \frac{\rho(\omega, k)}{-ik\epsilon(\omega, k)}, \quad (A1)$$

where

$$\rho(z, t) = qu_0(z - v_0 t). \quad (A2)$$

Performing a Laplace transform in time and a Fourier transform in space, we have

$$\rho(\omega, k) = \frac{q}{i(\omega - kv_0)}, \quad (A3)$$

so that

$$E(\omega, k) = \frac{q}{k(\omega - kv_0) \left(\omega - \frac{iv}{2} + \omega_0 \right) \left(\omega - \frac{iv}{2} - \omega_0 \right) \epsilon_0} \quad (A4)$$

Here, ω_0 is defined by Eq. 3. The pole in the k -plane at ω/v_0 is taken for positive z by the Bers-Briggs² criterion. This pole introduces a delay in time of z/v_0 . The pole at $k = 0$ is not placed by this criterion, but splitting this pole is found to give physically meaningful results. The poles in the ω plane at $\pm\omega_0 \pm iv/2$ are easily evaluated by Cauchy's theorem. The result, for $z > 0$, is

$$E(z, t) = -\frac{q}{\epsilon_0} e^{-\frac{v}{2}(t-z/v_0)} \cos \left[\omega_0(t-z/v_0) - \tan^{-1} \frac{v}{2\omega_0} \right] u_{-1}(t-z/v_0) \\ + \frac{q}{2\epsilon_0} e^{-\frac{v}{2}t} \cos \omega_0 \left(t - \tan^{-1} \frac{v}{2\omega_0} \right) u_{-1}(t), \quad (A5a)$$

and, for $z < 0$,

$$E(z, t) = -\frac{q}{2\epsilon_0} e^{-\frac{v}{2}t} \cos \left(\omega_0 t - \tan^{-1} \frac{v}{2\omega_0} \right) u_{-1}(t). \quad (A5b)$$

(XIII. PLASMAS AND CONTROLLED NUCLEAR FUSION)

The terms independent of z arise from the Laplace transform, in which the sheets **are** assumed to appear suddenly to $t = 0$. These terms are ignored, which means that the model assumes that a nonmoving ion sheet appears at $z = 0$ with the electron sheet.

The z/v_0 term in (A5b) can be generalized to an arbitrary $t_1(z)$, where $t_1(z)$ is the time at which the sheet crosses the plane $z \left(\frac{\partial t_1(z)}{\partial z} > 0 \right)$. $\rho(z, t)$ must be written

$$\rho(z, t) = q \frac{\partial t_1(z)}{\partial z} u_0[t - t_1(z)]. \quad (\text{A6})$$

This is necessary if $\int dz \rho(z, t) = q$. Hence

$$\rho(\omega, k) = \int_0^\infty dz e^{ikz} \int_0^\infty e^{-i\omega t} dt q \frac{\partial t_1(z)}{\partial z} u_0[t - t_1(z)].$$

Integrating by parts and noting that

$$\frac{d \exp[-i\omega t_1(z)]}{dz} = -i\omega \frac{dt_1}{dz} e^{-i\omega t_1(z)}, \quad (\text{A7})$$

we obtain

$$\rho(\omega, k) = \frac{q}{i\omega} + \frac{kq}{\omega} \int_0^\infty e^{ikz} e^{-i\omega t_1(z)} dz. \quad (\text{A8})$$

Inserting this into (A1), we obtain finally

$$E(\omega, k) = -\frac{q}{i\omega \epsilon(\omega, k)} \int_0^\infty dz e^{ikz} e^{-i\omega t_1(z)} + \frac{q}{\omega k \epsilon(\omega, k)} \quad (\text{A9})$$

If we take the transform of **Eq. 2**, we shall find it identical to the first term of (A9). The second term yields the spatially invariant response.

J. A. Davis

References

1. J. A. Davis, Quarterly Progress Report No. 80, Research Laboratory of Electronics, M.I.T., January 15, 1966.
2. R. J. Briggs, Electron-Stream Interaction with Plasmas (The M.I.T. Press, Cambridge, Mass., 1964).

6. THEORY OF PLASMA EXCITATION BY A LINE-CHARGE SOURCE

We are interested in excitation of the beam-plasma discharge (BPD) by a modulated beam.^{1,2} In the last report³ we considered the following theoretical model: Assume a linearized hydrodynamic representation of a fully ionized macroscopically neutral electron-ion plasma, with a longitudinal DC magnetic field, $B_0 \hat{i}_z$. The unbounded plasma is excited by a sinusoidally varying line-charge source oriented parallel to the DC magnetic field, $\rho = \rho_0 \delta(x) \delta(y)$, for $\exp(j\omega t)$ sinusoidal steady-state time dependence. The constant ρ_0 is in units of coulombs per meter. We are interested in quasi-static solutions that have azimuthal symmetry and no longitudinal variation.

The set of equations used to describe the system is solved by using Fourier transform theory. The set of equations and the spatial Fourier transforms of the first-order densities, potential, and velocities have been given previously.³

This report presents the exact solutions to the problem outlined above. The expressions for the first-order ion velocity and density and the first-order electric field follow.

$$v_{ir}(r) = \left\{ \begin{aligned} & \frac{j\rho_0 e \omega (-\omega^2 + \omega_{ce}^2)}{2\pi m_i \epsilon_0 \left[(-\omega^2 + \omega_{pe}^2 + \omega_{ce}^2)(-\omega^2 + \omega_{pi}^2 + \omega_{ci}^2) - \omega_{pe}^2 \omega_{pi}^2 \right]} \frac{1}{r} \\ & - \frac{\rho_0 e \omega (k_1^2 u_e^2 - \omega^2 + \omega_{ce}^2)}{4m_i \epsilon_0 \left[u_e^2 (k_1^2 u_i^2 - \omega^2 + \omega_{ci}^2 + \omega_{pi}^2) + u_i^2 (k_1^2 u_e^2 - \omega^2 + \omega_{ce}^2 + \omega_{pe}^2) \right]} \frac{H_1^{(2)}(k_1 r)}{k_1} \\ & + \frac{\rho_0 e \omega (k_2^2 u_e^2 - \omega^2 + \omega_{ce}^2)}{4m_i \epsilon_0 \left[u_e^2 (k_2^2 u_i^2 - \omega^2 + \omega_{ci}^2 + \omega_{pi}^2) + u_i^2 (k_2^2 u_e^2 - \omega^2 + \omega_{ce}^2 + \omega_{pe}^2) \right]} \frac{H_1^{(2)}(k_2 r)}{k_2} \end{aligned} \right\} \quad (1)$$

$$v_{i\theta}(r) = \left\{ \begin{aligned} & \frac{j\rho_0 \omega_{pi}^2 (k_1^2 u_e^2 - \omega^2 + \omega_{ce}^2)}{4e \left[u_e^2 (k_1^2 u_i^2 - \omega^2 + \omega_{ci}^2 + \omega_{pi}^2) + u_i^2 (k_1^2 u_e^2 - \omega^2 + \omega_{ce}^2 + \omega_{pe}^2) \right]} \frac{H_0^{(2)}(k_1 r)}{k_1} \\ & - \frac{j\rho_0 \omega_{pi}^2 (k_2^2 u_e^2 - \omega^2 + \omega_{ce}^2)}{4e \left[u_e^2 (k_2^2 u_i^2 - \omega^2 + \omega_{ci}^2 + \omega_{pi}^2) + u_i^2 (k_2^2 u_e^2 - \omega^2 + \omega_{ce}^2 + \omega_{pe}^2) \right]} \frac{H_0^{(2)}(k_2 r)}{k_2} \end{aligned} \right\} \quad (2)$$

$$n_i(r) = \left\{ \begin{aligned} & \frac{-j\rho_0 \omega_{pi}^2 (k_1^2 u_e^2 - \omega^2 + \omega_{ce}^2)}{4e \left[u_e^2 (k_1^2 u_i^2 - \omega^2 + \omega_{ci}^2 + \omega_{pi}^2) + u_i^2 (k_1^2 u_e^2 - \omega^2 + \omega_{ce}^2 + \omega_{pe}^2) \right]} \frac{H_0^{(2)}(k_1 r)}{k_1} \\ & - \frac{j\rho_0 \omega_{pi}^2 (k_2^2 u_e^2 - \omega^2 + \omega_{ce}^2)}{4e \left[u_e^2 (k_2^2 u_i^2 - \omega^2 + \omega_{ci}^2 + \omega_{pi}^2) + u_i^2 (k_2^2 u_e^2 - \omega^2 + \omega_{ce}^2 + \omega_{pe}^2) \right]} \frac{H_0^{(2)}(k_2 r)}{k_2} \end{aligned} \right\} \quad (3)$$

$$E_r(r) = \left\{ \frac{\rho_o (-\omega^2 + \omega_{ci}^2) (-\omega^2 + \omega_{ce}^2)}{2\pi\epsilon_o \left[(-\omega^2 + \omega_{pe}^2 + \omega_{ce}^2) (-\omega^2 + \omega_{pi}^2 + \omega_{ci}^2) - \omega_{pe}^2 \omega_{pi}^2 \right]} \frac{1}{r} \right. \\ + \frac{j\rho_o (k_1^2 u_i^2 - \omega^2 + \omega_{ci}^2) (k_1^2 u_e^2 - \omega^2 + \omega_{ce}^2)}{4\epsilon_o \left[u_e^2 (k_1^2 u_i^2 - \omega^2 + \omega_{ci}^2 + \omega_{pi}^2) + u_i^2 (k_1^2 u_e^2 - \omega^2 + \omega_{ce}^2 + \omega_{pe}^2) \right]} \frac{H_1^{(2)}(k_1 r)}{k_1} \\ \left. + \frac{j\rho_o (k_2^2 u_i^2 - \omega^2 + \omega_{ci}^2) (k_2^2 u_e^2 - \omega^2 + \omega_{ce}^2)}{4\epsilon_o \left[u_e^2 (k_2^2 u_i^2 - \omega^2 + \omega_{ci}^2 + \omega_{pi}^2) + u_i^2 (k_2^2 u_e^2 - \omega^2 + \omega_{ce}^2 + \omega_{pe}^2) \right]} \frac{H_1^{(2)}(k_2 r)}{k_2} \right\} \quad (4)$$

where $H^{(2)}$ is the Hankel function of the second kind and of the indicated order and argument.

The expressions for v_{er} and n_e are obtained from Eqs. 1 and 3 by the following manipulations: (a) replace the subscript e with i, (b) replace the subscript i with e, and (c) replace $\frac{\omega_{ce}}{\omega}$ with $-\frac{\omega_{ce}}{\omega}$. The velocity $v_{e\theta}$ is obtained from

$$v_{e\theta} = (-j \frac{\omega_{ce}}{\omega}) v_{er} \quad (5)$$

The propagation constants k_1 and k_2 are zeros of the dispersion relation $D(k_T) = 0$, that is, values of k_T for which

$$D(k_T) = \left[(k_T^2 u_i^2 - \omega^2 + \omega_{ci}^2 + \omega_{pi}^2) (k_T^2 u_e^2 - \omega^2 + \omega_{ce}^2 + \omega_{pe}^2) - \omega_{pi}^2 \omega_{pe}^2 \right] \quad (6)$$

is equal to zero. The constants k_1 and k_2 are either positive real or negative imaginary, dependent upon choice of operating frequency ω . The frequencies for which k_1 or k_2 are zero (the cutoff frequencies) satisfy the following equation:

$$\left[(-\omega^2 + \omega_{ci}^2 + \omega_{pi}^2) (-\omega^2 + \omega_{ce}^2 + \omega_{pe}^2) - \omega_{pi}^2 \omega_{pe}^2 \right] = 0. \quad (7)$$

We are particularly interested in finding the frequencies at which the ion response to the line-charge excitation is maximum. Note that the constants k_1 and k_2 appear in the arguments of the Hankel functions, so that at cutoff frequencies the responses are infinite. For very low densities or very high magnetic field the lower of the two cutoff frequencies is near the ion cyclotron frequency. For very high densities it becomes the lower hybrid frequency. For plasmas encountered in the BPD systems, however, this cutoff frequency is at least an order of magnitude greater than the ion cyclotron frequency, in the range 10-100 Mc. The second cutoff frequency is somewhat above the

(XIII. PLASMAS AND CONTROLLED NUCLEAR FUSION)

electron plasma frequency, for typical BPD parameters.

Note that the terms with Hankel functions contain bracketed factors involving the thermal velocities u_i and u_e . By proper choice of operating frequency, this term can cause the responses of the system to approach infinity. If the operating frequency is above cutoff, this frequency is greater than the ion plasma frequency. Below cutoff this value of ω^2 is less than ω_{pi}^2 .

It appears from this analysis that large response to the line charge excitation can be obtained by choosing the operating frequency close to a cutoff frequency. This theoretical model may fail, however, near a cutoff frequency, where the first-order magnetic field becomes important. For this reason, we are in the process of including first-order magnetic field in our model. Numerical evaluation of the results given here is also in progress.

G. D. Bernard

References

1. L. D. Smullin, "Beam-Plasma Discharge: Excitation of Ions at the Ion Cyclotron Frequency (Theory)," Quarterly Progress Report No. 80, Research Laboratory of Electronics, M.I.T., January 15, 1966, pp. 111-113.
2. W. D. Getty and G. D. Bernard, "Beam-Plasma Discharge: Excitation of the Ions at the Ion Cyclotron Frequency (Experiment)," Quarterly Progress Report No. 80, Research Laboratory of Electronics, M.I. T., January 15, 1966, pp. 113-115.
3. G. D. Bernard and A. Bers, "Theory of Plasma Excitation by a Line-Charge Source," Quarterly Progress Report No. 81, Research Laboratory of Electronics, M.I. T., April 15, 1966, pp. 102-104.

7. CROSS-FIELD BEAM-PLASMA INTERACTIONS

This is the first report on a new experiment that has been started in this group. The general object of the experiment is to study the properties of an electron beam with transverse energy comparable to its longitudinal energy. Properties of this beam will be investigated in the presence of varying plasma densities. At present, the basic experimental apparatus has been completed and the electron *gun*, which will be described in this report, is operating. Some initial observations of the beam current have been made and will be briefly discussed.

Experimental Apparatus

The experiment is being carried on in the pumped vacuum system shown in Fig. XIII-22. The discharge takes place in a Pyrex cross of 4 inches diameter, to the right of the magnetic circuit. The gun and the collector are in the horizontal arms of the cross. Gas can be admitted through the top, and the system is pumped by means

(XIII. PLASMAS AND CONTROLLED NUCLEAR FUSION)

of an oil diffusion pump and a forepump.

As mentioned, the *gun* is in one of the horizontal arms of the cross. It creates a hollow cylindrical beam of essentially monoenergetic electrons primarily with only axial velocity. This is accomplished by means of a hollow-cathode disk and a Pierce-type grid and anode as shown in Fig. XIII-23. The long and short dashed lines represent an

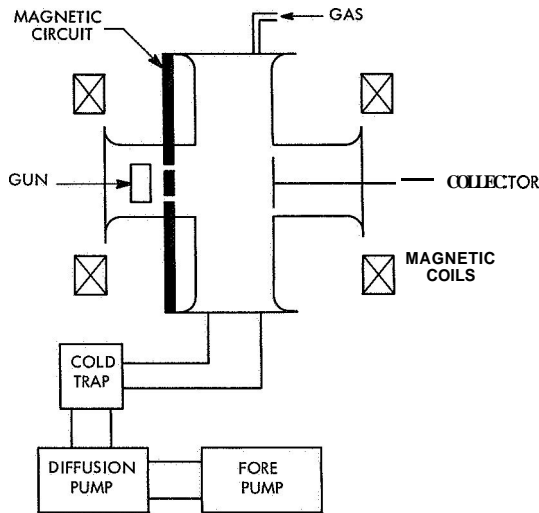


Fig. XIII-22. The System.

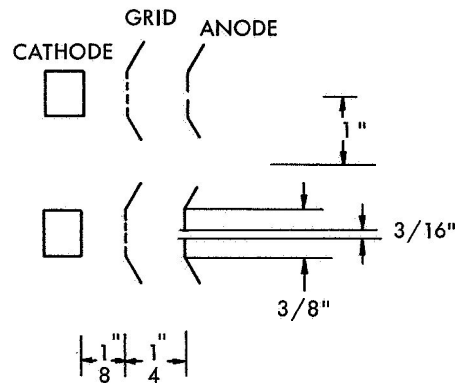


Fig. XIII-23. The Gun.

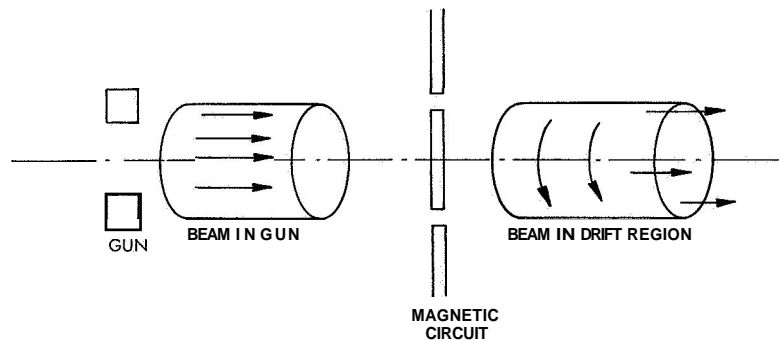


Fig. XIII-24. The Beam,

axis of revolution for the structures shown. The grid is used to control the perveance of the beam.

The beam, which is not intercepted by the anode but passes through it, is injected into a magnetic circuit that alters its velocity distribution. The initial experiments will be carried out by using a hollow cylindrical beam with drift along and rotation about its axis (see Fig. XIII-24). The ratio of transverse energy to axial energy of the beam

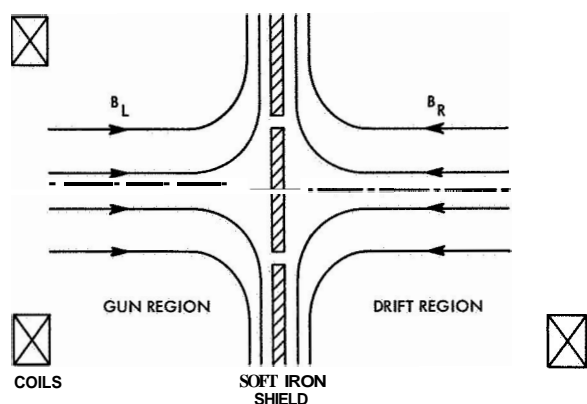


Fig. XIII-25. The magnetic circuit.

can be controlled by adjusting the field in the magnetic circuit.

Magnetic Circuit

The magnetic circuit is composed of a large soft-iron shield which allows the magnetic field in the gun region to be independent of the field in the drift region (see Fig. XIII-25). Ideally, the magnetic flux lines should be along the axis of symmetry except in the magnetic circuit where they should be radial. The beam

is injected from the gun region into the drift region through a disk-shaped hole in the soft iron shield. For various relative magnitudes of the magnetic field on the right, B_R , and on the left, B_L , many different

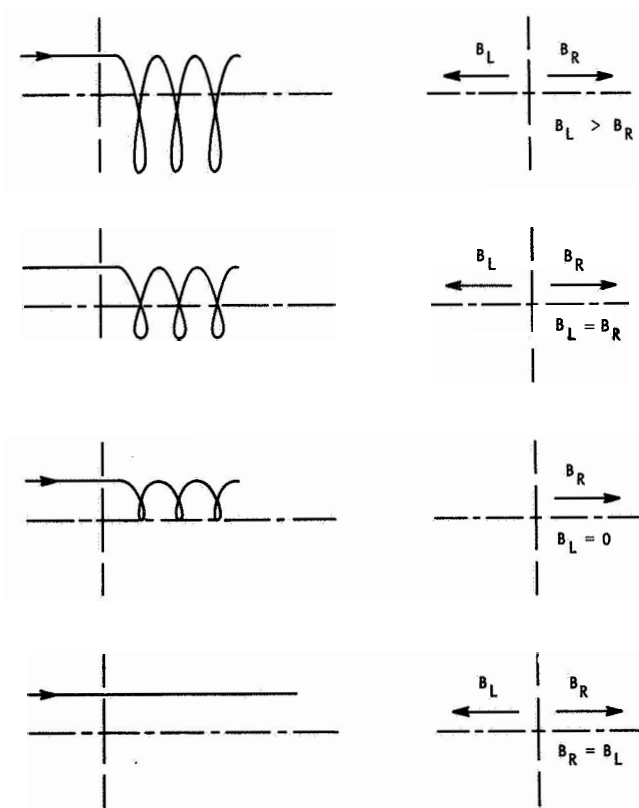


Fig. XIII-26. Beam configurations.

beam configurations can be obtained. In Fig. XIII-26 the trajectory of a single electron injected into the magnetic-field environment described at the right is traced out. The injected electron for all cases has the same total kinetic energy. This kinetic energy

must be greater than a minimum value given by

$$\text{Kinetic energy}_{\min} = \frac{q^2 (B_L - B_R)^2 r_o^2}{8 m},$$

where q is the charge, m the mass, and r_o the radius of the disk-shaped hole in the soft iron shield. The kinetic energy in excess of this amount goes into longitudinal energy. Therefore to obtain the beam described by Fig. XIII-24, it is necessary to make B_L and B_R equal in magnitude but oppositely directed.

Initial Measurements

Some of the initial measurements of the beam current have shown an interesting low-frequency oscillation. With a beam voltage of 500 volts and grid voltage of 50-75 volts the emission current varies from 100 ma to 200 ma. Of this emission current, 20-40 ma passed through the anode into the drift region. The magnetic field was adjusted as shown in Fig. XIII-24 to give a rotating hollow beam of approximately 1-inch radius and 1/8 inch thick. The magnetic field in the drift region was 25 gauss. Under these conditions, very clean, 1-2 per cent modulation of the DC collector current was observed in the neighborhood of 100 kc. This modulation was observed for varying degrees of argon plasma density associated with pressures ranging from 10^{-7} to 10^{-5} mm Hg.

B. Kusse. A. Bers

8. DYNAMICS OF THE PLASMA BOUNDARY

Previously, we have given computed trajectories of charge sheets in order to study the nonlinear oscillations of a finite plasma slab in the absence of a magnetic field.^{1, 2} It was observed that a "scrambling," initiated by a crossing or overtaking of trajectories

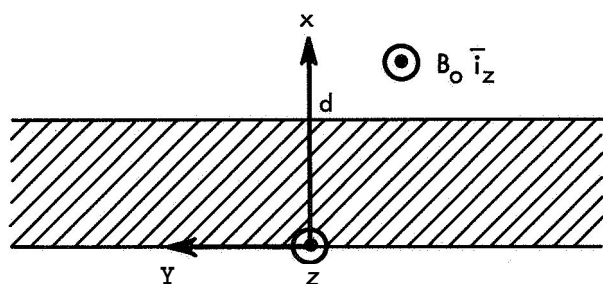


Fig. XIII-27. Plasma slab in equilibrium.

near the surface, gradually destroyed the coherent oscillations of the entire slab. Leavens and Leavens³ have derived an expression for the time of the first crossing, t_s , given by $\omega_p t_s = \pi t \sqrt{2}$.

In this report we present a derivation for the time of the first overtaking if the plasma slab is immersed in a DC magnetic field. The results are valid for electron-cyclotron frequencies, ω_c , in the range $0 \leq \omega_c \leq \omega_p$. A graphical

technique is used to display the formation of the overtaking for various values of (ω_c/ω_p) .

The plasma slab in equilibrium consists of a uniform number density of ions and

(XIII. PLASMAS AND CONTROLLED NUCLEAR FUSION)

electrons distributed over a thickness, d , in the x -direction, but infinite in the y - and z -directions. The important addition is the presence of a DC magnetic field, $B = B_0 \hat{z}$, as shown in Fig. WI-27. The ions are assumed to be infinitely heavy and hence are treated as a rigid slab. The instantaneous position, x , of an electron is a function of its equilibrium position, x_0 , and the time, or $x = x(x_0, t)$. We assume that at $t = 0$ all of the electrons have been displaced an amount δ in the x -direction, $x(x_0, 0) = x_0 + \delta$, and seek the motion of the electrons for $t > 0$. For simplicity, we study the electrons that were at $y = 0$ at $t = 0$, so $y = y(x_0, t)$.

The equations of motion for the electrons are

$$\frac{d^2 x}{dt^2} = -\frac{\omega_p^2}{\omega_c} (x - x_0) - \omega_c \frac{dy}{dt} \quad 0 < x < d \quad (1)$$

$$\frac{d^2 y}{dt^2} = \omega_c \frac{dx}{dt}$$

$$\frac{d^2 x}{dt^2} = \frac{\omega_p^2}{\omega_c} (x_0 - d) - \omega_c \frac{dy}{dt} \quad x > d \quad (2)$$

$$\frac{d^2 y}{dt^2} = \omega_c \frac{dx}{dt}$$

as long as no overtaking has taken place. Here, $\omega_p^2 = \frac{e^2 n_0}{\epsilon_0 m}$ and $\omega_c = \frac{eB_0}{m}$, where e is the electronic charge, n_0 is the equilibrium particle number density, and m is the mass of an electron.

The solution of Eqs. 1 and 2 is

$$x = x_0 + \frac{\omega_c^2 \delta}{\omega_0^2} + \frac{\omega_p^2 \delta}{\omega_0^2} \cos \omega_0 t \quad 0 < x < d$$

$$y = -\frac{\omega_p^2 \omega_c \delta}{\omega_0^3} (\omega_0 t - \sin \omega_0 t) \quad x_0 < (d - \delta)$$

$$x = x_0 + \delta + \frac{\omega_p^2}{\omega_c^2} (x_0 - d) (1 - \cos \omega_c t) \quad x > d$$

$$y = \frac{\omega_p^2}{\omega_c^2} (x_0 - d) (\omega_c t - \sin \omega_c t), \quad x_0 > (d - \delta)$$

where $\omega_o^2 = \omega_c^2 + \omega_p^2$.

Electrons that were outside the ion boundary at $x = d$ will go back into the ion background at time t_o , given by

$$\omega_o t_o = \cos^{-1} \left[1 + \frac{\omega_c^2}{\omega_p^2} \left(1 + \frac{\delta}{x_o - d} \right) \right]. \quad (3)$$

After this time these particles have the motion inside described by

$$\begin{aligned} x &= x_o + \frac{\omega_c^2}{\omega_o^2} \delta - \left(x_o - d + \frac{\omega_c^2 \delta}{\omega_o^2} \right) \cos \omega_o (t - t_o) + \frac{\omega_p^2 (x_o - d)}{\omega_c \omega_o} \sin \omega_c t_o \sin \omega_o (t - t_o) \\ y &= \frac{-\omega_p^2 \omega_c \delta t}{\omega_o^2} - \frac{\omega_c}{\omega_o} \left(x_o - d + \frac{\omega_c^2 \delta}{\omega_o^2} \right) \sin \omega_o (t - t_o) + \frac{\omega_p^2 t_o}{\omega_c} \left(x_o - d + \frac{\omega_c^2 \delta}{\omega_o^2} \right) \\ &\quad - \frac{\omega_D^2 (x_o - d)}{\omega_o^2} \sin \omega_c t_o \cos \omega_o (t - t_o) - \frac{\omega_p^4 (x_o - d)}{\omega_o^2 \omega_c^2} \sin \omega_c t_o. \end{aligned} \quad \begin{array}{l} x < 0 \\ x > d - \delta \end{array} \quad (4)$$

The condition for overtaking is $\partial x / \partial x_o = 0$. If t_s denotes the time at which overtaking occurs, the condition for earliest overtaking is $\partial t_s / \partial x_o = 0$.³

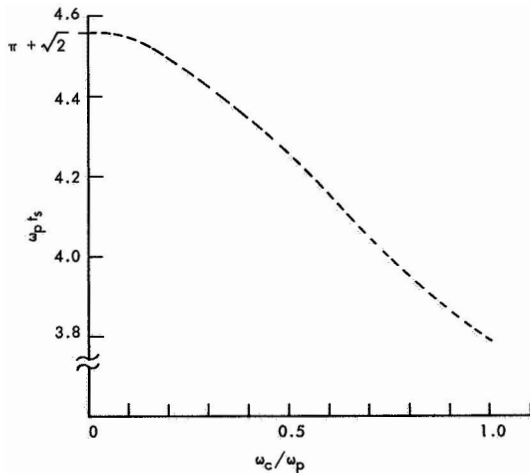


Fig. XIII-28. Overtaking time versus (ω_c/ω_p) .

Application of these two conditions to the equations describing the motion of the electrons that have returned to the ion background gives

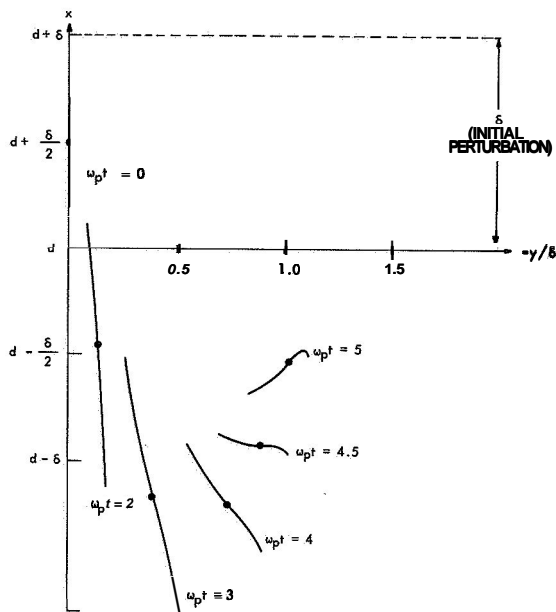


Fig. XIII-29. Onset of overtaking for $\frac{\omega_c}{\omega_p} = 0.2$.

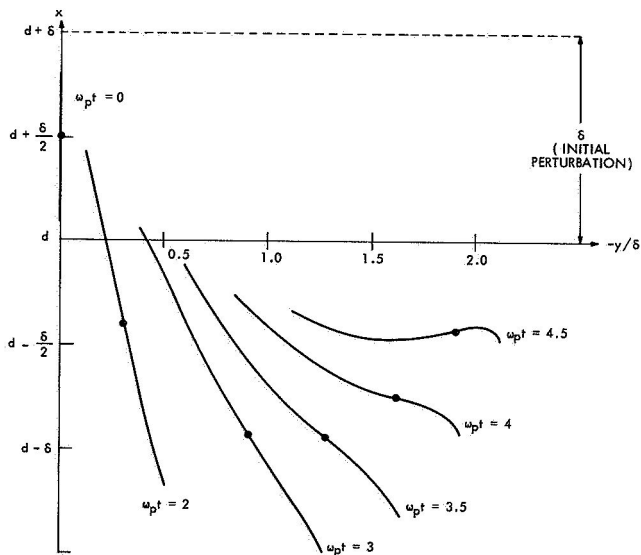


Fig. XIII-30. Onset of overtaking for $\frac{\omega_c}{\omega_p} = 0.5$.

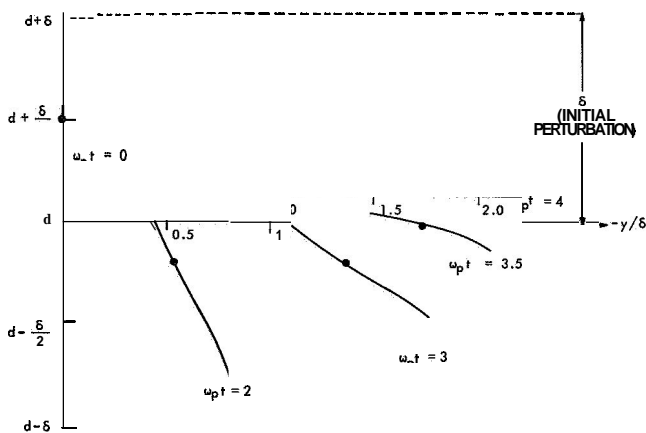


Fig. XIII-31. Onset of overtaking for $\frac{\omega_c}{\omega_p} = 1.0$.

$$-\left(1 + \frac{\delta}{x_o - d}\right) \cos \omega_o(t_s - t_o) + \frac{\omega_p^2}{\omega_c \omega_o} \sin \omega_c t_o \sin \omega_o(t_s - t_o) = -1 \quad (5)$$

and

$$\frac{-\omega^2 \delta}{\omega_o^2(x_o - d)} \omega_o \frac{\partial t_o}{\partial x_o} \sin \omega_o(t_s - t_o) = 0. \quad (6)$$

Equations 5 and 6 yield for the overtaking time, t_s ,

$$\omega_o t_s = \pi t \frac{\omega_o}{\omega_c} \cos^{-1} \left(1 - \frac{\omega_c^2}{\omega_p^2} \right). \quad (7)$$

In Fig. XIII-28 we plot $\omega_p t_s$ as a function of the ratio (ω_c/ω_p) . Note that as ω_c/ω_p approaches zero, $\omega_p t_s$ approaches the value $(\pi + \sqrt{2})$, as reported by Leavens and Leavens.

Equations 4 predict that the electron that is first involved in overtaking has the equilibrium position $x_o = d - (1/2)\delta$. The overtaking actually occurs at a position in the ion background given by

$$x = d - \delta \left(\frac{\omega_p^2 - \omega_c^2}{\omega_p^2 + \omega_c^2} \right). \quad (8)$$

Equation 8 reduces to $x = d - \delta$ as $\omega_c/\omega_p \rightarrow 0$, which again agrees with Leavens and Leavens.³ As ω_c/ω_p increases from zero, the overtaking occurs nearer the surface, until $\omega_c = \omega_p$, when it occurs exactly at $x = d$. The study of the motion has not been carried out for $\omega_c > \omega_p$.

The overtaking can be visualized more easily if we plot electron trajectories as a function of time. If at $t = 0$ a "line" is fixed to the electrons along $y = 0$ and to those that are in the vicinity of $x = d + \frac{1}{2}\delta$, the onset of overtaking can be seen if the deformation of this "line" is followed as a function of time. Figures XIII-29, XIII-30, and XIII-31 illustrate this approach for $\omega_c/\omega_p = 0.2$, $\omega_c/\omega_p = 0.5$, and $\omega_c/\omega_p = 1$, respectively.

It is important to note that we have only studied the overtaking that occurs near the surface of the ion background at $x = d$. An extension of the techniques used here must be made to determine when overtaking occurs for particles near the other boundary, namely $x = 0$.

H. M. Schneider

(XIII. PLASMAS AND CONTROLLED NUCLEAR FUSION)

References

1. **H. M. Schneider**, "Dynamics of the Plasma Boundary," Quarterly Progress Report No. 80, Research Laboratory of Electronics, M. I. T. , January 15, 1966, pp. 128-129.
2. **H. M. Schneider** and **A. Bers**, "Dynamics of the Plasma Boundary," Quarterly Progress Report No. 78, Research Laboratory of Electronics, M. I. T. , July 15, 1965, pp. 114-119.
3. **W. M. Leavens** and **I. B. Leavens**, Bull. Am. Phys. Soc. 1, 480 (1962).

XIII. PLASMAS AND CONTROLLED NUCLEAR FUSION*

B. Applied Plasma Physics Related to Controlled Nuclear Fusion

Academic and Research Staff

Prof. D. J. Rose
Prof. T. H. Dupree

Prof. L. M. Lidsky
Prof. E. P. Gyftopoulos

Graduate Students

R. W. Flynn
R. A. Hill

C. S. Ribbeck

C. E. Wagner
J. C. Woo

1. GENERATION OF A QUIESCENT ARC PLASMA

In our experimental study of the highly ionized plasma produced by a hollow cathode discharge, we have been able to produce a steady-state variable parameter, highly ionized plasma of density 10^{12} & $n \approx 10^{14}/\text{c.c.}$ and $T_i < T_e \approx 20 \text{ ev}$ that operates quies-

cently in a strong magnetic field of several kilogauss. Because of the apparent low noise and the adjustability of the operating parameters, this device possesses some advantages over the Q-machine commonly used for studies of highly ionized plasmas.

The apparatus, described in detail in a previous report,¹ is shown schematically in Fig. XIII-32 and consists of an arc column driven by a hollow cathode discharge at the left. Plasmas of this type often exhibit large scale fluctuations due to instabilities arising from differential drifts. Because the operation of the discharge requires high neutral density and strong electric field near the cathode, oscillations are generally excited at this source region and suppressions of the instability at the original locale is not feasible. The low noise and the high degree of ionization

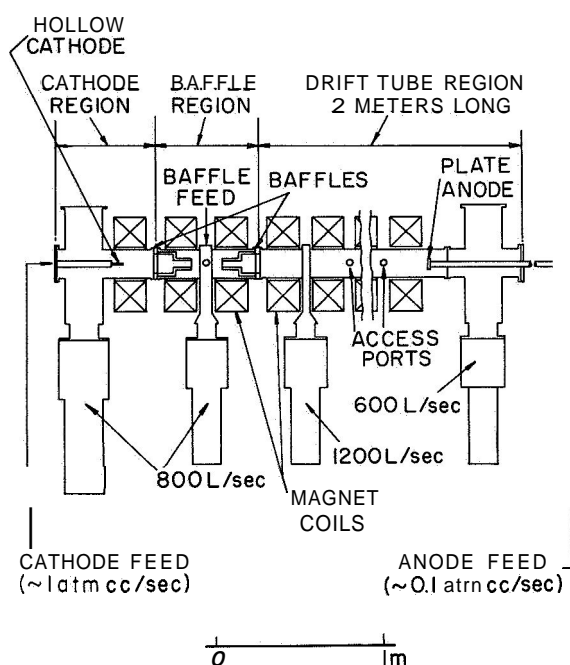


Fig. XIII-32. Schematic view of the apparatus.

features of the plasma result from the considerable separation of the drift-tube working region from the plasma-generation region by a double baffle chamber that damps

*

This work was supported by the National Science Foundation (Grant GK-614).

fluctuations originating at the cathode.

Analysis on such a plasma column in a strong magnetic field has shown that in the weakly ionized state the plasma is unstable against the well-known convective modes (see Kadomstev and Nedospasov). As the value of the ion confinement factor (the dimensionless product of the ion-cyclotron frequency and the ion-collision time) increases, a universal mode dominates and only perturbations of longer and longer wavelength can be **unstable**.² Therefore, in a plasma column of finite dimensions, the system can be operated stably without excitation drift waves.

In order to achieve this condition, it is only necessary to apply a sufficiently strong magnetic field in the baffle region, and at the same time to maintain the neutral pressure low in the working region. The effect of the magnetic field in the baffle region on the frequency spectrum of the fluctuations is clearly demonstrated by the isometric plot of the noise spectrum versus magnetic field, as picked up by a floating electrostatic probe shown in Fig. XIII-33. A strong magnetic field is increased, the dominant harmonics are severely damped and only low-level white noise remains. The effect on the plasma in the working region is illustrated in Figs. XIII-34 and XIII-35 which show the fluctuations in the probe current at various bias. When instabilities are excited in the baffle region, the fluctuations propagate into the drift tube as shown in Fig. XIII-34. When the conditions in the baffle are such that fluctuations are damped there, however, the fluctuation level of the plasma in the drift tube is remarkably low ($\sim 1\%$ rms) and exhibits no dominant frequency. Furthermore, the plasma in the drift tube, which is highly ionized, remains quiescent, irrespective of the magnetic field strength applied there if the neutral background is kept low by rapid pumping.

Since the fluctuation level depends on the magnetic field strength in the baffle region and the background pressure in the drift tube, we show in Fig. XIII-36 a contour map of constant rms noise level in such a space. The map demonstrated our previous remarks regarding the ingredients for the quiescent operation of such a plasma. In order to obtain a high plasma density in the drift tube, a supplementary anode feed was used. Therefore, in Fig. XIII-36 where the contour lines are closely spaced near 10^{-4} torr, the sharp rise in the percentage of fluctuations was not due to increase of fluctuation level (it remains relatively constant), but rather to drop in the steady-state density as the anode feed is cut off. A significant extension of the quiescent operating regime can be achieved by the addition of baffles to isolate the end-plate anode from the working region.

The successful generation of such a plasma represents an experimental demonstration of theoretical predictions of instabilities attributable to differential Hall

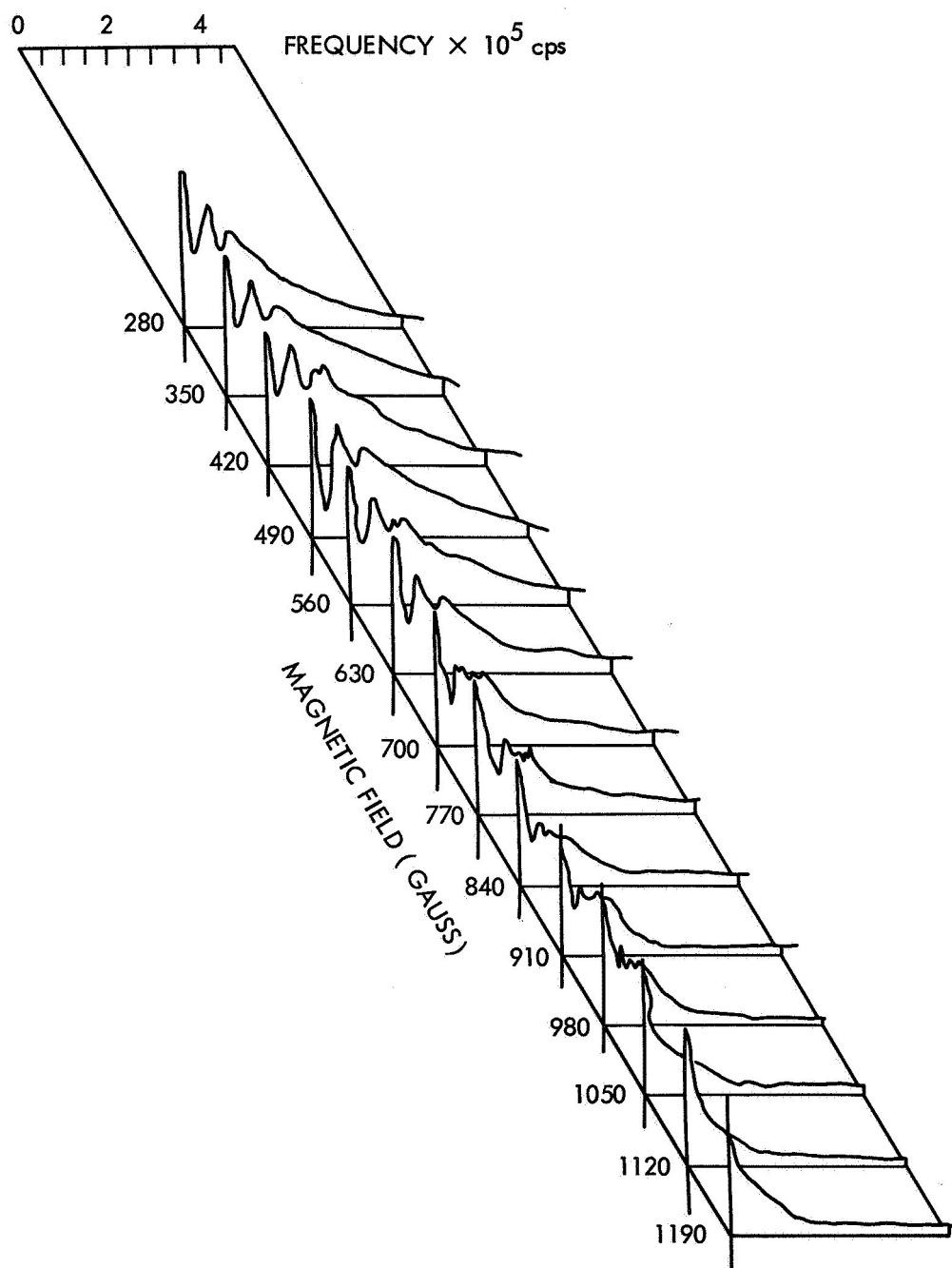


Fig. XIII-33. Noise spectrum vs magnetic field.

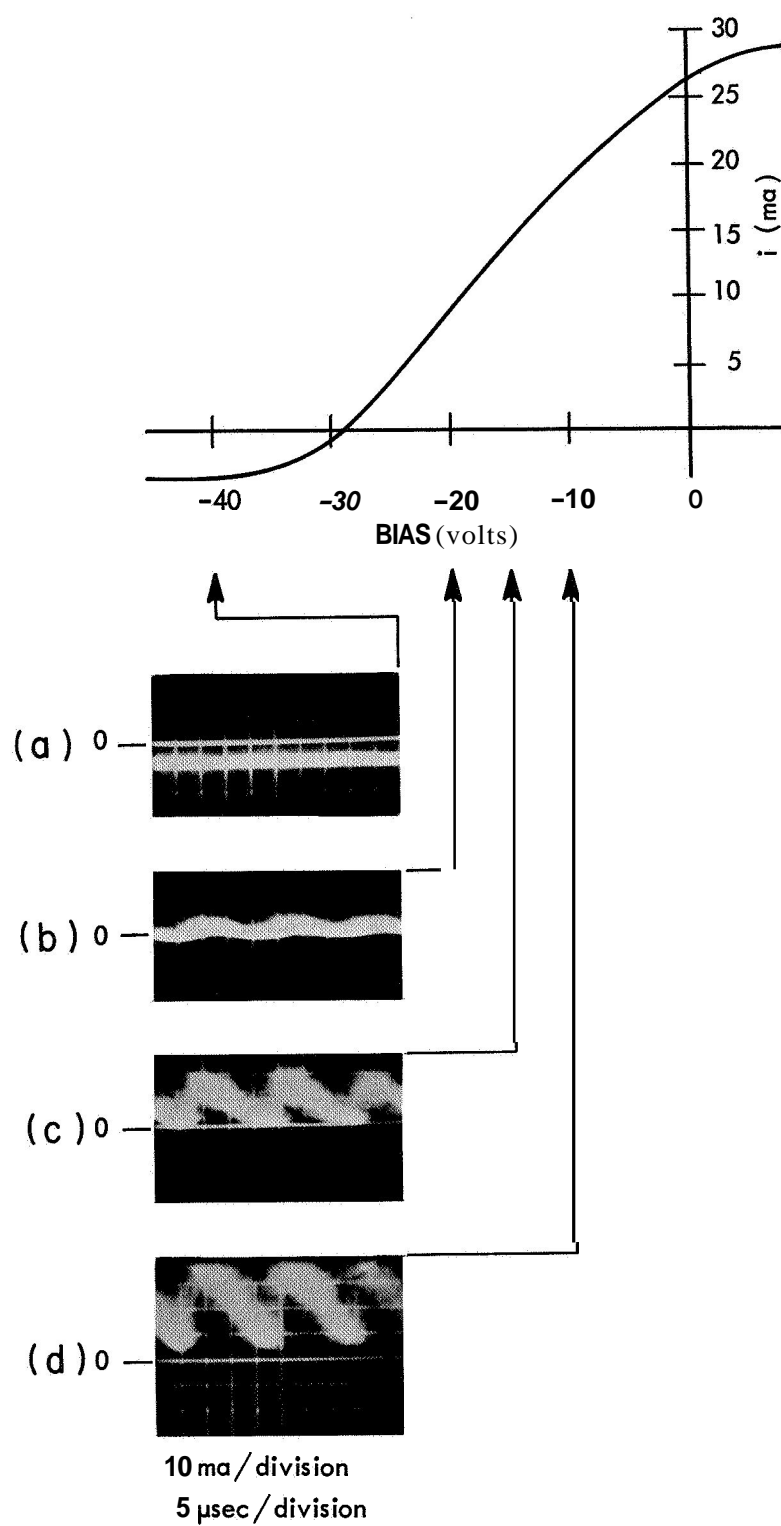


Fig. XIII-34. Probe current in the drift tube with instabilities excited.

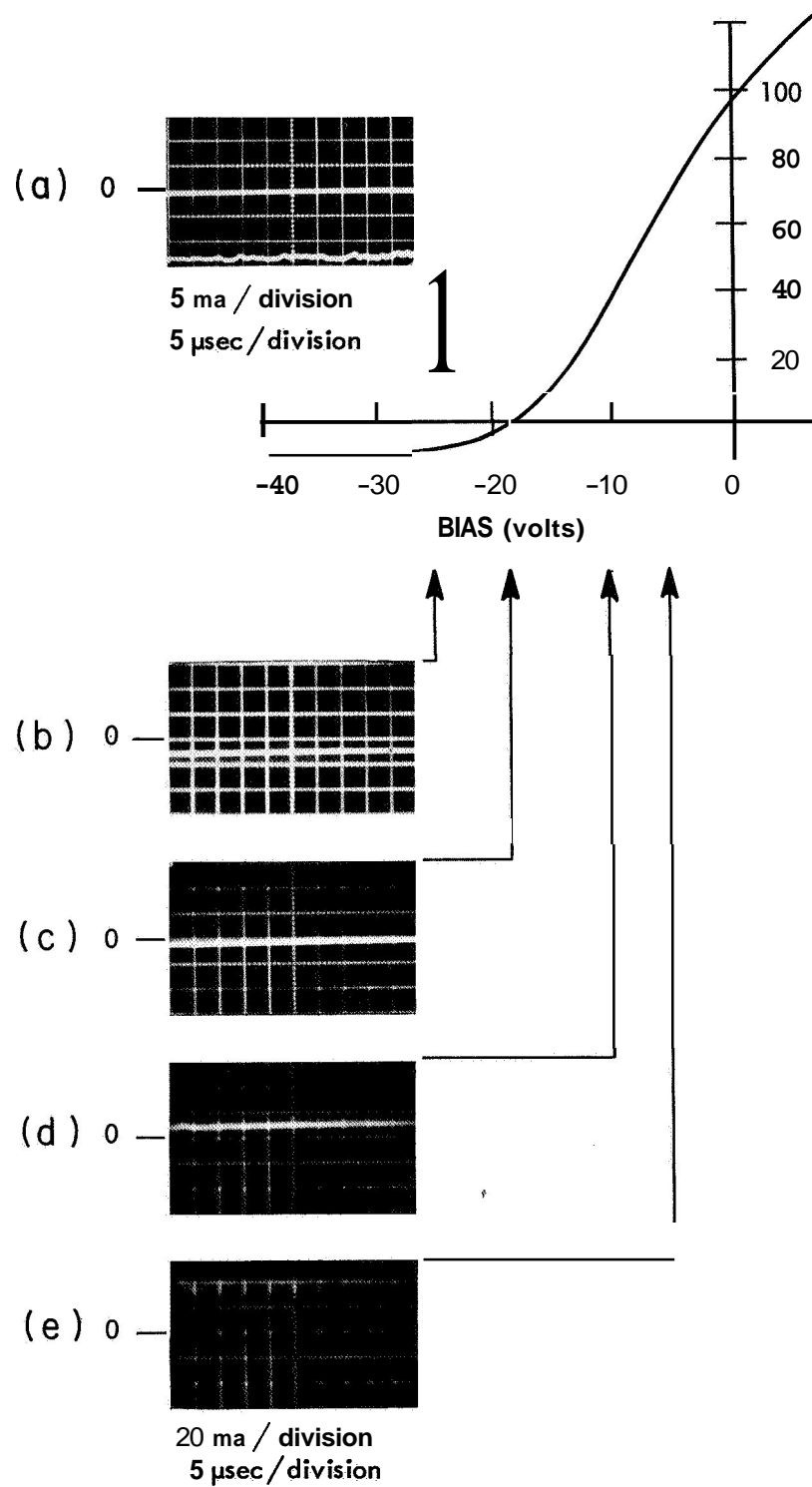


Fig. XIII-35. Probe current in the drift tube during quiescent operation.

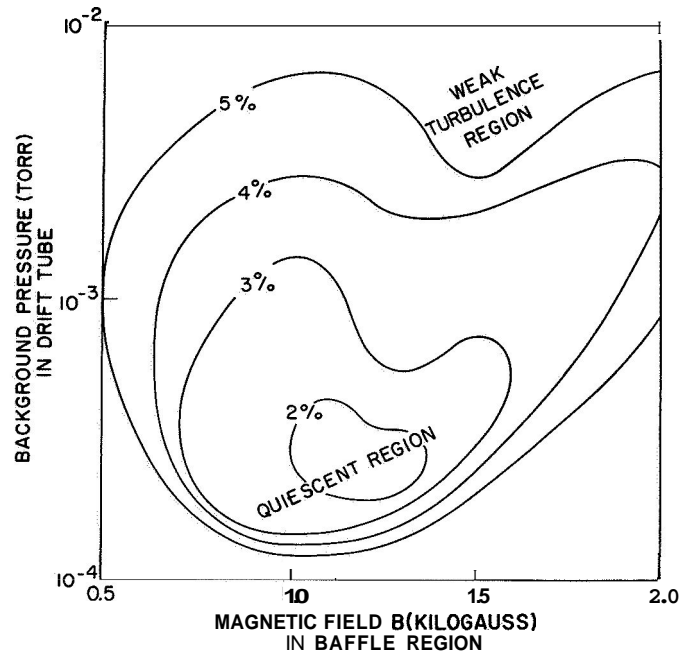


Fig. XIII-36. Contour map of constant rms noise level.

Table XIII-3 Comparison of parameters.

Operating Parameters	Hollow Cathode	Q-Machine	Stellarator
Plasma density n_o (m^{-3})	$<10^{14}$	$<10^{11}$	10^{12}
Electron temperature T_e (ev)	10	0.2	50
Ion temperature T_i (ev)	-1	0.2	0.2 - 100
Magnetic field B (gauss)	10^3	10^3	$1 - 4 \times 10^4$
Plasma dimensions			
R (m)	0.1	0.1	0.1
L (m)	1.0	1.0	10
Scaling Parameters			
$n_o \lambda d^3$ (in a Debye sphere)	10^3	10^2	10^5
$(\omega_{pe}/\omega_{ce})^2$	10^2	1	10^{-2}
$\omega_c \tau_e$	10^3	10^{-2}	10^6
$\omega_{ci} \tau_i$	10	10^{-6}	10

drift. Of greater interest, however, is the quiescent plasma itself whose parameters make it a versatile apparatus for experimental studies of plasma physics. In Table XII-3 we summarize the operating and scaling parameters of several plasma systems for comparison.

J. C. Woo, D. J. Rose

References

1. J. C. Woo, Quarterly Progress Report No. 81, Research Laboratory of Electronics, M.I.T., April 15, 1966, pp. 115-121.
2. J. C. Woo (unpublished data).

2. UNIVERSAL INSTABILITY IN A COLLISION-DOMINATED PLASMA

In our analysis of the stability of a highly ionized plasma column, we have rediscovered, and now interpreted, a destabilizing effect arising purely from the existence of a density gradient which in turn produces charge-separation fields that drive plasma into the initial density perturbation. We present here a simple physical derivation for the stability criteria that clearly illustrates the mechanism of this instability.

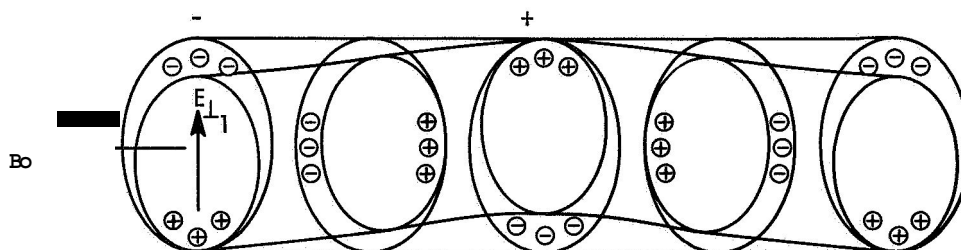


Fig. XIII-37. Effect of perturbing the long plasma column.

Consider a long plasma column confined by a steady magnetic field B_0 in a vacuum tube of transverse dimension x_0 . The length of the tube is infinite and the plasma is inhomogeneous only in the radial direction with the density given by

$$n_0 = N_0 \exp(-x/p). \quad (1)$$

Let this column be perturbed slightly as shown in Fig. XIII-37, then there is a density fluctuation n_1 along the field lines and the plasma electrons diffuse from the high-density region to the low-density region. The massive ions remain in the original locale; thus a potential

(XIII. PLASMAS AND CONTROLLED NUCLEAR FUSION)

$$\phi_1 = T_e n_1 / n_0 \quad (2)$$

is set up between the maximum and minimum density points along the field line. This potential difference also appears across the plasma column as a transverse electric field,

$$E_{\perp 1} = T_e n_1 / n_0 p, \quad (3)$$

in the direction shown.

This first-order electric field $E_{\perp 1}$ produces a drift of the entire plasma column in the $E_{\perp 1} \times B_0$ direction as shown in Fig. XIII-38. Because of the difference in the Hall mobility of the electrons $b_e / \omega_e \tau_e$ and of the ions $\omega_i \tau_i b_i / (1 + \omega_i^2 \tau_i^2)$, a charge imbalance grows at the rate

$$\frac{\partial}{\partial t} [e(n_e - n_i)] = \left[\frac{b_e}{\omega_e \tau_e} - \frac{\omega_i \tau_i b_i}{(1 + \omega_i^2 \tau_i^2)} \right] \frac{T_e}{p_z} n_i. \quad (4)$$

Here, ω_e and ω_i are the cyclotron frequencies, and τ_e and τ_i are the collision times of the electrons and ions.

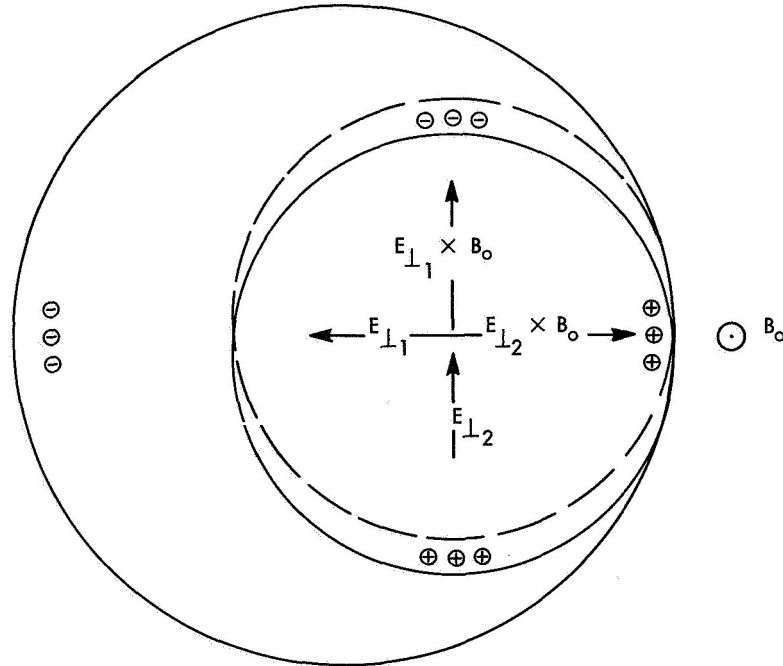


Fig-. XIII-38. Drift of plasma column produced by first-order electric field $E_{\perp 1}$.

The electric field $E_{\perp 2}$ resulting from the charge separation accelerates the plasma ions into the initial perturbation n_1 at the rate

$$\begin{aligned} \frac{\partial^2}{\partial t^2} n_1 &= \frac{a_i \tau_i b_i}{(1 + \omega_i^2 \tau_i^2)} \frac{\partial E_{\perp 2}}{\partial t} \nabla \cdot n_0 \\ &= \frac{\omega_i \tau_i b_i}{(1 + \omega_i^2 \tau_i^2)} \frac{e}{\epsilon_0} T_e \frac{n_0}{p} \frac{n_1}{p^2} \left[\frac{b_e}{\omega_e \tau_e} - \frac{\omega_i \tau_i b_i}{(1 + \omega_i^2 \tau_i^2)} \right] \end{aligned} \quad (5)$$

which accounts for the growth of the perturbation.

The stability criteria are determined by the competition between this growth rate and the damping effects. The charge imbalance produces a second potential also of the order of $T_e n_1 / n_0$. The ion transverse current from that resulting electric field, plus electron axial current, tends to reduce the charge build-ups. The net stabilizing flow is

$$\left[b_e k^2 + \frac{b_i}{(1 + \omega_i^2 \tau_i^2)} \gamma^2 \right] T_e n_0.$$

Thus the growth rate of the electric field $E_{\perp 2}$ is reduced, and the damping effect on the density perturbation is given by

$$- \frac{\partial^2 n_1}{\partial t^2} = b_i \frac{e}{\epsilon_0} T_e n_1 \left[k^2 b_e + \frac{b_i}{(1 + \omega_i^2 \tau_i^2)} \gamma^2 \right] \frac{n_0}{p}. \quad (6)$$

The net rate of change of the density perturbation is, therefore,

$$\frac{\partial^2 n_1}{\partial t^2} = \left\{ \frac{\omega_i \tau_i}{(1 + \omega_i^2 \tau_i^2)} \left[\frac{b_e}{\omega_e \tau_e} - \frac{\omega_i \tau_i b_i}{(1 + \omega_i^2 \tau_i^2)} \right] \frac{1}{p^2} - \left[b_e k^2 + \frac{b_i}{(1 + \omega_i^2 \tau_i^2)} \gamma^2 \right] \right\} \frac{e}{\epsilon_0} T_e n_1 \frac{n_0}{p} b_i \quad (7)$$

from which we obtain the stability criterion

$$\frac{p^2 \left[b_e k^2 + \frac{b_i}{(1 + \omega_i^2 \tau_i^2)} \gamma^2 \right] (1 + \omega_i^2 \tau_i^2)}{\omega_i \tau_i \left[\frac{b_e}{\omega_e \tau_e} - \frac{\omega_i \tau_i b_i}{(1 + \omega_i^2 \tau_i^2)} \right]} > 1. \quad (8)$$

(XIII. PLASMAS AND CONTROLLED NUCLEAR FUSION)

A more rigorous analysis² gives for the stability criterion

$$p^2 \frac{k^2}{\gamma^2} \frac{\left[T_e \left(\frac{\pi^2}{x_0^2} + \gamma^2 + \frac{1}{2p^2} \right) + T_i \left(\frac{\pi^2}{x_0^2} + \gamma^2 \right) \right] \left[b_e k^2 + \frac{b_i}{(1 + \omega_i^2 \tau_i^2)} \left(\frac{\pi^2}{x_0^2} + \gamma^2 + \frac{1}{2p^2} \right) \right]}{\left[\omega_i \tau_i k^2 T_e - T_i \left(\frac{\pi^2}{x_0^2} + \gamma^2 \right) \right] \left[\frac{b_e}{\omega_e \tau_e} - \frac{\omega_i \tau_i b_i}{(1 + \omega_i^2 \tau_i^2)} \right]} \quad (9)$$

In the limit $T_i = 0$ and with differences in the geometric factors $\frac{1}{\gamma}$ and x_0 ignored, Eqs. 8 and 9 are identical except for a factor $(1 + \omega_i^2 \tau_i^2)$, which is of the order of unity in the regime where this instability is important.

Since the growth of the perturbation requires the feeding of the ions into the original perturbation via Hall mobility and the perturbed field $E_{\perp 2}$, this instability can occur only when $\omega_i^2 \tau_i^2 = 1$. If $\omega_i^2 \tau_i^2 \gg 1$, the differential drift vanishes and no charge separation can occur. We note that the instability is initiated by the development of a longitudinal electric field because of the rapid diffusion of the electrons, and therefore the instability is analogous to the destabilization caused by longitudinal electron thermal conductivity (called "thermal Force" in Russian publications) considered by Galeev, Oraveskii, and Sagdeev.¹

J. C. Woo, D. J. Rose

References

1. A. A. Galeev, V. N. Oraveskii and R. Z. Sagdeev Soviet Phys. - JETP 17, 615 (1963).
2. J. C. Woo (unpublished).

XIV. ENERGY CONVERSION RESEARCH*

A. Power Systems with Liquid-Metal Generators

Academic and Research Staff

Prof. G. A. Brown
Prof. E. S. Pierson

Graduate Students

E. K. Levy
R. J. Thome

1. MAGNETOHYDRODYNAMIC POWER GENERATION FOR NUCLEAR-POWERED SEA-GOING VESSELS

Introduction

An initial feasibility study has been conducted to determine whether the advantages offered by an MHD conversion system for marine use are worth further investigations.¹ In this investigation a gas Brayton MHD cycle and one example of a liquid-metal Rankine MHD cycle were used: required were a power output of 11 megawatts and a given nuclear reactor capable of transmitting a temperature of 1500°K to the cooling fluid. This report describes these analyses briefly and gives the results.

Brayton Cycle MHD Power System

A theoretical investigation of the Brayton gas cycle was performed, with the working fluid of the MHD generator utilized as the reactor coolant, as illustrated in Fig. XIV-1

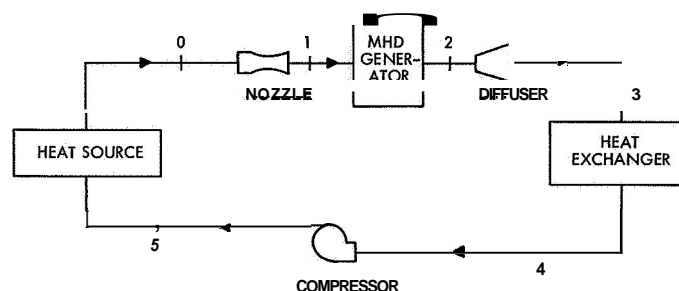


Fig. XIV-1. Brayton cycle MHD power generation system.

*

This work was supported by the U. S. Air Force (Research and Technology Division) under Contract AF33(615)-3489 with the Air Force Aero Propulsion Laboratory, Wright-Patterson Air Force Base, Ohio.

(XIV. ENERGY CONVERSION RESEARCH)

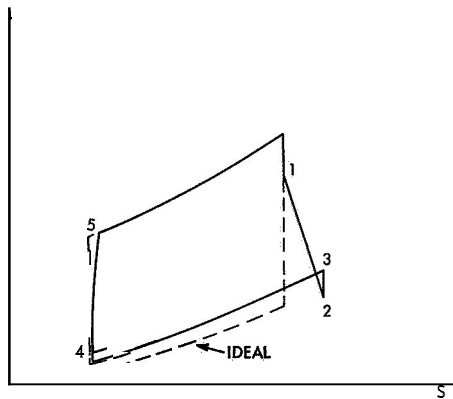


Fig. XIV-2. Diagram for the MHD Brayton cycle.

with its corresponding thermodynamic states diagrammed in Fig. XIV-2. The fluid undergoes isentropic expansion through the nozzle before the adiabatic extraction of energy in the MHD generator. The fluid is then diffused, transforming a large part of the remaining dynamic head to static pressure head, passed through a cooling heat exchanger, and finally returned to the heat source by means of an adiabatic compression process.

To provide the necessary electrical conductivity (for satisfactory operation of the MHD generator), the working fluid is seeded with a very small percentage of an easily ionizable material (cesium, potassium) and then subjected to an extra thermal ionization process. In selecting a working fluid, one must choose one that is capable of withstanding this treatment and still maintaining satisfactory heat-transfer characteristics. Added to these restrictions, the fluid must be available, be compatible with the nuclear reactor, and have thermal conductivity qualities that take into account the volumetric limitations of ships. As a result, we found that the gas that best suited these features at the temperatures and pressures considered was helium seeded with either cesium or potassium.

Utilizing this working fluid, we conducted thermodynamic cycle analyses under the assumption of an available reactor temperature of 1500°K and with a power requirement of 11 megawatts. Significant results are cycle efficiencies of approximately 20 per cent and magnetic field requirements of approximately 40 kilogauss. This efficiency is comparable with present steam turbine systems, but the large magnetic field indicates the need for superconducting magnets. The refrigeration requirements for this magnet were not included in the study, and it is feared that the power which would be necessary to support this would reduce the over-all efficiency below acceptable levels. Furthermore, the required electrical conductivity of the working fluid ($\sim 600 \text{ mhos/m}$) may be higher than is practicable under current ionization methods; this would result in an even higher magnetic field in the MHD generator. Thus, further investigation of these problem areas is needed before a substantial conclusion can be reached concerning the future use of this MHD cycle.

Rankine Cycle MHD Power System

Recent interest in liquid-metal MHD power cycles has resulted in several proposed Rankine cycles utilizing an MHD generator to convert from mechanical to electrical energy. One of these systems, the one-component, two-phase MHD cycle proposed by

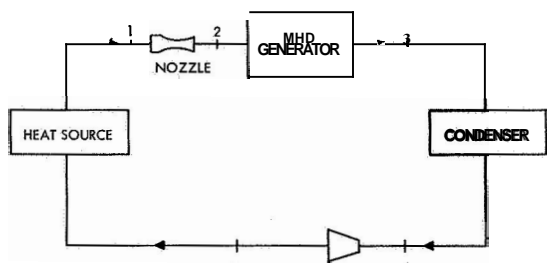


Fig. XIV-3. One-component, two-phase MHD Rankine power cycle,

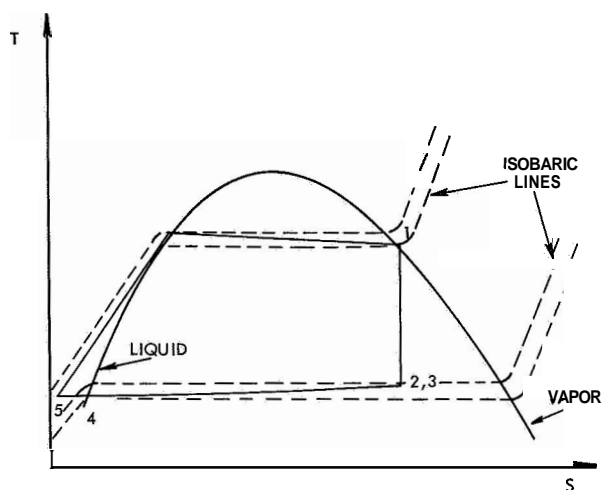


Fig. XIV-4. Thermodynamic state diagram for MHD Rankine cycle.

Petrack and Lee,¹ was chosen to typify a Rankine cycle analysis, and is schematically illustrated in Fig. XIV-3, and the thermodynamic diagram is shown in Fig. XIV-4. It is not felt that this cycle is necessarily better than other suggested liquid-metal MHD power cycles, but it was analyzed as an example of an MHD Rankine cycle. In this system, a two-phase mixture leaves the reactor heat source as a saturated vapor and increases its kinetic energy through the nozzle. The mixture then passes through the MHD generator (still in its two-phase state) where the electrical energy is removed, and into the condenser where the fluid is condensed into its liquid state and returned to the reactor by means of a diffuser.

'Because the fluid in the MHD generator turns out to be a two-phase flow, about which little is known, hearty assumptions concerning its electrical conductivity were necessary to complete the cycle. It is noteworthy here to mention that with other liquid-metal

MHD power cycles proposed by Elliott,³ and by Jackson and Brown,⁴ we are not faced with the particular problem of two-phase flow in the MHD generator, although they do involve troublesome components that are unnecessary in the one-component, two-phase MHD cycle. Since all of the liquid-metal cycles are still under intensive experimentation, it is not fair to pick any of them as superior at this early stage of development, but rather to bear in mind the particular advantages and complications of each.

Keeping this in mind, we conducted cycle analyses on the one-component, two-phase system, utilizing mercury and potassium as the working fluids. Significant results indicate that the thermodynamic cycle efficiency increases with the fluid's mixture quality in the generator, but the electrical conductivity of the two-phase mixture decreases markedly with increasing mixture quality, and thus the cycle may become impractical at the competitive thermodynamic efficiencies. Mercury showed a higher

(XIV. ENERGY CONVERSION RESEARCH)

efficiency than potassium (maximum mercury, 29 per cent; maximum potassium, 22 per cent), but the working pressures of mercury were extremely high (–3000 psi) which would militate against its use on a marine vessel. Both fluids resulted in abnormally low DC terminal voltages (–30 volts) and hence required the use of large current busses – an item that needs to be resolved if future use is anticipated.

An advantage of a Rankine MHD cycle is its capability to generate AC power (through the use of an MHD induction generator), as well as low-voltage DC power. This induction MHD generator, limited to liquid-metal flows, could be wound for usable voltages at suitable frequencies (i.e., 60 cps).⁵ The problem still remains, however, for the induction generator, as well as for the DC conduction generation, of including the effects of all loss mechanisms and simultaneously matching the generator to the thermodynamic cycle.

Usefulness as a Marine Power Source

Because steam turbine systems on ships are inherently noisy, it is felt that the MHD conversion scheme, which utilizes electric motors, would greatly resolve this undesirable feature, with the gas Brayton cycle believed to be somewhat quieter than any of the proposed liquid-metal Rankine cycles. Because higher temperatures are now available (and required) for the MHD cycles, the systems must contain materials to obviate this problem and the associated fluid-reaction problem. These materials problems are still unsolved, although giant strides have been made in this direction, and there is no reason to believe that future developments in this field will not overcome this present restraint. Because future effective development of the steam cycle seems unlikely, while the MHD cycle is just beginning to open up new avenues for investigation there is now no strong reason to believe that future MHD systems will not far surpass in efficiency the present steam turbine systems. In conclusion, we suggest that the possibility that this type of power generation will eventually replace the steam turbine system is high, and now is the time to initiate further studies aimed at achieving more practical results than are now possible.

J. D. Hutchinson, E. S. Pierson

References

1. J. D. Hutchinson, "Magnetohydrodynamic Power Generation for Nuclear-Powered Sea-Going vessels," NAV. E. Thesis, Department of Naval Architecture and Marine Engineering, M. I. T., June 1966.
2. M. Petrick and K. Y. Lee, "Performance Characteristics of a Liquid-Metal MHD Generator," ANL-6870, Argonne National Laboratory, Argonne, Illinois, July 1964.
3. D. G. Elliott, "Two-Fluid Magnetohydrodynamic Cycle for Nuclear-Electronic Power Conversion," Am. Rocket Soc. J. 32, 6(1962).

4. W. D. Jackson and G. A. Brown, "Liquid-Metal Magnetohydrodynamic Power Generator Utilizing the Condensing Ejector," Patent Disclosure, M. I. T., Cambridge, Mass., October 1961.
5. E. S. Pierson, "The MHD Induction Machine," ScD. Thesis, Department of Electrical Engineering, M. I. T., September 1964; also AFAPL-TR-65-107, May 1966.

2. INTERACTION OF A SINGLE SPHERE OR CYLINDER WITH TRAVELING MAGNETIC FIELD

As a first step in the study of the mist flow MHD induction machine, the interaction between a rigid conducting sphere and a traveling magnetic field is considered.

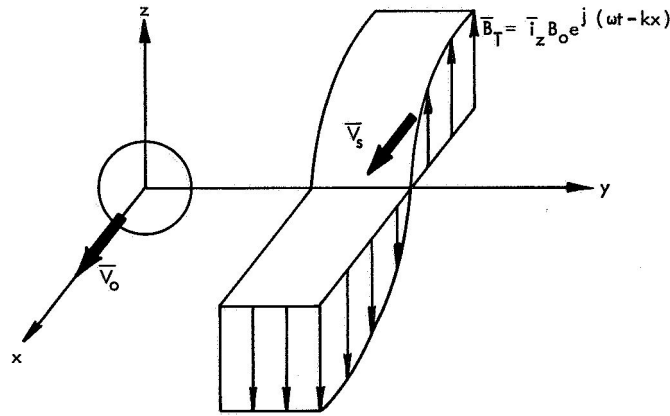


Fig. XIV-5. Configuration for sphere-field interaction.

Specifically, the configuration consists of a sphere traveling with the constant velocity $\vec{V}_o = \vec{i}_x V_o$ in an applied magnetic field with the component $\vec{B}_T = \vec{i}_z B_o e^{j(\omega t - kx)}$ transverse to the direction of motion of the sphere as shown in Fig. XIV-5. Here, ω is the frequency, $A = \frac{2\pi}{k}$ is the wavelength, and the field travels in the x-direction with the phase velocity $V_s = \frac{\omega}{k}$. The sphere is assumed to be small relative to the wavelength of the applied field (that is, $D \ll A$), and to have the permeability of free space.

Since $\frac{D}{A} \ll 1$, the applied field in the vicinity of the sphere may be represented by

$$\vec{B}_a = B_o [\vec{i}_z (j + kx) + \vec{i}_x kz] e^{j\omega t} \quad (1)$$

in the reference frame attached to the sphere, where

$$s = \frac{V_s - V_o}{V_s} \quad (2)$$

(XIV. ENERGY CONVERSION RESEARCH)

is the normalized velocity difference between the field and sphere.

The problem is governed by Maxwell's equations with the displacement currents neglected (the usual **MHD** approximation), and as such requires the solution of the vector diffusion equation within the conductor and Laplace's equation in the surrounding space, subject to four boundary conditions. The usual method for solving problems of this type is to utilize a coordinate system that allows the coordinate surfaces to match the boundaries of the problem and **also** allows separation of variables in the governing equations. The problem could not be solved by this standard technique as a result of the **"conflict"** between the two-dimensional nature of the applied field and the three-dimensional nature of the body; hence, an approximate method was developed.

Since the governing equations are linear, the applied field (1) may be thought of as consisting of two parts, a uniform field and a perturbation,

$$\underline{\underline{B}}_a = \underline{\underline{B}}_{ua} + \underline{\underline{B}}_{pa} = \bar{i}_z j B_o + B_o (\bar{i}_z kx + \bar{i}_x kz), \quad (3)$$

where complex notation is used and the $e^{j\omega t}$ is omitted. Then the total magnetic field is represented by (3) plus the induced magnetic field associated with each part of the applied field,

$$\underline{\underline{B}} = \underline{\underline{B}}_a + \underline{\underline{B}}_i = \underline{\underline{B}}_{ua} + \underline{\underline{B}}_{ui} + \underline{\underline{B}}_{pa} + \underline{\underline{B}}_{pi}. \quad (4)$$

If the current density distribution associated with $\underline{\underline{B}}_{ua}$ + $\underline{\underline{B}}_{ui}$ is designated $\underline{\underline{J}}_u$, and that associated with $\underline{\underline{B}}_{pa}$ + $\underline{\underline{B}}_{pi}$ is $\underline{\underline{J}}_p$, then the net time-average force on the sphere is

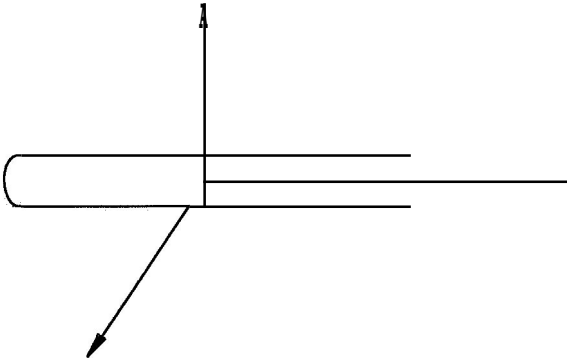
$$\underline{\underline{F}} = \frac{1}{2} \text{Re} \left\{ \iiint_V \left[\underline{\underline{J}}_u \times (\underline{\underline{B}}_{ua} + \underline{\underline{B}}_{ui})^* + \underline{\underline{J}}_p \times (\underline{\underline{B}}_{pa} + \underline{\underline{B}}_{pi})^* + \underline{\underline{J}}_u \times (\underline{\underline{B}}_{pa} + \underline{\underline{B}}_{pi})^* + \underline{\underline{J}}_p \times (\underline{\underline{B}}_{ua} + \underline{\underline{B}}_{ui})^* \right] dv \right\}. \quad (5)$$

For any body that is symmetric with respect to the three major planes through the origin, there can be no net force when either the uniform **or** the perturbation field alone is applied. As a result, the first two terms in (5) contribute nothing when the integration is carried out. When both the uniform and perturbation fields are applied, the net force arises only from the integral over the terms that couple the two fields.

In the case of a sphere, $\underline{\underline{B}}_{ui}$ and $\underline{\underline{J}}_u$ may be found when $\underline{\underline{B}}_{ua}$ is given, but $\underline{\underline{B}}_{pi}$ and $\underline{\underline{J}}_p$ cannot be found (in practice), given $\underline{\underline{B}}_{pa}$. In short, the net force cannot be determined exactly, but it is reasonable to ask if there are conditions under which the contribution of the $\underline{\underline{J}}_u \times \underline{\underline{B}}_{pa}$ term is large enough to be a reasonable approximation to the exact force. To answer this question, the approximate net force

$$\bar{F}_{upa} = \frac{1}{2} \operatorname{Re} \left\{ \iiint_v \underline{J}_u \times \underline{B}_{pa}^* dv \right\} \quad (6)$$

is determined for the case of a cylinder and compared with the exact force (5) for that case.



For the cylinder of infinite length (Fig. XIV-6) the exact time-average force per unit length is calculated and written in dimensionless form as

$$\bar{i}_x \bar{F} = \frac{\bar{F}}{\left(\frac{\pi}{4} D^2\right) \left(\frac{B_o^2}{\mu \lambda}\right)} = \bar{i}_x K_{cT} \left(sR_m, \frac{D}{\lambda}\right), \quad (7)$$

where

$$K_{cT} = 2\sqrt{2} \pi \frac{b}{U} \left[\frac{a}{b} + \frac{\pi^2}{2} \left(\frac{D}{\lambda}\right)^2 \right] \quad (8)$$

$$sR_m = 4U^2 = \mu \sigma s \omega D^2 \quad (9)$$

$$a = \frac{\operatorname{ber}_0 U (\operatorname{bei}_1 U + \operatorname{ber}_1 U) + \operatorname{bei}_0 U (\operatorname{bei}_1 U - \operatorname{ber}_1 U)}{[(\operatorname{ber}_0 U)^2 + (\operatorname{bei}_0 U)^2]} \quad (10)$$

$$b = \frac{\operatorname{ber}_2 U (\operatorname{ber}_1 U - \operatorname{bei}_1 U) + \operatorname{bei}_2 U (\operatorname{bei}_1 U + \operatorname{ber}_1 U)}{[(\operatorname{bei}_1 U)^2 + (\operatorname{ber}_1 U)^2]}, \quad (11)$$

and $\operatorname{ber}_\nu U$ and $\operatorname{bei}_\nu U$ are Kelvin functions of the first kind of ν . It may be shown that for

$$\frac{\pi^2}{2} \left(\frac{D}{\lambda}\right)^2 \ll 1, \quad (12a)$$

K_{cT} becomes

(XIV. ENERGY CONVERSION RESEARCH)

$$K'_{cT} = 2\sqrt{2} \tau \frac{a}{U}. \quad (12b)$$

When the approximate force (6) was determined for the cylinder, the result was found to be identical to (12b); hence, the only restriction on the approximate solution is the condition (12a).

Application of this technique to the case of the sphere yields

$$\bar{i}_x \bar{F} = \frac{\bar{F}}{\left(\frac{\pi D^3}{6}\right) \left(\frac{B_o^2}{\mu \lambda}\right)} = \bar{i}_x K_s(sR_m), \quad (13)$$

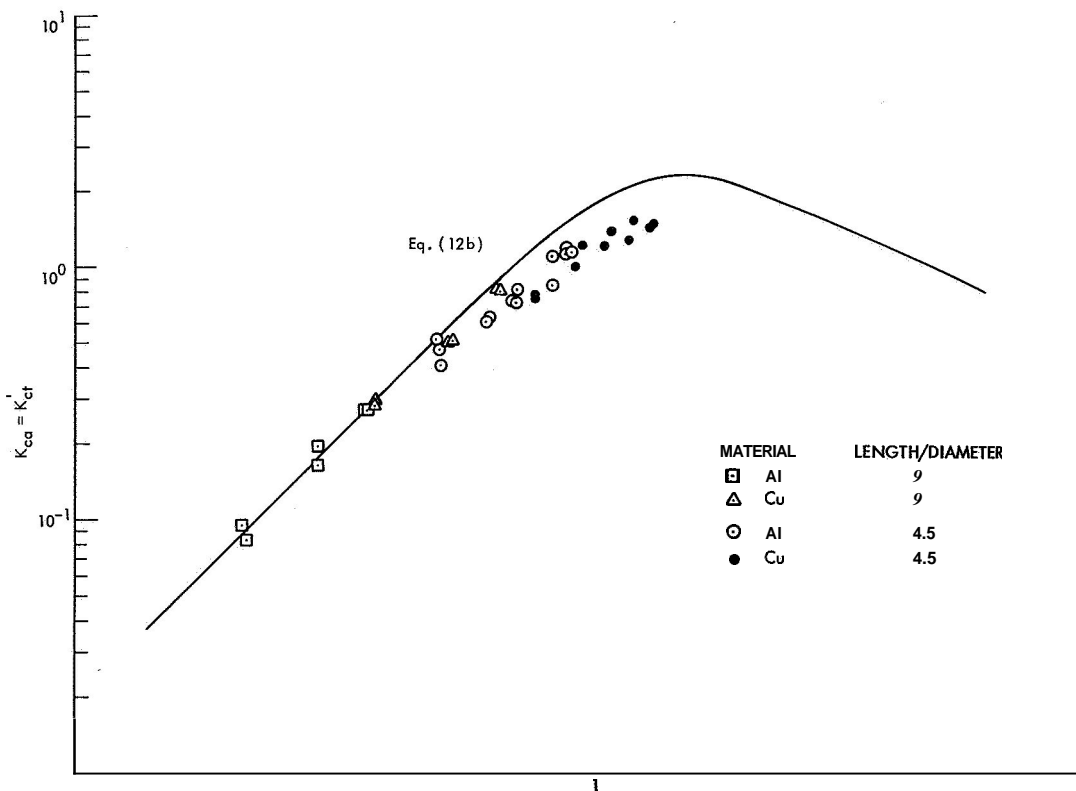
where

$$K_s(sR_m) = \frac{9}{4} \frac{\pi}{u^2} \left\{ 1 + u \frac{[\tan u(\tanh^2 u - 1) - \tanh u(\tan^2 u + 1)]}{[\tanh 2u \tan 2u]} \right\}, \quad (14)$$

and

$$sR_m = 8u^2 = \mu \sigma s \omega D^2. \quad (15)$$

The "K" functions for the case of the small cylinder (12) and the small sphere (14) are plotted in Figs. XIV-7 and XIV-8, respectively, together with the experimental data.



The latter were obtained by determining the force on a cylinder or sphere suspended in the field produced by the coil system designed by Porter.' The characteristics of the conductors used are given in the figures.

In Fig. XIV-7, agreement is quite good over the lower range of sR_m . Departure in

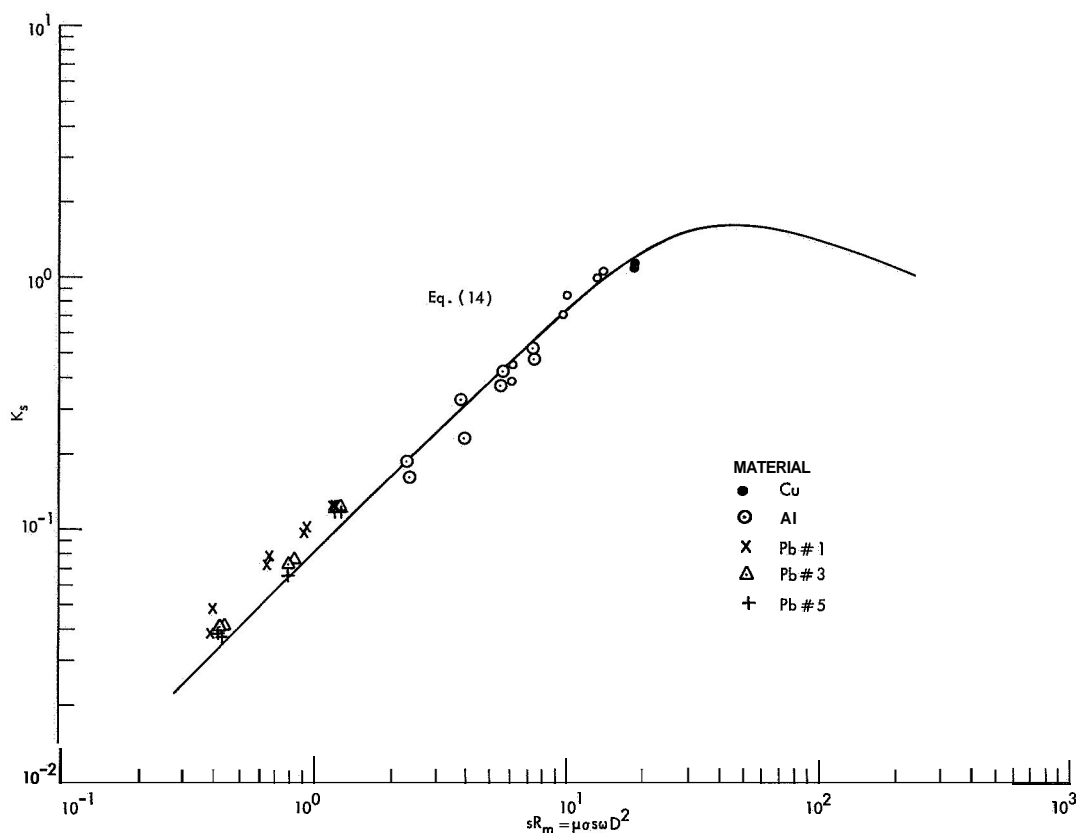


Fig. XIV-8. Correlation of theory with experiment for small spheres. $\frac{D}{\lambda}$, diameter of the test sphere, 1 inch.

the higher range may be attributed to length-to-diameter ratios that were too small to correspond to the two-dimensional model assumed in the solution.

For the sphere, Fig. XIV-8, disagreement is largest at low sR_m , where lead spheres were used. These spheres were cast, so that there was no guarantee of homogeneity, and their surfaces were pockmarked, which would reduce their effective diameter. Experimental error was also largest in this range, since the measured force was smallest.

A solution for the case of the sphere was also obtained by constructing a lumped-parameter model of the sphere and determining the force by the techniques of lumped-parameter electromechanics. This solution appears to converge to (14), so that this technique may be expected to be useful in any similar problem in which the direction,

(XIV. ENERGY CONVERSION RESEARCH)

or approximate direction, of the current density is **known** at each point in the conductor.

The results above indicate that the single-body interaction is fairly well understood. Therefore, this study will be extended theoretically to cover n noninteracting spheres with a size and velocity distribution, to gain an insight into the characteristics of a mist flow in a traveling magnetic field.

R. J. Thome

References

1. R. P. Porter, "A Coil System for an MHD Induction Generator," S. M. Thesis, Department of Electrical Engineering, M. I. T., 1965.

XIV. ENERGY CONVERSION RESEARCH*

B. Alkali-Metal Magnetohydrodynamic Generators

Academic and Research Staff

Prof. J. L. Kerrebrock
Prof. M. A. Hoffman
Prof. G. C. Oates

Graduate Students

R. Decher
M. L. Hougen

D. J. Vasicek
G. W. Zeiders, Jr.

1. STATUS OF RESEARCH: ALKALI-METAL VAPOR MAGNETOHYDRODYNAMIC GENERATORS

During the last quarter a second full-scale run of the large nonequilibrium generator was completed. All components of the facility operated satisfactorily. The test conditions were: stagnation pressure 4.5 atm, stagnation temperature 2000°K, Mach number 2.1, mass-flow rate 0.360 ks^{-1} of He.

The generator was operated at open circuit, and with 3-, 10-, and 25-ohm loads. The open-circuit voltage was between 50 and 70 volts, as compared with ideal values of 500-700 volts at the first and last electrode pairs. When the generator was loaded, the voltage remained nearly constant, while the current per electrode pair increased along the channel, from entrance to exit. For the 3-ohm loads (3 ohms on each electrode pair) the current varied from 5 amps to ~17 amps. The power for this condition was approximately 5 kilowatts.

This power, while greater than that expected from an equilibrium generator at the same load condition, is much less than that expected from the nonequilibrium generator. It is believed that the low-open-circuit voltage and the resultant low power were due to shorting either in the side-wall boundary layer or in the wall itself. In this generator the wall was made of boron nitride.

To correct this difficulty, new side walls, of an iron peg-wall construction, have been made. The generator was operated again near the end of May 1966.

During this quarter, the MHD pump for the potassium loop has been rebuilt to provide the higher pressures required for supersonic operation. The supersonic test section is nearly complete. It is expected that the loop will be run during June 1966.

J. L. Kerrebrock

*

This work is supported by the U. S. Air Force (Research and Technology Division) under Contract AF33(615)-3489 with the Air Force Aero Propulsion Laboratory, Wright-Patterson Air Force Base, Ohio.

XIV. ENERGY CONVERSION RESEARCH*

C. Hall Instabilities and Their Effect on Magnetohydrodynamic Generators

Academic and Research Staff

Prof. J. E. McCune

Graduate Students

W. H. Evers, Jr.

1. STABILITY CRITERION FOR MAGNETOACOUSTIC WAVES

It has been possible during the past quarter to extend previous work¹ to develop convenient stability criteria for magnetoacoustic waves in the two-temperature conduction regime. It turns out that one can express the stability condition very simply in terms of the convenient parameters

$$y = \frac{T_{eo}}{T_{go}}, \quad \delta_{\text{eff}}(Y), \quad \gamma, \quad \frac{E_i}{kT_{go}},$$

where T_{eo} and T_{go} are the DC electron and gas temperatures, E_i is the ionization potential, y is the ratio of specific heats, and $\delta_{\text{eff}}(Y)$ is the "effective collisional loss parameter," including the effect of radiation loss in cooling the electron gas. Various models of the response of the two-temperature ionized gas to magnetoacoustic waves have been assumed, which depend primarily on the rate of ionization relaxation and the effect of radiation "damping" on the waves. In each case the stability criterion can be given in the form

$$\begin{array}{l} \text{unstable if and} \\ \text{only if} \end{array} \quad \sqrt{\delta_{\text{eff}} Y} > \hat{P}\left(y, \frac{E_i}{kT_{go}}, \gamma\right).$$

The form of $\hat{P}(Y)$ depends on which model is assumed. Results are illustrated in Fig. XIV-9 and compared with the experimental data of Dethlefsen.²

* This work was supported by the U. S. Air Force (Research and Technology Division) under Contract AF33(615)-3489 with the Air Force Aero Propulsion Laboratory, Wright-Patterson Air Force Base, Ohio.

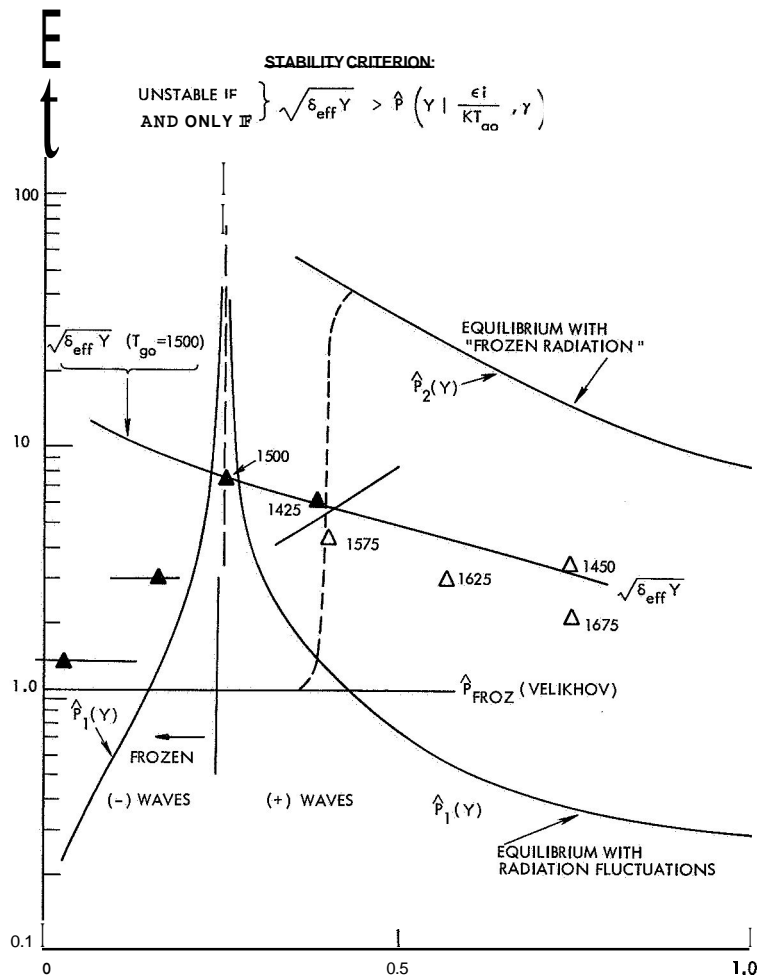


Fig. XIV-9. Stability chart with variables.
Dethlefsen's experimental points:
Quiet Δ , Noisy \bullet .

Up to a value of $Y = 0.4$ we expect the ionization to be frozen, in which case $\hat{E} = \hat{P}_{\text{FROZ}}$ is simply a constant $= \sqrt{2\gamma/3}$. In this regime the magnetoacoustic waves in Dethlefsen's experimental data should have been unstable; Dethlefsen, in fact, observed strong fluctuations (filled-in points). Above $Y = 0.4$, the degree of ionization should be in rough equilibrium with the electron gas and we expect one of two models to apply: with the DC state determined largely by radiation loss, either the waves themselves interact strongly with the radiation or they are unaffected by it. The first model leads to $P_1(Y)$ (see Fig. XIV-9), in which case the waves would be strongly unstable. The second model leads to $P_2(Y)$ which shows that they should be stable. Dethlefsen observed a relatively quiet plasma in this regime, which indicated that the waves are not strongly interacting with

(XIV. ENERGY CONVERSION RESEARCH)

the radiation field. This has helped define the need to determine more accurately the nature of the wave-radiation interaction, and work is progressing along these lines, both experimentally and theoretically.

J. E. McCune

References

1. J. V. Hollweg, Master's Thesis, M.I. T. , 1965.
2. R. F. Dethlefsen, Ph.D. Thesis, M.I.T., 1965.

XV. SPONTANEOUS RADIOFREQUENCY EMISSION FROM HOT-ELECTRON PLASMAS*

Academic and Research Staff

Prof. A. Bers

Graduate Students

C. E. Speck

A. OBSERVATION OF ENHANCED CYCLOTRON RADIATION FROM AN ELECTRON-CYCLOTRON RESONANCE DISCHARGE

We report the results of a preliminary investigation of the enhanced cyclotron radiation observed in the afterglow of our experimental electron-cyclotron discharge apparatus.¹ A low-density ($\sim 10^8/\text{cc}$) plasma is produced by RF breakdown of low-pressure hydrogen gas in a cylindrical microwave cavity. The plasma is confined by a mirror magnetic field (mirror ratio=3) of such value that the exciting RF frequency equals the local electron-cyclotron frequency at certain points within the cavity. Excitation at the cyclotron frequency produces a hot-electron plasma with observed energies around 20-40keV. The radiofrequency source is a magnetron producing 1- μsec pulses at $\sim 3\text{ kMc}$. The source is operated with repetition rate of 1 kc, and at power levels of $\sim 100\text{ kW}$ peak (100 watts average). A more complete description of the apparatus and the plasma that it produces has been reported previously.² In all of the observations reported here, the excitation frequency is 2.85 kMc, and the background pressure of hydrogen is 2×10^{-5} Torr.

Typical plots of the microwave emissions from the plasma are illustrated in Fig. XV-1 for a magnetic field at the center of the cavity of 1100 Gauss. The exciting microwave pulses occur at the extreme right and left ends of the traces and are barely visible. In each of the sequences of Fig. XV-1, the bottom trace is a plot of microwave power developed across a coupling loop on the cavity wall and detected by a microwave diode. The top trace is a plot of detected microwave power that has been passed by a radar transmit/receive switch located in the S-band waveguide which connects the magnetron to the cavity. This switch is a narrow-band device which in these measurements is tuned to the exciting frequency. Thus the plasma is seen to spontaneously emit pulses of microwave energy at or near the exciting frequency during the afterglow period. Figure XV-2 is an expanded view of the early part of the afterglow, and illustrates the facts that the signal across the coupling loop and that across the T/R tube are correlated in time. Thus we conclude that the power measured at the coupling loop also results from microwave emissions at or near the applied frequency.

*

This work was supported by the U. S. Atomic Energy Commission (Contract AT (30-1)-3581).

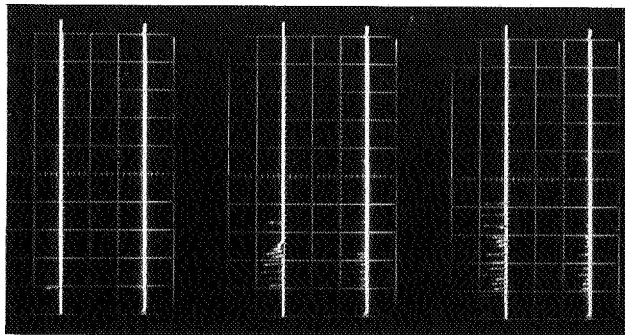


Fig. XV-1.

Characteristics of the observed microwave pulses during the afterglow of these different excitation pulses. Time = $100 \mu\text{sec}/\text{div}$. Top: Signal at transmit/receive switch. Bottom: Signal at coupling loop.

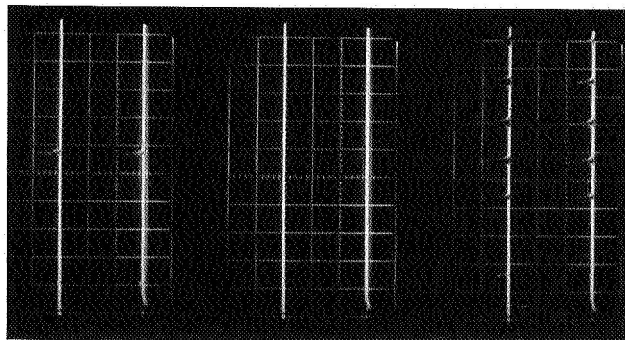


Fig. XV-2.

Observed microwave pulses during the early part of the afterglow. Time = $20 \mu\text{sec}/\text{div}$. Top: Signal at transmit/receive switch. Bottom: Signal at coupling loop.

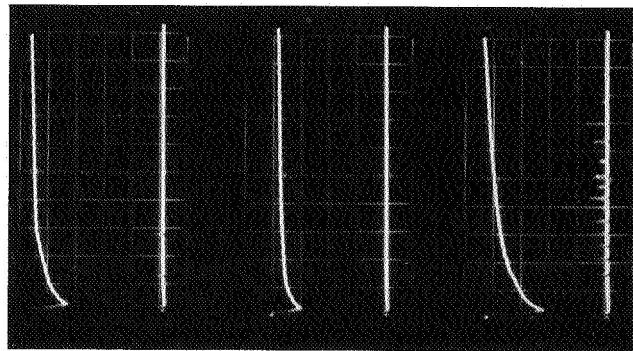


Fig. XV-3.

Correlation between the diamagnetic signal and the observed pulses of radiation when the central magnetic field is 1100 Gauss. Time = $50 \mu\text{sec}/\text{div}$. Top: Diamagnetic signal. Bottom: Signal at coupling loop.

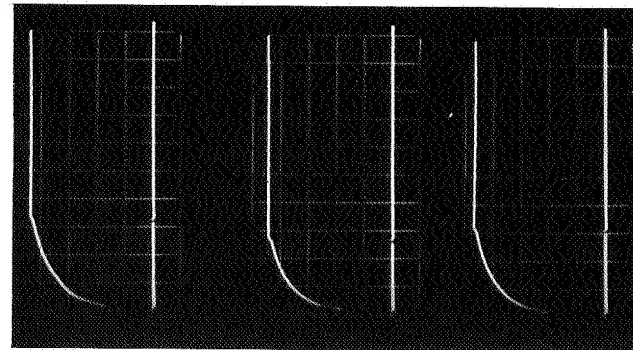


Fig. XV-4.

Correlation between the diamagnetic signal and the observed pulses of radiation when the central magnetic field is 1300 Gauss. Time = $50 \mu\text{sec}/\text{div}$. Top: Diamagnetic signal. Bottom: Signal at coupling loop.

(XV. SPONTANEOUS RF EMISSION FROM HOT-ELECTRON PLASMAS)

In Fig. XV-3 the bottom trace is again the power detected across the coupling loop while the top trace is the diamagnetic signal. This signal which is proportional to the energy density of the plasma is seen to decay quite smoothly, even in the presence of the strong emission of microwaves. This behavior is radically changed if the magnetic field is increased. In Fig. XV-4 the field has been increased to approximately 1300 Gauss at the center. Now, at the instant when the emitted microwave pulse is observed, the diamagnetic signal suddenly drops to zero, thereby indicating that the hot electrons have been lost from the plasma.

No correlation between the visible light radiated by the plasma and the emission of microwave pulses has been observed. This might indicate that the cold electrons are not involved in the instability mechanism.

These preliminary observations suggest that there are two types of instabilities. The first type results in enhanced cyclotron radiation in the form of several pulses of radiofrequency energy in the afterglow. The diamagnetic signal decays smoothly during these pulses. The second type occurs at higher magnetic fields, and is characterized by a single pulse of microwave energy and a sudden loss of the diamagnetic signal. This second type is obviously dependent upon the hot electrons in the plasma.

We are continuing a detailed study of the properties of the plasma and the observed radiation in order to formulate a model for the instabilities.

C. Speck, A. Bers

References

1. T. J. Fessenden, "Electron-Cyclotron Resonance Discharge," Quarterly Progress Report No. 73, Research Laboratory of Electronics, M. I. T., April 15, 1964, pp. 72-80.

B. INSTABILITIES IN THE EXTRAORDINARY WAVES ACROSS THE MAGNETIC FIELD

In this report we formulate the small-signal energy expression for the extraordinary wave that was reported last quarter.' In general, the total small-signal energy in a plasma is given² by

$$\langle w(\omega, \vec{k}) \rangle = \left[\frac{1}{4} \mu_0 |\vec{H}|^2 + \frac{1}{4} \epsilon_0 \vec{E}^* \cdot \frac{\partial}{\partial \omega} (\omega \vec{K}) \cdot \vec{E} \right]_{D(\omega, \vec{k}) = 0}, \quad (1)$$

where \vec{H} and \vec{E} are the small-signal magnetic and electric fields, respectively, and the expression is evaluated only for those real ω and real \vec{k} that satisfy the dispersion relation, $D(\omega, \vec{k}) = 0$. In terms of the elements of the dielectric tensor \vec{K} , it is found that the existence of free waves propagating in the x-direction requires

(XV. SPONTANEOUS RF EMISSION FROM HOT-ELECTRON PLASMAS)

$$\begin{vmatrix} \frac{\omega^2}{c^2} K_{xx} & \frac{\omega^2}{c^2} K_{xy} & 0 \\ -\frac{\omega^2}{c^2} K_{xy} & \frac{\omega^2}{c^2} K_{yy} - k^2 & 0 \\ & & \frac{\omega^2}{c^2} K_{zz} - k^2 \end{vmatrix} \cdot \begin{Bmatrix} E_x \\ E_y \\ E_z \end{Bmatrix} = 0. \quad (2)$$

For the extraordinary wave $E_z = 0$, from which it follows that for nonzero \underline{E} ,

$$\underline{E}_y = -\frac{K_{xx}}{K_{xy}} \underline{E}_x \quad (3)$$

and

$$\frac{k^2 c^2}{\omega} = K_{xx} \frac{K_{xy}^2}{K_{yy}}. \quad (4)$$

Furthermore, Maxwell's equations require

$$\underline{H} = \underline{H}_z \underline{i}_z = \frac{k \underline{E}_y}{\omega \mu_0} \underline{i}_z. \quad (5)$$

Evaluation of Eq. 1 with the use of Eqs. 3, 4, and 5 results in

$$\frac{\langle w \rangle}{\epsilon_0/4} = |\underline{E}_y|^2 \left[2K_{yy} + \omega \frac{\partial K_{yy}}{\partial \omega} + \omega \frac{\partial K_{xx}}{\partial \omega} \frac{|K_{xy}|^2}{K_{xx}^2} \right] \quad (6)$$

or

$$\frac{\langle w \rangle}{\epsilon_0/4} = |\underline{E}_x|^2 \left[2K_{yy} + \omega \frac{\partial K_{yy}}{\partial \omega} + \omega \frac{\partial K_{xx}}{\partial \omega} \frac{|K_{xy}|^2}{K_{xx}^2} \right] \frac{K_{xx}^2}{|K_{xy}|^2}. \quad (7)$$

Here, we have made use of the fact that K_{xx} is pure real and K_{xy} is pure imaginary for real ω and k . Combining Eqs. 6 and 7 yields

$$\frac{\langle w \rangle}{\epsilon_0 |\underline{E}|^2/4} = \frac{\frac{K_{xx}^2}{|K_{xy}|^2} \left[2K_{yy} + \omega \frac{\partial K_{yy}}{\partial \omega} \right] + \omega \frac{\partial K_{xx}}{\partial \omega}}{1 + \frac{K_{xx}^2}{|K_{xy}|^2}}. \quad (8)$$

(XV. SPONTANEOUS RF EMISSION FROM HOT-ELECTRON PLASMAS)

This is the expression for the time-averaged small-signal energy which is to be evaluated along those portions of the dispersion relation which both have real ω and k .

The sign of this expression has been determined for the waves reported last quarter so as to determine the positive (passive) and negative (active) energy branches of the dispersion diagram. The results are indicated in Figs. XII-2 and XII-3 of the previous report¹ as (+) for positive and (-) for negative energy branches. The unstable regions in those figures can now be interpreted as arising from the coupling between the active and passive wave branches.

A. Bers, C. E. Speck

References

1. A. Bers and C. E. Speck, "Instabilities in the Extraordinary Waves across the Magnetic Field," Quarterly Progress Report No. 81, Research Laboratory of Electronics, M.I.T., April 15, 1966, pp. 133-137.
2. W. P. Allis, S. J. Buchsbaum, and A. Bers, Waves in Anisotropic Plasmas (The M.I.T. Press, Cambridge, Mass., 1963).

XVI. INTERACTION OF LASER RADIATION WITH PLASMAS AND NONADIABATIC MOTION OF PARTICLES IN MAGNETIC FIELDS*

Academic and Research Staff

Prof. D. J. Rose
Prof. T. H. Dupree
Prof. L. M. Lidsky

Graduate Students

T. S. Brown
J. D. Callen
J. F. Clarke

D. E. Crane
W. T. Hebel
M. D. Lubin

R. W. Moir
A. A. Offenberger
M. A. Samis

A. LASER RADIATION THOMSON-SCATTERED BY AN ELECTRON BEAM

The experiment described in Quarterly Progress Report No. 79 (pages 143-144) has been completed and the results are summarized in this report.

The purpose of the experiment was to experimentally verify the derived relationship among the angle that the electron beam makes with the observation direction, the velocity of the electrons, and the shift in wavelength of the laser radiation. The components involved in the experiment were completed. The observation system was scanned from 6700 Å to 6800 Å. The angle of observation was varied from 110° to 125°, and the voltage was varied from 800 volts to 1100 volts. The experiment was done by first setting a voltage and angle for the electron beam, making a rough calculation of the position of the shifted wavelength, then scanning the interference filter over the scattered signal envelope in 2.5 Å steps. The signal amplitude was recorded at each wavelength and the wavelength of the center of the envelope was taken to be the scattered wavelength. The results agreed within 1 Å (in 150 Å) with the theoretical predictions, which gives evidence of the correctness of the theoretical transformation equation. Also, the amplitude of the scattered signal agreed with the calculated value. The experiment is discussed more fully in the author's S.M. thesis entitled "Study of Laser Radiation Thomson-Scattered by an Electron Beam," conducted in the Department of Nuclear Engineering and the Research Laboratory of Electronics of the Massachusetts Institute of Technology.

M. A. Samis

B. NONADIABATIC TRAPPING EXPERIMENT

1. Resonant-Particle Measurements

During the past quarter, considerable progress has been made in determining the modes of particle escape from the nonadiabatic trap described in Quarterly Progress Report No. 81 (pages 141-147). A new diagnostic, that of ion collection, has been added,

*

This work was supported by the United States Atomic Energy Commission (Contract AT(30-1)-3285).

(XVI. INTERACTION OF LASER RADIATION WITH PLASMAS)

and the problems of detector sensitivity mentioned in the last report have been solved by the development of a fast low-noise miniaturized preamplifier. A new 15-period corkscrew having a maximum perturbing field of 2 per cent was also installed. Figure XVI-6 shows the method of construction and illustrates schematically the changing pitch of the conductors. Because of the large number of periods in this corkscrew, some of the current windings were very closely packed. We found that displacements of the conductors by as little as their own diameter had an appreciable effect ($\sim 10\%$) on the local corkscrew field. As a result, any movement of the corkscrew windings in the course of the experiment produced small (less than 10%) changes in the quantities under investigation. Qualitatively, however, the results obtained were insensitive to these small changes in the perturbation.

Figure XVI-1 shows the measured amount of perpendicular energy possessed by the beam at the end of its initial transit through the corkscrew as a function of the helix current. With a 5:1 mirror ratio, $v_{\perp}^2/v^2 = 0.20$ is sufficient to trap the beam. With the mirrors turned on, the beam was pulsed, and the decay of the trapped particles through the end mirror was measured.

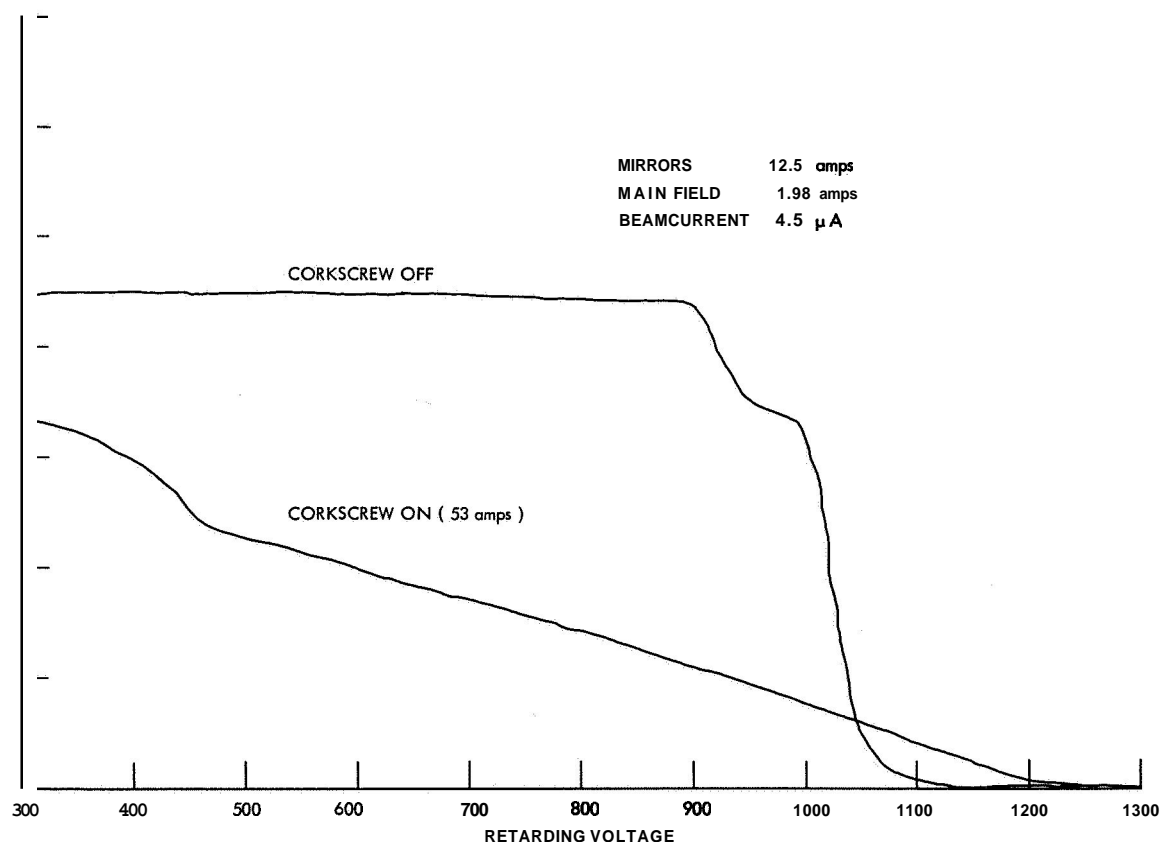


Fig. XVI-1. Magnetic moment after first transit.

(XVI. INTERACTION OF LASER RADIATION WITH PLASMAS)

Figure XVI-2 shows the decay curves obtained for three filling pulses. The rapid initial decay has a time constant of approximately 2 psec, independent of the length of the filling pulse. The time constants of the long-lived tails, on the other hand, increase as a function of pulse length. Also, integration of these decay curves shows that the fraction of trapped particles associated with the long-lived tails **also** increases with pulse length.

The value of the short decay constant can be obtained by associating the rapid initial particle loss with the preferential downward scattering¹ in that region of velocity space where particles can resonate with the corkscrew. The value of the long decay constant can be obtained by associating the long-lived particles with those scattered into and out of the region of velocity space above the resonant region.

The increase of the time constant and the number trapped in this long-lived group with increasing pulse length is then due to the fact that as the filling pulse lengthens, particles have time to diffuse farther and farther into the nonresonant region. No equilibrium is achieved here, because the diffusion coefficient drops so rapidly away from resonance.' Since the resonant region lies closer to the loss cone, all particles must exit by way of preferential downward scattering. Thus, when the beam is turned off, we see, first, a rapid decay of those particles in the resonant region, followed by the exit of the particles stored in the diffusive group.

Energy analysis of the escaping particles' confirms that they are scattered out in the large steps produced by resonance. This effect is especially pronounced in the case shown in Fig. XVI-3. Here a partially wound 1600 V-beam is injected into the trap. The top trace shows the energy analysis of the beam with no corkscrew current. The beam is double peaked; the data show that in the uniform field region of the device, the two components had 7 per cent and 8 per cent of their main magnetic field. When the corkscrew is energized, the beam is trapped and the escaping particles are energy analyzed in the lower trace. It is clear that the resonant scattering has given the escaping particles more parallel energy than the injected beam possessed.

Figure XVI-4 shows the energy analysis when the injected beam is adjusted to resonance with the entrance conditions of the corkscrew. This is the condition for maximum initial trapping and longest lifetime of the trapped particles.' The almost linear slope on the lower curve shows that under optimum trapping conditions the escaping particles fill the loss cone of velocity space almost uniformly.

The picture of field-particle scattering in tuned helical nonadiabatic traps that has emerged from these experiments is shown schematically in Fig. XVI-5. The trapping resonance is the largest possible scattering that the particle can experience. It places the injected beam somewhere between the dotted lines in the diagrams, the location depending on the precise adjustment of the main field, the beam energy, the beam energy distribution, and the corkscrew current. On the second forward transit, the trapped

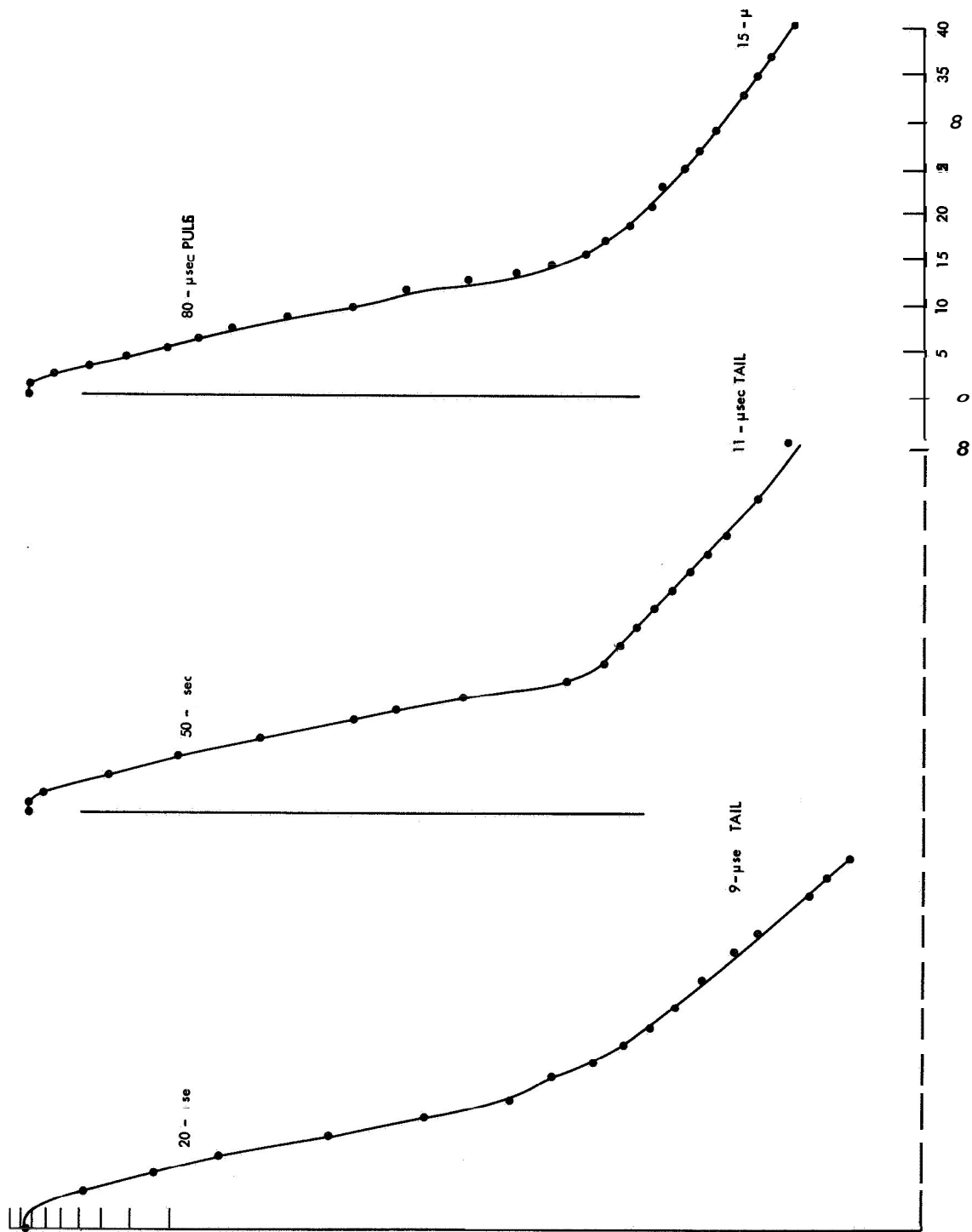


Fig. XVI-2. Variation of lifetime with pulse length.

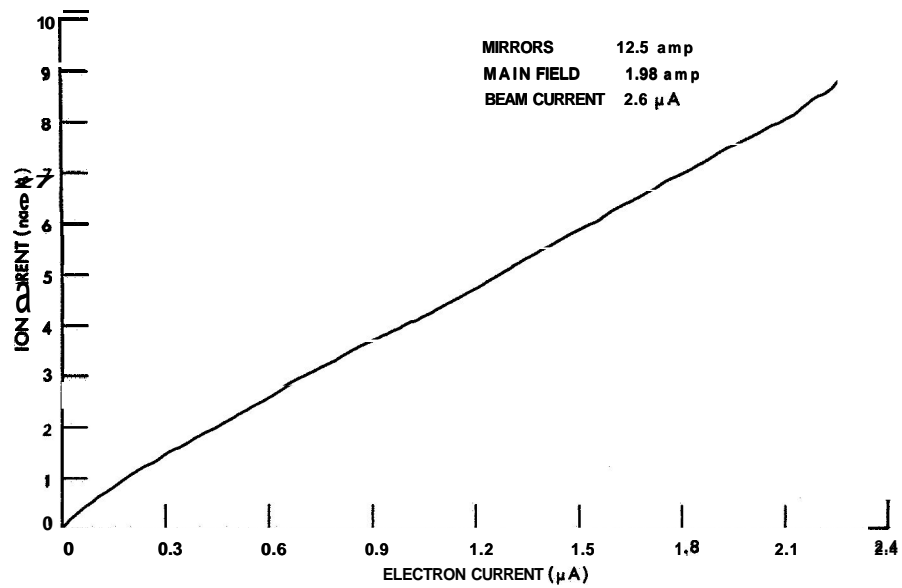


Fig. XVI-3. Energy distribution in the magnetic mirror.

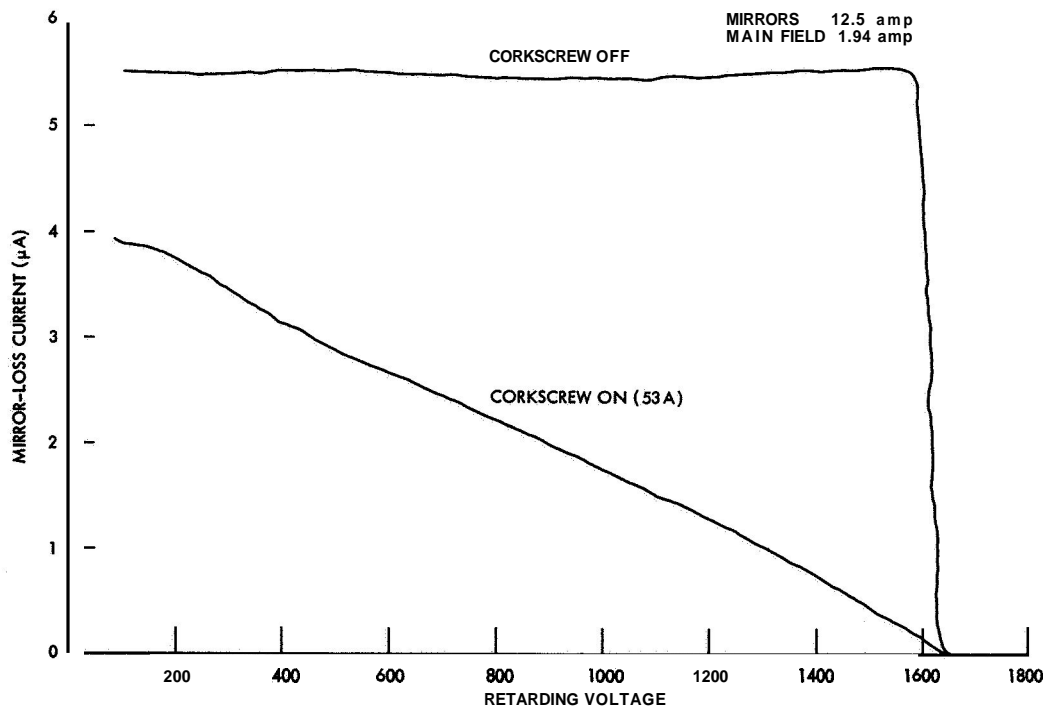


Fig. XVI-4. Energy distribution in the magnetic mirror.

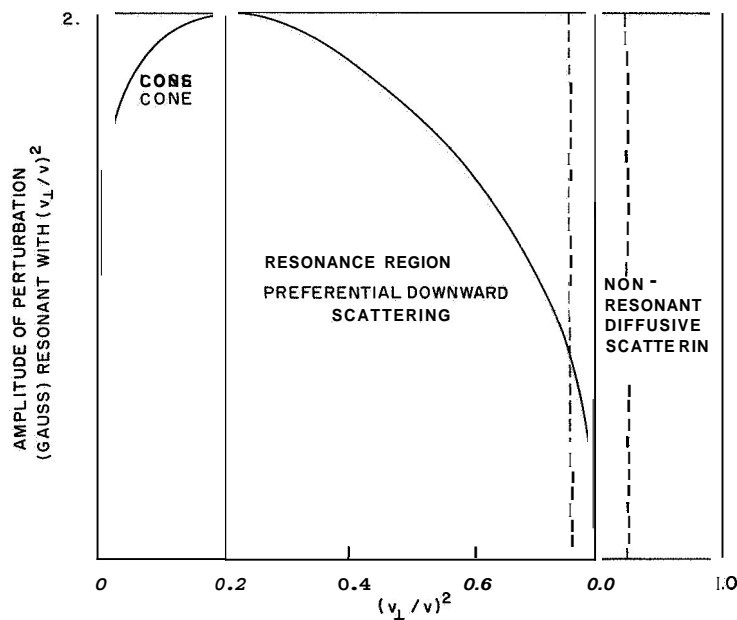


Fig. XVI-5. Summary of particle-corkscrew interaction.

particles that have an essentially random phase distribution are scattered either farther away from or back into the resonance region on the third transit. Because of the damping of the perturbation field those particles scattered downward on the second transit are resonantly scattered in a stronger field, make a larger downward step, and are rapidly lost. Those particles scattered away from resonance on the second transit interact with a weak nonresonant field and experience a small-step diffusive scattering with a lifetime that increases if they diffuse further from resonance. Unfortunately, from the viewpoint of trapping, this diffuse group is fed by only a small part of the injected beam. The existence of preferential downward scattering on the second transit insures that most of the beam scatters downward into the resonance region. The best measurement, thus far, shows 23 per cent of the total trapped particles in this diffusive group with a lifetime of approximately 11 psec. With 77 per cent of the trapped particles in the resonant scattered group with a lifetime of approximately 2 psec, the trap is operating at approximately 2 per cent efficiency as compared with the Liouville limit set by the experimental injected beam density.

2. Ion Detection

Figure XVI-6 shows the ion collector used in the experiment. In operation ions produced by electrons within the volume defined by the inner screen are trapped by this screen's -3 volt bias. Gas scattering eventually delivers a proportion of these ions to the collector that is biased at -300 volts, both to aid in the ion-collection efficiency and

(XVI. INTERACTION OF LASER RADIATION WITH PLASMAS)

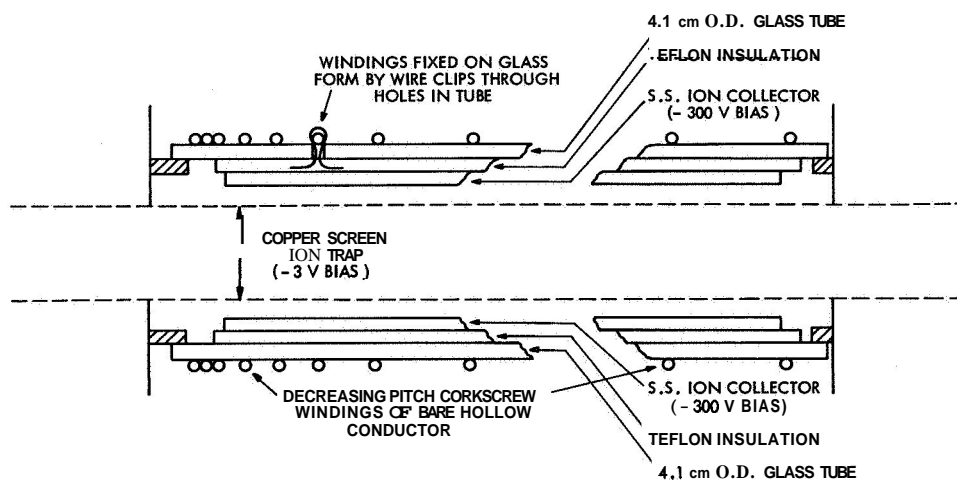


Fig. XVI-6. Ion collector and corkscrew assembly.

to repel secondary electrons. Particles whose orbits are the tightest spirals spend less time in mirror reflection and consequently make more ions within the collector per second. These particles constitute the long-lived diffusive group mentioned above. Thus lifetimes derived from ion-current measurements serve as upper limits to particle-confinement times, and it is difficult to gather more detailed information without knowledge of the distribution within the trap.

Another disadvantage of this technique is that it is very sensitive to the presence of secondary electrons produced by the injected beam when it strikes any material surface. These secondary electrons are mainly of low energy; consequently, their collision cross section with gas molecules is quite high, yielding an ion current out of proportion to their number. We have attempted to minimize this difficulty by using efficient beam collection outside the mirrors and eliminating high secondary emission coefficient materials within the trap. In spite of these limitations, ion collection has the advantage of the high accuracy of DC measurements, and constitutes a small perturbation probe of conditions within the trap.

The ion current is related to the trapped electrons by simple balance conditions. The time rate of change of the number of trapped particles, N_T , is

$$\frac{dN_T}{dt} = \frac{I_-}{q} \left(f + \frac{\tau}{\tau_g} \frac{A_T}{A} \right) - \frac{A_L}{A} \frac{N_T}{\tau_g} - \frac{N_T}{\tau_H} \quad (1)$$

where I_- is the injected beam, f is the fraction of the beam trapped by the initial corkscrew resonance, and τ , τ_g , and τ_H are the transit, gas-scattering, and helix-decay times, respectively. The A_T , A_L refer to the areas on the velocity surface of area A where particles are trapped by the magnetic mirrors or lost through the mirrors. Since

(XVI. INTERACTION OF LASER RADIATION WITH PLASMAS)

gas scattering is assumed to be isotropic in velocity space, a scattered particle has equal probability of landing anywhere on the velocity surface. Since the area associated with the loss cone is smaller than the total area, the probability of scattering out of the trap is reduced by A_L/A . Similarly, the probability of scattering into the trapped region is reduced by A_T/A . The ion-balance equation is

$$\frac{dN_+}{dt} = \frac{N_T}{\tau_+} - \frac{I_+}{q}, \quad (2)$$

where I_+ is the collected ion current, and τ_+ is the ionization time. In the steady state we have

$$I_+ = \frac{I_-}{\tau_+} \frac{f + \frac{\tau}{\tau_g} \frac{A_T}{A}}{\frac{1}{\tau_H} + \frac{A_L}{A} \frac{1}{\tau_g}} \quad (3)$$

With no corkscrew

$$I_+ = I_- \left(\frac{\tau}{\tau_+} \right) \frac{A_T}{A_L}. \quad (4)$$

Notice that the ion current is larger than one would expect on the basis of the beam alone. The factor (A_T/A_L) is due to the gas trapping of particles scattered out of the beam on its passage through one mirror and out of the other. When the corkscrew is turned on, we have

$$I_+ = I_- \frac{\tau_H}{\tau_t} \quad (5)$$

under the assumption that $\tau A_T/A \tau_g \ll 1$ and $\tau_H < \frac{A}{A_L} \tau_g$, which is certainly true for a 5:1 mirror ratio, where $A_T/A = 0.9$ and $A/A_L = 10$. Taking the ratio of Eq. 5 to Eq. 4, we get

$$\frac{I_+ \text{ (helix on)}}{I_+ \text{ (helix off)}} = \frac{A_L}{A_T} \frac{f \tau_H}{\tau}. \quad (6)$$

Figure XVI-7 shows an experimental measurement of I_+ as a function of helix current. The rise in I_+ at 32.5 amps corresponds to the measurement of wind-up as a function of helix current from retarding potential measurements shown in Fig. XVI-1. The critical nature of the adjustment to obtain the best trapping is illustrated by the narrowness of the peak. At the peak we can assume that $f = 1$ and obtain an estimate of particle lifetime in the trap.

(XVI. INTERACTION OF LASER RADIATION WITH PLASMAS)

$$\tau_H = \left(\frac{A_T}{A_L} \right) \frac{I_+ (\text{helix on})}{I_+ (\text{helix off})} \tau,$$

and

$$\tau_H = 18.2 \text{ psec.}$$

This is quite consistent as an upper limit on the long-lived group decay measured by the pulse technique. Because the function f is unknown away from the peak, this lifetime

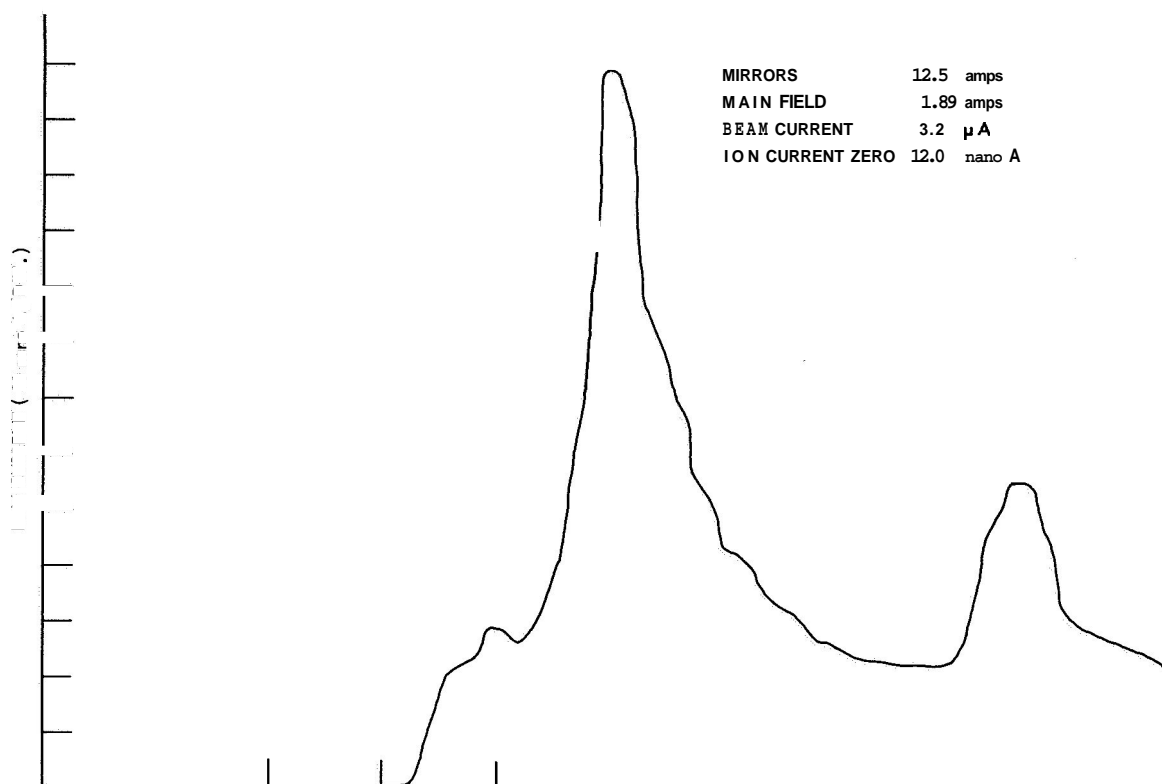


Fig. XVI-7. Ion current produced by corkscrew trapped particles.

estimate is the only piece of quantitative information obtainable from curves such as are shown in Fig. XVI-7; however, the adjustment of the system parameters for optimum trapping is indicated by the peak in such a trace and this was used as an optimizing criterion for the pulse measurements.

The second peak in Fig. XVI-8 shows that trapping occurs for currents higher than the corkscrew design current. This is due to the design equations for the corkscrew field which require

$$I_o \cos \chi_o = \text{constant},$$

where I_o is the helix current, and χ_o is the field-particle phase of a particle in the design orbit. As I_o increases the design orbit shifts toward $\chi_o = \pi/2$. Since the beam is adjusted for a specific entrance phase, increasing I_o shifts the beam into an unstable orbit. For sufficiently high currents, the unstable beam particle can be wound up and completely unwound in the first few turns of the corkscrew. The phase of these unwound particles is indeterminate. A simple consideration of the forces on the unwound particle shows, however, that it takes up a phase near $\pi/2$. This is near the phase of the design orbit, and the beam can be wound up again.

3. "Dissociation" Experiment

We have shown that the dominant loss mechanism for particles that have been trapped by means of a resonant nonadiabatic perturbation is the resonant scattering occurring when a trapped particle experiences a local resonance with the perturbation. It has been suggested^{3,4} that one can avoid this loss by dissociating the injected particles so that they can no longer satisfy the resonance relation

$$v_{||} = \frac{qB_o p(z)}{2\pi m}, \quad (7)$$

where $p(z)$ is the varying pitch of the perturbation super-imposed on a uniform field, B_o .

For molecular ion injection, the velocity of the dissociated ion is the same as that of the injected molecule, but its mass is decreased by half. Thus for this particle, Eq. 7 becomes an inequality,

$$v_{||} < \frac{qB_o p(z)}{2\pi(m/2)}, \quad (8)$$

and no local resonance is possible. Notice that Eq. 8 can be rewritten

$$v_{||} < \frac{q(2B_o) p(z)}{2\pi m}. \quad (9)$$

Now, if we design a corkscrew (that is, specify $p(z)$) to trap a particle of velocity v and mass m in a magnetic field B_o , and then study the interaction of the same particle with the corkscrew in a field $2B_o$, Eqs. 8 and 9 tell us that we are studying the dissociated-particle interaction. Figure XVI-8 shows the situation in velocity space with a loss cone equal to that in our experiment. In a full-scale injection experiment, molecular ions of mass $2m$ and velocity $v/2$ are trapped by a resonance on the inner velocity surface. Dissociated ions will remain on the same velocity surface, but since their mass is decreased by two, their resonance region is located on the outer surface in this figure.

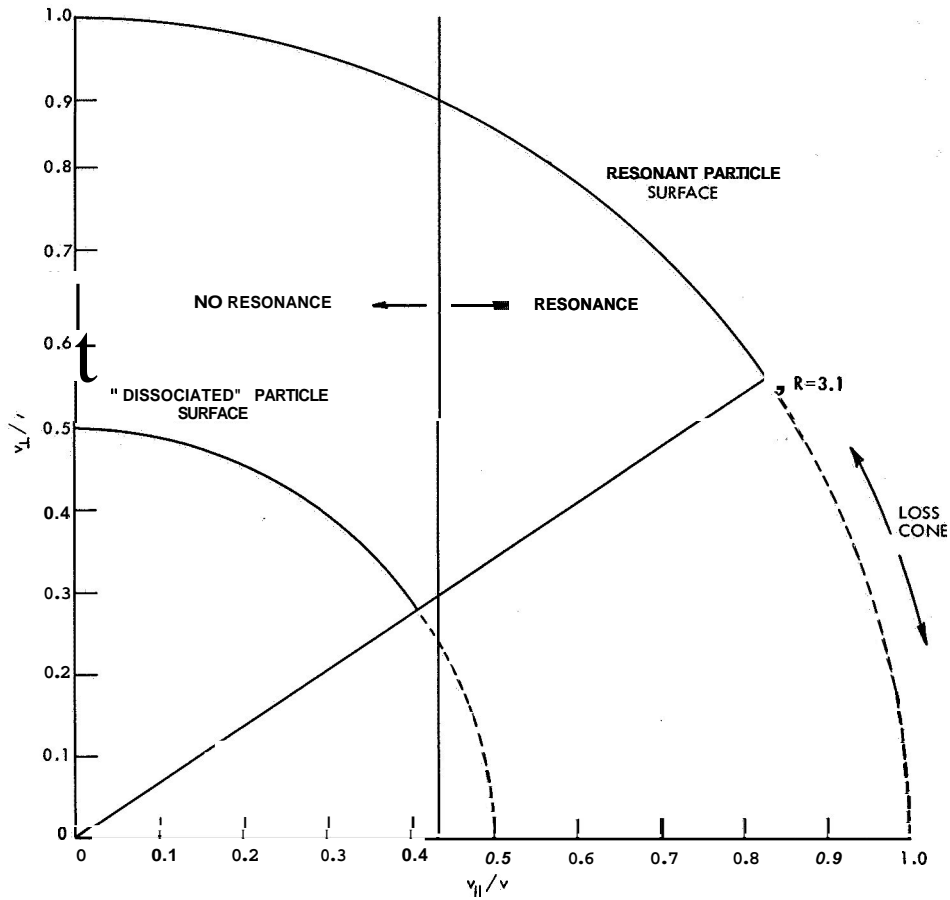


Fig. XVI-8. Velocity-space diagram of "dissociated" particle experiment.

In our experiment we can study the escape of these dissociated particles in a particularly simple fashion. We adjust the apparatus so that the trapping resonance lies on the outer surface of Fig. XVI-8 and inject a beam of electrons with $v_{\parallel}/v = 1/2$ and $v_{\perp}/v = 0$. Since these electrons are on the inner velocity surface, they cannot be trapped by the corkscrew resonance; however, while they pass through the region between two magnetic mirrors, gas scattering will trap some of them. In other words, gas scattering will populate the inner velocity surface with a low density of electrons. We can then study the nonresonant effects of the perturbation on these particles. Because the surface is thinly populated in a continuous fashion and the perturbation will cause only a small change in the gas-scattering equilibrium, the sensitive ion-collection technique was chosen as the initial diagnostic.

Figure XVI-9 shows a measurement of ion current as a function of electron beam current with no corkscrew. The linearity of the curve is predicted by Eq. 4 as

(XVI. INTERACTION OF LASER RADIATION WITH PLASMAS)

$$I_+ = \left(\frac{A_T}{-A_L} \right) \left(\frac{\tau}{\tau_+} \right) I_- \quad (10)$$

The gas within the apparatus was not known precisely, but the slope of this curve yields its average ionization cross section. For $p = 2 \times 10^{-6}$ Torr and a mirror ratio of 5,

$$\sigma_+ (?) = 2.4 \times 10^{-17} \text{ cm}^2.$$

For comparison, the ionization cross section for 1600-volt electrons on CO_2 is

$$\sigma_+(\text{CO}_2) = 7.8 \times 10^{-17} \text{ cm}^2.$$

Since the residual gas in the apparatus is probably composed of heavy molecules, the low ionization cross section indicates approximately 30 per cent collection efficiency.

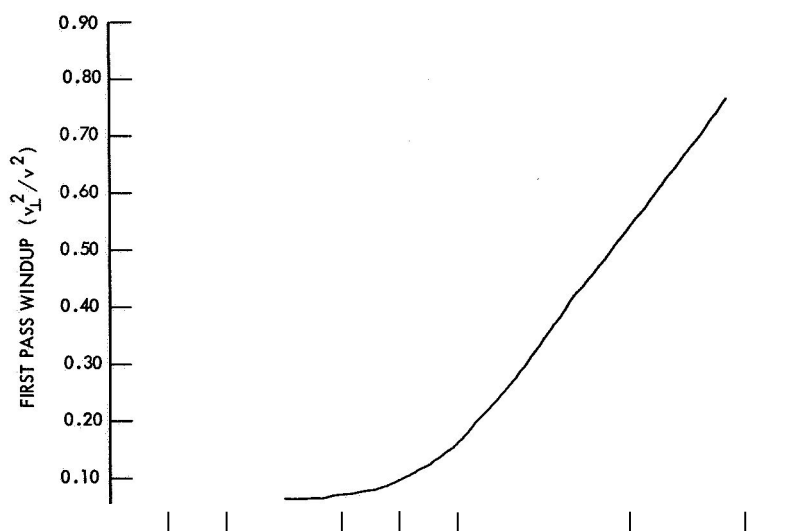


Fig. XVI-9. Calibration curve for ion collector.

Since the corkscrew does not contribute to the trapping, $f = 0$ in the particle-balance equations. Therefore the dependence of the ratio of ion-to-electron current on pressures as shown in Fig. XVI-10 is given by

$$\frac{I_+}{I_-} = \frac{\tau}{\tau_+} \left(\frac{A_T}{A} \right) \frac{1}{\frac{A_L}{A} + \frac{\tau_g}{\tau_H}} \quad (11)$$

The main pressure dependence is from τ_+ , but as the corkscrew is turned on and τ_H decreases from ∞ , the slope of the curve in Fig. XVI-10 is seen to change. The ratio

(XVI. INTERACTION OF LASER RADIATION WITH PLASMAS)

of ion current with the corkscrew off to that with the corkscrew on is given by

$$\frac{I_+ (\text{off})}{I_+ (\text{on})} = 1 + \frac{A}{A_L} \frac{\tau_g}{\tau_H}. \quad (12)$$

In Fig. XVI-10 the slight downward slope, as pressure is increased, is hidden in the fluctuations caused by the fact that the system pressure could only be varied in a gross manner by blanking off the pumps. The first and last points were the most

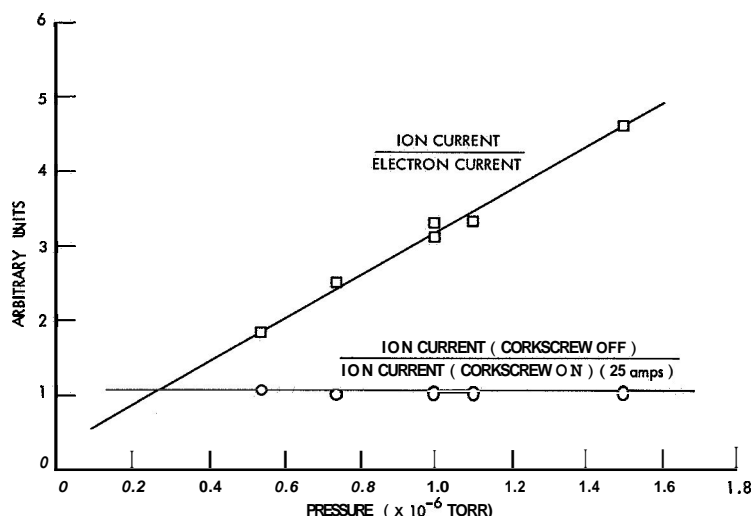


Fig. XVI-10. Pressure variation of ion current.

stable, and they do show a small downward slope of the correct magnitude (~3%). The general agreement between Figs. XVI-9 and XVI-10 and Eqs. 1-6 serves as an indication of the validity of these equations.

In order to study the dissociated-particle interaction, an x-y recorder was used to record the ion current as a function of helix current. Then Eq. 12 was used to obtain the lifetime of particles attributable to the helix scattering as a function of helix current. Figure XVI-11 shows the result plotted on a log-log scale. A power law fits the data over a sevenfold increase in the perturbation strength. At higher currents the ion current saturated because the helix itself began to trap particles. At lower currents the perturbation of the gas scattering was too weak to be seen accurately, but the curve does break away from the law in the direction of longer lifetime, as one would expect.

The surprising aspect of this result is the 3/2 power dependence of the lifetime. The diffusion theories that have been advanced to cover the nonresonant scattering^{2,3} regime led one to expect

(XVI. INTERACTION OF LASER RADIATION WITH PLASMAS)

$$\tau H \propto \left(\frac{B_{\perp}}{B_0} \right)^{-2} . \quad (13)$$

The result of this experiment indicates a much faster loss of particles than had been predicted on these earlier theoretical bases. A confirmation of this

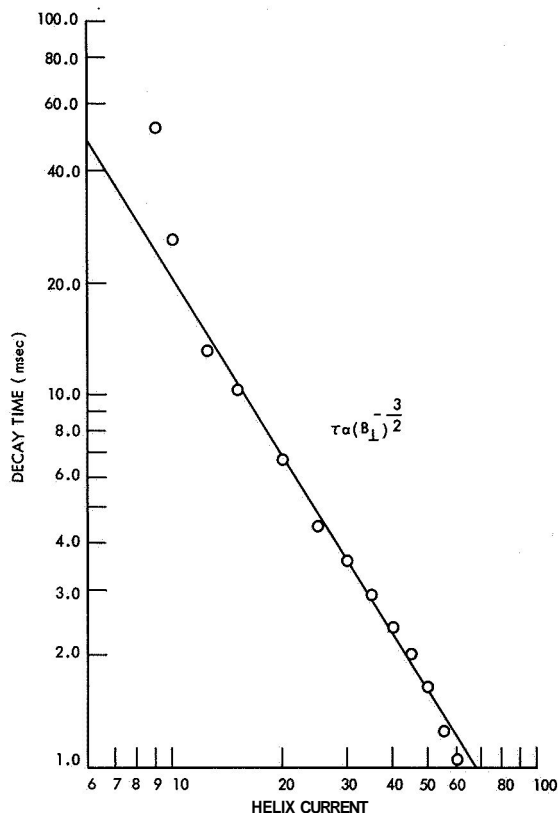


Fig. XVI- 11. Lifetime of "dissociated" electrons.

behavior by another diagnostic technique is clearly required to determine the origin of this enhanced loss.

J. F. Clarke

References

1. J. F. Clarke and L. M. Lidsky, Quarterly Progress Report No. 81, Research Laboratory of Electronics, M.I. T., April 15, 1966, pp. 147-159.
2. J. F. Clarke, Quarterly Progress Report No. 79, Research Laboratory of Electronics, M.I.T., October 15, 1965, p. 141.
3. R. C. Wingerson, T. H. Dupree, and D. J. Rose, Phys. Fluids 7, 1475 (1964).
4. E. W. Laing and A. E. Robson, J. Nucl. Energy (Part C, Plasma Physics) 3, 146 (1963).

COMMUNICATION SCIENCES
AND
ENGINEERING

XVII. STATISTICAL COMMUNICATION THEORY*

Academic and Research Staff

Prof. Y. W. Lee
Prof. A. G. Bose

Prof. H. L. Van Trees
Prof. J. D. Bruce

Prof. A. V. Oppenheim
J. J. Wawzonek

Graduate Students

M. E. Austin?
A. B. Baggeroer†
R. F. Bauer
V. Castellani
L. D. Collins?
T. Cruise
D. A. Feldman
T. Huang

R. W. Koralek
J. F. Kososki
V. Nedzelnitsky
D. E. Nelsen
L. R. Poulo
A. E. Rolland
R. W. Schafer

J. E. Schindall
D. L. Snyder?
J. C. Stafford
J. M. Steele
J. L. Walker
C. J. Weinstein
D. H. Wolaver
P. D. Wolfe

A. WORK COMPLETED

1. STATISTICS OF SWITCHING-TIME JITTER FOR A TUNNEL DIODE THRESHOLD-CROSSING DETECTOR

This study has been completed by D. E. Nelsen. It was submitted as a thesis in partial fulfillment of the requirements for the Degree of Doctor of Philosophy, Department of Electrical Engineering, M. I. T., May 1966.

A. G. Bose

2. STATE-VARIABLE APPROACH TO CONTINUOUS ESTIMATION

This study has been completed by D. L. Snyder. It was submitted as a thesis in partial fulfillment of the requirements for the Degree of Doctor of Philosophy, Department of Electrical Engineering, M. I. T., February 1966.

H. L. Van Trees

3. DIRECT-CURRENT CONVERTER USING TWO-STATE MODULATION

This study has been completed by D. H. Wolaver. It was submitted as a thesis in partial fulfillment of the requirements for the Degree of Master of Science, Department of Electrical Engineering, M. I. T., May 1966.

A. G. Bose

*This work was supported by the Joint Services Electronics Programs (U. S. Army, U. S. Navy, and U. S. Air Force) under Contract DA 36-039-AMC-03200(E), the National Aeronautics and Space Administration (Grant NsG-496), and the National Science Foundation (Grant GK-835).

†This work was supported by the National Aeronautics and Space Administration Grant (NsG-334).

(XVII. STATISTICAL COMMUNICATION THEORY)

4. DIGITAL SIMULATION OF AN FM BAND-DIVIDING DEMODULATOR

This study has been completed by V. Castellani. It was submitted as a thesis in partial fulfillment of the requirements for the Degree of Master of Science, Department of Electrical Engineering, M. I. T. , May 1966.

H. L. Van Trees

5. EFFECTS OF DIRECTIONAL RADIATION FROM VIOLINS UPON THEIR RECORDED SOUND

This study has been completed by V. Nedzelnitsky. It was submitted as a thesis in partial fulfillment of the requirements for the Degree of Bachelor of Science, Department of Electrical Engineering, M. I. T. , May 1966.

A. G. Bose

6. A TRANSISTORIZED FILTER FOR THE REDUCTION OF PULSE-TYPE NOISE

This study has been completed by J. M. Steele. It was submitted as a thesis in partial fulfillment of the requirements for the Degree of Bachelor of Science, Department of Electrical Engineering, M. I. T. , May 1966.

A. G. Bose

7. SUBJECTIVE STUDIES OF SPEECH QUANTIZATION

This study has been completed by R. W. Koralek. It was submitted as a thesis in partial fulfillment of the requirements for the Degree of Bachelor of Science, Department of Electrical Engineering, M. I. T. , May 1966.

J. D. Bruce

8. DESIGN AND CONSTRUCTION OF A TAPE DELAY SYSTEM

This study has been completed by P. D. Wolfe. It was submitted as a thesis in partial fulfillment of the requirements for the Degree of Bachelor of Science, Department of Electrical Engineering, M. I. T. , May 1966.

J. D. Bruce

XVIII. PROCESSING AND TRANSMISSION OF INFORMATION*

Academic and Research Staff

Prof. R. M. Gallager
Prof. E. V. Hoversten

Prof. I. M. Jacobs

Prof. R. E. Kahn
Prof. R. S. Kennedy

Graduate Students

D. S. Arnstein
J. D. Bridwell
E. A. Bucher
D. Chase
D. D. Falconer
R. L. Greenspan
D. Haccoun
H. M. Heggstad

J. A. Heller
M. Khanna
J. Max
J. H. Meyn
J. C. Moldon
G. Q. McDowell
G. C. O'Leary

R. Pilc
J. T. Pinkston III
E. M. Portner, Jr.
J. S. Richters
J. E. Robertson
M. G. Taylor
D. A. Wright
R. Yusek

A. BLOCK-CODING BOUND FOR COMMUNICATION ON AN INCOHERENT WHITE GAUSSIAN NOISE CHANNEL

1. Introduction

The system under consideration employs binary coding of antipodal waveforms to transmit information over a phase incoherent bandpass channel corrupted by white Gaussian noise.¹ The phase is uniformly distributed over the interval $(0, 2\pi)$, and is assumed to remain constant over the entire codeword. The codewords consist of N binary code letters, say "0" or "1". If the i^{th} code letter is a "0", the modulator forms the waveform $-\sqrt{E_N} \phi_i(t)$, likewise a "1" is mapped into $+\sqrt{E_N} \phi_i(t)$, where E_N is the energy per dimension, and the set of waveforms $\{\phi_i(t)\}$ is orthonormal. The codewords are chosen at random from an ensemble such that each code letter is equally likely to be a "0" or "1" and is independent of all other code letters. The resulting code-modulation system is that which would be obtained by assigning messages at random to the vertices of a hypercube.

Because of the random phase, the channel has memory, that is, the likelihood probably on the entire codeword, $p(\underline{r}/\underline{s}_1)$, does not factor into a product of probabilities over the individual code letters. Here \underline{s}_1 is an N -dimensional vector whose components are the projections of the signal representing the i^{th} message onto the set $\{\phi_i(t)\}$. The notation \underline{s}_1 will also be used to signify the codeword itself. Likewise, \underline{r} is a vector representation of the received signal.

It is known that for the equivalent phase-coherent system the ensemble average probability of error is bounded above by

*This work was supported by the National Aeronautics and Space Administration (Grant Nsg-334).

$$\bar{P}(e) \leq 2^{-N(R_0 - R_N)},$$

where $R_0 = 1 - \log_2 \left(1 + e^{-E_b/N_0} \right)$ is the largest value R_0 may take on for the inequality above to be valid for all N ; $R_N = (\log_2 M)/N$ is the source rate in bits/channel symbol when the source consists of M equiprobable messages. If a bound of the form

$$\bar{P}(e) \leq 2^{-N(R'_0 - R_N)}$$

is to be valid for the incoherent channel, R'_0 must necessarily be less than or equal to R_0 , since the error performance of the incoherent channel cannot be better than the coherent one. We shall show that in fact the bound on $\bar{P}(e)$ is valid for $R'_0 = R_0$.

2. Derivation of the Bound

For simplicity, assume that the $\{\phi_i(t)\}$ constitute a set of nonoverlapping time displacements of some pulse type of waveform. Thus the signals representing the code-words are a string of these pulses, some multiplied by $+1$ and some by -1 . Now say message m_k is sent, the ensemble average probability of error, given m_k sent, is

$$\bar{P}(e/m_k) = \sum_{\text{all codes}} P[\{\underline{s}_i\}] P[e/m_k, \{\underline{s}_i\}],$$

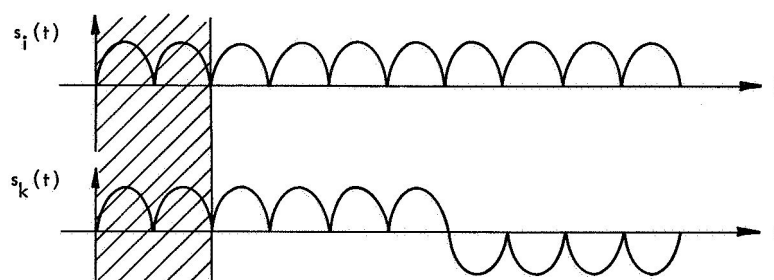
where $P[\{\underline{s}_i\}]$ is the probability of a particular code, $\{\underline{s}_i\}$. $P[e/m_k, \{\underline{s}_i\}]$ is the probability of error, given m_k sent and given the code $\{\underline{s}_i\}$ is used. This probability can be upper-bounded by using the union bound

$$\bar{P}[e/m_k, \{\underline{s}_i\}] \leq \sum_{\substack{i=0 \\ (i \neq k)}}^{M-1} \bar{P}_2(\underline{s}_i, \underline{s}_k),$$

where $P_2(\underline{s}_i, \underline{s}_k)$ is the probability of error between two equiprobable signals, \underline{s}_k and \underline{s}_i . Combining these relations yields

$$\bar{P}(e/m_k) \leq \sum_{\substack{i=0 \\ (i \neq k)}}^{M-1} \bar{P}_2(\underline{s}_i, \underline{s}_k).$$

Now consider two signals \underline{s}_i and \underline{s}_k , h of whose components differ $\left(h \leq \frac{N}{2} \right)$, as shown in Fig. XVIII-1 for $h = 4$, $N = 10$. The exact expression for $P_2(\underline{s}_i, \underline{s}_k)$ does not lend itself to obtaining a closed-form expression for $\bar{P}(e)$; an upper bound proves much more useful. To bound $\bar{P}_2(\underline{s}_i, \underline{s}_k)$ assume that signal \underline{s}_k is sent and a hypothetical receiver designed

Fig. XVIII-1. Example of two signals with $N \leq h/2$.

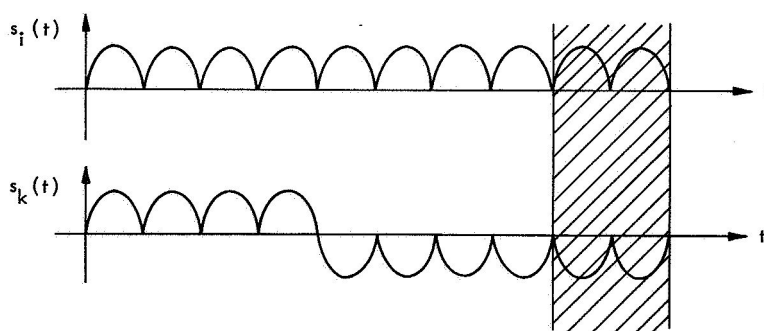
for the signal set $\{s_1, s_k\}$ is allowed to observe only the h positions where the signals differ and another set of h positions where the signals are the same. This receiver cannot have a smaller probability of error than the optimum receiver operating on all N positions, hence its performance upper-bounds $P_2(s_1, s_k)$. Notice now that deleting the segments of the signals that the receiver does not observe (the shaded segments in Fig. XVIII-1) leaves 2 orthogonal signals, each with energy $2hE_N$. It is well known that the optimum receiver for two equally likely, equal-energy signals in the incoherent white Gaussian noise channel has the probability of error, P_1 , given by

$$P_1 = \frac{1}{2} e^{-E/2N_0},$$

where E is the energy in a signal. Hence

$$P_2(s_1, s_k) \leq \frac{1}{2} e^{-hE_N/N_0}; \quad h \leq \frac{N}{2}.$$

The possibility still exists that h , the number of positions where the signals differ, is greater than $N/2$. For this case, $P_2(s_1, s_k)$ is bounded by restricting the hypothetical

Fig. XVIII-2. Example of two signals with $N \geq h/2$.

(XVIII. PROCESSING AND TRANSMISSION OF INFORMATION)

receiver to observe the $N-h$ positions where the signals are the same and only $N-h$ positions where the signals differ. Figure XVIII-2 shows two signals for which $N = 10$, $h = 6$; the shaded segment covers the two positions not observed by the suboptimum receiver. Again, the portions of the signals which the receiver observes are orthogonal — this time with energy $2(N-h)E_N$. Hence

$$P_2(\underline{s}_i, \underline{s}_k) \leq \frac{1}{2} e^{(N-h)E_N/N_0}; \quad h \geq \frac{N}{2}.$$

The next step is to take the average of $P_2(\underline{s}_i, \underline{s}_k)$ over the code ensemble. Since the bounds on $P_2(\underline{s}_i, \underline{s}_k)$ are functions only of h , the number of positions where the signals differ, this can be accomplished by averaging over h . For this code ensemble, the probability of signals differing in exactly h positions is

$$P(h) = 2^{-N} \binom{N}{h},$$

hence, for even N ,

$$\begin{aligned} \bar{P}_2(\underline{s}_i, \underline{s}_k) &= \sum_{h=0}^N P(h) P_2(\underline{s}_i, \underline{s}_k) \\ &\leq 2^{-N} \sum_{h=0}^{N/2} \binom{N}{h} \frac{1}{2} e^{-hE_N/N_0} + 2^{-N} \sum_{h=\frac{N}{2}+1}^N \binom{N}{h} \frac{1}{2} e^{-(N-h)E_N/N_0}. \end{aligned}$$

Relabeling indices, we have

$$\bar{P}_2(\underline{s}_i, \underline{s}_k) \leq 2^{-N} \sum_{h=0}^{N/2} \binom{N}{h} \frac{1}{2} e^{-hE_N/N_0} + 2^{-N} \sum_{h'=0}^{\frac{N}{2}-1} \binom{N}{h'} \frac{1}{2} e^{-h'E_N/N_0}.$$

The left summation is greater by one positive term than the right sum, therefore

$$\bar{P}_2(\underline{s}_i, \underline{s}_k) \leq 2^{-N} \sum_{h=0}^{N/2} \binom{N}{h} e^{-hE_N/N_0}.$$

Extending the summation to N gives

$$\bar{P}_2(\underline{s}_i, \underline{s}_k) \leq 2^{-N} \sum_{h=0}^N \binom{N}{h} e^{-hE_N/N_0}.$$

This can be expressed in closed form by using the binomial theorem.

$$\begin{aligned}\bar{P}_2(s_i, s_k) &\leq 2^{-N} \left(1 + e^{-E_N/N_0} \right)^N \\ &\leq 2^{-NR_0}, \quad R_0 = 1 - \log_2 \left(1 + e^{-E_N/N_0} \right)\end{aligned}$$

Completing the proof, we obtain

$$\bar{P}(e/m_k) \leq M \bar{P}_2(s_i, s_k) \leq 2^{-N(R_0 - R_N)},$$

where $M = 2^{NR_N}$.

This result is independent of k , hence

$$\bar{P}'(e) \leq 2^{-N(R_0 - R_N)},$$

and R_0 is identical to the exponential bound parameter for the coherent channel. A simple modification yields the same bound for odd N .

3. Discussion

It has been shown² that the bound

$$\bar{P}(e) \leq 2^{-N(R_0 - R_N)}$$

for the coherent channel is exponentially the tightest possible bound at the critical rate, R_c , less than capacity. It therefore follows that this is also true for the incoherent channel at the same rate, since

$$\bar{P}(e) \leq \bar{P}'(e) \leq 2^{-N(R_0 - R_N)}.$$

It is interesting to note that the tightest exponent was achieved by a random-coding scheme that forms codewords by choosing code letters independently. Although this is always the best strategy for a memoryless channel at R_c , there is no a priori reason to expect it to be optimum in a channel with memory.

An interesting comparison can be made between the result described in this report and binary coding of orthogonal waveforms on the incoherent channel. Here each code letter is mapped into one of two equal-energy orthogonal waveforms instead of antipodal waveforms. For this system it can be easily shown that the average probability of error is bounded by

$$\bar{P}''(e) \leq 2^{-N(R_0'' - R_N)},$$

where

$$R_o'' = 1 - \log_2 \left(1 + e^{-E_N/2N_o} \right)$$

is the largest value of R_o'' for which the bound is valid for all N , and E_N is the energy per orthogonal waveform. Notice that this signaling scheme requires twice as much energy as the antipodal case to achieve the same value of the exponential bound parameter; consequently, just as in the coherent case, binary orthogonal signaling is 3 db less efficient than binary antipodal signaling.

J. A. Heller

References

1. J. M. Wozencraft and I. M. Jacobs, Principles of Communication Engineering (John Wiley and Sons, Inc. , New York, 1965).
2. R. G. Gallager, "A Simple Derivation of the Coding Theorem and Some Applications," IEEE Trans., Vol. IT-11, No. 1, January 1965.

XIX. LINGUISTICS*

Academic and Research Staff

Prof. R. Jakobson	Prof. E. S. Klima	Dr. S.-Y. Kuroda
Prof. A. N. Chomsky	Prof. J. Kurlyowicz	Dr. A. Schwartz
Prof. J. A. Fodor	Prof. G. H. Matthews	Dr. D. E. Walker
Prof. M. Halle	Prof. Krystyna Pomorska	G. B. Gragg
Prof. J. J. Katz	Dr. S. Bromberger	P. L. Peterson
Prof. R. P. V. Kiparsky	Dr. M. F. Garrett	J. J. Viertel
	Dr. J. S. Gruber	

Graduate Students

G. R. Bedell IV	M. L. Geis	Amy E. Myers
T. G. Bever	R. Goldfield	A. J. Naro
E. W. Browne	J. W. Harris	D. M. Perlmutter
R. J. Carter	T. R. Hofmann	P. S. Peters, Jr.
P. G. Chapin	R. S. Jackendoff	C. B. Qualls
Janet P. Dean	L. Jenkins	J. R. Ross
R. P. G. DeRijk	R. S. Kayne	M. S. Snow
R. C. Dougherty	J. P. Kimball	Carol A. Spielman
J. E. Emonds	R. L. Mendelsohn	R. J. Stanley
J. L. Fidelholtz		Nancy H. Woo

A. A CHARACTERIZATION OF ESSENTIALLY CONTEXT-SENSITIVE LANGUAGES

The object of this report is to give a characterization of essentially context-sensitive languages (i.e., context-sensitive languages that are not context-free) and, for that matter, a characterization of context-free languages among context-sensitive languages.

We begin by introducing a restricted type of linear-bounded automata, linear-bounded automata with erasure:¹

Definition. A lba M is said to be a lba with erasure if M contains in its alphabet a special symbol ϕ that does not affect computation in any way, i.e., if M scans a square with the symbol ϕ it will not replace it by another symbol, will not change its states, and will continue to move in the same direction as it has moved into the scanned square (namely, continue to move to the right {left} if it has moved to the right (left) or stay on the scanned square if it has stayed there). More exactly, the set of states of M is divided into three disjoint subsets, S_{+1} , S_{-1} , and S_0 in such a way that M is in one of the states in S_{+1} (S_{-1} , or S_0) just after it has moved to the right (left or not moved), and further for every instruction of the form

$$(\phi, S) \rightarrow (a, T, D)$$

—*

This work was supported principally by the U. S. Air Force (Electronics Systems Division) under Contract AF 19(628)-2487; and in part by the Joint Services Electronics Programs (U.S. Army, U.S. Navy, and U.S. Air Force) under Contract DA 36-039-AMC-03200(E), the National Science Foundation (Grant GK-835), the National Institutes of Health (Grant 2 PO1 MH-04737-06), and the National Aeronautics and Space Administration (Grant NsG-496).

(XIX. LINGUISTICS)

a is ϕ , T is S, and D is +1, -1, or 0 according as S is in \underline{S}_{+1} , \underline{S}_{-1} , or \underline{S}_0 .

We define the notion of acceptance by a lba with erasure M as follows: a string x is accepted by M if there is a computation of M which accepts x in the usual sense of acceptance by a lba and if, moreover, at the end of the computation the tape contains only ϕ 's. Acceptance by a lba with erasure in this sense may be referred to by acceptance with erasure. In spite of the apparent specialization of the notion of lba, it is easy to see that lba with erasure are as powerful as lba in the general sense; we state without proof the following proposition.

Proposition. If a language L is accepted by a lba, there is a lba with erasure that accepts L with erasure.

Now, let M be a lba with erasure and for each pair of states (S_i, S_j) of M let $[S_i, S_j]$ be the set of strings accepted by the lba with erasure $M_{i,j}$ which is the same as M except that its initial and final states are redefined as S_i and S_j , respectively.

Let $x = yz$ be in $[S_i, S_j]$. We shall say that x is partitioned into y and z in $[S_i, S_j]$ if (i), given x as an input, there is a computation C of M with S_i and S_j as the initial and final states, respectively, which accepts x with erasure, and (ii) C is divided into two successive subcomputations C_1 and C_2 in such a way that, during C_1 and C_2 , M scans, respectively, only the subtapes on which y and z are printed originally. In other words, at the beginning of the computation C, M is scanning the leftmost element of x (it is also the leftmost element of y) in the state S_i ; at some moment M will scan the leftmost element of z for the first time, say, in the state S_k ; this must be the end of the subcomputation C_1 , and at the same time the beginning of the subcomputation C_2 ; at this moment y has all been replaced by ϕ 's; after this M will never go to the left of the square that it is then scanning.

If x is partitioned into y and z in $[S_i, S_j]$, then y and z are elements of $[S_i, S_k]$ and $[S_k, S_j]$, respectively, for some S_k . Conversely, if x is in $[S_i, S_j]$, $x = yz$, and y and z are in $[S_i, S_k]$ and $[S_k, S_j]$ with some S_k , respectively, then x is partitioned into y and z in $[S_i, S_j]$.

Let x be again in $[S_i, S_j]$ and let $x = vyw$, where v, y, and w are non-null. We say that x is decomposed into an interior y and two boundaries v and w in $[S_i, S_j]$ if there is a computation C with the initial and final states S_i and S_j which accepts x with erasure and will be divided into three consecutive subcomputations C_1 , C_2 , and C_3 in the following way. At the beginning of the first subcomputation C_1 (i.e., actually at the beginning of the entire computation) M is scanning the leftmost element of v (i.e., the leftmost element of x). During the subcomputation C_1 , M stays inside the subtape on which v is originally written. At the end of C_1 , M will drop off the right edge of that subtape and scan the leftmost element of y in the state, say, S_k . This is at the same time the beginning of the subcomputation C_2 . During C_2 , M stays entirely inside the subtape on which y is originally written. At the end of C_2 , this subtape contains only ϕ 's

and M drops off the right edge of this subtape, scanning the leftmost element of w in the state, say, S_ℓ . Then the final subcomputation C_3 begins. During C_3 , M may scan any square of the entire tape, but the subtape on which y is originally written does not affect the computation in any way, since it now contains only ϕ 's. At the end of C_3 (i.e., at the end of the entire computation) the entire tape contains only ϕ 's and M drops off the right edge of the entire tape in the state S_j .

In the sequel we are interested only in such cases for which the two boundaries v and w of a decomposition are elements (i.e., strings of length 1).

We have the following theorem.

Theorem. Let M be a lba with erasure. If for any pair of states (S_i, S_j) and for any string x of length greater than 1 in $[S_i, S_j]$, x can be either partitioned into two substrings or decomposed into an interior and two boundaries of length 1, then the language $L(M)$ accepted by M is context-free.

Proof. For each pair of states (S_i, S_j) , let us now consider $[S_i, S_j]$ as a nonterminal symbol for a grammar G , and let

$$[S_i, S_j] \rightarrow [S_i, S_k][S_k, S_j]$$

be a rule of G for any i, j , and k . Further, let

$$[S_i, S_j] \rightarrow a[S_k, S_\ell]b$$

be a rule if there exists x in the set $[S_i, S_j]$ which can be decomposed into an interior y and boundaries a and b in $[S_i, S_j]$, where y is in $[S_k, S_\ell]$. Further, if an element a is in $[S_i, S_j]$, let

$$[S_i, S_j] \rightarrow a$$

be a rule of G . Finally, let S be the initial symbol of G and for each final state S_f of M let

$$S \rightarrow [S_0, S_f]$$

be a rule of G , where S_0 is the initial state of M . Then, $L(M)$ is just the language generated by G .

From the theorem we obtain a well-known result that was first due to Chomsky and Schutzenberger:²

Corollary 1. If a language is accepted by a pushdown storage automaton, it is context-free.

Proof. A pushdown storage automaton can be simulated by a real-time pushdown storage automaton.³ It is easy to see that a real-time pushdown storage automaton can be regarded as a lba with erasure with the property stated in the theorem.

Actually, Haines derived this result from the equivalence of pushdown storage

automata to real-time pushdown storage automata.³ In his construction of a context-free grammar equivalent to a real-time pushdown storage automaton he refers to the instructions of the automaton rather than to its states as we did above in the proof of our theorem, and it would seem that the significance of the correspondence of the grammar and the automaton is not sufficiently clarified. Furthermore, he did not relate the notion of real-time pushdown storage automata to that of linear-bounded automata in an explicit way. Hence, although our theorem is a fairly straightforward generalization of his result, it may be of some interest, in particular, when we relate it to the fact that linear-bounded automata are the automata-theoretic counterpart of context-sensitive grammars, that is, that a language is context-sensitive if and only if there is a linear-bounded automaton that accepts it.⁴ In fact, our theorem will give a certain characterization of essentially context-sensitive languages. Let us first put it in the following way.

Corollary 2. A context-sensitive language L is not context-free if and only if for any lba M with erasure that accepts it there exists a string in it which cannot be accepted by a completely localized computation of M .

The precise meaning of completely localized computation is as follows. Given a string x , consider a computation C starting at the left end of x with a state S_i and ending at the right end of x with a state S_j , and with the tape filled entirely with ϕ 's. This computation is said to be localized if (i) x is partitioned into y and z in $[S_i, S_j]$, where y is in $[S_i, S_k]$ and z is in $[S_k, S_j]$ for some S_k , and the computation C consists of two successive subcomputations C_1 and C_2 which correspond to this partitioning of x into y and z , **or** (ii) x is decomposed into an interior y and two boundaries a and b and C consists of three successive subcomputations C_1 , C_2 , and C_3 which correspond to this decomposition of x into a , y , and b . A computation C of x is said to be completely localized if (i) x is of length 1, **or** (ii) if C is localized with respect to a partitioning of x into y and z and the corresponding subcomputations C_1 and C_2 are both completely localized, **or** (iii) C is localized with respect to a decomposition of x into a , y , and b , and the corresponding subcomputation of the interior y is completely localized. In brief, a computation is completely localized if x is processed by gradually partitioning and decomposing it until single elements are reached.

Let us reformulate Corollary 2 in terms of (general) lba. We define the notion of partition and decomposition with respect to a lba similarly to those notions with respect to a lba with erasure, except that in this case we do not require that after each subcomputation of a partition **or** after the subcomputation of the interior of a decomposition the corresponding subtape is filled with ϕ 's, but we do require of a decomposition that whatever is left on the interior subtape after the second subcomputation of the decomposition does not affect the computation during the last subcomputation of the decomposition.⁵ We

then define the notions of localized and completely localized computations with respect to a lba in the same way as with respect to a lba with erasure.

Now, given a lba M , we can construct a lba with erasure M' which is equivalent to M in such a way that if x is accepted by a localized computation of M it is accepted by a localized computation of M' . Indeed, M' can be constructed, in brief, by equipping M with a device that erases symbols (i.e., replaces them by ϕ) on the tape. Thus, we have the following corollary.

Corollary 3. A context-sensitive language L is not context-free if and only if for any lba M that accepts L there is a string in L which cannot be accepted by a completely localized computation of M .

L and M being as in Corollary 3, the set of all strings of L which cannot be accepted by a completely localized computation of M is obviously a subset of L which is responsible for the degree of complexity of L as a context-sensitive language and itself cannot be, for example, context-free.⁶

S.-Y. Kuroda

Footnotes and References

1. By linear-bounded automata (hereafter abbreviated as lba) we understand nondeterministic linear-bounded automata. For the definition of lba, see S.-Y. Kuroda, "Classes of Languages and Linear-bounded Automata," *Information and Control* **7**, 207-223 (1964). Note, however, that boundary symbol $\#$ is dispensable in the definition of lba, contrary to the remark made in footnote 3 of this paper; see S. Ginsburg and G. F. Rose, "Preservation of Languages by Transducers" (to appear in *Information and Control*).
2. N. Chomsky, "Context-free Grammars and Pushdown storage," Quarterly Progress Report No. 65, Research Laboratory of Electronics, M. I. T., April 15, 1962, pp. 187-194; M. P. Schützenberger, "Context-free Languages and Pushdown Automata," *Information and Control* **6**, 246-264 (1963).
3. L. Haines, "Generation and Recognition of Formal Languages," Ph.D. Thesis, M. I. T., 1965.
4. S.-Y. Kuroda, *op. cit.*
5. In this case the definitions of partition and decomposition are, in a sense, behavioristic. Thus, for example, we know that x is decomposed as ayb with respect to a computation only after having observed that the computation ended in the prescribed way, and not by means of a particular instantaneous description of computation that appears during the computation. Assume that we define $[S_i, S_j]$, analogously to the previous case of lba with erasure, as the set of strings that are accepted (this time in the general sense without erasure) with the initial and final states S_i and S_j , respectively. Then, on the one hand, it remains true that the product set $[S_i, S_k][S_k, S_j]$ is a subset of the set $[S_i, S_j]$. But, on the other hand, it does not hold that $a[S_k, S_\ell]b$ is a subset of $[S_i, S_j]$ if there exists a string x in $[S_i, S_j]$ which is decomposed as ayb with y in $[S_k, S_\ell]$. Thus, the proof of our theorem cannot be generalized directly to the general case without erasure.

(XIX. LINGUISTICS)

6. Actually, the notions of lba and context-sensitive grammars are not essential restrictions in developing the ideas pursued in this report, and ~~our~~ theorem and corollaries can be generalized as statements in terms of Turing machines and unrestricted rewriting systems. On the one hand, this generalization is rather straightforward conceptually, but, on the other hand, its exact formulation would become greatly involved, since we must formulate a type of Turing machine that is allowed (not only to add at ~~the~~ edges but also) to insert a piece of tape between two squares. Thus we have restricted ourselves here to dealing with cases within the machinery that is readily available at present.

XX. COGNITIVE INFORMATION PROCESSING*

Academic and Research Staff

Prof. S. J. Mason
Prof. W. L. Black
Prof. M. Eden
Prof. T. S. Huang

Prof. B. Prasada
Prof. O. J. Treliak
Prof. D. E. Troxel
Prof. D. Cohen
Dr. M. P. Beddoes

Dr. P. A. Kolers
Dr. N. Sezaki
K. R. Ingham
G. L. Wickelgren

Graduate Students

A. K. Bhushan
J. D. Bigham, Jr.
D. Caldwell
A. L. Citron
R. W. Cornew
A. Gabrielian
B. P. Golden

P. H. Hartmann
M. Kawanami
E. E. Landsman
M. B. Lazarus
F. F. Lee
J-H. Liu
J. I. Makhoul

J. A. Newell
L. C. Ng
D. H. Pruslin
C. L. Seitz
S. D. Shoap
A. Spiridon
J. A. Williams

A. COGNITIVE PROCESSES

1. AN ILLUSION THAT DISSOCIATES MOTION, OBJECT, AND MEANING

If one looks for a minute at a simple Archimedes (arithmetic) spiral that is rotating approximately 2-3 times per second, and then looks at something else, the second object will appear to change size and sometimes distance also. The direction of change in the second object is exactly opposite to that of the spiral: if the spiral rotates "inward," the aftereffect is an expansion of visual objects; and if the spiral rotates "outward," the aftereffect is a contraction. By "inward" we mean clockwise in the spiral of Fig. XX-1. It is sometimes assumed that this illusory motion of

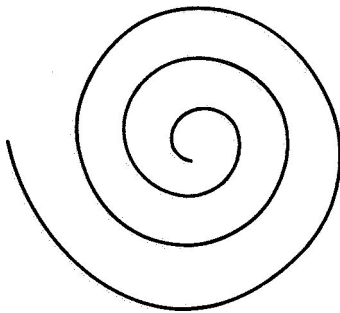


Fig. XX-1. Spiral of Archimedes.

the spiral is based on the same mechanism as that for the usual illusion of visual apparent motion, or "phi motion," as it is sometimes called. This assumption is probably wrong; the two illusions seem to have different mechanisms. We shall describe a new illusion that seems to dissociate the motion aspects of the spiral aftereffect from the location of objects in space and, in turn, from the interpretation of those objects.

Let a target be prepared that consists of

*This work was supported in part by the Joint Services Electronics Programs (U.S. Army, U.S. Navy, and U.S. Air Force) under Contract DA 36-039-AMC-03200(E), and in part by the National Science Foundation (Grant GK-835), the National Institutes of Health (Grant 2 P01 MH-04737-06), and the National Aeronautics and Space Administration (Grant NsG-496).

a regular matrix of crossing lines (Fig. XX-2), the whole target subtending, say, 20" of visual angle on each side, and the squares within it occupying approximately 0.5" each. A subject who looks at this matrix will report it as regular and with all the squares apparently of the same size (as in fact they are drawn.) He tends to see some lightening and darkening in the areas in which the vertical and horizontal lines cross, but this is eliminated if he is not permitted to look too long (more than a few seconds) at the matrix. Now let the subject look at a spiral whose diameter is 4" visual angle. As it rotates "inward" a number of curious and interesting visual distortions occur in its shape and color. Typically, there is

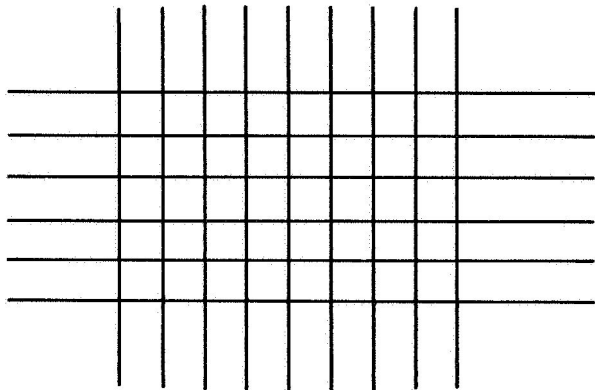


Fig. XX-2. Square matrix.

some lightening of the black regions and darkening of the white; all subjects see the motion of the spiral; and the larger number of them report a change in the apparent depth of the figure: the spiral takes on the appearance of a three-dimensional coil, the innermost part appearing most distant (or nearest when the rotation is outward"). These apparent changes have been noted many times in the past hundred years, but still are not satisfactorily explained; so we proceed, having acknowledged their existence, to the main observations.

After looking at the spiral for a minute, let the subject transfer his gaze to a single square of the large matrix, one near its center. He then reports that many of the small cells (Fig. XX-2) change size drastically; for example, by a factor of 10-20. Not all of the cells change size; rather, only those change that occupy a region of the matrix that corresponds in angular subtense to the region previously stimulated by the spiral. That is to say, if the spiral had occupied approximately 4" visual angle, the cells of the matrix that fall within a diameter of 4" centered on the square chosen for fixation are the ones that subsequently appear to change in size. Many subjects also report that the apparent distance of the cells also changes. In fact, then, what is usually reported is that a small region of the large matrix changes in size and apparent distance as a result of looking at the spiral. This itself is to be expected from what was said above. What is not expected is that simultaneously with a change in the apparent size and distance of some of the cells, no discontinuity with the remainder appears. The illusion therefore consists in the logically impossible situation that part of a two-dimensional array changes size and distance without undergoing any discontinuity

(XX. COGNITIVE INFORMATION PROCESSING)

in the lines that join it to the remainder of the figure. How can this be explained?

Let it be assumed that there are at least three distinguishably different "systems" in the visual nervous apparatus: one system is concerned with the perception of contours; a second with the perception of motion; and the third with interpretation or "meaning." We have shown previously that the usual form of illusory motion (the stroboscopic motion created by motion pictures or television) actually seems to have little to do with the actual processing of motion; rather, that effect seems to be due to a perceptual filling-in or impletion between the successive locations of a discontinuously displaced object.' That motion is truly illusory in that it is imposed on the output of the contour-perception system, and not of any motion-detection system. With the rotating spiral, on the other hand, the visual apparatus is actually stimulated by a truly moving figure. The changes in visual objects that are seen after looking at the rotating spiral must be interpretations imposed on the motion-detection system. This belief is supported by the fact that sustained observation of stroboscopic motion (an impletion from the contour-detection system) does not yield any of the changes in figure properties of a subsequently looked-at target that occur after looking at a rotating spiral. Thus we believe that a unique motion-detection system is activated by the rotating spiral, and a contour-detection system by stroboscopic motion. The failure to observe discontinuities in the large matrix results from the fact that such discontinuities, if they existed, would be detected by the contour-detection system, not by the motion system. Furthermore, the recognition of the logical paradox of the absence of discontinuities must be due to still another system, which is concerned with interpretation or "meaning" at a higher level than object recognition. It might also be pointed out that unlike the case with many perceptual illusions whose paradoxical nature causes some discomfort or annoyance, there is no such sense present with this illusion. In fact, most observers (and we have tested 50) usually fail to note the paradox until it is pointed out. Still, the precise mechanisms that mediate the interaction of the motion and object-detection systems have still to be worked out, as have the rules that govern the formation of impletions.

P. A. Kolars

References

1. P. A. Kolars, "The Illusion of Movement," Scientific American 211, 98-106 (1964).

B. PICTURE PROCESSING

1. OPTIMUM BINARY CODE

Introduction

Some progress has been made on the problem of optimum binary code as discussed in previous reports^{1,2}: (a) Conjectures 2 and 3 of an earlier report² have been proved

to be true; and (b) A computer simulation has been carried out for the special case of 3-bit codes. These will be described briefly here. Also, a general expression has been derived for the mean-absolute error of the natural code, which is reported in Section XX-B. 2.

Average Noise Power of Reflected-Binary Gray Code

A general expression was derived for the average noise power (i.e., mean-square error) of the reflected-binary Gray code.³ We state this result as

THEOREM 1. Consider the transmission of integers over a BSC, using fixed-length binary block codes. If the input data are uniformly distributed over the integers 0 to $2^n - 1$, then the mean-square error for the reflected-binary Gray code is

$$G_n = \frac{1}{6}(4^n - 1) - \frac{1 - 2p}{2} \frac{4^n - (1 - 2p)^n}{4 - (1 - 2p)}, \quad (1)$$

where p is the probability of error of the BSC.

After some manipulations, we have, from Eq. 1 and Eq. 1 of our previous report,¹ the following theorems.

THEOREM 2. Under the same assumptions as in Theorem 1, we have

$$(G_n - N_n) = (1 - 2p)G_{n-1}, \quad (2)$$

where N_n is the mean-square error of the n -bit natural code.

THEOREM 3. Under the same assumption as in Theorem 1, and assuming further that $p \leq \frac{1}{2}$, we have

$$N_n \leq G_n. \quad (3)$$

That is, the natural code yields a smaller mean-square error than the reflected-binary Gray code.

Computer Simulation of 3-bit Codes

A computer program has been written⁴ and **run**, which calculated the mean-square and the mean-absolute errors of all possible 3-bit codes and gave the results as polynomials in p , the error probability of the BSC.

It was found that the natural code yields both the minimum mean-square error and the minimum mean-absolute error, for $p \leq \frac{1}{2}$. The reflected-binary Gray code has the same mean-absolute error as the natural code, but has a larger mean-square error than the natural code for $p < \frac{1}{2}$.

T. S. Huang

References

1. Y. Yamaguchi and T. S. Huang, "Optimum Binary Fixed-Length Block Codes," Quarterly Progress Report No. 78, Research Laboratory of Electronics, M. I. T., July 15, 1965, pp. 231-233.
2. Y. Yamaguchi and T. S. Huang, "Optimum Binary Code," Quarterly Progress Report No. 79, Research Laboratory of Electronics, M. I. T., October 15, 1965, pp. 214-217.
3. K. A. Achterkirchen, Course 6.39 Term Project Report, Department of Electrical Engineering, M. I. T., May 20, 1966.
4. T. F. Strand, S.B. Thesis, Department of Electrical Engineering, June 1966.

2. ERROR IN FIXED-LENGTH NONREDUNDANT CODES

Let us assume that we have 2^n equiprobable signals with values $0, 1, 2, \dots, 2^n - 1$ and we wish to code these in terms of binary n -tuples, to be transmitted through a binary symmetric channel.

Harper¹ has proved the following theorem.

THEOREM. To obtain a code that minimizes the average absolute error when only one error per signal is considered, assign zero to an arbitrary vertex of the binary n -cube, and, having assigned $0, 1, 2, \dots, \ell$, assign $\ell + 1$ to an unnumbered vertex (not necessarily unique) which has the most numbered nearest neighbors.

The value of this minimum average error is $(2^n - 1)p(1-p)^{n-1}$ which is quite easy to compute.

We shall derive an expression for the absolute error of the "Harper codes" when all possible combinations of errors are allowed.

Define an equivalence relationship such that two possible coding schemes are in the same equivalence class if and only if they give the same mean absolute error for all values of p .

THEOREM. The codes obtained by the Harper scheme form an equivalence class.

The details of the proof will be omitted, but it hinges on the fact that in a serial listing of a Harper code corresponding to the signals $0, 1, \dots, 2^n - 1$ (see Fig. XX-3) if the group of codes on lines $\ell_1 \equiv 0 \pmod{\ell_0}$ through $\ell_1 \equiv \ell_0 - 1$; $0 < \ell_0 \leq 2^n$; $0 \leq \ell_1 \leq 2^n - 2$ are flipped around their mid-point, the average error for any particular combination of errors does not change. These flipping operations generate all of the Harper codes starting from any particular one, if we consider the different permutations possible on the columns of the codes.

It is conjectured that the above-mentioned class has the least average absolute error, but we have not been able to prove this yet.

THEOREM. The average absolute error for the class of codes obtained by the Harper scheme is $p(2^n - (1-p)^n)/(1+p)$.

(XX. COGNITIVE INFORMATION PROCESSING)

Proof: We shall prove this by calculating the average absolute error for a specific member of the class of codes obtained by the Harper scheme, namely the so-called "natural code" that assigns to each number its binary representation.

CODE	SIGNAL	LINE
0-----000	0	0
0----- --001	1	1
0----- --010	2	2
	⋮	⋮
1-----111	2^n-1	2^n-1

Fig. XX-3. Harper code.

Consider the occurrence of k errors in the codes such that the leftmost error in the binary representation is at the m^{th} bit from the right. For each signal there are $\binom{m-1}{k-1}$ such possible errors. We note that for any signal \mathbf{I} with binary representation $x_n x_{n-1} \dots x_{m+1} 1 x_m \dots x_1$; $x_i = 0$ or 1 , there exists also a signal ℓ' with binary representation $x_n x_{n-1} \dots x_{m+1} 0 x_m \dots x_1$. Now for any combination of k errors on bits $m_1, m_2, \dots, m_{k-1}, m$; $m_i < m \leq n$, the absolute error in ℓ is $2^{m-1} - (-1)^{x_{m_1}} 2^{m_1-1} - (-1)^{x_{m_2}} 2^{m_2-1} \dots - (-1)^{x_{m_{k-1}}} 2^{m_{k-1}-1}$. For this same combination of errors in ℓ' the absolute error in ℓ' is $2^{m-1} + (-1)^{x_{m_1}} 2^{m_1-1} + \dots + (-1)^{x_{m_{k-1}}} 2^{m_{k-1}-1}$. The probability of occurrence of such an error is $(1-p)^{n-k} p^k$ for both \mathbf{I} and ℓ' , and these two are assumed to be equiprobable themselves. It follows that the average absolute error for any k error with leftmost error at bit m is 2^{m-1} , as all of the other terms cancel out in computing the average over the ensemble.

The average absolute error is $\overline{|E|} = \sum_{m=1}^n p_m \cdot \overline{|\epsilon_m|}$, where p_m = the probability that the leftmost error is on bit m , and $\overline{|\epsilon_m|}$ is the average absolute error with leftmost error on bit m . Now we have just shown that $\overline{|\epsilon_m|} = 2^{m-1}$ and p is $(1-p)^{n-m} p$, so

$$\begin{aligned} \overline{|\epsilon|} &= \sum_{m=1}^n (1-p)^{n-m} p 2^{m-1} \\ &= p(1-p)^n / 2 \sum_{m=1}^n (2/(1-p))^m \end{aligned}$$

$$\begin{aligned} |\overline{\epsilon}| &= p(1-p)^n / 2 \left(\frac{(2/(1-p))^{n+1} - (2/(1-p))}{(2/(1-p)) - 1} \right) \\ &= p(2^n - (1-p)^n) / (1+p) \end{aligned}$$

Q. E.D.

Calculation of the number of equivalence classes and, in fact, a complete classification of them in terms of their associated errors appear to be within the realm of possibility and will form part of the further investigation of this problem.

A. Gabrielian, T. S. Huang

References

1. H. Harper, "Optimal Assignment of Numbers to Vertices," J. Soc. Indust. Appl. Math., Vol. 12, No. 1, 1964.

3. EFFECT OF BSC ON PCM PICTURE QUALITY

Introduction

The current trends in communication point in the direction of PCM.¹ In particular, the transmission of pictures by PCM has attracted wide attention.' In order to design a PCM picture-transmission system efficiently, it is desirable to collect data on the effects of system parameters on received picture quality.

An important factor in a communication system is the channel noise. The subjective effects of noise in analog picture-transmission systems have been studied extensively.³⁻⁸ No data are available, however, on digital systems. For binary PCM transmission systems, a first approximation to many practical channels is the binary symmetric channel (BSC) without memory. The error probability, p , of the BSC is a parameter which can be traded off with other system parameters such as the energy per bit of the signal.

The purpose of the present report is to give some results on the subjective effect of the noise introduced in the received pictures of a PCM system by the BSC. Specifically, such noise was compared, with regard to its subjective effect, with noise introduced by an additive white Gaussian channel to a PAM transmission system. The latter was chosen as a standard because its appearance is similar to that of the familiar "snow" that is observed on a home television screen. It was assumed that the pictures were of a general nature, and were transmitted for the purpose of entertainment.

The two systems were simulated on an IBM 7094 computer to produce noisy pictures. Subjective tests were then carried out to compare the objectionability of the two types of noise. Three original pictures, varying in the amount of details, were used. It was found true of all three pictures that for high signal-to-noise ratios the white Gaussian noise is more objectionable than the BSC noise, while for low signal-to-noise ratios the reverse is true. The crossover point lies approximately in the range 16-20 db peak signal-to-rms-noise ratio, and tends to occur at a higher signal-to-noise ratio for a picture having more details. The noise used in the signal-to-noise ratio calculation was the difference between the brightness of the received picture and that of the transmitted picture.

Generation of Noisy Pictures

The noisy pictures were generated on an IBM 7094 digital computer.

a. Digitalization of Pictures

A digital scanner⁹ was used to sample and quantize pictures and to record the digitalized data on magnetic tape in a format compatible with the IBM 7094 computer. For the present study, 256 X 256 samples were taken of each picture, and the brightness of

each sample was quantized to 128 levels, or 7 bits. The magnetic tape was used as input for computer processing. The processed picture was written on an output magnetic tape by the computer. The digital scanner was again used to display the processed picture from the output magnetic tape on a cathode-ray tube, from which a hard copy of the picture was taken.

b. PAM Picture Transmission through an Additive White Gaussian Channel

Independent Gaussian random variates with mean zero and variance one were generated, and then the received picture $r(x, y)$ was obtained from the transmitted picture $s(x, y)$ by the following equation:

$$r(x, y) = s(x, y) + n(x, y) \\ s(x, y) + \sigma n_1(x, y), \quad (1)$$

where x and y are the spatial coordinates of a picture sample, and $n_1(x, y)$ = Gaussian random variates with mean zero and variance one, independent from sample to sample, and independent of $S(X, Y)$. The peak signal-to-rms noise of the received picture $r(x, y)$ then is

$$\left(\frac{S}{N}\right)_{\text{db}} = 20 \log \frac{A}{\sigma}, \quad (2)$$

where A is the peak signal value. In our case, $A = 127$.

c. PCM Picture Transmission through a BSC

We assumed that a straight binary code was used for the brightness levels of the picture. The binary symmetrical channel (with error probability $0 \leq p \leq 1$) was simulated as follows. For each signal bit, an independent random variate with uniform distribution (over the unit interval $[0, 1]$) was generated. The received bit was set to be the same as or different from the transmitted bit, according as this random variate was greater than p , or was less than or equal to p .

Again, we use $s(x, y)$ to denote the transmitted picture, and $r(x, y)$, the received one. The noise is defined as

$$n(x, y) = r(x, y) - s(x, y) \quad (3)$$

Young and Mott-Smith¹⁰ have shown that, under certain conditions (in particular, if the probability distribution of the brightness levels in the picture $s(x, y)$ is flat, or if it is symmetrical with respect to the mean), the noise power $\overline{n^2}$ is related to the error probability by

$$\overline{n^2} = \frac{4^B - 1}{3} p, \quad (4)$$

(XX. COGNITIVE INFORMATION PROCESSING)

where B is the number of bits in each code word. In our case, $B = 7$. The probability distributions of the pictures used in our study did not exactly satisfy the conditions for the validity of Eq. 4; however, actual computer calculations of n^2 yielded results that fitted Eq. 4 almost perfectly.

d. Pictures Generated for This Study

Three original pictures were used: a face of a girl, a scene with a cameraman as a central object, and a crowd. Four signal-to-noise ratios were used for the face, and five each for the cameraman and the crowd. For each original picture and each signal-to-noise ratio, two noisy pictures were generated: one containing white Gaussian noise and the other BSC noise, resulting in eight noisy pictures for the face, and ten noisy pictures each for the cameraman and the crowd. The signal-to-noise ratios used are listed in Table XX-1. Some of the noisy pictures are shown in Fig. XX-4.

Subjective Tests and Results

Two types of subjective tests were carried out: paired comparison, and matching. In all tests, hard copies of the pictures were shown to the observers, and the viewing distance was 15 inches, which is six times the picture height. The size of the pictures was 2.5 in. \times 2.5 in.

a. Paired Comparison Tests

The objective of these tests was to find out, for a given signal-to-noise ratio, which of the two types of noise, Gaussian or BSC, was more objectionable to human observers.

Each observer was shown two noisy pictures at a time. These two pictures had the same subject matter and the same signal-to-noise ratio, but one picture had Gaussian noise and the other, BSC noise. The observer was asked to choose the picture he preferred to watch, say, on a television screen. Forty observers took the tests with the picture of the cameraman. For the pictures of the face and the crowd, there were 15 observers.

The results of these tests are given in Table XX-2. The number corresponding to (i.e., at the intersection of) a particular noise type and a particular S/N represents the total number of observers who preferred that noise type to the other type at that S/N. For example, 21 observers preferred BSC noise to Gaussian noise at an S/N of 24, for the picture of the cameraman.

b. Matching Tests

The objective of these tests was to find out, for two pictures with the same subject matter but different types of noise (Gaussian noise in one, and BSC noise in the other) to be equally objectionable to human observers, what should be the relation between their

Table **XX-1**. Peak signal-to-rms noise ratios, S/N , used in this study, with the corresponding rms noise, σ , and the error probability of the BCS, p .

	$\left(\frac{S}{N}\right)_{\text{db}}$	σ	P
Face	20	12.5	.03
	16.5	17	.055
	16	19.7	.07
	12	31	.18
Cameraman	24	8	.01
	22	10	.02
	20	12.5	.03
	16.5	17	.055
	12	31	.18
Crowd	22	8	.02
	20	12.5	.03
	16.5		.055
		19.7	.07
			.18



(a)



(b)



(c)



(d)

Fig. XX-4. Some noisy pictures. (a) BSC noise with $p = .03$ and $S/N = 20$ db. (b) Gaussian noise with $S/N = 20$ db. (c) BSC noise with $p = .18$ and $S/N = 12$ db. (d) Gaussian noise with $S/N = 12$ db.

Table XX-2. Results of paired comparison tests.

(a) Face

Type of noise				
	20	16.5	16	12
BSC	13	8	4	0
Gaussian	2	7	11	15

(b) Cameraman

Type of noise	Total number of preferences for picture with various $(S/N)_{db}$				
	24	22	20	16.5	12
BSC	21	24	28	5	1
Gaussian	19	16	12	35	39

Type of noise	Total number of preferences for picture with various $(S/N)_{db}$				
	22	20	16.5	16	12
BSC	11	13	6	4	0
Gaussian	4	2	9	11	15

Table XX-3. Results of matching tests.

(a) Face

Type of noise	Rank for picture with various $(S/N)_{db}$			
	20	16.5	16	12
BSC	1	2	3	4
Gaussian	1.8	2.2	2.6	3.3

(b) Cameraman

Type of noise	Rank for picture with various $(S/N)_{db}$				
	24	22	20	16.5	12
BSC	1	2	3	4	5
Gaussian	1.7	2.5	3.2	3.7	4.5

(c) Crowd

Type of noise	Rank for picture with various $(S/N)_{db}$				
	22	20	16.5	16	12
BSC	1	2	3	4	5
Gaussian	1.3	1.9	2.5	3.0	4.4

(XX. COGNITIVE INFORMATION PROCESSING)

signal-to-noise ratios.

The pictures with BSC noise were ordered according to their signal-to-noise ratios. The picture with the highest S/N was given rank 1, the picture with the second highest S/N was given rank 2, and so forth. This set of pictures was put in front of the observer. He was then shown a picture chosen at random from the set of pictures with Gaussian noise, and asked to match it, according to noise objectionability, with the set of pictures with BSC noise. The Gaussian picture was assigned a rank equal to that of the BSC picture to which it was matched. If the Gaussian picture was rated between two BSC pictures, it was given a rank equal to the average of the ranks of the two BSC pictures.

Thirty-five observers were tested for the picture of the cameraman, and 15 for the pictures of the face and the crowd. The ranks of the Gaussian pictures averaged over all observers are given in Table XX-3.

Evaluation of Data

a. General Trends

From Tables XX-2 and XX-3, we see that for high signal-to-noise ratios, more observers preferred BSC noise to Gaussian noise, while the reverse was true for low signal-to-noise ratios. The ranges in which the crossover points lie can be obtained from either Table XX-2 or Table XX-3. They are listed in Table XX-4.

	From Paired Comparison	From Matching
Face	16-16.5	16-16.5
Camerman	16.5-20	16.5-20
Crowd	16.5-20	20-22

We see that the results from the two methods agree with each other except in the case of the crowd. Even in that case, however, inspection of Table XX-3(c) reveals that the crossover point according to the matching tests is very close to 20 db. The data of Table XX-4 indicate that as the amount of detail in a picture increases, the crossover point moves to a higher signal-to-noise ratio.

The general trends discussed here may probably be explained in the following manner. It is evident from Fig. XX-4 that the Gaussian noise degrades the entire picture

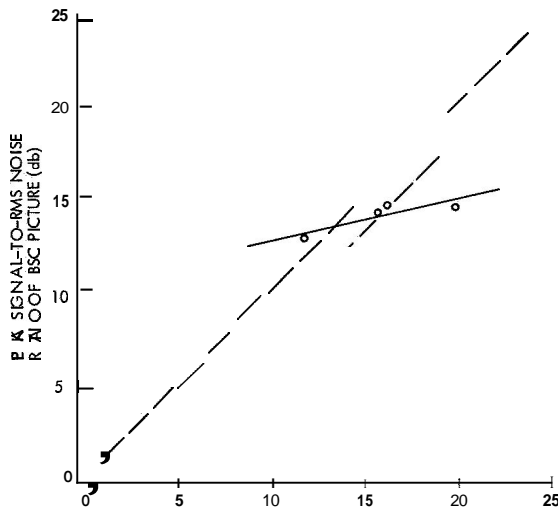


Fig. XX-5. Isopreference curve for the picture of the face.

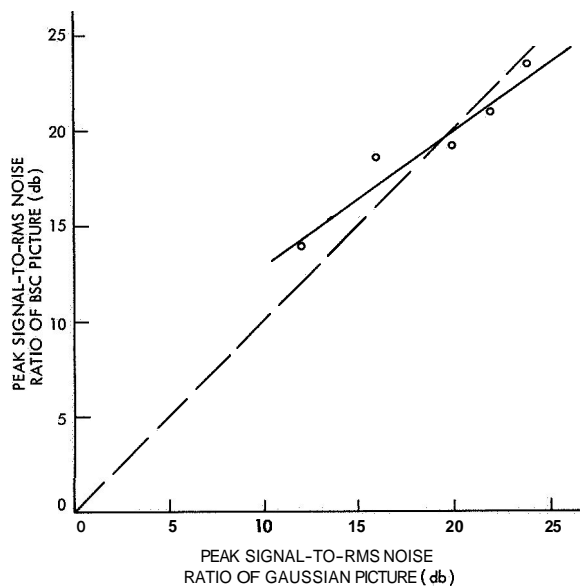


Fig. XX-6. Isopreference curve for the picture of the cameraman.

Also, at a given signal-to-noise ratio, more details would tend to be obscured by the dots (and therefore the noise would appear more objectionable) in a picture with a large amount of detail such as the crowd picture, than in a picture with a small amount of detail such as a face picture.

b. Isopreference Curves

Isopreference curves (i.e., curves expressing the relation that the signal-

to be equally preferable) were obtained from Table XX-3. This was done by estimating the signal-to-noise ratios of BSC pictures corresponding to the ranks of the Gaussian pictures listed in Table XX-3. If a rank m satisfied

$$k < m < k + 1, \quad (5)$$

where k was an integer, and if the signal-to-noise ratios of BSC pictures corresponding to ranks k and $k + 1$ were a and b , then, c , the signal-to-noise ratio of the BSC picture corresponding to rank m was estimated as

$$c = a - (m-k)(a-b). \quad (6)$$

The isopreference curves for the three original pictures are plotted in Figs. XX-5, XX-6, and XX-7. The solid

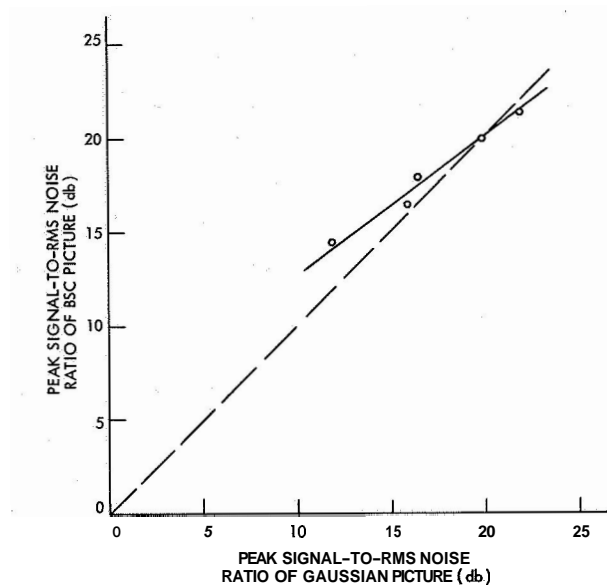


Fig. XX-7. Isopreference curve for the picture of the crowd.

lines are the linear least-mean-square fit to the data points. The dotted lines are the lines with unit slope on which the Gaussian and BSC pictures have the same signal-to-noise ratios. These plots express in a quantitative way the general trends that we have discussed.

T. S. Huang, M. T. Chikhaoui

References

1. E. M. Deloraine and A. H. Reeves, "The 25th Anniversary of Pulse Code Modulation," *IEEE Spectrum*, Vol. 2, No. 5, pp. 56-63, May 1965.
2. T. S. Huang, "PCM Picture Transmission," *IEEE Spectrum*, Vol. 2, No. 12, pp. 57-63, December 1965.
3. J. M. Barstow and H. N. Christopher, "The Measurement of Random Monochrome Video Interference," *Trans. AIEE*, Vol. 73, Part 1, pp. 735-741, January 1954.
4. J. M. Barstow and H. N. Christopher, "The Measurement of Random Video Interference to Monochrome and Color Television Pictures," *Trans. AIEE, Communications and Electronics*, Vol. 63, pp. 313-320, November 1962.
5. R. C. Brainard, F. N. Kammerer, and E. G. Kimme, "Estimation of the Subjective Effects of Noise in Low-Resolution Television Systems," *IRE Trans.*, Vol. IT-8, No. 2, pp. 99-106, February 1962.
6. T. S. Huang, "The Subjective Effect of Two-Dimensional Pictorial Noise," *IEEE Trans.*, Vol. IT-11, No. 1, pp. 43-53, January 1965.
7. P. Mertz, "Perception of Television Random Noise," *J. SMPTE*, Vol. 54, pp. 8-34, January 1950.
8. P. Mertz, "Data on Random-Noise Requirements for Theater Television," *J. SMPTE*, Vol. 57, pp. 89-107, August 1951.

9. T. S. Huang and O. J. Tretiak, "Research in Picture Processing," in Optical and Electro-Optical Information Processing, edited by J. Tippet, et al. (The M.I.T. Press, Cambridge, Mass., 1965).
10. I. T. Young and J. Mott-Smith, "On Weighted PCM," IEEE Trans., Vol. IT-11, No. 4, pp. 596-597, October 1965.

C. PATTERN-RECOGNITION STUDIES

1. COMPUTER SIMULATION OF BIOLOGICAL PATTERN GENERATION: A PRELIMINARY REPORT

Introduction

A complete survey of the field will not be attempted here. Rather, reference is made to the excellent book by C. H. Waddington¹ which discusses in some detail the problems of biological pattern generation, or morphogenesis, and its relation to genetic information.

Several lines of evidence suggest that although the DNA base sequence in the genome may only be specifying a particular sequence of bases in RNA molecules, and through it a collection of amino-acid sequences in proteins, the over-all pattern of development and morphogenesis is the result of a hierarchically ordered set of interactions between genes and gene products, and between genes and the external environment. This set of interactions is analogous to an ordered list of instructions concerning the way in which any particular pattern is going to be generated. This contrasts sharply with the old-fashioned notion that morphogenetic information is like a blueprint of the generated pattern.

In the work reported here, an attempt is made to simulate the generation processes of a variety of biological patterns. A successful simulation of a generation process is an analog of the natural process. Such an analog may contribute toward the understanding of the following problems.

(i) The setting of an upper limit to the minimal amount of information required to specify any particular pattern. This limit could then be expressed as a number of genes, or an amount of DNA, and compared with what is known to be required.

(ii) The organized set of generation rules may be the most economical language with which to describe and classify complex biological patterns. Any particular pattern in a class would then be described by the set of values of the adjustable parameters of the generation program for its class.

(iii) Although several different simulation programs may generate the same pattern, it is very likely that the characteristics of such programs might suggest some general requirements for the natural generation process of any one class of patterns. More definite conclusions might be reached about the minimal degree of

(XX. COGNITIVE INFORMATION PROCESSING)

complexity which is required.

(iv) For complex biological patterns, the simulating analog programs may be very useful in suggesting plausible hypotheses to explain the mechanisms of the natural generation processes, and in designing experiments to test these hypotheses.

Problems of Determinism] Randomness, Autonomy, and Resolution in Pattern Generation

Many natural biological patterns contain a great deal of redundancy in terms of repeating substructures. They also vary a great deal in the degree of deterministic reproducibility which they attain. A hierarchically ordered list of morphogenetic instruction seems to be the most efficient way to generate such patterns with a minimal amount of information in their specifications. Following the Dancoff-Quastler principle of the natural tendency of stored information to be degraded unless balanced by selection, we may expect therefore that the generation of any particular pattern will contain the minimum amount of determinism and resolution which is compatible with an optimal performance of its task **or** function.

We may now classify biological patterns according to their performance functions and the type and amount of information which they can receive while they are being generated.

a. CLASS I

In this class, performance depends critically on accurate matching **or** complementing an existing pattern with no possibility of interaction **or** exchange of information during the generation process. In this class of patterns] the generation process must be accurately specified intrinsically and be free from noise above **the** level of tolerance.

Common examples are genetically determined morphological **or** behavioral patterns that are important in the interaction between individuals, either of the same species, such as sexual **or** parental patterns of color and innate behavior, **or** of different species, such as in parasite-host interactions **or** in mimicry.

The level of tolerance of deviation from the norm must be measured by different scales in different cases. We may consider the elementary building blocks to be of the size of the average protein molecule, i. e. , $\sim 10^5 \text{ \AA}^3$ **or** $\sim 10^{-18} \text{ cm}^3$, **or** possibly the size of an 'active site,' which is of the order **of** $\sim 10^3 \text{ \AA}^3$ **or** $\sim 10^{-20} \text{ cm}^3$. This degree of resolution in the specification of patterns may be reached in the structure of viruses and in structures that are responsible for specificity in cellular interaction, including fertilization and conjugation. In most other patterns, however, the degree of resolution is much coarser, being of the order of cell size, i. e. , $\sim 10^{-9} \text{ cm}^3$, **or** even of the order of organ pattern, i. e. , $\sim 10^{-3} \text{ cm}^3$. For each pattern it should be possible to relate loss of performance with increasing relative variance, **or** relative noise, at each level of

resolution. Alternatively, loss of performance can be related to the absolute magnitude of the deviation from the norm. A better way to express and compare deviations may be by using a relative scale. This takes care of the tremendous range of size of different patterns, and is intuitively in agreement with a natural scale for comparing amplitudes.

b. CLASS II

Performance in this class depends on an accurate matching **or** complementing by a forming pattern of another pre-existing pattern with which it has considerable interaction during the generation process. Examples are many patterns of differentiation in which patterns develop in intimate contact with each other and are regulated one by another.

In this class of patterns, the generation processes must be specified in terms **of** intrinsic responses to external signals from neighboring pre-existing patterns. The information content of a pattern in this class is derived in part from adjacent pre-existing patterns. The dependence on signals from other patterns may be restricted to some limited phases of the generation process. Thus, it is possible that the general layout of a branching pattern is the result of signals received from a pre-existing branched pattern, but that the details of the pattern are determined autonomically.

c. CLASS III

Patterns in this class have a performance function that depends only on certain few properties of the patterns and does not depend on detailed structure. Such patterns are, **for** example, the distribution of small vessels in many tissues of both animals and plants, the distribution of hairs, small feathers, and so forth. It is suggested that the generation process of such patterns involves a repeated operation of a few generation rules under some specific boundary conditions and constraints. It might also respond to signals from other pre-existing patterns **or** from the external environment.

Hierarchical Patterns and Their Generation by a Sequential Process

One useful assumption about many patterns seems to be that they have a hierarchical structure. **By** this is meant that they appear to have several levels of organization which are only loosely interdependent. For example, the pattern of distribution of many multiple organs, such as hairs, may have little effect on the structure of each hair and on its associated structures. Thus it is most likely that the generation process determines at first the spatial distribution of such organs and only later on, and somewhat independently, it determines the detailed structure of each organ, apparently by applying repeatedly an identical subroutine. In many cases, the distribution at some levels varies with only a few constraints on spacing and angles of branching, while the detailed structure of each element **or** the large-scale distribution is highly deterministic and autonomous.

In motile animals, the level of basic large-scale organization is highly deterministic

and is accurately specified genetically. The intermediate level of detailed spacing is, in many instances, much less deterministic, the detailed pattern having a large random component. The level of organization of specific small patterns may again be highly deterministic. Finally, at the intercellular level, the patterns are again less precisely determined.

In plants, on the other hand, the large-scale level of organization is much more plastic. It usually follows some branching rules and interacts strongly with the environment. This is similar to the case of colonial forms of corals, in which the form of the colony is the result of the interaction of some branching rules with external signals.

One would expect to find in general that (I) At those levels of organization in which the generation process is less accurate there is a greater tolerance of deviation from the mean. (II) On the other hand, when the generation process is deterministic and accurate, one might expect to find (a) that small induced deviations from the norm will cause a large decrease in performance **or** viability; (b) alternatively, an accurate and deterministic generation process may be the result of a simple deterministic generating procedure may be most economical in the information content of its instructions. In such a case, it would be possible to modify extensively the detailed outcome without decreasing very much the viability.

The above-mentioned expectations may be restated so as to predict equal changes in expectation of reproduction when relatively equal changes are induced in patterns, as measured in units of relative variance. These expectations could hold independently for different hierarchical levels of a pattern. Thus, the tolerance at one level may be very different from the tolerance at another level, which is in agreement with observed differences in natural variance at different hierarchical levels.

Developmental and Genetic 'Noise' **or** Variance

Developmental variance may be defined as made up of two parts. The first part is the variance of the pattern when both genetic and environmental factors are uniform. The second part is the additional variance that results when the genetic factors are uniform and the environmental factors vary within their normal range. The first part may be called the 'intrinsic' developmental variance, and the second part, the 'normal' **or** naturally induced variance.

Both the intrinsic and the induced developmental variances are under genetic control and are subject to selection. An optimal distribution of developmental variances is expected to be reached and remain stable under any particular combination of genetical and environmental conditions.

The measurement of variance can be made between **or** within patterns of a single organism, **or** between organisms in a population. The genetic variance can only be measured between different organisms in a population. It is the additional variance in

a population when all normally occurring genotypes are taken into account. The expression of genetical factors usually depends on environmental conditions during development. Alternatively, genetic variance may be looked upon as a factor determining the developmental variance. When genetic constitution is identical, such as in identical twins, pure inbred lines, and so forth, and under identical external conditions, the variance between organisms may be expected to approach the variance within organisms.

Methods

The generation of particular biological patterns has been simulated by the application of an ordered set of generation rules. The set of rules has been derived for any particular pattern from what was thought to be known about the way this pattern was generated naturally. The rules were modified and extended so as to increase the resemblance between the output of the simulation and the natural pattern which was being simulated. Furthermore, alternative sets of rules have been tried in order to test their uniqueness in generating the pattern.

Simple patterns in two dimensions were tried first, because of the relative simplicity of their generation and representation. Success with this class of patterns will be followed by exploring the possibilities of generating more complex, interacting patterns in three dimensions. Special display techniques will be needed in order to represent computer output for three-dimensional patterns in a form that could be simply and clearly visualized and recognized.

Thus far, our results deal only with simulation of two-dimensional branching patterns. This class of patterns is characteristic of venation patterns in leaves and in other flat or layered structures. As we have said, we attempted to simulate the generation process of such patterns by using the smallest number of arbitrary parameters, and the simplest possible generation rules.

a. Growth Rules

(i) Growth occurs at the tips of branches.

(ii) The amount and angle of growth is determined by the intensity of the local density field, the direction and magnitude of the gradient of this field, the previous angle of the free end of the branch, and the tendency of the growing branch to persist in its original direction in spite of the gradient in density field.

(iii) The density field around a point is computed by taking 36 sample points at 10° intervals at a unit distance from the central point and taking as a measure of the density at each sample point the sum of the squares of the reciprocals of the distances to all neighboring parts of the pattern. The direction of the negative gradient and its magnitude are then computed by interpolation.

(iv) The extent of growth UG is given by

(XX. COGNITIVE INFORMATION PROCESSING)

$$UG = U \cdot \frac{DGT - DMIN}{DGT},$$

where U is the unit distance, $DMIN$ is the local minimum in the density field, and DGT is a limiting density above which no growth can occur. (Negative growth is not allowed.) The value of DGT determines the limiting density of the pattern as a whole.

(v) Growth angle GA is given by

$$GA = \frac{SA \cdot ST + GRA \cdot GR}{ST + GR},$$

where SA is the angle of the free end of the branch, ST is the inertial factor for growth direction, GRA is the direction of the negative gradient of the local density field, and GR is the magnitude of the gradient.

A continuous iterative application of these growth rules leads to unlimited growth except when the minimum local density exceeds the limiting density for growth, i. e. , when $DMIN > DGT$. In general, the growth will be directed toward the unoccupied space in the periphery of the already existing pattern.

(vi) Growth may be directed to various extents by biasing the density field in any one direction in space, or in the direction of a particular area or boundary in the growth space.

b. Branching Rules

It is the branching rules that, to a large extent, determine the final form and texture of the generated pattern.

(i) The density is computed for each potentially branching point in the pattern in exactly the same way as for the growing points.

(ii) Branching probability PRB is computed according to the equation

$$PRB = \frac{DBT - DMIN}{DBT} \cdot \frac{DB - DBL}{DB} \cdot \frac{DD - DDL}{DD},$$

where DBT is the limiting density for branching, DB and DD are the distance from base and apex of the segment, respectively, and DBL and DDL are the respective limiting distances. $DMIN$ has the same meaning as in the growth equation.

(iii) A random trial decides in each iteration whether branching will actually occur.

(iv) Branching angle BRA is determined in the same way as growth angle with the addition of a standard angle $BRAS$ and a persistence factor, $STBR$. Thus

$$BRA = \frac{BRAS \cdot STBR + GRA \cdot GR}{STBR + GR}$$

A continuous application of these branching rules, together with the unidirectional growth rules (i)-(v), will generate uniformly spreading patterns which will assume an approximately circular shape, irrespective of the initial direction and asymmetry.

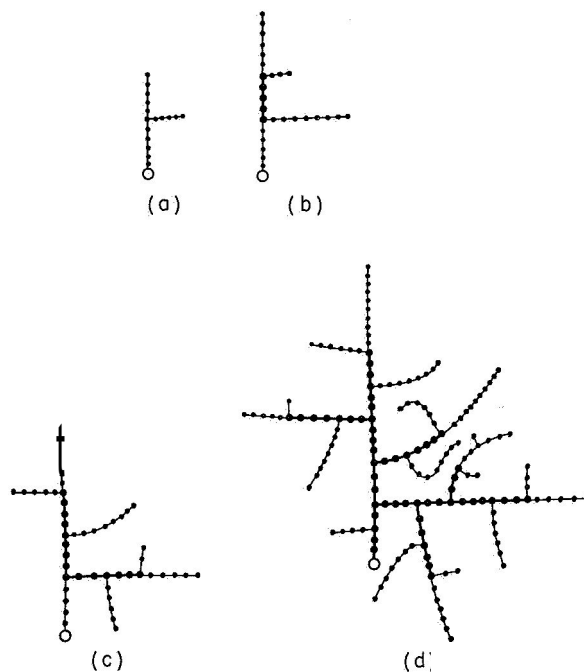


Fig. XX-8. Several stages in the growth of a simulated branching pattern (a-d). The persistence factors for growth and branching, ST and STBR respectively, are both zero, so that both growth and branching always follow the negative gradient of the local density field. An intermediate spacing of the branches is caused by intermediate distances between branching points, DBL for the distance from a basal branching point and DDL for the distance from the distal end of the segment.

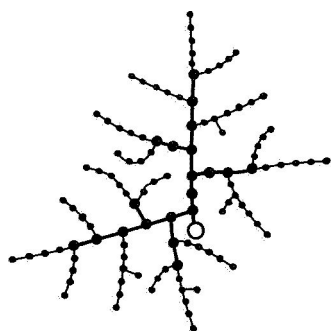


Fig. XX-9. The only change from the patterns in Fig. XX-8 is that dense branching is caused by low values of the limiting distances between branching points, $DBL = 1.0$ and $DDL = 1.0$. The tendency to assume a diffuse circular shape is obvious.

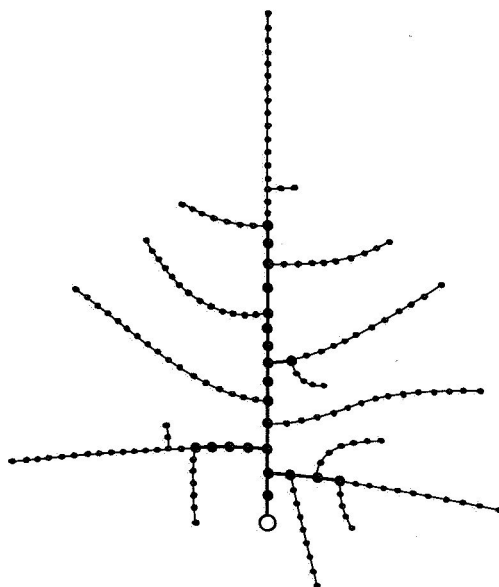
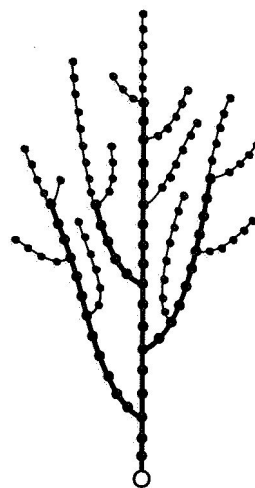


Fig. XX-10. This treelike pattern is caused by increasing the limiting distance from the distal end of the segments, $DDL = 10.0$, while maintaining the limiting distance from the basal end at a low level, $DBL = 1.0$.

Fig. XX-11. A directed treelike pattern is generated by biasing both growth and branching in the direction of the Y axis.



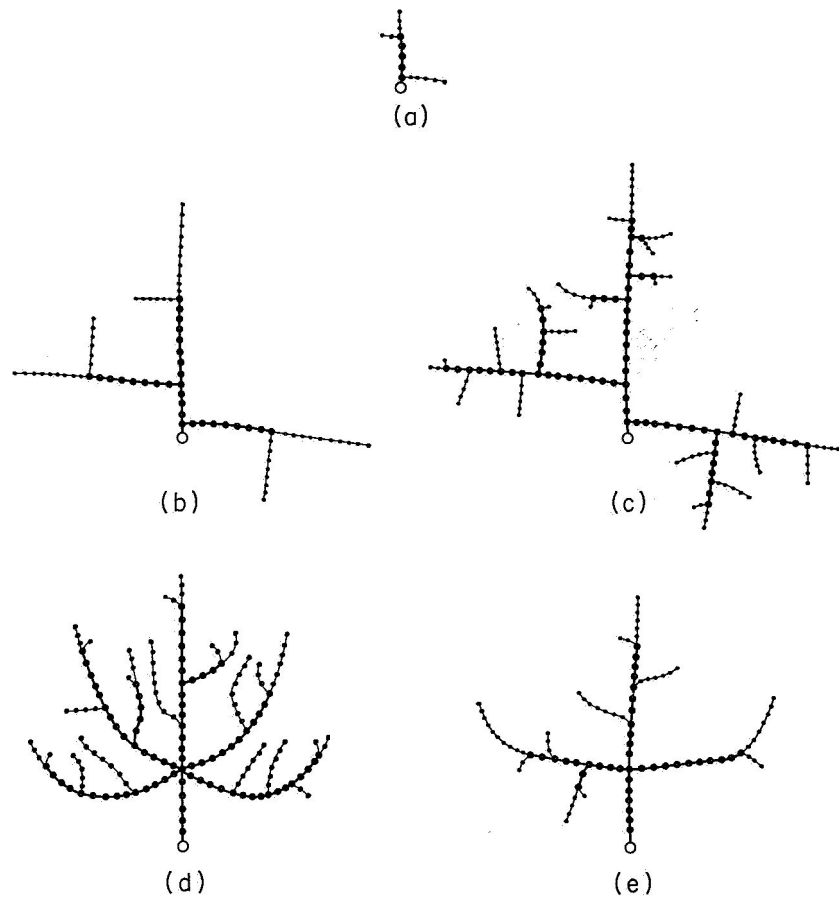


Fig. XX-12. (a-c) A hierarchically organized pattern is generated by having the limiting distances for branching vary with the total number of points in the pattern, NT. Both growth and branching are undirected.

NT range	DBL	DDL	Figure
0-20	1.0	1.0	(a)
20-100	8.0	1.0	(b)
100-200	1.0	1.0	(c)

(d-e) These patterns are generated by the operation of a special branching rule once early in the generation process. This rule generates a number of branches symmetrically spaced in relation to the primary axis, and with equal angles between them. Growth is slightly biased upwards during some stage of the generation process to give a leaf-like pattern.

(XX. COGNITIVE INFORMATION PROCESSING)

(v) Branching may become directed in the same way as growth by introducing a bias in the local density field in any one direction in space **or** in the direction of a particular area **or** boundary. Growth bias and branching bias may be entirely independent, although they tend to reinforce each other if they are in the same direction. The whole pattern may thus be made to assume a directional asymmetric shape by growing and branching in a preferred direction.

Both growth and branching rules may have their parameters changed as a function of either some local property of the pattern **or** some property of the pattern as a whole. This introduces a hierarchical element into the generation process, as required for the simulation of biological pattern generation. Thus, a specific branching subroutine may be applied only once at a particular early stage in the growth of the pattern which will determine the shape and relations of the primary branches of the pattern. Alternatively, the parameters may be a function of distance from a local perturbation in the growth space, which may result in specific morphogenetic effects of the perturbation. Also, branching may be completely inhibited in segments that have some particular connectivity characteristics, such as having a particular rank order, being a side branch to a main branch, **or** not having a free growing end, and so forth.

Results and Conclusions

Some representative examples of stages in the growth of the simulated patterns are shown in Figs. XX-8 through XX-12. Detailed descriptions and explanations are given in the legends for each figure **or** group of figures.

Note that in all figures a circle indicates the initiation point. Segments marked with a thick line are 'old' segments, i. e. , they no longer branch **or** grow.

Although preliminary in nature, our results seem to show the usefulness of the approach: First, by demonstrating the variety and richness of patterns that can be generated by a very limited set of adjustable parameters; second, by establishing an unambiguous and quantitative method for investigating the generation process of an important class of patterns; and third, by providing a working language for a synthetic approach to the problem of specification and classification of growing patterns in general.

D. Cohen

References

1. C. H. Waddington, New Perspectives in Genetics and Development (Columbia University Press, New York and London, 1962).

XXI. COMMUNICATIONS BIOPHYSICS*

Academic and Research Staff

Prof. D. B. Geselowitz	Prof. T. F. Weiss†	Dr. N. Y. S. Kiang\$
Prof. P. R. Gray	Prof. H. Yilmaz††	Dr. R. R. Pfeiffer†
Prof. H. B. Lee	Dr. J. S. Barlow††	Dr. R. Rojas-Corona
Prof. W. T. Peake†	Dr. A. W. B. Cunningham	Dr. G. F. Songster
Prof. W. A. Rosenblith	N. I. Durlach	R. M. Brown†
Prof. W. M. Siebert	Dr. H. Fischler***	A. H. Crist†
Prof. R. Suzuki**	Dr. R. D. Hall	D. P. Langbein†

Graduate Students

J. A. Anderson	D. K. Hartline	M. Nahvi
G. von Bismarck	A. J. M. Houtsma	P. H. O'Lague
L. D. Braida	L. K. Krakauer	D. J-M Poussart
S. K. Burns	R. G. Mark	M. B. Sachs
H. S. Colburn	E. G. Merrill	M. M. Scholl
J. E. Evans	P. J. Metz III	J. J. Singer
J. A. Freeman	D. C. Milne	I. H. Thomae
J. J. Guinan, Jr.	C. E. Molnar	M. L. Wiederhold
	E. C. Moxon	

Undergraduate Students

D. Assael	S. J. Hayashi	R. L. MacDonald
J. E. Brown III	J. L. Lehr	W. A. Plice III
J. M. Hahn		D. G. Tweed

A. WORK COMPLETED

These reports summarize S. B. theses submitted to the Department of Electrical Engineering, M. I. T., May 1966.

1. HIGH SPEED ELECTROMECHANICAL SHUTTER FOR VISUAL NEUROPHYSIOLOGY

An electromechanical shutter capable of interrupting a light beam, 7 mm in diameter, in less than one millisecond was needed for use in a visual stimulator. By overdriving a

⁸This work was supported by the National Institutes of Health (Grants 2 PO1 MH-04737-06 and 5 RO1 NB-05462-02), the Joint Services Electronics Programs (U. S. Army, U. S. Navy, and U. S. Air Force) under Contract DA 36-039-AMC-03200(E), the National Science Foundation (Grant GK-835), and the National Aeronautics and Space Administration (Grant NsG-496).

† Visiting Associate Professor from the Moore School, University of Pennsylvania.

† Also at Eaton-Peabody Laboratory, Massachusetts Eye and Ear Infirmary, Boston, Massachusetts.

** Visiting Assistant Professor from the Research Institute of Dental Materials, Tokyo Medical and Dental University, Tokyo, Japan.

†† Visiting Professor from Arthur D. Little, Inc., Cambridge, Massachusetts.

\$\$ Research Affiliate in Communication Sciences from the Neurophysiological Laboratory of the Neurology Service of the Massachusetts General Hospital, Boston, Massachusetts.

† From the Department of Electronics, Weizmann Institute of Science, Rehovoth, Israel.

pen motor with a vane mounted on the stylus to interrupt the light, a rise time of 0.7 msec and a fall time of 0.8 msec were achieved.

J. M. Hahn

2. COMPUTER SIMULATION OF SEQUENCE OF ACTIVATION IN FIBRILLATING HEART

A program for simulating a trial fibrillation, similar to one reported by Moe, Rheinholdt, and Abildskov¹ was developed for a PDP-1 computer. A square array of 2500 cells (50 X 50) was used to represent a cylindrical surface. Wave fronts leaving the right edge re-enter on the left. A cathode-ray oscilloscope display was used, with spots of light indicating active cells.

Once a cell has fired, it can activate the adjacent four cells (two on upper or lower edge) in succeeding time intervals that depend on the time at which the inactive cell last fired. If an adjacent cell is in the "absolute refractory" period, it will not fire at all; if it is in the "resting state" it will fire on the next cycle. During the "relative refractory" period delays of 1 to 5 intervals are introduced. Heterogeneity in the population of cells was introduced in a separate program that distributed randomly the length of the absolute refractory period between two limits.

With no randomness present, circus movements were observed with specific excitation patterns, and the failure of stimulation at one or more points to produce sustained activity was noted. These results are consistent, for example, with those predicted by Wiener and Rosenblueth.²

When the refractory period was randomized in the range of 10-30 time steps, response to an ectopic focus was quite regular and sustained activity was not observed after the stimulation ceased. The range was then extended to 8-30 time steps, and then spontaneous, apparently turbulent, activity was observed as reported by Moe. New runs were made with an ectopic focus continually firing. The activity appeared to be just as random. The model, then, appears to be unable to distinguish re-entry mechanisms from ectopic foci as the basis of fibrillation. The use of autocorrelation to study the nature of the firing patterns in the model was suggested.

S. J. Hayashi

References

1. G. K. Moe, W. C. Rheinholdt, and J. A. Abildskov, "A Computer Model of Atrial Fibrillation," *Heart J.* **67**, 200-220 (1964).
2. N. Wiener and A. Rosenblueth, "The Mathematical Formulation of the Problem of Conduction of Impulses in a Network of Connected Excitable Elements, Specifically in Cardiac Muscle," *Archivos del Instituto de Cardiologia de Mexico* **16**, 205-265 (1946).

3. CONTROL OF A SERVO RESPIRATOR USING MUSCLE POTENTIALS

The advantages of a respirator which is under full-time patient control is discussed. Efforts to record electromyograms from skeletal musculature involved in respiration are described. The system finally developed derives a control signal from an esophageal electrode which picks up muscular activity from the patient's diaphragm. A simple but effective method of discriminating the muscle activity of the diaphragm from the electrocardiogram is presented. Included is a tentative design of a respirator control system which uses this signal and includes fail-safe features.

J. L. Lehr

4. COCHLEAR POTENTIALS IN GUINEA PIGS WITH SURGICALLY PRODUCED ENDOLYMPHATIC HYDROPS

Cochlear microphonic potentials (CM), DC endolymphatic potentials (EP), and auditory-nerve compound action potentials (N_1) were measured for a variety of stimulus conditions from both cochleas of animals with unilateral hydrocs. Comparison of measurements between the normal and operated ears for 14 guinea pigs showed a definite tendency for CM, EP, and N_1 to be smaller in the operated ears, although in a few animals the differences were not significant. Although only fragmentary histological results are available now, there appears to be a correlation between the diminution of the potentials and the degree of hydrocs.

These experiments were carried out in cooperation with Mr. Robert Kimura of the Electron Microscopy Laboratory, Massachusetts Eye and Ear Infirmary.

R. L. MacDonald

5. TEMPERATURE-AND HUMIDITY-REGULATING APPARATUS FOR A MICROSCOPE-STAGE INCUBATOR

An automatic temperature-controlling device was designed and constructed for a small, partially open incubator mounted on a microscope stage. Also, an independently operating humidity supply designed to maintain high water vapor content of the same incubator is described. Although the basic parts of the temperature-controlling device are applicable to other situations, the microscope-stage incubator places restrictions on the choice of heating and temperature-sensing elements which, being reflected in the overall design, results in a somewhat specialized instrument.

W. A. Plice III

6. A HIGH SPEED ANALOG-DIGITAL CONVERTER INPUT AND COMPARATOR CIRCUIT DESIGN

The design of an input amplifier, sample-and-hold comparator circuit is described in this thesis. The design is described from the initial specifications through to the

(XXI. COMMUNICATIONS BIOPHYSICS)

final design and includes comments on circuitry which was not used in the final device, as well as a description of the completed system. Particular attention was given to the effects of thermal drift and component selection. The final specifications are:

Input dynamic range	1 volt peak-to-peak
Input impedance	100,000 ohms
Input coupling	DC
Sampling time	0.5 psec
Hold time	10 psec
Comparison time	0.04 psec
Total drift	0.1% for 60°C temperature change

D. G. Tweed

B. PSYCHOACOUSTICS

1. GENERAL REMARKS

The work in psychoacoustics during the past year can be divided into the following categories: (a) binaural unmasking, (b) perception of frequency ratio, and (c) preparation for future research. The work on binaural unmasking has consisted of preparing previous results for publication, analyzing certain aspects of the phase-detector model of binaural unmasking, and performing an experiment to determine the dependence of binaural unmasking on the bandwidth of the masking noise. The research on the perception of frequency ratio has been concerned with the difference between the physical and subjective octaves and with the ability to detect small changes in frequency ratio. The work related to future research has consisted of an attempt to formulate a language in which one can construct a model for short-term memory of sounds, construct an overview of psychoacoustics that will allow one to relate certain topics in psychoacoustics which are now treated separately, and develop instrumentation that is more flexible and efficient. The effort to prepare previous results for publication has resulted in two journal articles^{1,2} and a chapter in a book.³ The work on the phase-detector model of binaural unmasking, the perception of frequency ratio, and the development of new experimental facilities, is outlined below.

N. I. Durlach

References

1. L. R. Rabiner, C. L. Laurence, and N. I. Durlach, "Further Results on Binaural Unmasking and the EC Model" (to be published in J. Acoust. Soc. Am.).
2. N. I. Durlach, "Note on Application of EC Model to Interaural JND's" (submitted to J. Acoust. Soc. Am.).
3. N. I. Durlach, "Binaural Signal Detection: Equalization and Cancellation Theory," Chapter 16 in Modern Foundations Of Auditory Theory, edited by J. V. Tobias and E. D. Schubert (to be published by Academic Press, Inc., New York).

2. ANALYSIS OF PHASE-DETECTOR MODEL OF BINAURAL UNMASKING

(S. B. Thesis)

The phase-detector model of binaural unmasking was proposed by Webster¹ in 1951 and Jeffress, Blodgett, Sandel, and Wood,' in 1956, to account for certain results on the binaural unmasking of tones masked by random noise. It is assumed that there exists a narrow-band peripheral filter (the "critical band") and that the effective masking noise can be regarded as a sine wave of the same frequency as the tone, but with a slowly varying amplitude and phase. The interaural phase of the total signals (signal plus noise) can be shown to depend on the interaural differences in amplitude and phase of the tone and noise, and the amplitude and phase of the noise relative to the tone. The fundamental assumption of the model is that binaural detection is based on observations of this interaural phase. Since the amplitude and phase of the noise are random, this interaural phase is also random. In previous work on the model, the statistical properties of this variable have not been adequately analyzed. In this thesis, an attempt was made to compute the probability distribution function on the interaural phase for a variety of stimulus configurations. The results (which are far from complete) are presented in integral form and require the use of a computer for numerical evaluation.

J. E. Brown III

References

1. F. A. Webster, "The Influence of Interaural Phase on Masked Thresholds. I. The Role of Interaural Time Deviation," J. Acoust. Soc. Am. 23, 452-462 (1951).
2. L. A. Jeffress, H. C. Blodgett, T. T. Sandel, and C. L. Wood III, "Masking of Tonal Signals," J. Acoust. Soc. Am. 28, 416-426 (1956).

3. SUBJECTIVE OCTAVES (S. B. Thesis)

An experiment was performed to determine, for a given reference frequency, the frequency ratios corresponding to a subject's estimate of the 1st upper octave, the 2nd upper octave, and the 1st lower octave. In each case, the estimate was obtained by presenting the subject with a sequence of two alternating tones, one of which was fixed and one of which was variable, and instructing the subject to adjust the variable tone to the required octave. The results indicate that there is a general tendency for the estimates of the 1st and 2nd octaves to exceed the frequency ratios 2:1 and 4:1, respectively. In most cases, the results were consistent with those obtained by Ward on "subjective musical pitch."¹

D. Assael

References

1. W. D. Ward, "Subjective Musical Pitch," J. Acoust. Soc. Am. 26, 369-380 (1954).

4. JUST-NOTICEABLE DIFFERENCES IN FREQUENCY RATIO (S.M. Thesis)

It is well known that our natural musical scale employs tones whose frequencies are related by simple whole numbers. A sequence of tones in this scale sounds "natural," whereas sequences of tones whose frequencies form more complicated ratios sound "strange" or "unnatural." The purpose of this project was to determine whether or not this phenomenon is reflected in the auditory system's ability to detect small changes in frequency ratio. Specifically, an attempt was made to determine the just-noticeable difference, Δk , in frequency ratio, k , in the vicinity of the octave ($1.90 \leq k \leq 2.10$) and at the major third ($k = 1.25$). The results of this work indicate that in the frequency region 350-1000 Hz and in the frequency-ratio region $1.25 \leq k \leq 2.10$, the Weber fraction $\Delta k/k$ is independent of k and has a value of approximately 0.006.

A. J. Houtsma

5. CBL 16-B: AN INSTRUMENT FOR MULTISUBJECT TWO-ALTERNATIVE FORCED-CHOICE EXPERIMENTS

CBL 16-B was designed to make random selections between two stimuli in a two-alternative forced-choice experiment, and to decode, record, and display the answers of up to 10 subjects simultaneously. The apparatus allows the experimenter considerable freedom in the choice and timing of the stimuli, and permits him to control the feedback of information to the subjects concerning correctness of response. It also allows him to control the probability of presentation and to observe the current and cumulative performance of the subjects. When used in the multisubject mode, presentations are paced by external timing devices. When used in the single-subject mode, the subject may be allowed to pace the presentations himself. Interlock mechanisms prevent the subjects from answering more than once on a given trial. When used in conjunction with a paper-tape punch, CBL 16-B provides a complete record of the experiment suitable for computer analysis. Although this instrument was designed primarily for two-alternative forced-choice experiments with up to 10 subjects, it can also be used in experiments in which the response set consists of more than two elements, provided the number of subjects is appropriately limited.

L. Braida, N. Jordan

6. PSYCHLOPS: A SYSTEM FOR USING THE PDP-4 COMPUTER FOR ON-LINE ADAPTIVE PSYCHOPHYSICAL EXPERIMENTS

A system of computer programs, called "PSYCHLOPS," has been developed for using the PDP-4 computer on-line to conduct psychophysical experiments. Although any sort of experiment may be performed with this system, the power of the computer is not

generally needed unless the experiment is adaptive. (An adaptive experiment is one in which the parameters of each stimulus presentation may be a function of the past record of the subject's responses.)

Using the PDP-4 remote console as an interface, the computer can control a variety of units, which in turn generate and shape the stimuli that reach the subject. Output from the remote console's digital-to-analog converter may be used to control a voltage-controlled oscillator, or for any other purpose. Level outputs from a remote console lamp register are used to set a digitally controlled attenuator, and to generate pulses which may be used to control electronic switches, feedback lights, and so on. The subject may signal the computer via the remote console trigger inputs.

The PSYCHLOPS programs handle all of the stimulus presentation timing, and record all responses by the subject. A user of the system wishing to conduct a particular experiment need supply only three things. First, he must give a table specifying all parameters of a stimulus presentation. This table may be altered under program control between stimulus presentations. Second, he must give a machine-language subroutine that computes, after each subject response, the parameters of the next stimulus presentation. Finally, he must give a machine-language subroutine with final output instructions.

When writing his two subroutines, a PSYCHLOPS user has at his disposal a large number of useful subroutines that are included in the system. These subroutines perform such services as table lookup, pseudo-random digit generation, and the formation of DO loops (as in FORTRAN), among others. Also, all output is handled through PSYCHLOPS subroutines. The user may give print or punch output commands at any time, and they will be properly processed by the system, in the program interrupt mode, without interfering with the stimulus and response timing.

To use the system, the user simply assembles his source tapes with the PSYCHLOPS system tapes. The remote console is wheeled over to the analog equipment rack, and connected to the appropriate units. Operation of the system may then be directed via the remote console lever switches, and, if necessary, the computer teletype keyboard.

The system has now been in use for some time, although it is still undergoing final debugging. Preliminary documentation is available. It has proved to be fairly easy to use PSYCHLOPS to conduct complicated adaptive experiments. The ease with which experiments may be altered merely by making small program changes makes the system particularly useful for experiments that are in the developmental stage.

L. Krakauer

C. GENERAL-PURPOSE COMPUTER FACILITY

During the past 18 months, we have undertaken to integrate a medium-sized digital computer (Digital Equipment Corporation PDP-4) into our laboratory facilities. This computation system provides a versatile tool for members of the group who are working on a variety of different projects. The computer is located in the center of the laboratory and has been specially adapted to handle easily real-time, on-line experimental problems. The facility contains an analog-to-digital conversion system, analog display, and analog outputs, a special real-time clock, a magnetic tape system for mass storage, a special switch and digital signal interface, and provisions for operating the computer remotely from the experimental stations. These features offer many of the conveniences of the LINC computer system,' but in a substantially larger and more powerful machine.

The full power of the computer can be focused on a particular problem simply by writing an appropriate program. This enables the computer to replace a variety of special-purpose devices, each built to do a specific job of data handling or experimental control. The computer system offers additionally more power and flexibility than are usually obtainable in a special-purpose device for a single application.

As examples of applications in connection with electrophysiological experiments, the PDP-4 computer has been used to perform quite flexible average-response computations with a minimum interval between points as low as 8.3 psec, up to 16 simultaneous averages, variable time-base averaging, and averaging data simultaneously before and after a trigger or synchronizing pulse. The computer has been used to compute histograms of firing patterns of single neurons with simultaneous computation and display of both interval and post stimulus time (PST) histograms for up to 4 different units. The simultaneous computation of average responses and histograms for single neurons has also been done.

All of these operations can be done in "real time" and the programs are equally well-suited for use during an experiment or for later off-line processing from analog magnetic tape. In many instances, however, the last advantage offers substantial savings of computation time.

In another application, the PDP-4 computer was used to determine the dependence of the amplitude of evoked responses on the phase of on-going alpha activity. Stimuli were randomly presented and EEG and stimulus information recorded on digital magnetic tape. The tape was then scanned for the occurrence of the alpha rhythm. Individual evoked responses were separated according to the phase of the alpha cycle in which they occurred. Average response computations were then made for a particular alpha phase. A family of average evoked responses showed the dependence of evoked response on alpha phase. This type of analysis was possible because the data were temporarily stored,

and average evoked responses were computed after decisions on alpha occurrence and phase had been made.

In one psychophysical study,¹ the PDP-4 computer used the cathode-ray tube display to present a visual stimulus to a number of subjects (up to 8) in a forced-choice experiment. Simultaneously, the computer checked individual response keys operated by each subject. The response times were recorded, displayed, and various statistics could be computed. The system can be arranged to present automatically randomly distributed stimuli and to record performance. Similar uses include the computer control of auditory signals in forced-choice experiments.

The computer has also been used in waveform detection problems to analyze electrical activity observed in explanted chick embryo cultures,³ and to evaluate, manipulate or display data in a variety of ways.

1. Hardware Description

The computer shown in Fig. XXI-1 is a basic Digital Equipment Corporation PDP-4 computer with 8192 words of 18-bit memory (8.333 μ sec/cycle). The system includes an IBM compatible magnetic tape unit and a 16-channel analog-to-digital system with an accuracy of 1 part in 256. Also, part of the system consists of hardware multiply and divide, a special real-time clock, and an analog system that drives a cathode-ray tube display and x-y plotter. A special relay, a switch, and a digital signal interface complete the system.

The 8.33-psec cycle time is moderately fast and sufficient for most purposes. The machine time is accurately controlled, and hence used by program loops as a time base. The 18-bit word memory is usually sufficient for calculations involving analog data (8 bits), and there is no need for multiple precision arithmetic in handling most of the data. The 8192 words of memory are all directly addressable, and allow rather long and involved programs to reside in memory together with a substantial amount of data. This allows a rather elaborate data display program to be used essentially as a subroutine. The magnetic tape system provides mass storage for data and programs, and also permits transfer of data to or from other more elaborate systems.

The A-D conversion system is easily programmed and provides 16 inputs to a single 8-bit converter. The maximum sample rate is 120,000 samples/sec, while the maximum continuous rate of analog conversion to IBM format magnetic tape is 20,000 samples/sec.

2. Remote Operation

A remote console has been constructed to provide convenient and efficient use of the PDP-4 for on-line use in experimental control and analysis of data. This remote console is shown in the left foreground of Fig. XXI-2. Five switch registers (18 bits) are

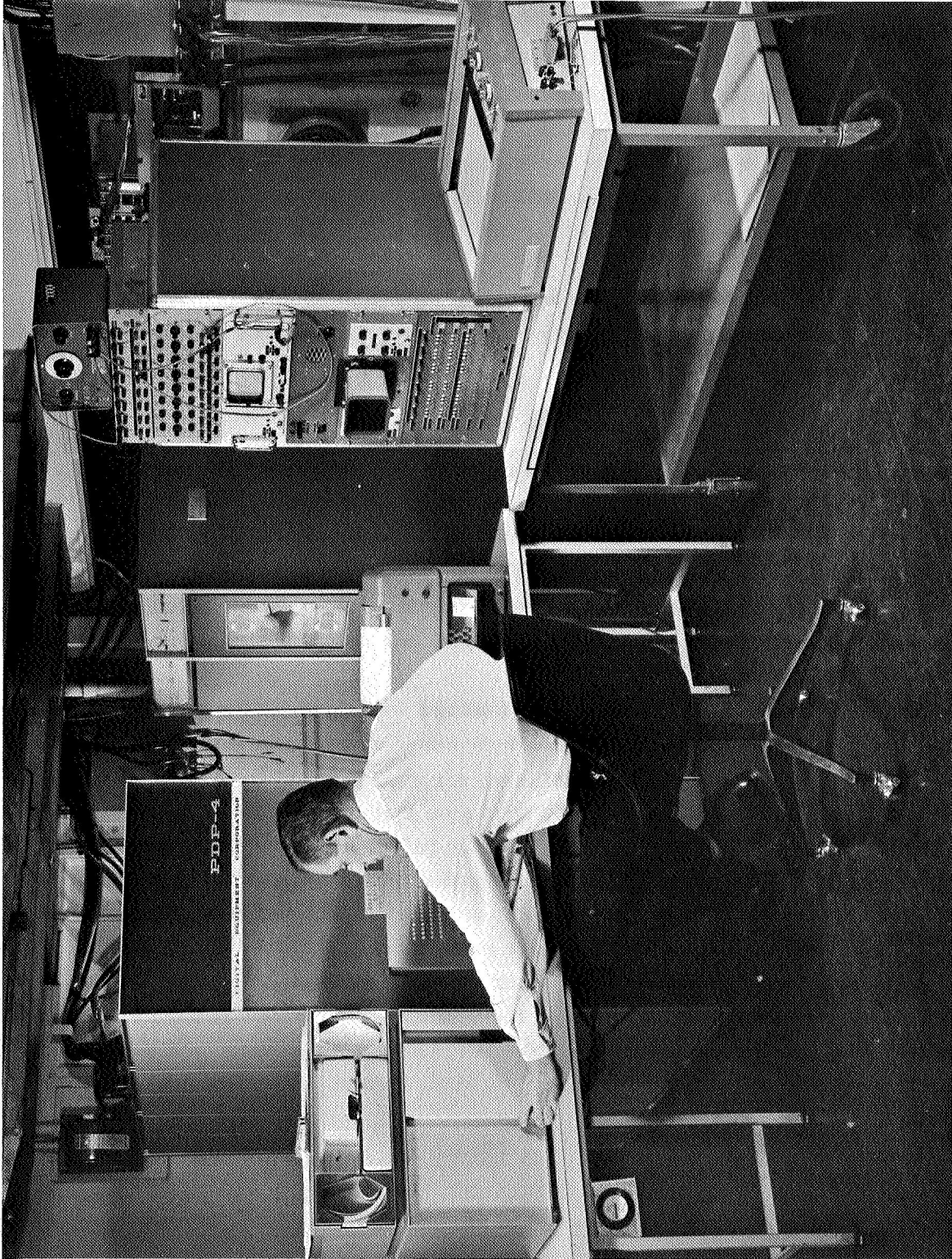


Fig. XXI-1. General view of the PDP-4 computer system.

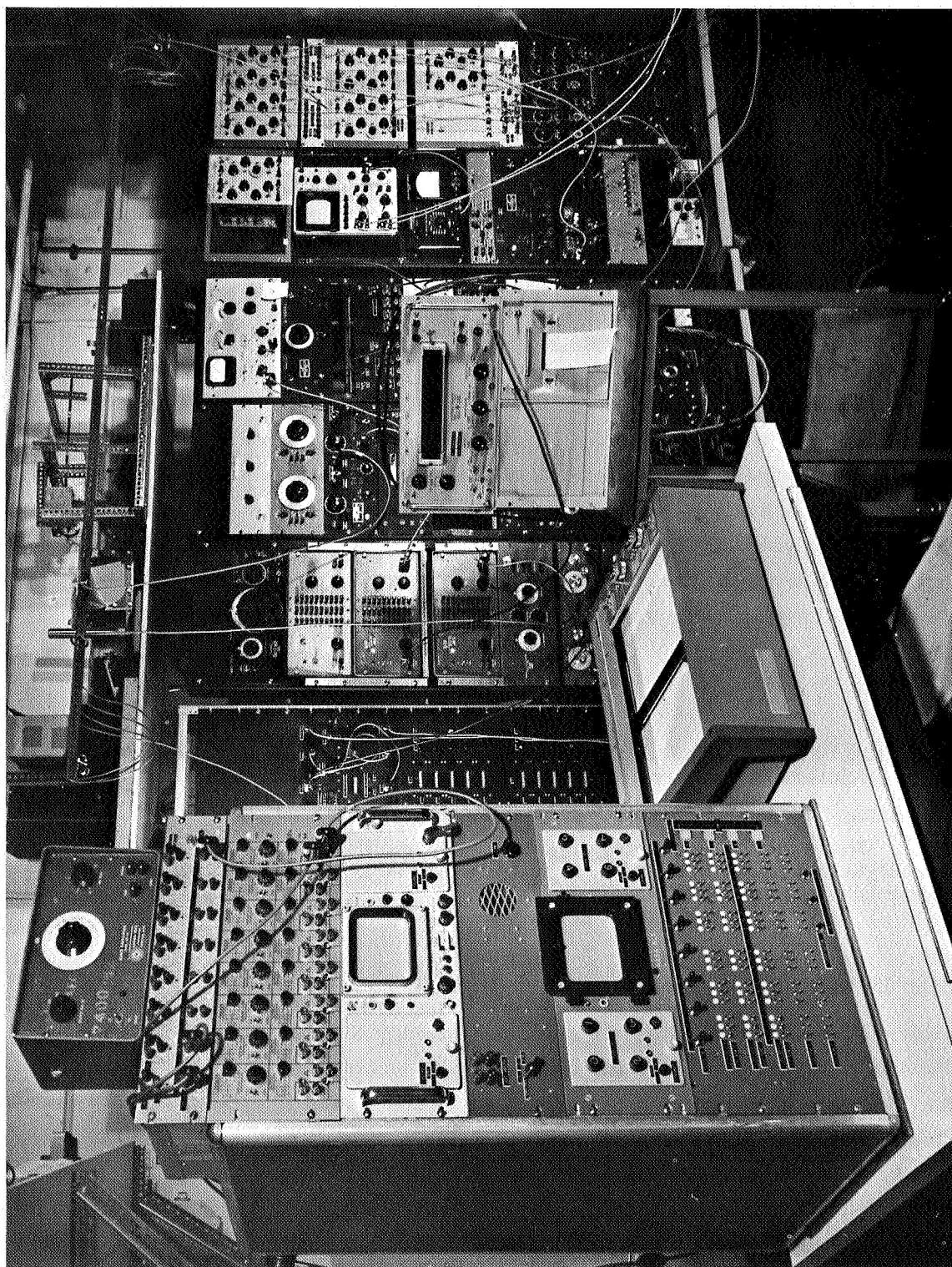


Fig. XXII 2. Remote console (left) as employed in a μ -chophysical experiment.

provided for the control of experimental parameters. The oscilloscope display presents both alphanumeric text and graphical data. The potentiometers located on either side of the display provide additional controls for various parameters. Connectors are provided on the console for inputs to the A-D conversion system, pulse inputs for synchronizing the computer to experiments, and relay and digital output lines for controlling experiments. Forty-eight indicator lights provide additional output to the operator, while lever and push-button switches may be used to control computer operation. The entire remote console, connected by permanent cabling, can be moved to any of the experimental stations in the laboratory. Programs are generally written to make use of the remote console for input, output, and control.

3. Summary

A PDP-4 computer has been incorporated into the facilities of our group. The computer is used to assist with a number of different experimental problems. A number of special features have been added to make the PDP-4 especially well suited for real-time, on-line use in electrophysiological and psychophysical experiments for both experimental control and data analysis. Because of the flexibility of the computer, it is possible for a number of different users to use the same machine, and thus allow each to have access to a more powerful system than would be easily justifiable for a single user.

R. J. Clayton

References

1. W. A. Clark, "The LINC," a paper presented at the Annual Meeting, National Academy of Sciences, National Research Council, Washington, D. C., April 12, 1962.
2. S. K. Burns, Course 6.37 Class Notes, M.I. T., 1966.
3. A. W. B. Cunningham, R. R. Rojas-Corona, J. A. Freeman, and P. H. Levine, "Tissue Dynamics of Brain Tissue in vitro," Quarterly Progress Report No. 79, Research Laboratory of Electronics, M. I. T., October 15, 1965, pp. 247-261.

D. TISSUE DYNAMICS OF BRAIN TISSUE IN VITRO

Few microelectrode studies on the electrophysiology of brain tissue in culture have been published thus far. In 1962, Hild and Tasaki¹ reported cellular membrane potentials (50 mV or less and electrically stimulated action potentials (up to 70 mV) from cells within explants of new born rat or 7-14 day-old kitten cerebellar tissue. More recently, Crain and Bornstein² have observed after-discharges lasting 4-5 seconds caused by a single electrical stimulus applied to long-term tissue cultures of neonatal mouse cerebellar and cerebral cortex. These authors present strong evidence that functional, as well as anatomical, connections between nerve cells are present in these long-term brain-tissue cultures, thereby substantiating the potentialities of

electrophysiological studies of the behavior of brain tissue in vitro.

For the past few months, we have been conducting microelectrode investigations of spontaneous electrical activity occurring in small pieces (1 mm^3) of living brain tissue in a suitable in vitro environment. In 1959, such spontaneous potentials were first detected by our group, using gross platinum electrodes. These potentials were spontaneous in the sense that we did not knowingly stimulate the tissues, mechanically or otherwise. Subsequent experiments (using gross electrodes) showed that these potentials respond reversibly to anesthetics, changes in the O_2 , N_2 , CO , concentrations³ in the immediate environment of the explants, the addition of drugs such as strychnine and brucine, and changes in temperature. These changes altered the spontaneous activity in a manner similar to that expected from experience with in vivo preparations.

The microelectrode observations reported here were carried out on 14 day-old chick embryo telencephalic tissue (that used in the gross platinum electrode experiments). Details of the culture technique employed in these experiments have been reported previously.⁴

The culture chamber was a piece of glass tubing, 18 mm in diameter, 4.3 mm high, 1.5 mm thick, with a 4-mm arc-shaped gap in the wall. Round coverglasses, 18 mm in diameter, were cemented on either end of the glass ring to enclose a piece of fritted glass of coarse porosity which filled the chamber, except for a sector opposite the opening in the glass ring. A 40-gauge platinum-wire recording electrode, insulated to its tip with Teflon, lay between the upper coverglass and the frit, with its tip at the angle of the missing sector of fritted glass.

The frit was saturated with nutrient fluid which differed from that previously reported,³ in that chick serum was used as a source of protein and 1 cc each of a concentrated solution of methylene blue in balanced salt solution, multivitamin solution and amino-acid solution was added to each 100 cc of nutrient fluid. Methylene blue's well-known property of vitally staining the granules in neurons was used, along with phase-contrast microscopy, to identify neurons within the explants. The concentration of methylene blue used here was approximately 1 per cent of that used by others for staining neurons. Previous experiments on the spontaneous activity detected with platinum gross electrodes showed that the presence of such concentrations of methylene blue increased the amplitude of the spontaneous potentials and revived such activity once it had ceased. Methylene blue's known depolarizing effect may be a possible factor in causing these changes. In our experience, spontaneous activity could be detected by the microelectrode in cultures with or without methylene blue.

Approximately 1 mm^3 of the posterolateral aspect of the right telencephalic lobe of 14-day-old chick embryo brain was excised rapidly with the sharp edge of a razor and floated in cold nutrient fluid to remove blood and membranes. Within 15 seconds, the tissue was transferred into the specially designed microchamber (described above)

(XXI. COMMUNICATIONS BIOPHYSICS)

containing warm (35°C) nutrient fluid.

The microchambers containing the excised tissue were transferred immediately after explantation to an incubator at 35°C. The microelectrode insertions were made within 48 hours after explantation. For this, the microchamber was carefully transferred to a specially designed microscope stage incubator,* which was maintained as close to 35°C and 100 per cent humidity as possible. Groups of spontaneous potentials similar in form to those previously reported⁴ were detected by the platinum gross electrodes within these microchambers.

In any explant, only the cells within a small distance of surface oxygen and of a source of nutrient can survive. Calculation and experiment indicate that with a tissue of respiratory rate of some 100 micromoles of O₂ per gram fresh wt. per hour, such as cerebral cortex, diffusion of oxygen from a solution in equilibrium with an atmosphere of 100 per cent O₂ gives adequate oxygenation to a depth of 0.2 mm.⁵ This value is somewhat less if atmospheric O₂ is used. With the use of dimensions of 1 mm² for surface area and depth of 0.1 mm for the live portion of tissue, and the volume of pyramidal cell (soma plus apical dendrite) approximated as a sphere of radius 50 μ, the number of living cells in the tissues used here turns out to be 200.

The microelectrodes were 3MKCL-filled glass micropipettes with tip diameters of less than 1 μ, which typically gave the electrodes resistances between 15 and 50 MΩ. A Medistor headstage with negative capacity compensation was used for the first-stage amplification (x10), and its output was fed into both a Dana DC amplifier (x30) and the vertical (AC) amplifier of a Tektronix 502A oscilloscope. The outputs from all 3 devices were recorded on a modified P105 Ampex tape recorder at 7 1/2 ips (1.25 kc).

Placement of the electrode either into the film of nutrient fluid surrounding the explant or into the explant itself was done under direct vision.

The durations of the spontaneous signals detected with a microelectrode were divided into three overlapping classes.

1. Long duration signals lasting from 1/3 to 1 minute.
2. Intermediate-duration signals lasting 50-500 msec, similar to those detected with platinum gross electrodes.
3. Short-duration signals lasting 1 to 2 msec, similar to "extra cellular" and "intra-cellular!! potentials observed in vivo."

The general structure of the activity was one of repetitive patterned sequences of the intermediate-duration signals separated by long periods (as long as 12 minutes) of no detectable activity. The long-duration signals only occurred as parts of these sequences. Short-duration signals were detected in the explant, and occurred in bursts or alone. The intervals between these bursts were often regular and comparable to the interval between sequences of the intermediate signals.

Figure XXI-3 shows a typical sequence of intermediate signals detected by a

microelectrode in the nutrient fluid around the explant. In this figure the long-duration signal is the long rise off the DC base line which occurs during the sequence. Many

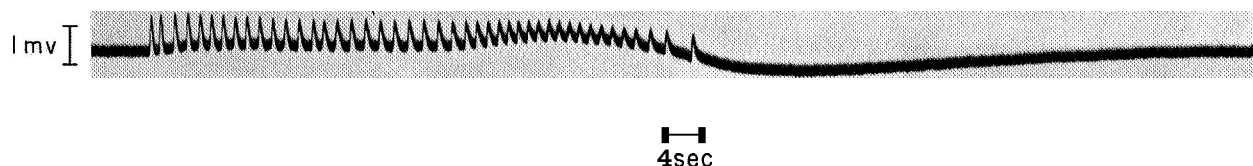


Fig. XXI-3. D-C recording of a typical sequence of potentials of intermediate duration detected in the nutrient fluid around the explant, Positive deflection upward.

consecutive sequences of intermediate signals were detected in the film of nutrient fluid surrounding the explant or within the tissue, and appeared to originate from discrete foci within the explant. A microelectrode placed close to the explant and moved along the periphery of the explant detected activity at some points in the film of nutrient fluid but not in others. The patterned sequences of intermediate-duration potentials detected in this way differ significantly in these different small regions of activity. A 200-300 μ lateral movement of the microelectrode tip may make the activity no longer detectable, and return of the tip to its original position reveals the original pattern of activity. The localness of the activity within the explant was suspected from multiple gross electrode studies on similar explants.⁴

Figure XXI-4 shows bursts of extracellular spikes (1-2 msec) detected within the

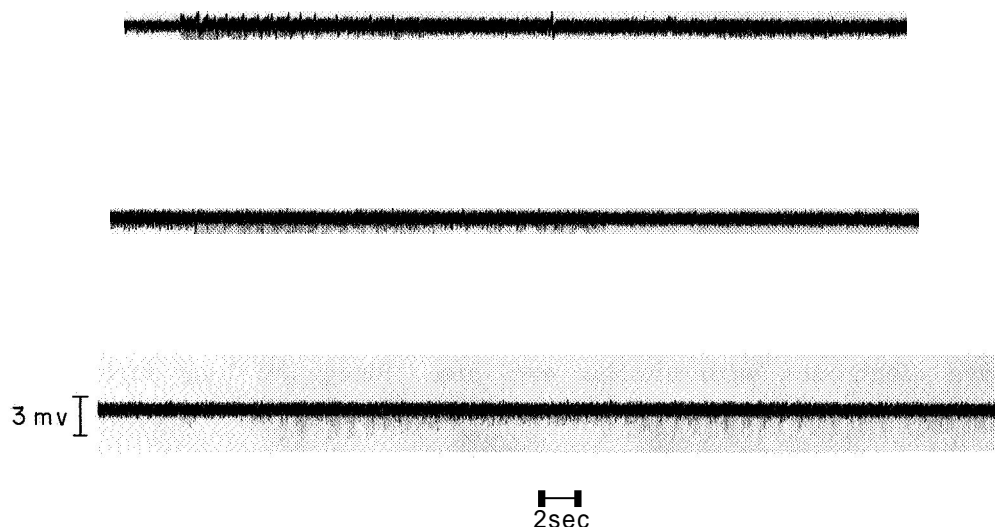
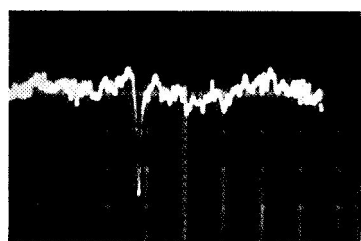


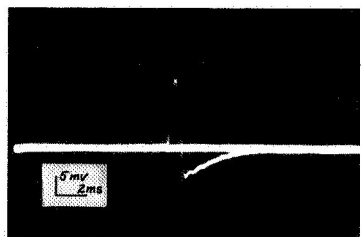
Fig. XXI-4. A-C recording of negative "extracellular" spikes detected within an explant. A sequence of potentials of intermediate duration can be seen occurring with the burst of extracellular potentials in the upper film.

(XXI. COMMUNICATIONS BIOPHYSICS)

explant. The interval between these bursts was approximately 5-6 minutes. In this figure a sequence of intermediate signals can be seen occurring simultaneously with a burst of short-duration potentials. Figure XXI-5a shows details of a typical



(a)



(b)

Fig. XXI-5.

(a) Details of a typical "extracellular" spike shown in Fig. XXI-4. Positive deflection upward. Horizontal scale: 5 msec/cm. Vertical scale: 1.25 mV/cm. (b) Details of an "intracellular" potential (AC recording).

"extracellular" spike in Fig. XXI-4. Figure XXI-5b shows an intracellular potential, one of a burst of potentials, detected after visually penetrating a cell whose granules were stained with Methylene Blue. The spike potentials were preceded by a 30-mV DC shift. The discharge pattern of the cell lasted approximately 3 minutes and consisted of a series of bursts of activity whose durations varied. Thus the neurons in these explants appear to be physiologically active.

To summarize, three types of spontaneous signals arise within the explant from living cells having the appearance of neurons. These signals can be detected with a microelectrode placed in the film of nutrient fluid surrounding the tissue or within the tissue close to groups of histologically identifiable neurons. The intermediate signals occurred in repetitive patterned sequences similar to those previously reported using gross electrodes with similar explants. Since the long-duration signals occurred with the intermediate signals and the intermediate spikes were detected simultaneously with the fast spikes, presumably all three types of activity are related.

A full report on this work has been submitted by the first author to the Department of Electrical Engineering, M. I. T. , in June 1966, as an S. M. thesis.

P. H. O'Lague, A. W. B. Cunningham

1. W. Hild and I. Tasaki, "Morphological and Physiological Properties of Neurons and Glial Cells in Tissue Culture," *J. Neurophysiol.* 25, 277 (1962).
2. S. M. Crain and M. B. Bornstein, "Bioelectric Activity of Neonatal Mouse Cerebral Cortex during Growth and Differentiation in Tissue Culture," *Experimental Neurol.* 10, 425-450 (1964).
3. A. W. B. Cunningham, "Qualitative Behavior of Spontaneous Potentials from Explants of 15-day chick Embryo Telecephalon in vitro," *Gen. Physiol.* 45, 1067-1076 (1962).
4. A. W. B. Cunningham, R. R. Rojas-Corona, J. A. Freeman, and P. H. Levine, "Tissue Dynamics of Brain Tissue in vitro," Quarterly Progress Report No. 78, Research Laboratory of Electronics, M. I. T., July 15, 1965, pp. 247-261.
5. P. J. Heald, H. McIlwain, and G. H. Sloane-Stanley, "Central Nervous System Metabolism in vitro," in *Handbook of Physiology*, Sec. 1, *Neurophysiology*, Vol. III (American Physiological Society, Washington, D. C., 1960), Chap. LXXVI.

E. TIME PATTERN OF COMPLEX BASILAR-MEMBRANE VIBRATIONS AND ITS RELATION TO PITCH PHENOMENA

The tonal residue pitch² that arises in the perception of complex sounds presents an interesting subject for study for psychologists dealing with the perceptual attributes of hearing, as well as those concerned with the mechanisms of hearing. Understanding of the processes involved in production of the residue effect may help in the solution of a number of audition problems and also contribute to knowledge about the conversion of mechanical sound vibrations into perceptive manifestations.

The residue effect can be demonstrated under a variety of conditions but the most studied^{2,3} is that of a sinusoidally modulated pure tone, e.g., a pressure wave described by

$$p(t) = P(1 + \cos \omega t) \cos \omega_0 t, \quad (1)$$

where typically $\omega_0/2\pi$ is of the order of 600-4000 Hz and $\omega/2\pi$ is the order of 80-500 Hz. The subjective pitch (residue pitch) corresponding to such a complex sound is approximately equal to $\omega/2\pi$, but not precisely so unless ω_0 is an integer multiple of ω . To a first approximation, the residue pitch is given by

$$\omega_r = \omega + \frac{\Delta\omega}{n}, \quad (2)$$

where n is an integer, and $\Delta\omega$ is determined by

$$\omega_0 = n\omega + \Delta\omega. \quad (3)$$

(Under appropriate circumstances, listeners can identify several pitches for the same pressure wave corresponding to values of n differing from the integer nearest ω_0/ω by ± 1 .) The pitch given by (2) can be explained by observing that for ω/ω_0 not equal to an

integer the peaks of the carrier do not occur precisely at the peaks of the modulating waveform. The spacing between carrier peaks near the peaks of the modulating waveform is, in fact, $2\pi/\omega_r$. Presumably, then, the residue pitch is largely determined by this time interval. Physiological manifestations accompanying the process of conversion of the basilar membrane vibrations into neuronal events⁴ seem to make such an assumption possible.

More careful measurements have shown, however, that there is a second residue effect² resulting in a slightly larger pitch deviation from ω than (2) would suggest. No convincing explanation for this second effect has been proposed. In the following discussion it will be argued that a possible explanation lies in the asymmetry introduced in the sideband energy as a result of the mechanical filtering of $p(t)$ by the middle and inner ear.

In accordance with (1) and (3) we assume that the pressure spectrum of the stimulating signal impinging on the tympanic membrane can be presented (for 100% modulation) as

$$p(t) = P \left\{ \frac{1}{2} \cos [(n-1)\omega + \Delta\omega]t + \cos [n\omega + \Delta\omega]t + \frac{1}{2} \cos [(n+1)\omega + \Delta\omega]t \right\} \quad (4)$$

We shall also assume that for the intensities of interest the middle ear and basilar membrane act as a linear mechanical device. The superimposed effect of the incoming stimulating components can be computed for any particular point of the membrane. The most important point is presumably that which is most sensitive to the central frequency component of the stimulus. In order to perform the computation for the displacement at a particular location on the basilar membrane, the transfer characteristics for the signal components would have to be known. Possible computational models for basilar-membrane displacements has been presented by Flanagan⁵ and Siebert.⁶ It will be sufficient for our purposes merely to suggest the algebraic form of the result.

At the point which is maximally sensitive to the frequency ω_0 presumably the energy in both side bands will be reduced relative to the carrier, but the upper side band will be reduced more than the lower, since the tuning curves are steeper on the high-frequency side. For narrow-band signals we may assume that the phase characteristic is approximately linear and hence choosing the time reference appropriately may express the displacement of the membrane as

$$d(t) = D \left\{ \left(\frac{a+\delta}{2} \right) \cos [(\omega_0 - \omega)t + \phi] + \cos \omega_0 t + \left(\frac{a-\delta}{2} \right) \cos [(\omega_0 + \omega)t - \phi] \right\}, \quad (5)$$

where δ (which we shall assume is small) represents the effect of the asymmetry in the tuning curve. As a result, $d(t)$ shows both amplitude and phase modulation; specifically, we may write (for small δ)

$$d(t) \approx D[1+a \cos(\omega t - \phi)] \cos \left[\omega_0 t - \frac{\delta \sin(\omega t - \phi)}{1 + a \cos(\omega t - \phi)} \right]. \quad (6)$$

The phase modulation in (6) can, we believe, account for the second residue effect as we shall now show. The envelope of $d(t)$ has a maximum at $\omega t - \phi = 0$. In the vicinity of $t = \phi/\omega$ we may write the argument of the carrier approximately as

$$\omega_0 t - \frac{\delta(\omega t - \phi)}{1 + a}, \quad (7)$$

and thus the carrier maximum near $t = \phi/\omega$ will occur at

$$\omega_0 t - \frac{\delta(\omega t - \phi)}{1 + a} = 0 \quad (8)$$

or

$$t = \frac{-\delta\phi}{\omega_0(1+a) - \delta\omega} \quad (9)$$

Similarly, the next maximum of the envelope is at $\omega t - \phi = 2\pi$ and in that vicinity the carrier has a maximum at

$$\omega_0 t - \frac{\delta(\omega t - \phi - 2\pi)}{1 + a} = n2\pi \quad (10)$$

or

$$t = \frac{2\pi n(1+a) - 2\pi\delta - \delta\phi}{\omega_0(1+a) - \delta\omega} \quad (11)$$

Subtracting (9) from (11) to get the time interval between the peaks (which we assume is the reciprocal of the residue pitch, $\omega_r/2\pi$) we obtain

$$\omega_r = \frac{\omega_0 - \frac{\delta\omega}{1+a}}{n - \frac{\delta}{1+a}} = \omega + \frac{\Delta\omega}{n - \frac{\delta}{1+a}}. \quad (12)$$

Compared with (2) this shows exactly the effect desired, i. e. , an increased slope in the plot of ω_r vs $\Delta\omega$.

The calculation has, of course, considered only one spot along the basilar

membrane — albeit the most sensitive one — as contributing to the perception of pitch. Other nearby areas will certainly contribute, however, and will have a different timing between peaks than that implied by (12). Further studies are in progress.

H. Fischler

References

1. J. F. Schouten, "The Perception of Subjective Tones," Proc. Koninkl. Ned. Akad. Wetenschap, 41, 1086-1093 (1938).
2. J. F. Schouten, R. J. Ritsma, and B. Lopes Cardozo, "Pitch of the Residue," J. Acoust. Soc. Am. **34**, 1418-1424 (1962).
3. R. J. Ritsma, "Existence Region of the Tonal Residue I," J. Acoust. Soc. Am., 34, 1224-1229 (1962).
4. N. Y. S. Kiang, "Discharge Patterns of Single Fibers in the Cat's Auditory Nerve," Research Monograph No. 35 (The M. I. T. Press, Cambridge, Mass. , 1965).
5. J. L. Flanagan, "Models for Approximating Basilar Membrane Displacement- Part II. Effects of Middle-Ear Transmission and Some Relations between Subjective and Physiological Behavior," Bell System Tech. J. 41, 959-1009 (1962).
6. W. M. Siebert, "Models for the Dynamic Behavior of the Cochlear Partition," Quarterly Progress Report No. 64, Research Laboratory of Electronics, M. I. T. , January 15, 1962, pp. 242-258.

F. STATISTICAL THEORY OF FIELDS

In this report we continue to explore some of the consequences of the statistical theory of fields described in Quarterly Progress Report No. 80 (pages 243-247). Our calculations will be based on a soluble neutral scalar field, mainly to illustrate the general dynamical features. It will become quite clear that if the theory is valid other fields can be treated similarly. For each problem only a minimum of statistical features will be introduced to keep the number of parameters as low as possible. For example, in a self-energy problem or the structure of the source, only the total momentum of each mode is assumed to be known, whereas more realistically a knowledge of the average field $\bar{\phi}$ could be added to correspond to coulomb behavior for large distance. In the present calculations this behavior is achieved by a boundary condition on the field.

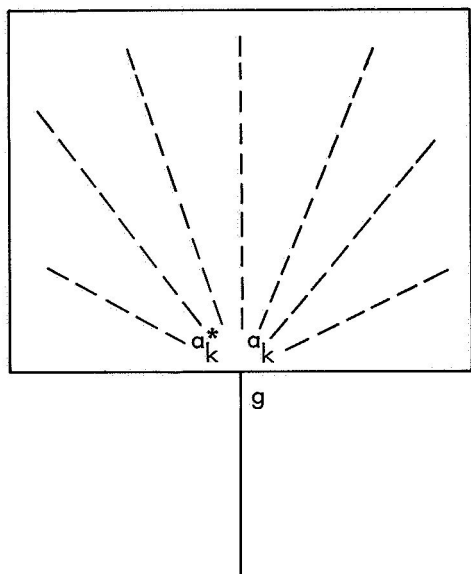


Fig. XXI-6. The cavity.

For simplicity, let us first consider the case of a cavity field. This problem is of importance not only because it is the original area in which the quantum hypothesis was first introduced by Planck but also because it can serve as a model in which the concepts of equilibrium, interaction, coherence, and the processes of production, scattering, detection, and observation, can be examined in their bare essentials. In fact, in our theory the concept of an elementary particle has a close kinship with radiation trapped in a cavity. We start with a cavity of rigidly reflecting walls and provide a means of interacting with the radiation inside the cavity through a coupling placed on the wall (Fig. XXI-6). The coupling can

serve as a means of injecting radiation into the cavity, but it can also serve as a detector through which we may examine the state of the cavity. With this wider concept of a source in mind, let us write the Hamiltonian of the system in the rest frame of the cavity. Since the field is real, we have

$$H = \sum_{\mathbf{k}} \omega_{\mathbf{k}} \left(a_{\mathbf{k}}^* a_{\mathbf{k}} + \frac{1}{2} \right) + H_w - \int \sum_{\mathbf{k}} g(2\omega_{\mathbf{k}} V)^{-1/2} \left(a_{\mathbf{k}}^* e^{-i\mathbf{k}\mathbf{x}} + a_{\mathbf{k}} e^{i\mathbf{k}\mathbf{x}} \right) F(t, \mathbf{x}) d^3x, \quad (29)$$

where H_w is the Hamiltonian of the rest of the system including the walls. Whatever energy is drawn from the cavity will, of course, go into H_w ; aside from this, we

temporarily ignore the function of H_w and concentrate on the cavity and its coupling.

The following field-theoretical results are derivable¹ through the conventional action principle: (a) Starting from the ground state of the cavity, a prescribed time-dependent function $F(t, x) = F(t)$ will inject into the cavity for each frequency a Poisson distribution $P_n = e^{-N} N^n / n!$, where $N = g^2 (2\omega_k V)^{-1} |F(\omega)|^2$. $F(\omega)$ is the Fourier transform of the function $F(t)$. (b) Poisson distributions are coherent superpositions corresponding to minimum uncertainty wave packets. They can be obtained directly from the ground state by unitary transformations $U(\lambda) = e^{\lambda a^\dagger - \lambda^* a}$, where $|\lambda| = g(2\omega_k V)^{-1/2} |F(\omega)| = \bar{N}^{1/2}$. (c) The energy transfer to the cavity is $\Delta E = g^2 (2\omega_k V)^{-1} |F(\omega)|^2$, which depends only on the Fourier component of the function $F(t)$. (d) Poisson distributions are localizable, since they are correlated only with the prescribed source at the given point x . (e) The effect of a time-independent interaction $F(t, x) = F(x)$ is to displace the system of states of the cavity into a new system, where $b_k = a_k - g(2\omega_k V)^{-1/2} F_k$. Here, F_k is the Fourier component $F_k = (2\pi)^{-3} \int F(x) e^{-ikx} dx$. The number of particles (virtual) is in this case $N_k = g^2 (2\omega_k V)^{-1} |F_k|^2$ and they still obey a Poisson distribution. The total shift in energy is $\mathcal{E}_0 = - \sum_k g^2 (2\omega_k V)^{-1} |F_k|^2$. All of these are actually elementary consequences of the solution $|out\rangle = e^{iW_I} |in\rangle$, where $W_I = \int \sum_k g(2\omega_k V)^{-1/2} (a'' e^{-ipx} + a e^{ipx}) F(t, x) d^3x dt$. To see it clearly, take item (a) with $|in\rangle = |0\rangle$ and assume that only one frequency and only $F(t)$ are involved. Then $W_I = g(2\omega_k V)^{-1/2} (a^\dagger F(\omega) + a F^*(\omega))$. Using the Baker-Hausdorff formula and the fact that $e^{a^\dagger F(\omega)} |0\rangle = |0\rangle$, we have $|out\rangle = e^{-|\lambda|^2/2} e^{\lambda a^\dagger} |0\rangle = e^{-|\lambda|^2/2} \sum_n \frac{\lambda^n (a^\dagger)^n}{n!} |0\rangle = e^{-\bar{N}/2} \sum_n (\bar{N}^n / n!)^{1/2} |n\rangle$, from which the Poisson law follows.

In connection with our theory we now make the following remarks: (a) Poisson distributions correspond to states of zero entropy. (b) No prescribed interaction term can increase the entropy even if we start from a state of finite entropy. (c) The energy of a cavity in contact with a point source or a 6-pulse necessarily diverges. The proofs are quite elementary. Poisson distributions can be shown to have zero entropy by direct computation. In our context this is almost obvious because we are working under a constraint $S = 0$. The second point corresponds to the circumstance that $\Delta S = 0$, since the transformation is strictly unitary. The third point follows from the fact that for 6-interaction $F_k = 1$, and for 6-pulse $F(\omega) = 1$, which leads to divergent results. For the sake of completeness we may also give, without proof, the case of a Planck distribution plus a coherent state. In this case the distribution is $\sigma = (1 - e^{-2\omega_k V})^{-1/2} e^{-\zeta \omega (a^\dagger + a)(a^\dagger + a)}$

with energy $\bar{\mathcal{E}} = \omega \left(\bar{n} + \frac{1}{2} \right) \pm \omega / (e^{2\omega\zeta} - 1)$ and entropy $\bar{S} = - \frac{d}{d\gamma} \gamma \ln (1 - e^{-1/\gamma})$, $\gamma\omega = \frac{1}{25}$, $\frac{1}{25} = \bar{n}\omega$. The characteristic function of this distribution is $C_{\mathcal{E}}(i\xi) = e^{i\xi\bar{\mathcal{E}} - \xi^2 \bar{\mathcal{E}}/2}$, where ϕ is just the sinusoidal waveform.

Let us now consider how our new concepts may help us. We recall that at the beginning of this century there was a problem of ultraviolet divergence for the cavity radiation. This difficulty was removed by Planck with the introduction of the idea of energy quanta. Note, however, that the quantum idea by itself did not remove the difficulty. Rather, the introduction of the quantum concept in connection with statistics accomplished the desired result. The decreasing exponentials that cut off the efficiency of the high-energy quanta are provided by the statistical part. Without the aid of statistics (that is, when all states are equally probable) the field quantization would have led to $\mathcal{E}_\nu = \sum_n (8\pi/c^3) \nu^2 (nh\nu)$ which diverges even worse than the Rayleigh-Jeans distribution. Thus, quantum field theory does not provide, without the aid of its proper statistics, a solution to the original problem of the cavity radiation, and we should not expect it to give finite results when more elusive concepts such as the virtual particles and their energies are involved.

In our theory the virtual particles are on an equal footing with the real particles, and we must try to remove the self-energy difficulty in a manner similar to cavity divergence. A way of doing this was presented in the previous report. Now we exploit further this simple model with regard to the scattering and production processes.

The apparent spread of the source may be calculated as,

$$\rho(r) = \frac{g}{(2\pi)^3} \int F_k e^{+ik \cdot r} d^3k = \frac{g}{(2\pi)^3} \int \frac{k^{1/2} d^3k e^{ik \cdot r}}{(e^{2\mu k} - 1)^{1/2}}, \quad (34)$$

which at large r vanishes, which corresponds to Coulomb behavior. For small distances, $r \sim \mu$, the source behaves in the rest frame as though it were an extended object. This behavior is reminiscent of the usual cutoff theories, but the similarity is illusory. Here the object is a statistical distribution of virtual particles and, in general, this cannot be interpreted as an extended body nor as a smearing of the δ -function.

Clearly, the nature of the source and the behavior of the function $F(t, \mathbf{x})$ are not accessible to direct experimental examination. We may, however, infer from field theory that the source particle itself is a solution of some field equations, and, therefore, describable as coherent or incoherent superposition of waves, $F(t, \mathbf{x}) \rightarrow \sum_k c_k e^{-ip_k(\zeta_k + i\mathbf{x} \cdot \mathbf{k})}$ or $\int \sum_k \bar{\psi}_k \gamma \psi_k d^3k$, and so on.

We may now consider the behavior of the source point. Evidently, we cannot imagine it as permanently fixed or in a state of prescribed motion. Our concepts lead us to

conclude that the behavior is more like a fluctuation depending on the situation and the particular statistics that it obeys. Here it finds itself in an incoherent superposition of virtual photons, and, like a particle in a heat bath, undergoes an unpredictable jittery motion. From the general entropy law we may infer that the two parts, the virtual cloud and the source particle, should be in a state of statistical equilibrium. If we assign to the source the parameter ζ_{ψ}^{μ} and to the cloud ζ_{ϕ}^{μ} , we may write $\zeta_{\psi}^{\mu} = \zeta_{\phi}^{\mu}$. Although the situation is no longer soluble in the usual sense and the full iteration process is required, we know ahead of time that the integrals are convergent. Let the total energy be

$$\overline{\mathcal{E}} = \overline{\mathcal{E}}_{\psi} + \overline{\mathcal{E}}_{\phi} \geq 0, \quad \zeta_{\psi}^{\mathbf{r}} = \zeta_{\phi}^{\mathbf{r}} = 5, \quad (35)$$

which is to be identified as the observed rest mass. Bare masses, the coupling constant, and the additional statistical parameter, ζ , are then to be related. Since we have three phenomenological constants and four theoretical parameters, we must have an additional condition to determine them all. A reasonable assumption seems to be to invoke some partition postulate between the two representations ϕ and ψ . If one interprets this as $\overline{\mathcal{E}}_{\phi} = \alpha \overline{\mathcal{E}}_{\psi}$, where α is a theoretically inferable constant, then the dynamics of the source could be considered reasonably complete, at least as far as the neutral scalar theory is concerned, although for electrodynamics the problem of gauge and extra complications caused by the magnetic moment have to be separately faced.

Coming to problems of more immediate experimental interest, we have examined scattering and production cross sections. Low-energy limits of the cross sections agree with the usual formulas. At extreme high energy, the exponential factors make their presence felt and all contributions tend to zero. This is due to the scarcity of high-momentum virtual particles which mediate the interactions, and can be understood by analogy to cutoff theories. The number of bosons produced in a Bremsstrahlung experiment thus behaves as

$$\bar{n} = \frac{g^2}{(2\pi)^3} \int_0^{\infty} \frac{\mu dk}{e^{2\mu k} - 1} d\cos\theta d\phi \left[1 - \left(1 - \frac{\Delta p}{m} \cos\theta \right)^{-1} \right], \quad (38)$$

where Δp is the momentum transfer. At low energy we have the usual behavior, whereas at high energy the result is no longer divergent. It seems therefore, possible to test the theory with extreme high-energy scattering and production experiments. For example, deviations from the well-known Klein-Nishina formula (or pair production cross sections) are expected at extreme high energy. The magnitude of the deviations is not exactly deducible at the present stage, since we do not yet know the size of μ and what other interactions are involved for any given particle. All that we may infer within reason is that, if our ideas are valid, the theory is convergent, exponentials are there, and they

will make their presence felt beyond some definite limit. This general feature would be of some importance with regard to meson theory. Since the statistical factors seem to provide convergence, irrespective of the strength of the coupling, the strong interaction physics may not necessarily fall outside field theoretical approach.

The theory is expected to lead to differences over the existing theory for bulk material at extremely low temperatures. Preliminary calculations show that critical temperatures for superfluid and superconducting materials would be affected. This comes about mainly because of different weighting over virtual phonons. Differences are, however, not as large as it might be expected at first sight, because of natural cut-off of high-energy phonons at wavelengths corresponding to lattice spacings. A systematic re-evaluation of contributions to specific heats and thermodynamic properties is in progress and might provide testing possibilities for the theory. A reconsideration of the Lamb shift in hydrogenlike atoms indicated that no observable difference is expected over the usual theory. Since the largest contributing factor in Lamb shift (-1015 Mc/sec) is the self-energy difference between a bound electron and a free electron, our statistical weight is expected to reduce the theoretical value $\Delta\mathcal{E}_{\text{Theor.}} = 1058.03$ Mc/sec slightly. Preliminary calculations indicate, however, that the difference $\Delta\mathcal{E}_{\text{Exp.}} - \Delta\mathcal{E}_{\text{Theor.}} = 0.26$ Mc/sec is too large, unless we give unrealistic values to ζ^μ . It is probably safer to assume that the present experimental difference is due to some other contribution and that the effect of the theory on Lamb shift is undetectably small. It is doubtful, at present, whether any new features are produced regarding the high-energy diffraction peaks or Regge-pole structure. In particular, the problem of mass spectrum seems as remote as ever; however, the problem of unstable particles seems to take some physical form. If the statistical theory presented here is valid, the ζ^μ -parameter, as applied to elementary systems, might be interpretable as a state index, and the conditions of two-way stability and metastability in the presence of all existing fields may have something to do with the mass spectrum. In this case the question of elementary-particle physics would appear to be shifted to the question of elementary fields. In this connection it would be interesting to study the implications of irreversibility as applied to elementary processes to see if new selection rules are implied. For example, it would appear that the β -decay increases entropy, and therefore the inverse process can take place only in relation to other processes which provide the necessary decrease. Similarly, annihilation of protons with antiprotons, which by themselves are stable, emission of a photon, and sending of a single quantum as a signal to some given direction should perhaps be counted as irreversible processes. We should take caution, however, with regard to such far out considerations before we have some experimental tests as to the usefulness of the theory.

We conclude with a few ancillary remarks: (i) The interpretation of $e^{-H(\zeta+it)} | \rangle$ as probability amplitude is perhaps not so forbidding, but $2\zeta = \beta$ as the inverse of

temperature would seem to lose its meaning for single particles. We believe this difficulty can be removed by interpreting β , in the case of elementary particles, as an information parameter in the Shannon sense, rather than as actual physical temperature. Note in this connection that in general we need to cast information theory in amplitude form, and construct the probabilities as $\omega = f^* f$, since ordinary information theory is based on objects (switches, levers) of stochastic stability. For objects of stationary stability (consider, for example, the problem of using metastable states of atoms as memory devices), phase information is important, and probability amplitude, rather than the probability itself, would be more useful. Such an extension of information theory is formally possible and reverts essentially to field-theorylike formulas. (ii) The general method may be adapted to wave propagation and dissipation problems by noticing that $\delta(2|1) = -(2|\partial_\mu \Gamma + i\partial_\mu W|1)\delta x^\mu$. The Schrodinger equation analogue of this would be $i\partial/\partial t|) = (H+iK)|$, where H is the Hamiltonian operator, and K is the rate of entropy production. The last quantity is in general not constant; however, it is a positive definite quantity. Evidently, one may construct it as a quadratic function $K = \sum X^\mu O_{\mu\nu} X^\nu$. It follows that $O_{\mu\nu}$ can be taken as symmetric (Onsager's reciprocity principle), since the nonsymmetric part does not contribute. (iii) Our introduction of statistical weight seems to suggest complex Lorentz transformations. Since the problem of the representations of the ordinary Lorentz transformations is nebulous enough, we should try to avoid this as much as we can. But if we cannot, we should probably swing all the way and interpret all representations statistically in the sense of some random theory. Already, the published statistical interpretations of reflections and the "zitterbewegung" of the electron seem to point in this direction. In this case, the equivalence of Lorentz frames, the problem of normalization, stability, ergodic hypothesis, and so forth will all have to be restated in terms of more general (completed) representations. But if the simpler situation adopted in the present theory in which the imaginary part is identified as the presence of incoherent superpositions is valid, then no extra complication beyond the power of known statistical methods seems to arise.

The present approach has many roots in the past literature of the subject. As early as 1932, Block pointed out the similarity of the Schrodinger equation and statistics by his equation $\partial Z/\partial \beta = -(H/k)Z$, where Z is the partition function.' Landau and Lifschitz, Rosenfeld, Guth and Callen discussed the fluctuation relations $\Delta d \cdot \Delta \beta \geq k$; especially Guth pointed out its formal connection with the Heisenberg uncertainty relations.³ The Green's function method of Matsubara, Schwinger and Martin, and others is well known. These take advantage of the analogy between $i\beta$ and t . Feynman gave the field-theory analogue of the expansion of the partition function: Landau and Lifschitz, and Rosenfeld have also discussed, to some extent, the physical unity and epistemological background of the statistics and ordinary quantum mechanics. Fano⁵ and Ter Haar⁶ stressed, on the basis of the density matrix, the operational and statistical nature of physical

observations. Rosen⁷ made an attempt toward a statistical interpretation of the Lorentz transformation. The author⁸ has studied the nature of observation, first on the basis of a principle that is reminiscent of the present one, and later in connection with a theory of human perception. The author's old associate and friend, Stanley Schneider,⁹ realized, as we do, that the structure of field theory is that of a gas at infinite temperature, and attempted a solution of divergence problems by applying conventional statistical methods to the vacuum. He also realized the role of entropy and considered a special case of the uncertainty relations $\Delta S \Delta n \geq k$, where n is the number of particles, and S is the entropy. He concluded on the basis of his ideas that for $v = c$ all cross sections vanish. Therefore, he considered scattering of light by light a decisive test area for his theory. At the time when we exchanged our ideas, he did not have a general principle or a definite conceptual procedure to carry out his program. He had in mind a non-Hermitian Hamiltonian to allow continuous dissipation and decay. Although this idea is not clearly related to his concept of vacuum statistics, it has definite appeal from the point of view of unstable particles, and it might be possible to approach the problem from this angle [see remark (ii)].

To our knowledge, no previous work has attempted a unification of quantum field theory with statistical mechanics by combining entropy and action and introducing microscopically the space of four-dimensional ζ^μ -variables, although such an idea is imminently plausible from Gibb's original argument regarding the derivation of the Boltzmann factor $e^{-\beta H}$, and also from the formal analogies between statistical mechanics and field theory.

H. Yilmaz

References

1. E. M. Henley and W. Thirring, Elementary Quantum Field Theory (McGraw-Hill Book Co., Inc., New York, 1962), Chapters 13 and 14.
2. F. Block, Z. Physik **74**, 295 (1932).
3. L. D. Landau and E. M. Lifschitz, Statistical Physics (Pergamon Press, New York and London, 1958); V. L. Rosenfeld, "Questions of Irreversibility and Ergodicity," Varenna School, 1960; E. Guth, Phys. Rev. **126**, 1213 (1962) and private conversations; H. B. Callen, Thermodynamics (John Wiley and Sons, Inc., New York, 1963).
4. R. P. Feynmann, Phys. Rev. **103**, 1301 (1953).
5. U. Fano, Rev. Mod. Phys. **29**, 74 (1957).
6. D. ter Harr, Rept. Progr. Phys. **24**, 304 (1961).
7. N. Rosen, Phys. Rev. **72**, 298 (1947).
8. H. Yilmaz, Perception and Science (being prepared for publication).
9. S. Schneider, Private conversations, 1966.

XXII. NEUROPHYSIOLOGY*

Academic and Research Staff

Dr. W. S. McCulloch	Dr. K. Kornacher	Dr. T. G. Smith, Jr.
Dr. J. Y. Lettvin	Dr. R. Moreno-Diaz	Dr. A. Taub
Prof. P. D. Wall	Dr. T. McLardy	B. Howland
Prof. M. Blum	Dr. A. Natapoff	Diane Major
Prof. J. E. Brown	Dr. S. A. Papert	W. H. Pitts
Dr. H. Hartman	Dr. Barbara C. G. Pickard	Sylvia G. Rabin
	Dr. W. F. Pickard	

Graduate Students

E. E. Fetz	J. I. Simpson	Barbara G. Wickelgren
L. M. Mendell		W. A. Wright

A. SUMMARY OF RESEARCH PROGRESS: THEORY OF THE RETICULAR FORMATION

Research on the functional organization of the reticular core of vertebrate control nervous systems has reached a significant landmark. Our problem is as described in Quarterly Progress Report No. 76 (page 313), but our progress has been achieved with a somewhat different model than that mentioned there.

The new model is enclosed within heavy lines in Fig. XXII-1, with everything outside only for generating an appropriately structured environment for computer simulation. The γ_{ij} in Fig. XXII-1 are all 3-variable symmetric switching functions of the binary σ_i . The typical module interconnection scheme is suggested by the M_5 hookup. Each module in Fig. XXII-1 is a hybrid probability computer, with schematic as shown in Fig. XXII-2. It receives 4-component probability vectors $P_{\delta i}$ from above and $P_{\alpha i}$ from below, as well as generating a corresponding $P_{\pi i}$ from its N_{ia} part. The j^{th} component in each case is the probability as computed by the module of origin that the over-all reticular formation model's present y_{ij} input-signal configuration is properly a mode j one. The $P_{\alpha i}$, $P_{\delta i}$, and $P_{\pi i}$ vectors are passed componentwise through an f function as shown in Fig. XXII-3, and weighted in the subsequent 'Av' units according to formulas of the type

$$P = \frac{C_{\pi} P_{\pi} + C_{\alpha} P_{\alpha} + C_{\delta} P_{\delta}}{C_{\pi} + C_{\alpha} + C_{\delta}},$$

where $C_{\pi} = C_{\pi_1} C_{\pi_2} Q$, with all factors variable and determined according to two module decoupling principles and a potential command principle which demands that information

*

This work was supported by the National Institutes of Health (Grant NB-4897-03), the U.S. Air Force (Aerospace Medical Division) under Contract AF33(615)-3885, and by a grant from The Teagle Foundation, Inc.

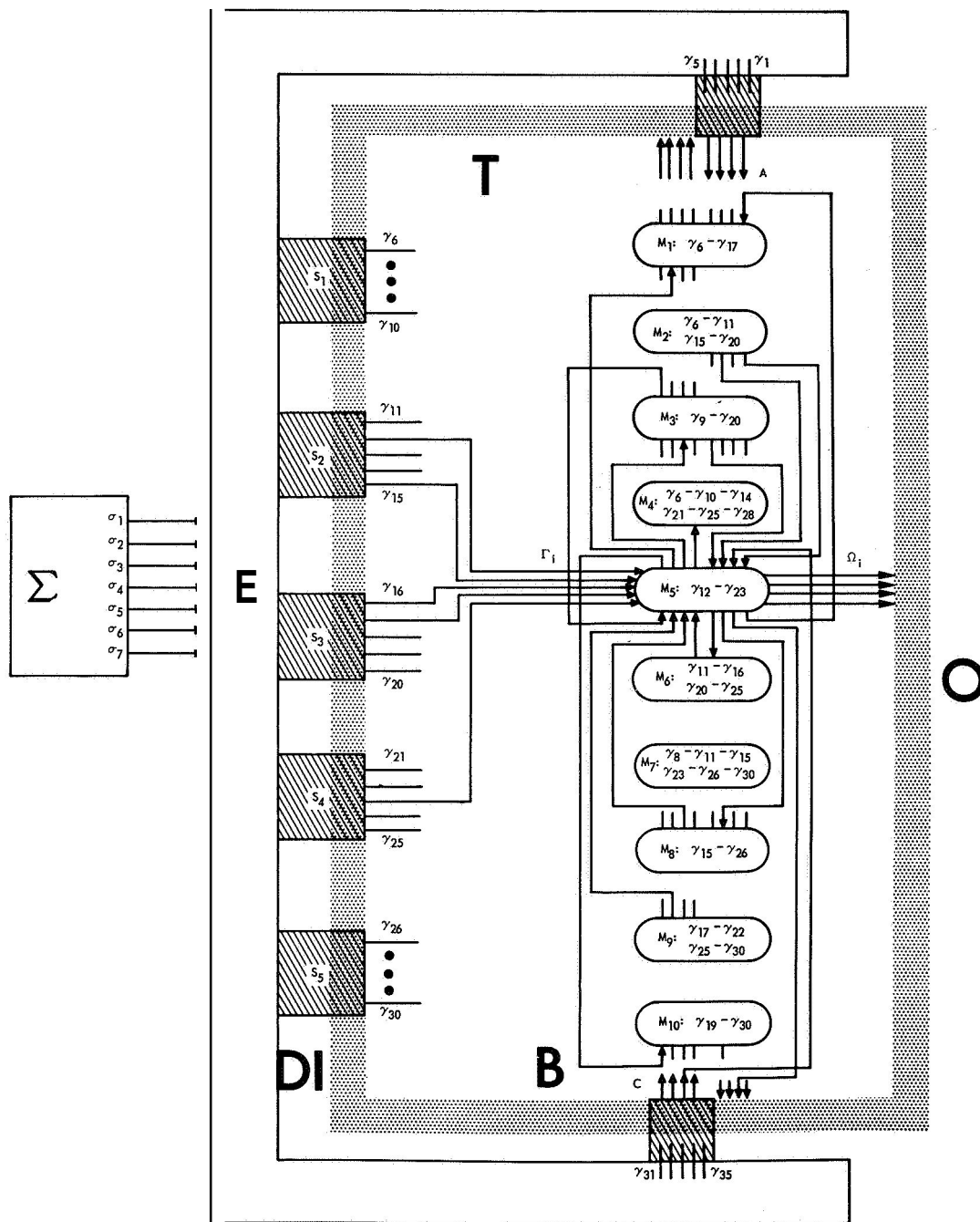


Fig. XXII-1. Simulation model (S-Retic).

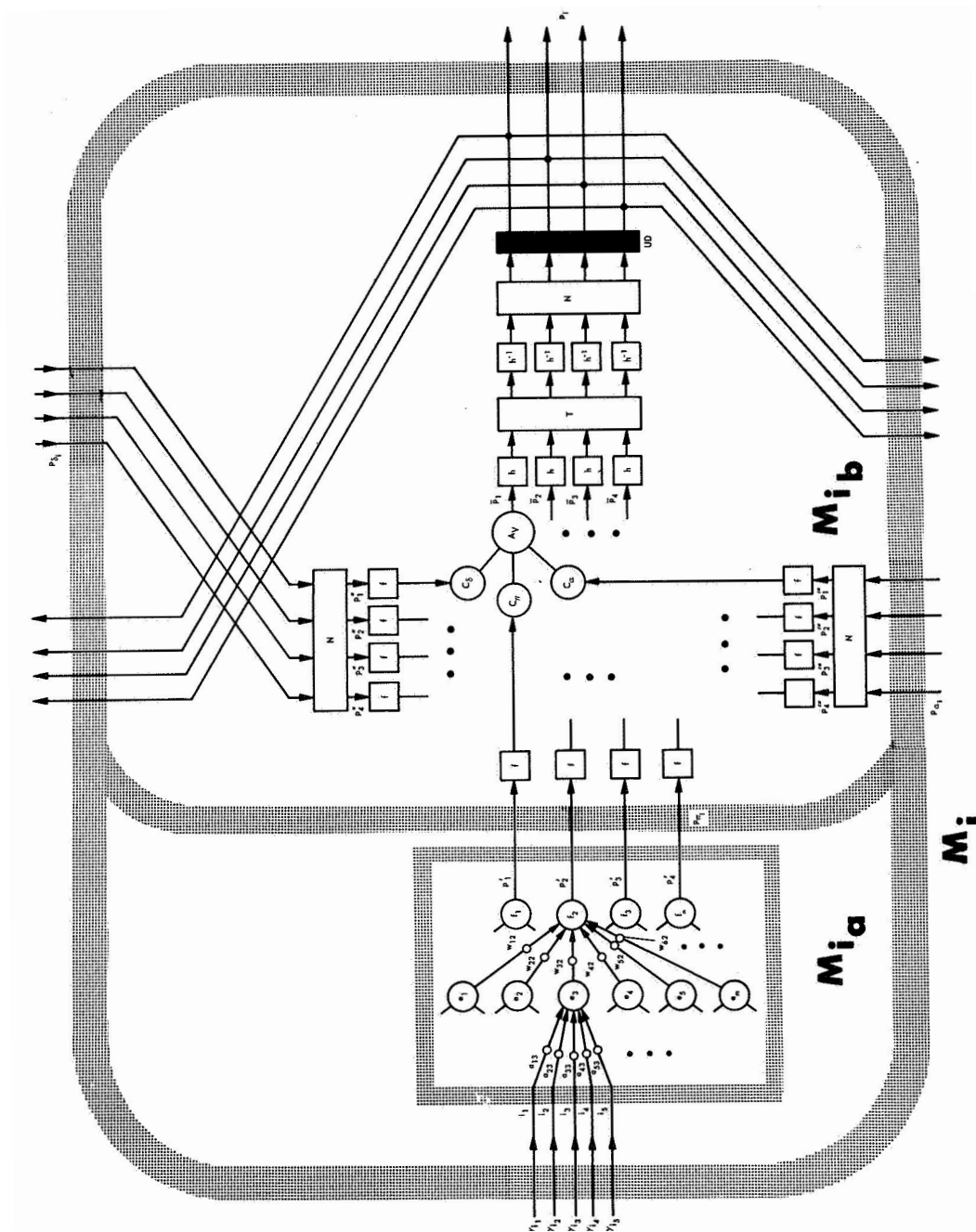


Fig. XXII-2. A typical M_i of Fig. XXII-1.

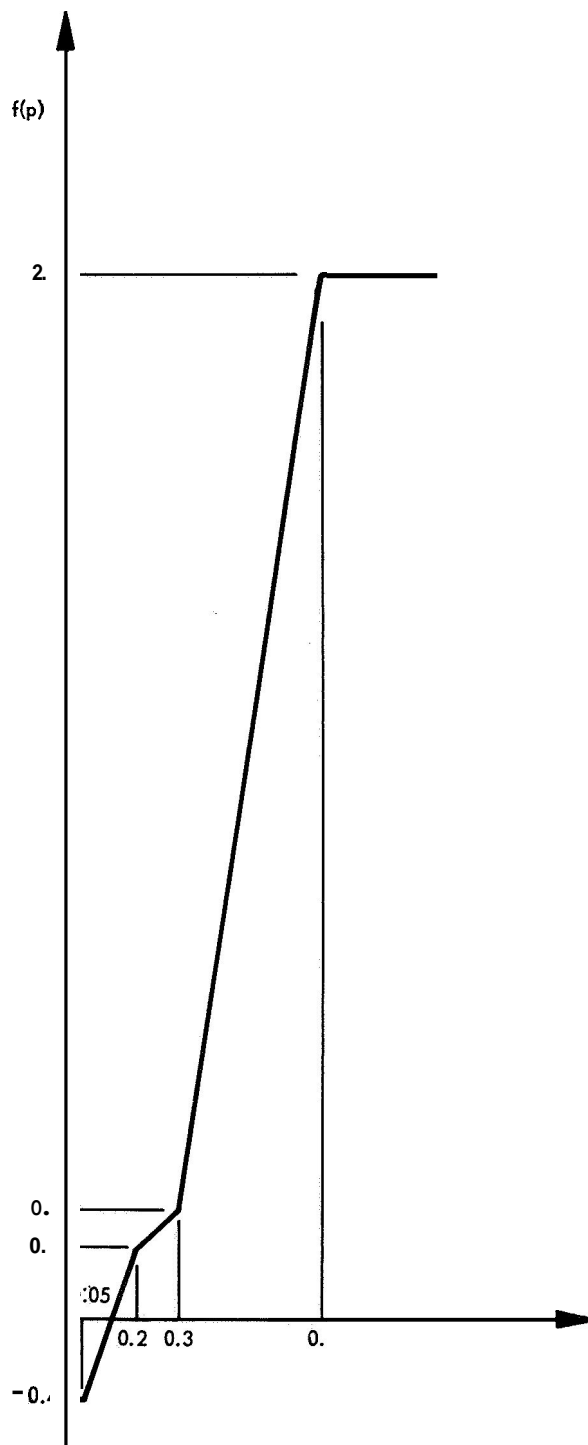


Fig. XXII-3. The $f(p)$ function.

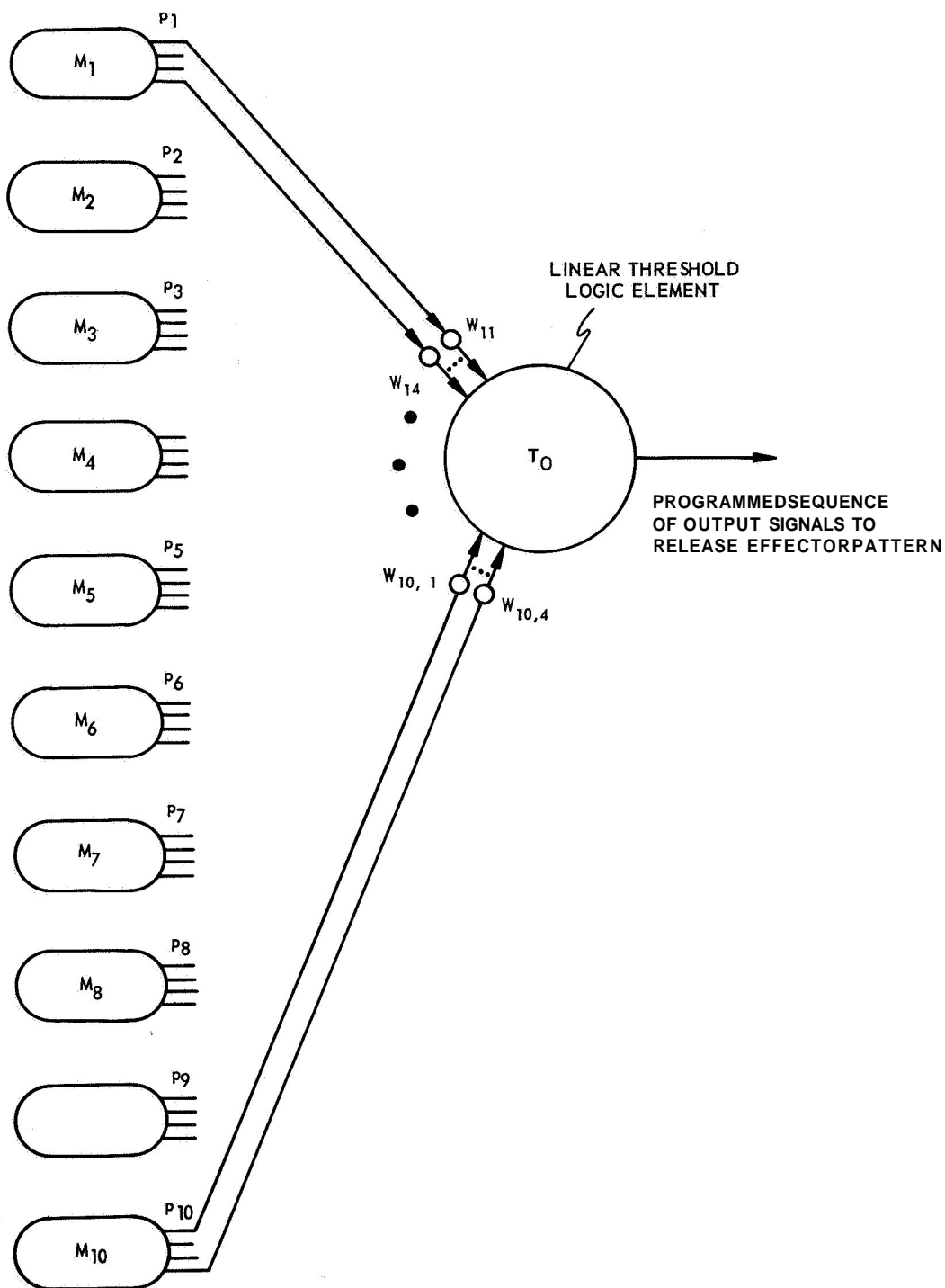


Fig. XXII-4. S-Retic output scheme.

constitute authority. The h , T , h^{-1} , N , and UD blocks in Fig. XXII-2 are to insure that every P_i is an appropriately normalized and delayed probability vector. Figure XXII-4 shows our Fig. XXII-1 model's output model detection scheme.

The model has been successfully simulated on the Honeywell Computer at Instrumentation Laboratory, M. I. T., in collaboration with J. Blum, W. L. Kilmer, E. Craighill, and D. Peterson. The model converged to the correct output model indication in each of approximately 50 test cases, and always in from 5 to 25 time steps. This is just what we had hoped for.

We are now concentrating on the functional design of a considerably enriched model that can handle conditioning and extinction in a satisfactory time-domain sense. The design will again be programmed for simulation on the Instrumentation Laboratory computer.

W. S. McCulloch, W. L. Kilmer

[Dr. W. L. Kilmer is now at Michigan State University, East Lansing, Michigan.]

References

1. W. S. McCulloch, W. L. Kilmer, J. Blum, and E. Craighill, "Toward a Theory of the Reticular Formation," a paper presented at the IEEE/Cybernetics Session, IEEE International Convention, New York, March 14, 1966.
2. W. S. McCulloch, W. L. Kilmer, J. Blum, and E. Craighill, "A Cybernetic Theory of the Reticular Formation," a paper presented at the Bionics Symposium, Dayton, Ohio, May 2-5, 1966.

B. REALIZABILITY OF A NEURAL NETWORK CAPABLE OF ALL POSSIBLE MODES OF OSCILLATION*

1. Introduction

Dr. McCulloch has called our attention to the need for investigating the modes of oscillation of neural nets with feedback and under constant input. The question "How many possible modes of oscillation are there for N neurons?" has already been answered by C. Schnabel.¹ There are $\sum_{K=2}^{K=2^N} (K-1)! \binom{2^N}{K}$ possible modes of oscillation. The next question is, "Are all of these modes realizable with a fixed anatomy?" The answer is affirmative, provided there is a minimum number of input lines to the network. The proof is presented here.

— *

This report was prepared at the Instrumentation Laboratory under the auspices of DSR Project 55-257, sponsored by the Bioscience Division of National Aeronautics and Space Administration, Contract NSR 22-009-138.

2. \mathcal{L} -Networks

Consider N formal neurons with interactions of afferents (those described by McCulloch in "Agathe Tyche"²) forming a one-layer network with M binary inputs, and in which each neuron binary-output feeds back to the same neuron and to all the others. The number of inputs to each neuron is, then, $M \leq N$. At any time t the output (or state) — 0 or 1 — of any neuron is determined by the value of its inputs at time $t - 1$. Therefore, the state of any neuron at time t is determined by the states of all of the neurons and the inputs to the network, both at time $t - 1$. At any time t , the state of the network is defined as the array of N zeros and ones that indicate the state of each neuron at this time. Thus, we can say that the state of the network at time t is determined by the state of the network and the input configuration, both at time $t - 1$.

For a network of N neurons, there are 2^N possible states. We can imagine some particular networks in which some of these 2^N states are never reached. We are interested in those networks in which any of the 2^N states may be reached from any initial state by at least 1 input sequence. Such networks are here referred to as 3-networks. Thus, an 3-network is a network of N neurons forming one layer in which the output of each neuron is connected to itself and all of the others, and any of the 2^N states may be reached from any initial state by some input sequence.

Consider the set of all possible states $S = (S_1, S_2, \dots, S_N)$ and the set of all possible configurations of the inputs $S = (W_1, W_2, \dots, W_M)$ of an \mathcal{L} -network with M inputs. From these sets, we form all possible doubles

$$(S_i, W_k),$$

where $W_k \in W$ and $S_i \in S$. We have $2^M \cdot 2^N = 2^{M+N}$ doubles. We now generate 2^{M+N} successors of the form

$$(S_i, W_k) \rightarrow S_j$$

by arbitrarily assigning to each double (S_i, W_k) an element $S_j \in S$ and only one, and using any $S_j \in S$ at least once. The set of 2^{M+N} successors generated in this manner is referred to as a "set of successors, $v(N, M)$." We generate all possible sets $v(N, M)$, and form from them a new ensemble \mathcal{V} . Thus, \mathcal{V} is the ensemble of all possible sets of successors $v(N, M)$.

Returning to any one \mathcal{L} -network, if S_i is the state at any time $t - 1$, W_k is the input configuration at time $t - 1$, and S_j is the state at time t , we can form a set, v , of 2^{M+N} successors of the form

$$[S_i(t-1), W_k(t-1)] \rightarrow S_j(t).$$

which describes completely the behavior of the net. Obviously $v \in \mathcal{V}$. We will prove that the inverse is also true, i. e., given any arbitrary v , there is an \mathcal{L} -network that is described by v .

LEMMA 1. Given an arbitrary set of successors $v(N, M) \in \mathcal{V}$, it is always possible to design an \mathcal{L} -network of N neurons and M inputs that verifies $v(N, M)$.

Proof. The proof consists in generating, from $v(N, M)$, N Venn diagrams of $N \neq M$ inputs each. The network can be designed from the N Venn diagrams (see Blum³).

We first note that each double (S_i, W_k) of each successor $(S_i, W_k) \rightarrow S_j$ of $v(N, M)$ determines one area in a Venn diagram of $N \neq M$ inputs.

Let us assume that we have drawn the Venn diagram for the first neuron. Then, we put a jot in those areas of the Venn represented by all (S_i, W_k) for which the S_j indicate that the state of that neuron is 1 (fires). We repeat the same for all of the N neurons. Thus, for each combination (S_i, W_k) , the corresponding S_j is determined.

3. Modes of Oscillation

Consider a system of N formal neurons and M inputs. If we define the state of the system at time t as the array of N zeros and ones that indicate the state of each neuron at time t , there are 2^N possible states. A mode of oscillation of the system is defined as any sequence of states that is repeated under a constant input and involves more than one member state. A k -dimensional mode of oscillation is a mode that passes through k different states.

The number N_o of possible modes of oscillation of N neurons is (see Schnabel¹)

$$N_o = \sum_{k=2}^{2^N} (k-1)! \binom{2^N}{k}.$$

LEMMA 2. All N_o possible modes of oscillation of N neurons can be described by a set of successors $v(N, M)$ such that

$$M \geq \log, \sum_{k=2}^{2^N} \frac{1}{\left(\frac{2^N}{k}\right)_E} (K-1)! \binom{2^N}{k},$$

where $\left(\frac{2^N}{k}\right)_E$ indicates the maximum whole number that is less than or equal to $2^N/k$.

Proof. Any k -dimensional mode of oscillation can be divided in k -steps. Each step can be expressed by a successor

$$(S_i, W_k) \rightarrow S_j,$$

where S_i and S_j are the states of the step, and W_k is the constant input word that

produces the mode. If we require that two modes with at least one state in common cannot be specified by the same input configuration, we can insure that for each double (S_i, W_k) there is one and only one S_j .

Thus the number of k -dimensional modes of oscillation that may result from any one input configuration is the largest integer that is less than or equal to $2^N/k$. We denote this integer by $\left(\frac{2^N}{k}\right)_E$. The number of input configurations necessary to specify all k -dimensional modes, is

$$\frac{(k-1)! \binom{2^N}{k}}{\left(\frac{2^N}{k}\right)_E}$$

(number of k -dimensional modes divided by the number of k -dimensional modes specified by each input configuration). The minimum total number of input configurations then is

$$\sum_{k=2}^{k=2^N} \frac{(k-1)!}{\left(\frac{2^N}{k}\right)_E} \cdot \binom{2^N}{k}$$

and therefore the number of input lines, M , has to be such that

$$2^M \geq \sum_{k=2}^{k=2^N} \frac{(k-1)!}{\left(\frac{2^N}{k}\right)_E} \binom{2^N}{k}$$

or

$$M \geq \log_2 \sum_{k=2}^{k=2^N} \frac{(k-1)!}{\left(\frac{2^N}{k}\right)_E} \binom{2^N}{k}.$$

Since $\sum_{k=2}^{k=2^N} k! \binom{2^N}{k}$ doubles have been used in describing all modes of oscillation, we can arbitrarily assign one and only one S_j to each of the remaining doubles; that is, to $2^{M+N} - \sum_{k=2}^{k=2^N} k! \binom{2^N}{k}$ doubles. This could be, for example, the state $S_{000\dots 00}$ to all of the doubles left.

THEOREM. Given N neurons and M input lines such that

$$M \geq \log_2 \sum_{k=2}^N \frac{(k-1)!}{\left(\frac{2^N}{k}\right)_E} \cdot \binom{2^N}{k},$$

it is always possible to design an \mathcal{N} -network that verifies all possible modes of oscillation.

Proof. All possible modes of oscillation of N neurons can be expressed by a set $v(N, M)$ of successors such that

$$M \geq \log_2 \sum_{k=2}^N \frac{(k-1)!}{\left(\frac{2^N}{k}\right)_E} \binom{2^N}{k} \quad (\text{Lemma 2}).$$

According to Lemma 1, it is always possible to design an \mathcal{N} -network that verifies any $v(N, M)$, in particular, that which describes all possible modes of oscillation.

The minimum number of jots, \mathcal{N} , per Venn diagram for such an \mathcal{N} -network is the same for all of the neurons of the network. This number can be computed as follows. The number of modes of oscillation that pass through any one state is

$$\sum_{k=2}^N (k-1)! \binom{2^N-1}{k-1}.$$

This number gives the number of doubles that correspond to the same S_j in all successors $(S_i, W_k) \rightarrow S_j$. In describing the first neuron, for example, we put jots in the Venn areas for which S_j indicates that the neuron fires. There are 2^{N-1} of these states S_j . Therefore, the number of jots, \mathcal{N} , for the Venn of that neuron is at least

$$\mathcal{N} = 2^{N-1} \cdot \sum_{k=2}^N (k-1)! \binom{2^N-1}{k-1},$$

and \mathcal{N} is the same for all neurons.

R. Moreno-Diaz

References

1. C. P. G. Schnabel, "Number of Modes of Oscillation of a Net of N Neurons," Quarterly Progress Report No. 80, Research Laboratory of Electronics, M. I. T., January 15, 1966, p. 253.

2. W. S. McCulloch, Embodiments of Mind (The M.I.T. Press, Cambridge, Mass., 1965), pp. 203-215.
3. M. Blum, "Properties of a Neuron with Many Inputs," Principles of Self-Organization, H. Von Foerster and R. Zopf (eds.) (Pergamon Press, Oxford, London, New York and Paris, 1962), pp. 95-119.

XXIII. CARDIOVASCULAR SYSTEMS*

Academic and Research Staff

Prof. W. D. Jackson
Prof. P. G. Katona
Dr. G. O. Barnett

Graduate Students

A. N. Chandra
J. F. Young

A. STATUS OF RESEARCH

Work has continued on the analysis of the blood-pressure regulatory system, with emphasis placed on the detailed understanding of the functioning of the components that constitute this system. Arnold N. Kramer and Michael C. Raezer completed Bachelor's theses on "Irregularities in the Normal Heart Beat: A Statistical Analysis," and "Nerve Firing Patterns of Cardio-Inhibitory Vagus Nerve Fibers," respectively. A short account of their results follows.

1. Irregularities in the Normal Heart Beat: A Statistical Analysis

It has been observed¹ that the heart period (reciprocal of heart rate) of chloralose-anaesthetized dogs becomes irregular when high blood pressure raises heart period above a critical value. This is illustrated in Fig. XXIII-1, which shows that to the right of arrow B the heart period undergoes very large and sudden variations. Similar results can be obtained by raising the heart period with morphine. The origin of these irregular beats is vagal, since atropine or the sectioning of the vagus nerves abolishes the effect. The ECG appears to be completely normal during these irregular beats: neither the P-wave nor the P-Q interval shows any discernible change.

Although some results have been reported on the statistical properties of heart period during atrial fibrillation,^{2,3} the irregularity during normal beating described above does not appear to have been studied. The purpose of this work is to obtain preliminary results on some of the statistical properties of these irregular beats. The techniques that are used are similar to those described by Gerstein and Kiang⁴ and Rodieck et al.⁵ for the analysis of interspike intervals of auditory neurons. Throughout the investigation great care is exercised to choose stretches of stationary data, since the results vary with the depth of anaesthesia of the experimental animal.

An illustration of the results obtained in a dog during a run consisting of 379 cardiac cycles is shown in Fig. XXIII-2. Figure XXIII-2a shows the distribution of heart periods

* This work was supported by the Joint Services Electronics Programs (U. S. Army, U. S. Navy, and U. S. Air Force) under Contract DA 36-039-AMC-03200(E).

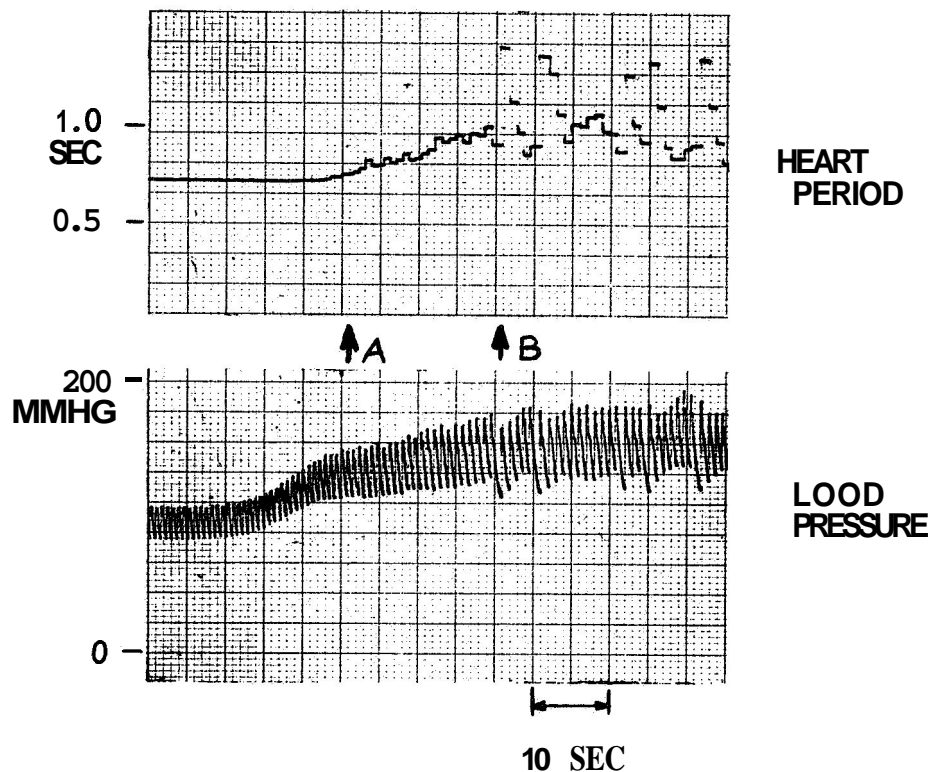


Fig. XXIII-1. Development of irregular heart rate at a high level of blood pressure and heart period. The pressure was raised by the infusion of Levophed.

in the form of a histogram, while Fig. XXIII-2b displays dependence between successive heart beats in the form of a joint interval histogram.⁵ Figure XXIII-2c and 2d shows conditional histograms. The first one gives the distribution of heart periods of those beats that follow a short beat (shorter than the average), and the second gives the distribution of heart periods of those beats that follow a long beat (longer than the average). Figure XXIII-2e is a plot of the average heart period as a function of the duration of the preceding beat. These values of the "conditional mean" can be obtained by the averaging of vertical slices of the joint interval histogram.⁵ Finally, Fig. XXIII-2f is a stretch of the original record, showing heart period as a function of time. Each jump corresponds to one heart beat.

The interesting feature of this record is that the heart period is mainly clustered about three values. This is shown by the three peaks in the histograms, the three clusters of points in the joint interval histogram, and the three horizontal bands of density in the original recording. The plot of conditional means indicates that, on the average, long beats tend to follow short ones, and short beats to follow long ones.

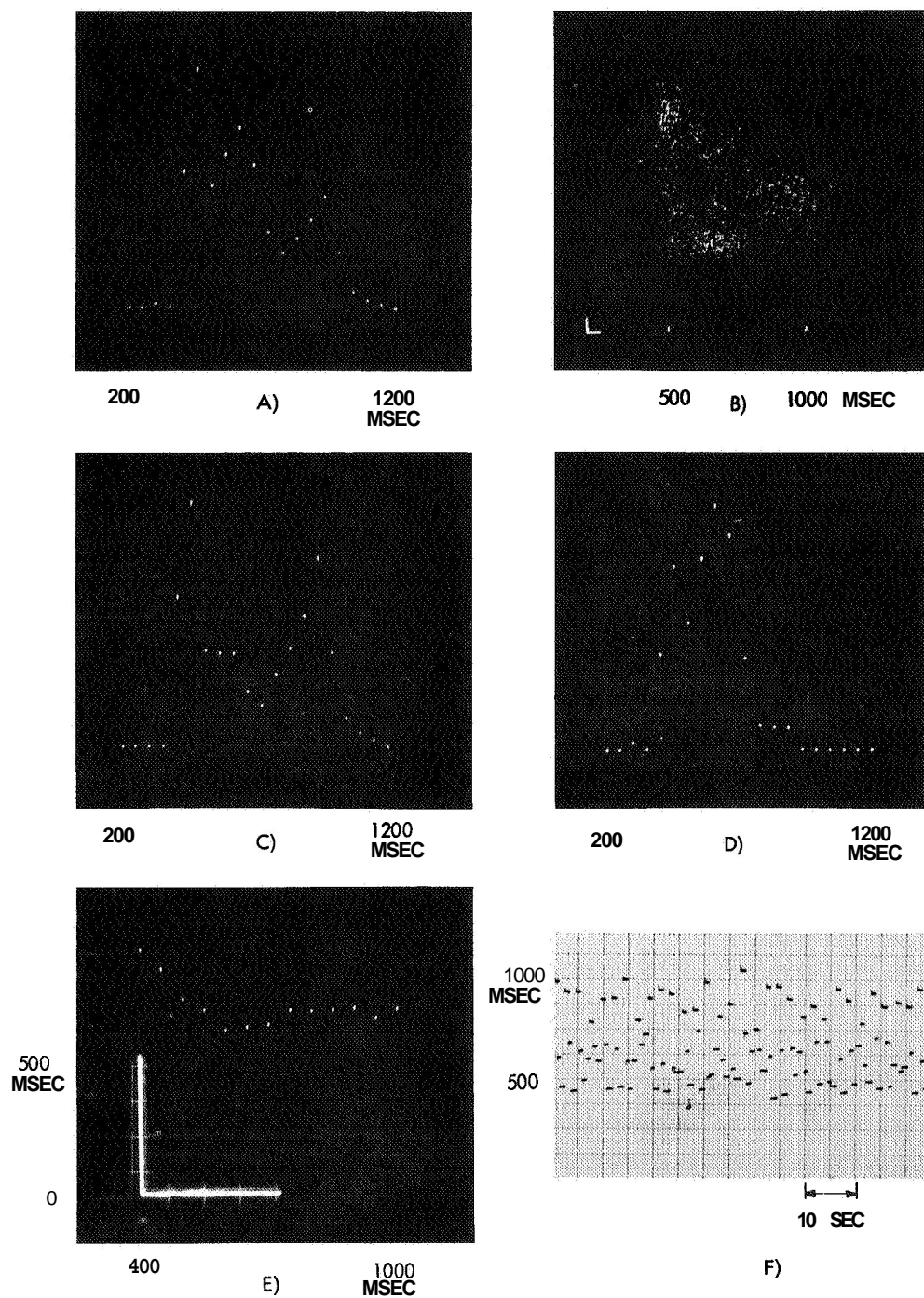


Fig. XXIII-2. Distribution of lengths of irregular heart periods. (a)Histogram. (b)Joint interval histogram. (c) Conditional histogram of beats following a short beat. (d) Conditional histogram of beats following a long beat. (e) Conditional mean vs length of previous heart beat. (f) Heart period vs time.

2. Nerve Firing Patterns of Cardio-Inhibitory Vagus Nerve Fibers

It is well known that the heart rate is influenced by the sympathetic (accelerator) and vagus (decelerator or cardio-inhibitory) nerves. It is also known that short, transient changes of blood pressure affect the speed of the heart primarily through the vagus nerves. As part of the pressure regulatory reflex, a rise in the pressure reflexly increases the vagal firing frequency, thereby slowing the heart, while a drop in the pressure inhibits vagal firing and causes an increase in heart rate.

Recently, several characteristics of the control loop which changes heart rate as a result of a change in blood pressure have been described.¹ The system was shown to be nonlinear, but the physiological mechanism responsible for the nonlinearity was not determined. In order to characterize the system more completely, it is desirable to record the neural activity both on the afferent (pressure receptor) and efferent (vagal) side. This work is concerned with the recording and analysis of the efferent cardio-inhibitory vagal activity.

Reports of successful recordings from the efferent vagal fibers have appeared quite recently. Weidinger, Hetzel and Schaefer⁶ have reported that, in the cat, small vagal fibers in the vicinity of the heart show discharges with a cardiac rhythm. Calaresu and Pearce,⁷ however, failed to see any activity with a cardiac rhythm in the cervical vagus of the cat, and questioned the accuracy of the findings of Weidinger. Shortly before this, Jewett⁸ reported recording from cardiovascular fibers of the cervical vagus of the dog. These fibers showed cardiac synchronization, although the initial burst of activity shortly following the systolic rise of the blood pressure was not nearly as conspicuous as is the well-known, sudden increase in the activity of the pressure receptors during the steep rise in the pressure.

Thus far, we have recorded efferent vagal activity from the cervical vagus of three anaesthetized dogs and one cat. Computer analysis has shown that out of the 37 firing patterns examined, 22 exhibited a cardiac rhythm. Three of these recordings were obtained from the cat. For several preparations it was demonstrated that a slowing of the heart was preceded by an increase in vagal firing frequency.

Further work is being done on the quantitative characterization of the relationships between blood pressure and efferent vagal firing frequency, and between efferent vagal firing frequency and heart rate.

The technical assistance of N. Pantelakis and J. Poitras of the Massachusetts General Hospital in obtaining the nerve recordings is gratefully acknowledged.

P. G. Katona

References

1. P. G. Katona, "Computer Simulation of the Blood Pressure Control of Heart Period," Sc.D Thesis, Department of Electrical Engineering, M. I. T. , June 1965.

(XXIII. CARDIOVASCULAR SYSTEMS)

2. J. R. Braunstein and E. K. Franke, "Autocorrelation of Ventricular Response in Atrial Fibrillation," *Circulation Res.* 9, 300 (1961).
3. E. J. Battersby, "Pacemaker Periodicity in Atrial Fibrillation," *Circulation Res.* 17, 296 (1965).
4. G. L. Gerstein and N. Y. S. Kiang, "An Approach to the Quantitative Analysis of Electrophysiological Data from Single Neurons," *Biophys. J.* 1, 15 (1960).
5. R. W. Rodieck, N. Y. S. Kiang, and G. L. Gerstein, "Some Quantitative Methods for the Study of Spontaneous Activity of Single Neurons," *Biophys. J.* 2, 351 (1962).
6. M. Weidinger, R. Hetzel, and M. Schaefer, "Aktionsströme in zentifugalen vagalen Herznerven und deren Bedeutung für den Kreislauf," *Pflügers Arch.* 276, 262 (1962).
7. F. R. Calaresu and J. W. Pearce, "Electrical Activity of Efferent Vagal Fibres and Dorsal Nucleus of the Vagus during Reflex Bradycardia in the Cat," *J. Physiol.* 176, 228 (1965).
8. D. L. Jewett, "Activity of Single Efferent Fibres in the Cervical Vagus Nerve of the Dog with Special Reference to Possible Cardio-inhibitory Fibres," *J. Physiol.* 175, 321 (1964).

XXIV. COMPUTATION RESEARCH*

Research Staff

Martha M. Pennell
T. H. Brooks

Gail M. Fratar

Veronica E. McLoud
R. M. Nacamuli

A. A COMPUTER INDEXING PROGRAM

Today there are several indexes (e. g., KWIC, Chemical Titles) which have been prepared essentially by computer techniques. For the most part the computer programs involved are too sophisticated to be used for indexing a small number of titles such as would be found in one's personal library or that of a small research group.

We have written a computer program that permutes and alphabetizes the key words in a title of, at most, 132 characters for a maximum of 70 titles. The index obtained consists of entries 132 characters wide with the key word made to lie in column 67 and the rest of the title shifted and folded over if it extends beyond the allotted length.

The most difficult obstacle to overcome in such a program is to define what is meant by a key word. In our program a key word was said to have at least four letters. After alphabetization those entries in the index whose key words were not of interest were manually discarded. Such a method is possible only if the number of titles is small. Some other indexing programs have used a table of non-key words which the program referred to each time. Such a method has the disadvantage that titles consisting of non-key words are ignored. Moreover, if several groups with diverse interests are to use such a program, the table of non-key words changes radically and must be reconstructed each time.

Thus far, we have indexed 212 titles with the following results:

output	1555	titles
Acceptable titles	1275	
Unacceptable titles	286	
Number of acceptable key words	75	
Average occurrence	3.73	
Percentage of unacceptable titles	8%	

The program is now being used to help update "Basic Data." ¹

Martha M. Pennell, R. M. Nacamuli

*This work was supported in part by the Joint Services Electronics Programs (U. S. Army, U. S. Navy, and U. S. Air Force) under Contract DA 36-039-AMC-03200(E).

References

1. S. C. Brown, Quarterly Progress Report No. 80, Research Laboratory of Electronics, M.I.T., January 15, 1966, pp. 83-85.

B. EXAMPLE OF SYMBOLIC MANIPULATION OF POLYNOMIALS IN MAD

The ease of solution of numerical problems by means of a digital computer is often lessened by necessary prior tedious mathematical manipulations such as the example discussed here, the multiplication of polynomials. The problem from which this example arose is the following.

$$\text{Let } x = \sin \theta \cos \phi, \quad y = \sin \theta \sin \phi, \quad z = \cos \theta \quad (1)$$

$$w_1 = x^4 + y^4 + z^4 - 3/5$$

$$w_2 = x^6 + y^6 + z^6 - 15/11[x^4 + y^4 + z^4] + 30/77 \quad (2)$$

$$w_3 = x^8 + y^8 + z^8 - 28/15[x^6 + y^6 + z^6] + 154/143[x^4 + y^4 + z^4] - 7/39.$$

Let $f(x, y, z)$ be a product of 2 to 4 factors each of which is w_1 , w_2 or w_3 . We want to evaluate integrals of the form

$$\int_0^{2\pi} d\phi \int_0^\pi f(x, y, z) \sin \theta d\theta. \quad (3)$$

We can approach the problem in two ways, either by numerical approximation or formal integration. The latter method, which is preferable, would involve so much tedious algebra to expand the product $f(x, y, z)$ that it would be futile to attempt it unless the process could be mechanized. Investigation proved that this could be done quite easily.

Our problem is to find an algorithm that will construct symbolically the product $P(x, y, z) \cdot Q(x, y, z)$, where P, Q are polynomials in x, y, z .

If n is the highest power of x, y, z occurring in P , then P can be represented by the $(n+1) \times (n+1) \times (n+1)$ array $P1$, where $P1(I, J, K)$ is the value of the coefficient of the term $P(x, y, z)$ in which the powers of x, y, z are I, J, K , respectively. If m is the highest power of x, y, z occurring in Q , then Q can be defined similarly by an $(m+1) \times (m+1) \times (m+1)$ array $Q1$. If we define a new array ANS , where $ANS(I', J', K')$ is the coefficient of the term of the product $P(x, y, z) \cdot Q(x, y, z)$ in which the powers of x, y, z are I', J', K' , then

$$\text{ANS}(I', J', K') = \sum_{\substack{I+II=I' \\ J+JJ=J' \\ K+KK=K'}} P1(I, J, K) \cdot Q1(II, JJ, KK).$$

This algorithm was programmed in the MAD¹ language as listed below. Here $X1, Y1, Z1$ are the maximum pbwers of x, y, z in $P(x, y, z)$, and $X2, Y2, Z2$ are the maximum powers of x, y, z occurring in $Q(x, y, z)$.

```

EXTERNAL FUNCTION(P1,Q1,ANS,X1,Y1,Z1,X2,Y2,Z2)
E'C MULT.
INTEGER I,J,K,II,JJ,KK,X1,Y1,Z1,X2,Y2,Z2
T'H ZERO, FOR I=0,1,I.G.X1+X2+1)*(Y1+Y2+1)*(Z1+Z2+1)
ZERO
ANS(I)=0.
T'H LOOP, FOR I=C,1,I.G.X1
T'H LOOP, FOR J=C,1,J.G.Y1
T'H LOOP, FOR K=C,1,K.G.Z1
T'H LOOP, FOR II=C,1,II.G.X2
T'H LOOP, FOR JJ=C,1,JJ.G.Y2
T'H LOOP, FOR KK=C,1,KK.G.Z2
LOOP
ANS(I+II,J+JJ,K+KK)=ANS(I+II,J+JJ,K+KK)+P1(I,J,K)
I*Q1(II,JJ,KK)
FUNCTION RETURN
E'N

```

The routine may be called repeatedly if the product of more than two polynomials (2) is desired. From (1) the powers of $\sin \theta$, $\cos \theta$, $\sin \phi$, $\cos \phi$ in the term whose coefficient is $\text{ANS}(I', J', K')$ are easily obtained. The desired integration (3) can now be performed analytically term by term with the use of the recurrence relation

$$\int \sin^m x \cos^n x dx = \frac{\sin^{m+1} x \cos^{n-1} x}{m+n} + \frac{n-1}{m+n} \int \sin^m x \cos^{n-2} x dx,$$

$m, n > 0.$

The calling program and the subroutine were debugged and run on the time-sharing system at the Computation Center, M. I. T.

Veronica E. McLoud, Martha M. Pennell

References

1. B. Arden, B. Galler and R. Graham, "The Michigan Algorithm Decoder," University of Michigan, April 1965.

Author Index

- Allen, R. J. , 17
 Andrews, J. M. , Jr. , 12, 16
 Assael, D. , 251
 Barrett, A. H. , 17, 30
 Bartsch, R. R. , 131
 Bernard, G. D. , 152
 Bers, A. , 154, 187
 Billman, K. W. , 1
 Bose, A. G. , 207, 208
 Braida, L. , 252
 Brown, J. E. , III, 251
 Bruce, J. D. , 208
 Chikhaoui, M. T. , 228
 Clarke, J. F. , 193
 Clavton, R. J. , 254
 Cohen, D. , 237
 Cunningham, A. W. B. , 258
 Davis, J. A. , 146
 Durlach, N. I. , 250
 Engelmaier, W. , 71
 Fehrs, D. L. , 77
 Fischler, H. , 263
 Flannery, D. L. , 97
 Gabrielian, A. , 225
 Gadzuk, J. W. , 65
 Gaut, N. E. , 33
 Gentle, K. W. , 90
 Getty, W. D. , 131, 138, 144
 Hahn, J. M. , 247
 Haus, H. A. , 91
 Hayashi, S. J. , 248
 Heller, J. A. , 209
 Houtsma, A. J. , 252
 Huang, T. S. , 223, 225, 228
 Hutchinson, J. D. , 173
 Ingraham, J. C. , 99, 123
 Jordan, N. , 252
 Katona, P. G. , 287
 Kerrebrock, J. L. , 183
 Kierstead, J. D. , 11
 Kilmer, W. L. , 275
 Kinsey, J. L. , 7
 Kolers, P. A. , 221
 Krakauer, L. , 252
 Kronquist, R. L. , 109
 Kuroda, S.-Y. , 215
 Kusse, B. , 154
 Lehr, J. L. , 249
 Lenoir, W. B. , 33, 36
 Llewellyn-Jones, D. T. , 93
 Lou, S. , 83
 Mattison, E. M. , 93
 MacDonald, R. L. , 249
 McCulloch, W. S. , 275
 McCune, J. E. , 184
 McLoud, Veronica E. , 294
 McWhorter, A. L. , 91
 Moreno-Diaz, R. , 280
 Nacamuli, R. M. , 293
 Neal, R. W. , 30
 Novenski, A. E. , 123
 O'Lague, P. H. , 258
 Papadopoulos, G. D. , 30
 Parker, R. R. , 127
 Pauwels, H. J. , 55
 Penfield, P. , Jr. , 91
 Pennell, Martha M. , 293, 294
 Perozek, D. M. , 138
 Perry, C. H. , 45, 48
 Pierson, E. S. , 173
 Plice, W. A. , 111, 249
 Rafuse, R. P. , 43
 Reifenstein, E. C. , 30
 Reilly, R. D. , 144
 Reintjes, J. F. , Jr. , 48
 Rogers, A. E. E. , 30
 Rogoff, G. L. , 114
 Rose, D. J. , 163, 169
 Samis, M. A. , 193
 Schneider, H. M. , 154
 Schulz, H. M. , III, 87, 90
 Schwartz, P. R. , 33
 Silk, J. D. , 99
 Skull, C. G. , 1
 Speck, C. E. , 187
 Staelin, D. H. , 33
 Stickney, R. E. , 71, 77, 83
 Strandberg, M. W. P. , 9, 10, 11
 Thome, R. J. , 177
 Tweed, D. G. , 249
 Van Trees, H. L. , 207, 208
 Wedgwood, F. A. , 1
 Woo, J. C. , 163, 169
 Wrigley, J. D. , Jr. , 45
 Yamamoto, S. , 83
 Yilmaz, H. , 267

PRECEDING PAGE BLANK NOT FILMED.